Non-invasive cytometry of tumours using diffusion MRI, measuring water exchange across the cell membrane with Diffusion Exchange Spectroscopy (DEXSY)

A thesis submitted in fulfilment

of the degree of Doctor of Philosophy by

James Olav Breen-Norris

Division of Medicine

UCL

26/04/2019

I James Olav Breen-Norris confirm that the work presented in this thesis is my own. Where information is derived from other sources, I confirm that this has been indicated in the thesis.

26/04/2019

Abstract: The aim of this thesis was to develop a technique to carry out non-invasive cytometry in tumours using diffusion MRI, by measuring water exchange across the cell membrane. My thesis is built on previous work done to characterise tumour micro-structure in-vivo, using Vascular Extracellular and Restricted Diffusion for Cytometry in Tumours (VERDICT) MRI by E. Pangiotaki and S. Walker-Samuel et al. [81], and work on Diffusion Exchange Spectroscopy (DEXSY) by Dr Bernard Siow [93] and P. T. Callaghan who first developed DEXSY as a technique for studying porous media [18]. In particular I aimed to develop DEXSY to measure cell membrane permeability. These advanced diffusion MRI techniques could reduce the need for invasive tissue biopsies, enable earlier diagnosis and better monitoring of disease progression in cancer, through in-vivo characterisation of tissue micro-structure. These advanced diffusion techniques could also be used to gain a better understanding of barriers to drug delivery in mouse models of cancer. I have developed a biological phantom for validating diffusion MRI techniques, and used physical phantoms to demonstrate the accuracy of diffusion measurements made with DEXSY. My computational simulations suggest that DEXSY can be used to provide a quantitative indicator of cell membrane permeability, as I observe a monotonic relationship between Diffusion Exchange Index (DEI) and permeability in-silico, for a range of permeabilities greater than the physiological range. The DEXSY data acquired from yeast phantoms confirm that we can observe diffusion exchange in-vitro with this technique. Further work to evaluate the technique in-vivo suggests that DEXSY is sensitive to diffusion exchange and tissue micro-structure in tumours. The work in this thesis demonstrates that DEI could be used as a quantitative indicator of cell membrane permeability, and as a potential imaging biomarker in cancer.

Impact statement: The findings presented in this thesis suggest that DEXSY may be used to make in-vivo measurements of diffusion exchange, and that Diffusion Exchange Index (DEI) could be used as a quantitative indicator of cell membrane permeability, in a range of pathologies including neurological disorders and cancer. If DEXSY can be successfully adapted for preclinical and clinical imaging, then DEI can be used as an imaging biomarker in cancer. As such it is possible that in the future DEXSY could be applied in clinical radiology to diagnose and stage cancer. It is also clear that DEXSY can be used for research, in the fields of neuroscience and cancer research, to evaluate variations in cell membrane permeability in health and disease. The biological phantom presented in this thesis could be used by other researchers as a tool to validate new MRI techniques. The research impact of the work that contributed towards this thesis can be seen in the 5 international conference abstracts which have been published and the journal article that has been accepted for publication. In addition to this one journal article is currently in preparation, and one new international conference abstract has been submitted.

Contents

List of Tables

List of Figures

Chapter 0

Acknowledgements, publications and thesis structure

0.1 Acknowledgements

I am grateful to Petrik Galvosas (Victoria University of Wellington) for providing the inverse Laplace software and Dr Damien McHugh (University of Manchester) for providing the yeast substrate. My supervisors and I have received funding from Kings College London and UCL, CR-UK and EPSRC Comprehensive Cancer Imaging Centre, in association with the MRC and Department of Health (England) (C1519/A10331), the Wellcome Trust (WT100247MA) and EPSRC (M020533/N018702/R006032). I also acknowledge the assistance provided by Dr Claire Walsh and Dr John Connell who enabled the in-vivo experiments by taking responsibility for anaesthesia and assisting with animal handling. Dr Claire Walsh also produced the two phantoms made using the raft 3D culture kit. I would like to thank Yanan Zhu for teaching me the basics of tissue culture and cancer biology, and I would also like to thank Dr Stephen Patrick and Dr Thomas Roberts for their advice on experiments. Whilst Dr Andrada Ianus has provided advice and guidance on the simulations presented in this thesis. I also acknowledge the contribution made by Dr Matt Hall who modified CAMINO in order to enable the implementation of the fluid-exchange model of diffusion exchange. I am grateful to Dr Bernard Siow for writing the DEXSY sequences used in this

thesis and for his advice and guidance. I am also grateful to Dr Simon Walker-Samuel and Professor Daniel Alexander for their supervision and guidance over the period in which the work contained in this thesis was produced. I would also like to acknowledge the support provided by my father Dennis Graham Norris.

0.2 Publications

International conference abstracts

Simulating measurements of diffusion across the cell membrane with DEXSY and FEXSY, James O Breen-Norris, Bernard Siow, Ben Hipwell, Ioana Oprea, Thomas A. Roberts, Mark F. Lythgoe, Andrada Ianus, Daniel C. Alexander, Simon Walker-Samuel, Proceedings of ISMRM 2017, Honolulu, HI, USA, Abstract 1740

Assessing the feasibility of measuring the diffusion exchange of water in nerve tissue using diffusion exchange spectrocopy (DEXSY), James O. Breen-Norris, Bernard Siow, Thomas A. Roberts, Andrada Ianus, Simon Walker-Samuel, Proceedings of ICMRM 2017, Halifax, Nova Scotia, Canada, P64

Using Diffusion Exchange Spectroscopy (DEXSY) to observe diffusion exchange in yeast, James O. Breen-Norris, Bernard Siow, Ben Hipwell, Thomas A. Roberts, Mark F. Lythgoe, Andrada Ianus, Daniel C. Alexander, Simon Walker-Samuel, Proceedings of MRPM, Gainsville, Florida, USA, P26, 2018

Measurement of diffusion exchange in yeast with Diffusion Exchange Spectroscopy (DEXSY), James O. Breen-Norris, Bernard Siow, Ben Hipwell, Thomas A. Roberts, Mark F. Lythgoe, Andrada Ianus, Daniel C. Alexander, Simon Walker-Samuel, Proceedings of ISMRM 2018, Paris, France, Abstract 1104

Understanding the relationship between DEXSY (diffusion-diffusion exchange spectroscopy) measurements and cell membrane permeability in yeast in-silico and in-vitro, James Breen-Norris, Bernard Siow, Ben Hipwell, Ioana Hill, Thomas

A. Roberts, Mark F. Lythgoe, Andrada Ianus, Daniel C. Alexander, Simon Walker-Samuel, Proceedings of ISMRM Workshop on Advances in Multiscale Cancer Detection: From Micro to Macro, Dublin, Ireland, P6, 2018

In-vivo Diffusion Exchange Spectroscopy (DEXSY), to measure water exchange in tumours. James O. Breen-Norris, Bernard Siow, Claire Walsh, Mark. F. Lythgoe, Andrada Ianus, Daniel C. Alexander, Simon Walker-Samuel, submitted as an abstract to be presented at ISMRM 2019, Montreal, Canada

Journal articles

Using Diffusion-Diffusion Exchange Spectroscopy to observe diffusion exchange in yeast, James O. Breen-Norris, Bernard Siow, Ben Hipwell, Thomas A. Roberts, Mark F. Lythgoe, Andrada Ianus, Daniel C. Alexander, Simon Walker-Samuel, *accepted diffusion-fundamentals.org volume 31 (2018)*

Measuring diffusion exchange across the cell membrane with DEXSY (Diffusion Exchange Spectroscopy), James O. Breen-Norris, Bernard Siow, Claire Walsh, Ben Hipwell, Ioana Hill, Mark F. Lythgoe, Andrada Ianus, Daniel C. Alexander, Simon Walker-Samuel, In preparation for Magnetic Resonance in Medicine

Publications to which the author has contributed

Quantification of tumour microstructure in low and high-grade brain tumours using VERDICT MRI: an initial feasibility study, Thomas A. Roberts, Harpreet Hyare, Ben Hipwell, Andrada Ianus, James O. Breen-Norris, Eleftheria Panagiotaki, David Atkinson, Shonit Punwani, Jeremy Rees, Sebastian Brandner, Daniel Alexander, Simon Walker-Samuel, Neuro-oncology, 2018

Quantifying microstructure in low and high-grade brain tumours using VERDICT MRI, Thomas A. Roberts, Harpreet Hyare, Ben Hipwell, Andrada Ianus, James O. Breen-Norris, Eleftheria Panagiotaki, David Atkinson, Shonit Punwani,

Jeremy Rees, Sebastian Brandner, Daniel C. Alexander, Simon Walker-Samuel, Proceedings of the International Society for Magnetic Resonance in Medicine 2017, Honululu, HI, USA, Abstract 3394

0.3 Structure of the thesis

In this thesis there are nine chapters, the first chapter gives a brief introduction to the thesis and describes the purpose of the thesis. The second chapter provides a context to the work presented in the thesis, whilst chapter three provides the theory necessary to understand the contents of the thesis. Chapters four to eight present experimental data including results from biological phantoms, data acquired using DEXSY from physical and chemical phantoms, simulations measuring diffusion exchange across the cell membrane with DEXSY and FEXSY, in-vitro data acquired with DEXSY from yeast suspensions and in-vivo data acquired with DEXSY from tumour xenograft models. The final chapter presents a discussion of the contents of the thesis and a conclusion to the thesis.

Chapter 1

Introduction

1.1 Background

Cancer is one of the world's leading causes of death, responsible for 11.8 % of female and 13.4 % of male deaths globally [106]. Cancer is characterised by uncontrolled cell growth and proliferation, which can lead to the eventual spread of the disease, through the invasion of neighbouring tissue and metastasis [41]. Early diagnosis is vital in order to effectively treat cancer [29]. However the identification of clinically insignificant disease or over-diagnosis, may lead to over-treatment [92]. Structural imaging techniques such as planar X-ray, X-ray CT, ultrasound and structural MRI are used to locate potential tumours and to identify the response of a tumour to treatment. However these techniques are typically only used to identify the gross structural changes that occur in tumours, such as changes in size and shape. X-ray imaging works by measuring the attenuation of X-rays travelling through the body, whilst structural MRI works through the detection of a spatially localised NMR signal [14]. Functional techniques such as nuclear medicine procedures, including FDG-PET are often used to track the spread of the disease through metastasis, as they are sensitive to metabolic changes that occur in cancer such as the Warburg effect [29].

Although there has been great progress in the field of medical imaging the information provided by imaging techniques is still limited, and in many cases

biopsies are still required in order to make a diagnosis. However biopsies are invasive and only extract a small tissue sample, which can result in false negatives [1]. A non-invasive imaging technique for characterising tissue microstructure, could enable accurate diagnosis of cancer with fewer invasive biopsies.

Diffusion MRI is a technique that probes tissue micro-structure through the motion of water [22]. Recently a new diffusion MRI technique has been developed specifically to quantify tissue micro-structure, this technique is called VERDICT (Vascular Extracellular and Restricted Diffusion for Cytometry in Tumours) MRI. VERDICT provides estimates of cell size and intracellular volume fraction, but it does not account for cell membrane permeability [81]. The aim of this thesis was to develop Diffusion Exchange Spectroscopy (DEXSY) as a technique for measuring diffusion exchange across the cell membrane. Cell membrane permeability alters through cell death via apoptosis, oncosis and necrosis [58, 7, 28]. Aquaporins regulate water transport in and out of the cell, and aquaporin expression also alters between healthy cells and cancer cells [65]. A quantitative indicator of cell membrane permeability could help differentiate healthy and diseased tissue, as well as monitor response to cancer therapy. Measurement of diffusion-diffusion exchange across the cell membrane with DEXSY could be used to calculate a quantitative indicator of cell membrane permeability. A quantitative indicator of cell membrane permeability could also serve as a potential biomarker in cancer. There is a clinical need for more comprehensive microstructure measurements, and DEXSY could help fulfil this need.

1.2 Purpose

There is currently a clear need to understand how diffusion MRI acquisitions, can be confounded by diffusion exchange across the cell membrane. There is also a clear scientific and clinical need to quantify water transport across the cell membrane and cell membrane permeability. This is because water transport in and out of the cell is a vital physiological process, that alters in health and disease.

Measuring water transport across the cell membrane is necessary, to understand cellular physiology and could be required to characterise certain pathologies. Any quantitative measure of cell membrane permeability is also a potential biomarker in cancer. The comprehensive measurement of diffusion exchange in-vivo, could also enable the robust measurement of cell membrane permeability. As such there is currently a need for a method to make comprehensive measurements of diffusion exchange in tumours, in-order to provide a quantitative indicator of cell membrane permeability, in cancer. The purpose of the work presented in this thesis is to fulfil these needs and to develop DEXSY as a method for making comprehensive measurements of diffusion exchange across the cell membrane in tumours, and to use these measurements to produce a quantitative indicator of cell membrane permeability in cancer. A quantitative indicator of cell membrane permeability could potentially enable earlier diagnosis, assist in monitoring treatment response and enable the characterisation of cells in malignant disease.

In this thesis there are nine chapters, the first three are introductory. The structure of the thesis is such that phantom work and simulation work, carried out to validate DEXSY are presented first. In-vitro work in yeast suspensions is then presented as the final step before in-vivo validation of DEXSY. In the fourth chapter the aim of the work presented is to develop a biological phantom for validating diffusion MRI techniques. Significant progress is made towards this goal. In chapter five the aim is to make diffusion exchange measurements using DEXSY in chemical and physical phantoms. The experiments with chemical phantoms demonstrate the accuracy of diffusion measurements made using DEXSY. In chapter six the aim is to use numerical simulations to demonstrate the feasibility of measuring diffusion exchange across the cell membrane. The results of the simulations presented demonstrate that DEXSY can measure diffusion exchange in a nervous tissue substrate and a yeast substrate in-silico. The results also demonstrate that the Diffusion Exchange Index (DEI) can be used as a quantitative indicator of cell membrane permeability in-silico. In chapter seven in-vitro diffusion exchange measurements made in a yeast suspension provide in-vitro

validation of the yeast substrate simulations. In chapter eight the final experimental chapter DEXSY is evaluated in-vivo. The in-vivo DEXSY data acquired from tumour xenograft models suggests that DEXSY can measure diffusion exchange in-vivo. Chapter nine is the final chapter and the thesis concludes by suggesting that DEXSY can measure diffusion exchange in tumours in-vivo, and that DEI is a quantitative indicator of cell membrane permeability and a potential imaging biomarker in cancer.

Chapter 2

Cancer Imaging

2.1 Introduction

The introduction explained the purpose of this thesis, and this chapter gives an overview of cancer imaging and provides context for our application of DEXSY to cancer. In section 2.1 cancer is introduced and in section 2.2, the cell membrane is described and the potential of any quantitative indicator of cell membrane permeability to serve as a biomarker in cancer is discussed. Whilst section 2.3 gives a brief overview of cancer imaging techniques which leads on to section 2.4, which explains how diffusion MRI can be applied to cancer in order to provide information about tissue micro-structure and potentially even cell membrane permeability. The next chapter covers diffusion MRI.

2.2 Cancer

Cancer is a group of diseases including breast cancer, prostate cancer, and Hodgkin's lymphoma, that develop from seemingly normal tissue. In cancer, the body attacks itself, and malignant disease can emerge from any of the body's tissues. Tumours are formed from uncontrolled cell growth and proliferation, a tumour that is able to invade neighbouring tissue is malignant, and a tumour that is unable to invade neighbouring tissue is benign. The spread of this pathology throughout the body is known as metastasis. Malignant tumours are cancerous

but there are also other forms of metastatic disease such as leukaemia. Carcinomas are the most common form of tumour and these form from epithelial cells [105].

Tumours form from colonies that grow from cells that have undergone mutations causing uncontrolled cell growth [75]. Cancer cells are characterised by a number of properties, including an increased rate of cell growth, an increased rate of cell proliferation, and a decreased rate of cell death [41]. As a result we find that cancer cells are often larger than the healthy cells found in neighbouring tissue [55], and that there is often an increased cell density in tumours [56]. These properties are due to alterations in a number of important cell signalling pathways regulating cell growth, proliferation and cell death. The cell signalling pathways affected include the Ras pathway which affects cell proliferation [30]. Other cell signalling pathways affected include the p53 pathway associated with the regulation of cell death through apoptosis [28], and the pathways controlling cell growth such as the mTORC pathway, which also regulates cell size [55, 41]. These cells evolve, with the most rapidly proliferating cells dominating the colony. As a colony evolves it grows to form a mass known as a tumour. The process of clonal evolution is known as tumourogenesis [75]. Tumours typically have disrupted vasculature which, in many tumours, results in hypoxia. The extracellular matrix also differs in tumours and the tumour stroma is often stiffer than in healthy tissue [35].

Invasion and metastasis are the processes by which cancer spreads throughout the body. During invasion cancer cells emerge from a primary tumour and grow into neighbouring tissue. Metastasis occurs when some of these cells break off and enter into the blood stream or lymphatics (and other routes), which transports the cells into another part of the body, where cells settle and grow into a colony of cells that form a secondary tumour [31]. Certain cancers are more likely to form secondary tumours in specific organs, for example, colorectal cancer is more likely to form metastases in the liver. As with primary tumours angiogene-

sis can occur enabling tumours to grow so large that they can kill their host, the majority of cancer deaths are due to metastases [8].

2.3 Cell membrane permeability in cancer

The cell membrane consists of a lipid bilayer, which is considered to be almost impermeable to water-soluble molecules, although it is possible for water to diffuse across the lipid bilayer. The cell membrane is punctuated by trans-membrane transport proteins that allow water and larger molecules in and out of the cell. Lipids with a hydrophobic tail and a hydrophilic head form the lipid bilayer as the heads face the cytoplasm and the extracellular fluid whereas the hydrophobic tails face each other. There are trans-membrane proteins responsible for regulating ion-channels and the transport of water soluble molecules in and out of the cell. The trans-membrane proteins responsible for water transport are called aquaporins [3]. Thus water exchange across the cell membrane occurs through diffusion across the lipid bilayer or water transport through the aquaporins. Without these two mechanisms the cell membrane would be impermeable to water molecules.

Whilst there is little variation in the structure of the lipid bilayer between different cells, there are at least 10 different aquaporin isomers. Aquaporins are formed of a polypeptide chain that traverses across the cell membrane, crossing the lipid bilayer multiple times, forming a hydrophilic path through the cell membrane, enabling water to be transported in and out of the cell [96]. Differences in the aquaporin isomers present in cells result in differences in the rate at which water is transported across the cell membrane, and this causes variations in cell membrane permeability. There is a wide range of water exchange rates found in different cell types ranging from 1 m/s in nervous tissue to 170 m/s for red blood cells [86]. Aquaporins play a role in cell migration [91], and carcinogenesis with AQP 5 being involved in cell proliferation in colorectal cancer [47], however it is unclear how aquaporins play a role in these processes. Aquaporin expression

differs between colorectal cancer cells and colonic epithelial cells [32, 103]. The cell undergoes a number of changes during cell death due to necrosis, apoptosis and oncosis which alter cell membrane permeability [58, 7, 28]. The variation in cell membrane permeability between healthy tissue, carcinoma and necrotic tissue suggests that any quantitative indicator of cell membrane permeability, could be used as a potential biomarker in cancer.

2.4 Imaging in cancer

Medical imaging can be used in order to aid diagnosis, assessment and management of cancer. Imaging biomarkers in cancer can be identified radiologically using certain well established imaging modalities [76]. In a recent review a number of classic imaging biomarkers in cancer were identified. These included radiological tumour, node, metastasis (TNM) staging as staged clinically using structural imaging and nuclear medicine procedures, and a range of nuclear medicine procedures specific to metabolic processes and organs affected by metastatic disease. Whilst, other measures such as left ventricular ejection fraction calculated using functional imaging modalities, act as biomarkers for the safe management of cancer patients [76]. Structural imaging techniques were the first to be used to verify the presence of tumours clinically, as certain tumours may be easily identified with planar X-ray imaging. Whilst structural imaging can acquire certain anatomical information, functional imaging techniques such as nuclear medicine procedures enable clinicians to acquire physiological information [15].

The first functional imaging modalities were nuclear medicine procedures and X-ray flouroscopy, and these were followed by doppler ultrasound and early forms of MRI [29]. Nuclear medicine procedures use the signal from radio pharmaceuticals to target specific physiological processes, which are disturbed by disease. There are a wide variety of radio pharmaceuticals used which target different organs and metabolic processes, these are know as radio tracers. Radio tracers

synthesised using Technetium 99m or Iodine 131m are available which target the thyroid, parathyroid and adrenal system. There are also radio tracers that act as markers of liver function and that are used to measure perfusion in the brain. These radio tracers are typically imaged using gamma cameras or single photon emission tomography (SPET) systems [15]. Both produce an image of the distribution of a radio tracer by recording the intensity and distribution of the gamma rays emitted. Other radio tracers have been used to target metabolic processes disturbed by metastatic disease. The Warburg effect causes tumours to have a higher glucose metabolism than healthy tissue. This effect forms the basis of flourodeoxyglucose positron emission tomography (FDG PET) which uses a glucose based radio tracer, and is commonly used to stage and monitor the progression of metastatic disease. The PET detector works by recording the signal from photons, that are emitted simultaneously as a result of the annihilation of positrons emitted from the Flourine-18 radio-isotope in the flourodeoxyglucose radio tracer [29]. X-ray/CT flouroscopy uses a barium contrast agent and images its flow through the digestive system whilst other contrast agents are used to image venous blood flow, and dual energy radiological procedures can also be used for X-ray angiography [104]. Doppler ultrasound can be used to measure blood flow in and around tumours [15]. Certain forms of MRI can provide information on human physiology, and Dynamic Contrast Enhanced MRI can determine if the presence of a tumour has disturbed vascular perfusion. Dynamic Contrast Enhanced - MRI (DCE-MRI) works through imaging a gadolinium contrast agent as it flows around the body after the administration of a bolus of the contrast agent [63].

Structural imaging modalities used in cancer imaging include X-ray/CT, ultrasound and MRI. These techniques are sensitive to different sorts of anatomical abnormalities, with X-ray/CT being more sensitive to fractures and calcification, ultrasound being more sensitive to cysts, and MRI being more sensitive to edema and haematoma. X-ray/CT relies on the contrast caused by different types of tissue having different X-ray attenuation factors. Bone and soft tissue differ sig-

nificantly in terms of their X-ray attenuation, however there is less variation in X-ray attenuation in soft tissues resulting in less soft tissue contrast. Nevertheless CT imaging is capable of producing high resolution images (1mm resolution or better). CT has demonstrated the ability to identify the invasion of neighbouring tissue by prostate tumours, bladder tumours, bronchial tumours. CT imaging has also demonstrated the ability to clinically stage numerous solid tumours [104]. Ultrasound can be used clinically to identify cysts and tumours in kidneys, bladder, prostate, ovaries and can be used to guide needle biopsies [104]. MRI has excellent soft tissue contrast, and this enables the identification and staging of solid tumours. Other MRI techniques such as, chemical shift imaging and magnetic resonance spectroscopy can provide information about the metabolites present in the tissue being imaged [104]. Susceptibility imaging can be used for MRI venography [38]. Diffusion MRI can provide information about the tissue microstructure and is already established as a technique for assisting in the diagnosis of prostate cancer [97]. The next section covers the application of diffusion MRI to cancer in more detail.

2.5 Diffusion MRI in cancer

Diffusion MRI is an imaging technique that has demonstrated sensitivity to changes that occur in cancer, including cell density [22, 24, 27, 34, 44, 45, 56, 90, 95, 108]. Diffusion MRI developed from the initial work of Stejskal and Tanner published in 1965, which demonstrated that the diffusion properties of a sample can be measured in an NMR experiment [94]. The next chapter will give an overview of diffusion MRI theory. Later work carried out in 1983, demonstrated the sensitivity of diffusion NMR to the diffusion of water within cells [98]. Diffusion MRI was first applied to studying cell density in cancer, as it seemed likely that the apparent diffusion coefficient (ADC) would correlate with the cell density and the necrotic fraction of tumours, two properties which are useful in determining how advanced a tumour is and how well it will respond to therapy [95, 56]. The

highly cellular nature of some cancers is expected to result in more restricted diffusion due to decreased interstitial space, which results in reduced ADC, when compared to less advanced tumours and normal tissue [95]. Cell necrosis should have the opposite effect resulting in increased interstitial space and cell membrane permeability, which would be expected to result in an increase in ADC [22]. More recently a number of authors have found a relationship between cellularity and ADC [24, 27, 45, 90, 108].

Tissue biopsies have traditionally been used to confirm a diagnosis of prostate cancer, with histology confirming the micro-structural abnormalities characteristic of cancer [79]. However more recently Vascular Extracellular and Restricted Diffusion for Cytometry in Tumours (VERDICT) MRI, has been developed, as a potential alternative to tissue biopsies [79]. VERDICT is a technique which can probe tumour micro-structure, measuring a range of properties including cell size and intracellular volume fraction [81, 79]. The first VERDICT study used two colorectal cancer cell lines in mouse models, and found that VERDICT was sensitive to changes occurring in response to therapy with a cytoxic agent. The study also found that the model parameters corresponded to different properties of the cancer cells [81]. A latter study showed that VERDICT could be used to differentiate between cancerous and normal tissue in the prostate, and that it could provide useful information about tissue microstructure in the prostate [79]. This model provides some of the information that could traditionally only be acquired from histology. However one important property that VERDICT does not consider is cell membrane permeability, which alters during cell death due to necrosis, apoptosis and oncosis [58, 7, 28]. Other techniques such as Filter Exchange Imaging (FEXI) [50, 51, 70, 71] and Diffusion Exchange Spectroscopy (DEXSY), [93] may enable the measurement of cell membrane permeability with diffusion MRI. In the next chapter these techniques are explained in more detail.

A number of different diffusion MRI techniques have been used to look at cell membrane permeability. Diffusion weighted MRI has been used to identify differ-

ences in aquaporin expression in modified cell lines [67]. FEXI has been used to investigate diffusion exchange in the brain [71], and to identify changes in diffusion exchange due to modified urea transporter gene expression [88]. These studies suggest that a quantitative indicator of cell membrane permeability could be used as a potential biomarker for use in cancer diagnosis, or to asses response to therapy.

2.6 Conclusion

This chapter introduces cancer and explains how structural and functional imaging techniques play a role in the diagnosis and management of cancer. These techniques include diffusion MRI which demonstrates sensitivity to changes in cancer micro-structure, and is capable of identifying changes in cell membrane permeability. Any quantitative indicator of cell membrane permeability is a potential imaging biomarker in cancer. In the next chapter diffusion MRI is discussed in more detail.

Chapter 3

Diffusion MRI

3.1 Introduction

This chapter introduces the theory behind diffusion MRI. The application of diffusion MRI to cancer forms the focus of this thesis. MRI theory is introduced in 3.2, whilst diffusion MRI is introduced in 3.3. Section 3.4 covers advanced diffusion MRI. In section 3.5 we give an in depth overview of DEXSY, FEXSY and compartment models of diffusion exchange. Section 3.6 gives an overview of methods used to evaluate MRI techniques.

3.2 Basic MRI theory

MRI is an imaging technique using spatially localised Nuclear Magnetic Resonance (NMR). NMR was first discovered by Rabi in molecular beams passing through a magnetic field in 1938 [87], and NMR in condensed matter was discovered by Bloch and Purcell in 1946 [13, 84]. Spin is a quantum mechanical property in which a particle's angular momentum is quantized. However, a quantum mechanical approach is not needed to understand the basics of MRI theory [16]. A nuclear spin subject to a magnetic field precesses round a 'longitudinal' axis aligned in the direction of the magnetic field. The spin precesses at a rate known as the Larmor frequency, and this is also the spin's resonant frequency. Equation 3.1 gives the relationship between the Larmor frequency f, the mag-

netic field applied B, and γ, the gyromagnetic ratio [15] ($\frac{\gamma}{2\pi} = 42.6MHzT^{-1}$ for hydrogen nuclei [16]).

$$f = \frac{\gamma}{2\pi}B \tag{3.1}$$

In an ensemble of spins subject to a magnetic field the ensemble's net magnetisation vector will be aligned in the direction of the magnetic field. However, the majority of spins will have random orientations, and only a minority of spins will be aligned in the direction of the magnetic field due to thermal energy present in the ensemble. The proportion of spins in alignment with the net magnetisation vector determines the vector's magnitude [16].

The NMR effect occurs in an ensemble of spins subject to a fixed magnetic field, when the ensemble's net magnetisation vector is rotated away from the longitudinal axis by a resonant radio frequency pulse applied in a direction perpendicular to the fixed magnetic field [13]. This process is illustrated using two diagrams shown in figure 3.1 a) and b). This results in the net magnetisation vector moving into the transverse plane. However, the net magnetisation vector continues to precess round the longitudinal axis producing a rotating net magnetic moment which creates a rapidly rotating magnetic field in the transverse plane. This rapidly altering magnetic field induces current in a radio frequency coil with an axis perpendicular to the fixed magnetic field. After the radio frequency pulse has been applied, the spins constituting the ensemble relax.

There are two types of relaxation referred to as longitudinal or T_1 relaxation and transverse or T_2 relaxation. Longitudinal relaxation can be understood classically as a result of the interaction of the ensemble of spins with the local environment. The thermal motion of molecules affects the ensemble of spins by perturbing the orientation of the individual spins. These perturbations result in the net magnetisation of the ensemble of spins rotating back towards the longitudinal axis whilst the spins attempt to establish thermal equilibrium [59]. Transverse relaxation occurs due to variations in the local magnetic field experienced by the ensemble of

spins. Minor variations in the local magnetic field, result in small differences in the rate at which the spins forming the ensemble precess, which results in the spins dephasing (precessing out of phase with each other) causing a decrease in the net magnetisation in the transverse plane [16]. There is a decay in the current induced in the radio frequency coil as the net magnetisation in the transverse plane diminishes while the spins relax, and this decay is known as a free induction decay (FID) [59]. Figure 3.1 c) illustrates the change in magnetisation in the transverse plane during the free induction decay. The decay in transverse magnetisation M_T due to relaxation is described by equation 3.2, where T_E is the echo time, T_R is the repetition time, T_1 is the longitudinal relaxation time and T_2 is the transverse relaxation time [16].

$$M_T = M_0(1 - e^{-T_R/T_1})e^{-T_E/T_2} \tag{3.2}$$

The rates of T_1 and T_2 relaxation differ in different tissues, and this can be used to help identify certain pathologies [104]. Relaxation can occur very rapidly and MRI data is usually acquired using a spin or gradient echo rather than a single excitation. A spin echo is an induction decay formed as a result of constructive interference due to a series of radio frequency pulses. Each pulse in a spin echo acts to rotate the net magnetisation vector into the transverse plain. The first pulse rotates the net magnetisation vector through 90° whilst the second rotates the net magnetisation vector through 180° this counteracts the de-phasing that occurs between the first and second pulse resulting in the spins re-phasing at the echo time. The spin echo was first discovered by Hahn in 1950, the spin echo enables longer acquisitions, and this results in an NMR experiment which can gather more information about the spin's environment [39, 16].

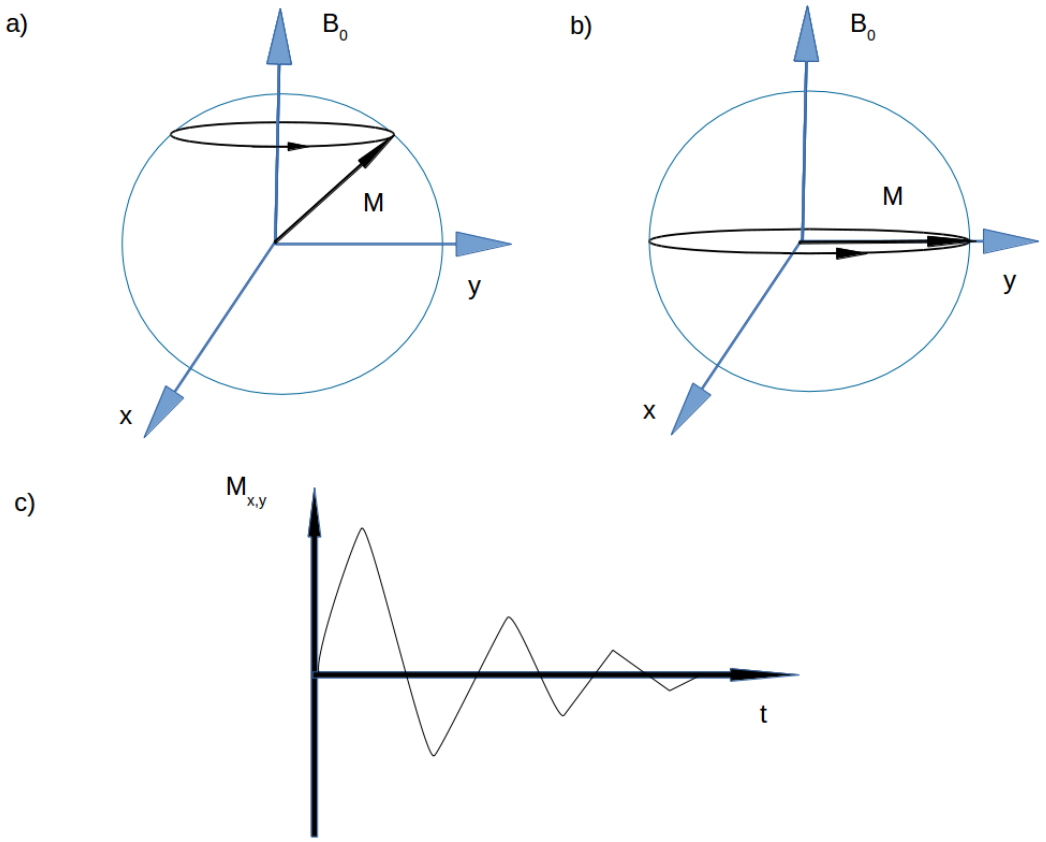

Figure 3.1: a) An ensemble of spins' net magnetisation vector precessing at the Larmor frequency as seen from the laboratory frame of reference. b) The ensemble of spins' net magnetisation vector processing immediately after a 90° RF pulse seen from the laboratory frame of reference. c) The FID that occurs after the RF pulse has been applied. Figure adapted from [104].

3.2.1 Spatially localised NMR

Spatially localised NMR, or Magnetic Resonance Imaging (MRI), relies on spatial encoding of the NMR signal using applied imaging gradients. Mansfield and Lauterbur pionered this work independently and received the Nobel prize for medicine in 2003. They developed the work that forms the basis of slice selection and frequency encoding and the gradient echo technique was translated into clinical use in the 1980s, whilst Edelstein went on to develop phase encoding in 1980 [83, 60, 52, 73, 25]. In this chapter we refer to the slice encoding direction as z, the frequency encoding direction as x and the phase encoding direction as y. In an MRI machine there is a fixed B_0 field. Slice selection works by applying an additional gradient in the z direction (z can take any orientation relative to the B_0 field) and this then alters the resonant frequency of the spins dependent on their position on the z-axis. As a result, a radio frequency pulse will only rotate an ensemble of spins away from the longitudinal axis at a position along the slice selective gradient where the ensemble's resonant frequency matches that of the radio frequency pulse. Even when the imaging gradients are applied the net magnetic field will be in the direction of B_0. Equation 3.3 gives f the frequency required for a slice selected at position z along an applied magnetic field gradient G_z, B_0 is the magnitude of the fixed magnetic field and γ is the gyromagnetic ratio.

$$f = \frac{\gamma}{2\pi}(B_0 + zG_z) \tag{3.3}$$

A frequency encoding gradient is applied when the NMR signal is being acquired. This encodes the x position in terms of frequency, due to the change in frequency of the NMR signal that results from the variation in the rate at which the spins precess along the length of the applied gradient. Equation 3.4 gives f the frequency of the signal acquired from an ensemble of spins at position x along an applied magnetic field gradient G_x, B_0 is the magnitude of the fixed magnetic field and γ is the gyromagnetic ratio [83].

$$f = \frac{\gamma}{2\pi}(B_0 + xG_x) \tag{3.4}$$

In phase encoding, a series of gradients are applied orthogonally to the slice select and frequency encoding gradients over a series of acquisitions. The phase encoding occurs in-between slice selection and frequency encoding. Each phase encoding gradient is applied for a duration of time, and this phase encoding step alters the phase of the spins. When data is acquired, only the spins that are precessing in phase contribute toward the signal acquired. The data acquired after each phase encoding step represents a line in frequency space, and when the data is 2D Fourier transformed a 2D image is produced. Equation 3.5 relates the phase encoding step n to the other phase encoding parameters including L_y the field of view in the phase encoding direction, τ the duration for which the phase encoding gradient G_y is applied, and γ is the gyromagnetic ratio [25].

$$2\pi n = \gamma L_y \int_{\tau} dt G_y \tag{3.5}$$

3.3 Diffusion MRI

Diffusion MRI uses the diffusion of water to probe tissue micro-structure which can restrict or hinder the diffusion of water molecules [80]. The free diffusion of water is the process by which water diffuses due to the random motion of molecules as a result of the kinetic energy in the water molecules and this phenomenon was first described by Einstein in 1905. The relationship between mean displacement λ and the free diffusion coefficient D in a time period t is given in equation 3.6 [26].

$$\lambda = \sqrt{2Dt} \tag{3.6}$$

Diffusion MRI is sensitive to how the diffusion of water in tissue differs from the free diffusion described by Einstein. The fundamental basis of diffusion MRI was developed by Stejskal and Tanner in 1965 [94]. They developed a technique for measuring the diffusion of liquids with NMR using a spin-echo experiment and a pair of diffusion encoding gradients [94]. The greater the diffusion in the direction of an applied bipolar gradient the greater the reduction in signal magnitude

due to the applied diffusion encoding graidient. This means a series of diffusion encoding gradients can be applied to determine the diffusivity of a sample [94].

Stejskal and Tanners research built on work by Hahn, Carr and Purcell who discovered the effects of diffusion on NMR measurements, [20, 39]. Later, Torrey developed a formal framework for incorporating diffusion effects into NMR measurements by adding a diffusion term to the Bloch equation [99]. The Bloch equations gives the relationship between nuclear induction, magnetisation and the applied magnetic field in an NMR experiment [13]. Equations 3.7-3.9 give the Bloch-Torrey equations [99].

$$\frac{\partial M_x}{\partial x} = \gamma(M \times B)_x - M_x/T_2 + \nabla \cdot D\nabla(M_x - M_{x0}) \tag{3.7}$$

$$\frac{\partial M_y}{\partial y} = \gamma(M \times B)_y - M_y/T_2 + \nabla \cdot D\nabla(M_y - M_{y0}) \tag{3.8}$$

$$B_x = -\frac{1}{2}G_x, B_y = -\frac{1}{2}G_y, B_z = B_0 + G_z \tag{3.9}$$

Equation 3.10 shows the solution to the Bloch-Torrey equations describing the decay in signal due to diffusion following a 90° RF pulse [99].

$$S = S_0 e^{(-\frac{1}{3}D\gamma^2G^2t^3)} \tag{3.10}$$

The decay in signal is due to the spins of the diffusing molecules dephasing, as a result of their motion in the direction of the applied diffusion gradients [53]. The decay in signal in the case of isotropic unrestricted diffusion is given by the following equation:

$$C = e^{(-b \cdot D)} \tag{3.11}$$

where C is the attenuation factor, D is the diffusion coefficient and the b is the b-value which represents the diffusion weighting of the pulse sequence [54], this equation takes the same form as equation 3.10. In isotropic unrestricted diffusion we can assume Brownian motion, where diffusion can be assumed to occur through a series of random movements [53]. The diffusion coefficient, D, is given

by the following equation

$$D = \frac{lv}{6}. \tag{3.12}$$

where *l* is the mean distance travelled and v is the mean velocity of the particle [54].

3.3.1 Restricted and hindered diffusion

In biological tissue it is unreasonable to assume unrestricted diffusion as the tissue is composed of cells, which restrict or hinder diffusion. In addition to this we can also expect diffusion effects to be confounded by perfusion effects that occur because of the blood supply from the microvasculature [54]. This means that the diffusion coefficient measured in tissue will only be an Apparent Diffusion Coefficient (ADC), as its measurement will be confounded by other factors. In order to provide a summary measure of diffusion in tissue, Le Bihan developed an intravoxel incoherent motion (IVIM) MRI imaging experiment which measures both perfusion and diffusion, and separates perfusion and diffusion effects to give a measure of the ADC [53]. In the original IVIM experiment the diffusivity D was believed to be equivalent to ADC_2 which is calculated by the following equation:

$$ADC_2 = \frac{log(S_1/S_2)}{(b_2 - b_1)} \tag{3.13}$$

whilst ADC_1 which represents both diffusion and perfusion is calculated by the following equation:

$$ADC_1 = \frac{log(S_0/S_1)}{(b_0 - b_1)} \tag{3.14}$$

and a pure perfusion image can then be calculated by the following equation:

$$f = 1 - e^{-b_1 \dot{(} ADC_1 - ADC_2)} \tag{3.15}$$

where f is the fraction of blood perfusing in the tissue, S is the signal intensity and b is the b-value [53]. Restricted diffusion occurs when a barrier prevents diffusion across the barrier entirely, whereas hindered diffusion occurs when diffusion is

hindered by a permeable membrane or another obstacle. In hindered diffusion ADC is related to the free diffusion coefficient D by the following equation:

$$ADC = \frac{D}{\lambda^2} \tag{3.16}$$

where λ is the coefficient of 'tortuousity' that signifies the degree to which diffusion is impeded [54].

3.3.2 Diffusion anisotropy

It is often unreasonable to assume isotropic diffusion in biological samples, on the same grounds that it is unreasonable to assume unrestricted diffusion. In the case of anisotropic diffusion, a three dimensional model is required. Diffusion tensor imaging achieves this using a diffusion tensor model [54]. The diffusion tensor model relies on representing diffusion using a second order tensor. This accounts for the multi-dimensional nature of unrestricted anisotropic diffusion, but requires much more intensive post-processing. The relationship between the amplitude of the signal *S* and the diffusion tensor, *D*, is given by the following relationship:

$$ln(\frac{S(b)}{S(0)}) = -\Sigma_{i=1}^{3}\Sigma_{j=1}^{3} b_{ij} D_{ij} \tag{3.17}$$

where *b* is the b-value of the pulse sequence and i,j represent elements of the b-matrix used to encode the b-vector [54].

The diffusion tensor can then be used to provide two measures of diffusivity; the fractional anisotropy (FA) and the mean diffusivity (MD), which provide an indication of the degree of anisotropy in the diffusion tensor and the average diffusivity of a voxel [9]. However, the diffusion tensor still only accounts for the average properties of the sample being imaged. Even in the case of the most simple biological sample there will be a distribution of diffusivities, as the diffusion environment in the intracellular and extracellular space is different [54]. In these cases a model consisting of the summation of a number different diffusion models,

can be used to represent the signal due to different compartments of the tissue sample [54].

3.4 Advanced diffusion MRI

All of the work reviewed so far uses relatively simple measures of diffusion, and fails to account for the origin of different components of the diffusion MRI signal in different parts of the tissue micro-structure. The work reviewed so far demonstrates a relationship between ADC and other measures of diffusion and cellularity, and fails to demonstrate a strong enough correlation to be able to predict cell properties from the ADC, or to accurately discriminate between cancerous tissue and normal tissue. Recently research has been conducted to develop diffusion MRI techniques that are sensitive to cell properties. Some of this research has been conducted using compartment models of the signal obtained from diffusion MRI. Xu et al. used simulations of the diffusion in cells involving a compartment model of diffusion to compare oscillating gradient spin echo (OGSE) and pulse gradient spin echo (PGSE) pulse sequences, in a study which showed that ADC fails to take account of many cellular properties [107]. Recently a three compartment model of diffusion has been developed by Pangiotaki and Walker-Samuel et al., called vascular extracellular and restricted diffusion for cytometry in tumours (VERDICT) [81]. The VERDICT model is a compartment model using a one directional diffusion tensor model to model the vascular compartment, a spherical diffusion tensor to model the extracellular-extravascular compartment and an isotropic spherical restricted diffusion model for the intracellular compartment. The study used two colorectal cancer cell lines in mouse models, and found that VERDICT was sensitive to changes occurring in response to therapy with a cytoxic agent. The study also found that the model parameters corresponded to different properties of the cancer cells, including cell size and cell density [81]. In another study Pangiotaki et al showed that VERDICT could be used to differentiate between cancerous and normal tissue in the prostate, and that it could

provide useful information about tissue microstructure in the prostate [79]. However the model does not account for cell membrane permeability, intracellular compartments and cell shape [81].

However it became clear that VERDICT has a number of limitations. In particular it does not take account of cell membrane permeability. As such diffusion exchange across the cell membrane could effect the estimation of cell size, intracellular volume fraction and the other VERDICT model parameters. Diffusion exchange across the cell membrane will influence a PGSE acquisition in a number of ways, but the main effect would be signal loss [71], which could confound the estimation of all VERDICT parameters. However diffusion exchange across the cell membrane could also effect the estimation of cell size by violating the assumption underling the use of the sphere compartment in VERDICT, namely that the cell membrane fully restricts the motion of intracellular water to the intracellular compartment. This prompted my interest in diffusion exchange across the cell membrane.

3.5 DEXSY, FEXSY and compartment models of diffusion exchange

Cell membrane permeability alters during the course of cell death due to apoptosis, necrosis and oncosis [58, 7, 28]. In addition, aquaporins, which control water transport across the cell membrane, differ between healthy cells and cancer cells [65, 103]. The physiological importance of cell membrane permeability has motivated the development of techniques aimed at measuring cell membrane permeability, such as FEXSY (Filter Exchange Spectroscopy)/FEXI (Filter Exchange Imaging) developed by Nilson et al [71]. The first attempt to quantify cell membrane permeability using NMR, was done using the Kärger framework developed in 1985 [48]. The Kärger framework uses a two compartment model, with the signal explained by a combination of two exponentials [48]. Models such as the

Kärger model have been used with Pulse Field Gradient (PFG) acquisitions to study the properties of cell membranes with NMR spectroscopy [101]. A number of different techniques have been developed to study diffusion and exchange in NMR spectroscopy including VEXSY (Velocity Exchange Spectroscopy) [19], DOSY (Diffusion Ordered Spectroscopy) [66] and DEXSY (Diffusion Exchange Spectroscopy) [18]. In this thesis the term diffusion exchange is used to describe the exchange of diffusing spins across the cell membrane, between different compartments and between different populations of diffusing spins.

3.5.1 DOSY

DOSY is a spectroscopic technique which acquires an NMR spectrum, with a range of diffusion encoding gradients. It produces a 2D data set with a diffusion dimension and a spectroscopic dimension. Different chemical groups have different spectral peaks, which allows for different chemicals to be discerned in the spectral dimension, whilst the diffusivity of each chemical group can be measured in the diffusion dimension. The technique allows for the diffusivities of different substances in a solution or a mixture to be measured [66].

3.5.2 DEXSY and FEXSY

DEXSY is a double diffusion encoding technique [18]. The data acquired is 2-D inverse Laplace transformed to give a diffusion-diffusion exchange plot [18]. The diffusion-diffusion exchange plot compares the diffusion measurements made using the two pairs of diffusion encoding gradients. Diffusion-exchange can be observed when the two diffusion measurements differ [18]. DEXSY measures diffusion exchange over a range of diffusivities, which can result in lengthy acquisition times. In order to measure diffusion exchange in-vitro and in-vivo, a FEXSY sequence was developed from a modified DEXSY sequence [6]. In a FEXSY/FEXI sequence one pair of diffusion encoding gradients are fixed whilst the other pair of diffusion encoding gradients and the mixing times used are varied, thus producing a limited subset of the information available in a full DEXSY

sequence [6]. In FEXSY/FEXSY the first pair of diffusion gradients act as a filter and cause the fast diffusing water signal to drop out. Whilst the second pair of diffusion gradients are used to measure an apparent diffusivity. A range of mixing times are then used to separate the first and second pair of gradients so that the relationship between the mixing time and the apparent diffusivity of the filtered signal can be determined. In FEXSY it is assumed that the filtered apparent diffusivity will return to a value equivalent to the unfiltered measurement as a result of equilibrium being established between the intracellular and extracellular space due to diffusion-exchange. FEXSY/FEXI provides a more limited measurement of diffusion-exchange than DEXSY, as the first pair of gradients are fixed. FEXSY/FEXI also relies on a two compartment diffusion exchange model using a monoexponential model of diffusion exchange, between the two compartments, producing a single apparent exchange rate (AXR) coefficient [50, 93].

The DEXSY pulse sequence (Figure 3.2) consists of two pulsed gradient spin echo (PGSE) blocks each incorporating a pair of diffusion-encoding gradients, G_1 and G_2. The two PGSE blocks are separated by a mixing time, t_m, which allows for diffusion exchange to occur. The two PGSE blocks encode the diffusion measured before and after the mixing time. Once the data has been processed these measurements can be compared. A difference in the measurement encoded by each block, indicates that the diffusing spins environment has changed during the mixing time. DEXSY's ability to detect a change in the diffusing spins environment enables the technique to detect diffusion-exchange [17, 33]. Data are processed using a 2D inverse Laplace transform. The signal from the DEXSY acquisition is 2D inverse Laplace transformed to produce a distribution of diffusion coefficients; producing a 2D spectrum in which diffusivities encoded with G_1 are plotted against diffusivities encoded with G_2. Peaks that lie along the diagonal of these diffusion-diffusion exchange spectra represent spins exhibiting the same diffusivity during both sets of diffusion encoding gradients, whereas the off-diagonal peaks represent spins that have exchanged between two different

diffusion environments [17, 33]. The signal equation for the DEXSY sequence is:

$$\frac{S}{S_0} = \Sigma p(D_1, D_2) e^{(-b_1 D_1)} e^{(-b_2 D_2)} \tag{3.18}$$

where subscripts correspond to parameters associated with either G_1 or G_2. The summation is across all spins in the system. For a pair of gradient pulses, $b = \gamma^2 \delta^2 G^2 (\Delta - \delta/3)$, where γ is the gyromagnetic ratio, G is the gradient strength, δ is the duration of the diffusion encoding gradient, Δ is the diffusion time; D is the distribution of diffusivities, S is the acquired signal S_0 is the signal acquired with no diffusion encoding gradients and p is the probability of the contribution to the signal from D_1 and D_2 [33]. An inverse Laplace transform, can transform the multi-exponential decay of the DEXSY signal into into the probability of the contribution to the signal from D_1 and D_2. In other words in DEXSY the 2D inverse Laplace transform, transforms $\frac{S}{S_0}$ to $p(D_1, D_2)$ when b_1 and b_2 are known [33]. A true inverse Laplace transform can not be calculated using computational methods. However, computational methods can be used to calculate a so-called inverse Laplace transform, which is an approximation to the true inverse Laplace transform. It is these so-called inverse Laplace transforms which are used to process DEXSY data.

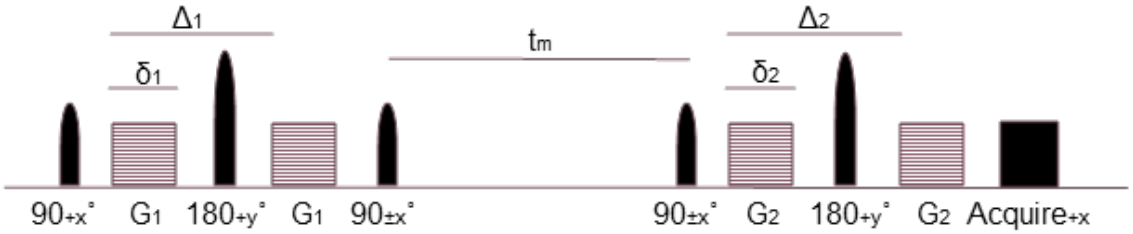

Figure 3.2: DEXSY pulse sequance without imaging gradients

Much of the data acquired in DEXSY experiments has been processed using so-called Laplace inversion software developed at the university of Wellington [36, 17, 33]. For 2D data the software uses a singular value decomposition (SVD) to reduce the the 2D data into a vector, that is then regularised before a non-negative least squares (NNLS) fit is applied [36, 100].

Regularisation is required to perform a so-called inverse Laplace transform, as signal noise results in non-unique solutions to the transform when the NNLS is applied to noisy data. However, if too much smoothing is applied important information that would be represented in smaller peaks such as diffusion exchange peaks, can disappear. There are also non-unique solutions to Laplace transforms at 0, which means that so-called inverse Laplace transforms can not process signal from points where the exponents of the multi-exponential function are 0 [36, 100].

The use of so-called inverse Laplace transforms such as the one developed by the university of Wellington, are dependent on using the right regularisation parameter. It is recommended that a Chi squared plot is used to identify the values of the regularisation parameter above which the data has not been regularised, and below which the data has been over smoothed [36, 100].

3.6 Methods used to evaluate MRI techniques

This section gives a brief introduction to methods used to evaluate MRI techniques.

3.6.1 MRI phantoms

Phantoms are used for sequence development and quality assurance. The most common phantoms are physical phantoms which are often used for quality assurance, these are often made of glass and silica and are frequently used to validate new techniques [63]. Chemical phantoms can be used to validate techniques involving exchange processes [88]. Biological phantoms consisting of nerve cells or cancer cells in-vitro have been used to study the relationship between ADC and cell size and density in nervous tissue and cancer [12, 61, 5]. These phantoms can help sequence development to a point where the technique can be translated into in-vivo imaging.

3.6.2 Simulations

Diffusion MRI problems were initially treated analytically [53], however many problems involving applying diffusion MRI to tissue micro-structure are too difficult to deal with analytically and in order to resolve the problems Monte Carlo simulations have been used [64]. Monte Carlo simulations have been applied to resolve problems involving diffusion imaging of nervous tissue [64, 42, 74, 40, 4]. Monte Carlo simulations have also been applied to simulate diffusion MRI acquisitions in cancer [77, 82]. Monte Carlo methods involve random sampling of probability distributions [43]. In Monte Carlo simulations of diffusion MRI acquisitions, spins move through a substrate following a random walk and their magnetisation varies with time, position and magnetic field [40]. The signal generated is the sum of the signal from each spin [40]. Monte Carlo simulations can be used to validate new sequences and a diffusion simulation packages such as CAMINO can use or generate substrates to act as in-silico phantoms, enabling in-silico validation of new diffusion MRI sequences [23].

3.6.3 Animal models

Animal models are used extensively in preclinical neuroscience [2], whilst xenograft models formed from the inoculation of mice with cancer cells have been used in cancer imaging. Xenograft models consisting of subcutaneous tumours resulting from the subcutaneous injection of carcinoma cells into nude mice with compromised immune systems, have been successfully used to model human tumours in imaging experiments [102]. The carcinoma cell lines used in xenograft models are often derived from human carcinoma cells, and they produce tumours that are similar to the human carcinomas from which they are derived.

3.7 Conclusion

This chapter introduces the theory behind diffusion MRI, and gives an overview of VERDICT, DEXSY and FEXSY/FEXI. In the next five chapters experimental

work and simulations using the ball and sphere model (cellular and extracellular component of VERDICT), FEXSY and DEXSY are presented. The application of diffusion MRI to cancer forms the main focus of this thesis.

Chapter 4

Biological phantoms for diffusion MRI

4.1 Introduction

This chapter is focused on developing a biological phantom to test and evaluate diffusion MRI techniques for cytometry in cancer. Initially we focused on a diffusion MRI technique called VERDICT MRI [81]. This technique is intended to provide some of the information that could traditionally only be acquired from histology. Concerns regarding the accuracy of the estimates of cell size made using the VERDICT model, suggest that predictions of cell size made using the extracellular and intracellular component of the VERDICT model need to be evaluated. The ball and sphere model provides the extracellular and intracellular component of the VERDICT model. The initial aim of the work presented in this chapter was to evaluate the predictions of cell size and intracellular volume fraction made using the ball and sphere model.

The work presented in this chapter demonstrates that progress was made in evaluating the predictions made by the ball and sphere model using a biological phantom. However, further work did not seem sensible as ex-vivo validation of VERDICT [46], rendered it unnecessary. Ex-vivo tumour xenograft model studies using perfusion fixed tissue provide a tumour model with no vascular compart-

ment which can be represented by the ball and sphere model. However, the fixation process reduces the size of the cells. The study demonstrated that the VERDICT model could be applied to in-vivo data acquired from a subcutaneous tumour xenograft model and the ball and sphere model could be applied to data acquired ex-vivo from the same tumour after perfusion fixation. The results show that the difference in predicted cell size and intracellular volume fraction between the in-vivo and ex-vivo data is consistent with the change in cell size due to tissue fixation [46]. However, it is also clear that VERDICT has a number of limitations. In particular, it does not take account of cell membrane permeability. Diffusion exchange across the cell membrane can result in signal loss in PGSE acquisitions [72], which could confound the estimation of all VERDICT parameters. However, diffusion exchange across the cell membrane could also affect the estimation of cell size by violating the assumption underling the use of the sphere compartment in VERDICT, namely that the cell membrane fully restricts the motion of intracellular water to the intracellular compartment over the time course of the MRI measurement. This prompted my interest in diffusion exchange across the cell membrane. Whilst my initial interest was prompted by the effects of diffusion exchange on diffusion MRI measurements, it soon became clear that this would be a phenomenon worth studying in its own right. As mentioned in chapter 2, water transport across the cell membrane is an important physiological process, and cell membrane permeability alters in health and disease. Any quantitative indicator of cell membrane permeability is also a potential biomarker in cancer.

Once it was established that there was no longer a need to evaluate the ball and sphere model, and that measuring diffusion exchange across the cell membrane could provide information about an important physiological process, my attention turned towards DEXSY. I aimed to measure diffusion exchange across the cell membrane in a biological phantom using DEXSY. In this chapter the sections are split into separate subsections. The first uses biological phantoms to evaluate the ball and sphere model's prediction of cell size and intracellular volume fraction, and the second uses biological phantoms to evaluate DEXSY's measurements of

diffusion exchange across the cell membrane.

4.2 Methods

In this section we present methods used to evaluate diffusion MRI techniques using biological phantoms. The first subsection covers the methods used to evaluate the ball and sphere model estimates of cell size and intracellular volume fraction using a biological phantom. The second subsection covers the methods used to evaluate measurements of diffusion exchange across the cell membrane in a biological phantom acquired using DEXSY.

4.2.1 Methods used to evaluate the ball and sphere model

In this subsection the methods used to evaluate the ball and sphere model estimates of cell size and intracellular volume fraction using a biological phantom are presented. I used a similar methodology to that which was used by Anderson et al. and Matsumoto et al. [61, 5] to look at the relationship between cell properties and ADC. The biological phantom was produced from cells that came from the SW1222 and LS147T colorectal carcinoma cell lines. We used luciferase positive cells as these can be imaged using biouminescence imaging. In our final version of the protocol used to evaluate the ball and sphere model 5 T-175 cell culture flasks of either luciferase positive SW1222 or LS147T cells were washed with 7 ml of PBS (Phosphate Buffer Solution), before being trypsinised (detached from the flasks) using 3 ml of trypsin each, and incubated at 37 $^\circ$ C in 5% CO_2 for 5 minutes. Each flask was then neutralised using 5 ml of media. The media and cells were transferred to a 50 ml centrifuge tube. The cells were counted using a cell counter slide and trypan blue, whilst the 50 ml centrifuge tube was centrifuged for 5 minutes at 1290 rpm. The media and trypsin were aspirated out of the centrifuge tube leaving a cell pellet. Then 50 ml of PBS was added to the cell pellet, which was broken down and mixed with the PBS using a pipette gun before being centrifuged for another 5 minutes at 1290 rpm. The PBS was aspirated out

of the centrifuge tube leaving a cell pellet.

Before the experiment the extracellular matrix gel (ECM -gel) was left in the refrigerator at 5 $^\circ$ C to defrost overnight. The ECM-gel was placed on ice alongside the 0.5 ml micro-centrifuge tube and the 1000 micro-litre Gilson pipette tips, before being transferred to the biological safety cabinet (all tissue culture has to be conducted in a biological safety cabinet). The centrifuge tube with the cell pellet was then placed on ice inside the biological safety cabinet. Ice is required to ensure that the ECM-gel, cells, media and pipettes are chilled so that the ECM-gel can be manipulated without it solidifying. The ECM-Gel and media were then added to the cell pellet using the Gilson pipette. The mixture was mixed with the 1000 micro-litre Gilson pipette before 0.75 ml of the mixture was transferred to the micro-centrifuge tube. We intended to produce a mixture that consisted of 3/5 cell pellet, 1/5 Dubulcos Modified Eagle Media (DMEM media) and 1/5 ECM-Gel in order to create a phantom with an intracellular volume fraction of 60 %. This experiment was conducted twice as the the number of cells harvested from the T-175 flasks in the first experiment conducted using this protocol was less than expected. A second experiment was then conducted using this protocol and the expected number of cells, were harvested from the T-175 flasks.

The micro-centrifuge tube containing the cells, ECM-gel and media was imaged in a 15 ml centrifuge tube full of paper and water to keep it stable and reduce artifacts. Ideally the cells would have been scanned at 37 $^\circ$ C however the cells were scanned at room temperature 21 $^\circ$ C. The MRI data used to evaluate the ball and sphere model was acquired using a 9.4 T Varian MRI scanner (Agilent technologies) using a 26 mm RF coil (Rapid MR International). A diffusion weighted SEMS (Spin Echo Multi Slice) sequence was used with a range of Δ = 10, 20, 30, 40 ms and δ = 3 for all values of Δ and δ = 10 ms for Δ = 30, 40 ms to give 6 diffusion weighted shells, with an additional 42 direction diffusion tensor shell with Δ = 10 ms and δ = 3 ms. The gradient strength varied in 10 even increments between 40 mT/m and 400 mT/m for δ =3 and it was 44.4 mT/m, 88.9 mT/m and

133.3 mT/m for δ =10 ms, the maximum gradient strength for the diffusion tensor shell was 400 mT/m. The TE used was close to the minimum in each case and the TR used was 350 ms. This is a slightly modified version of the acquisition scheme used in the original VERDICT study [81].

After the scan was finished, 15 micro-litres of luciferin, an enzyme that causes luciferase positve cells to release light, was added to the micro-centrifuge tube containing the cells. The bioluminescence emited from the cells was imaged with the AMI-X (Spectral Instruments) to measure the distribution of viable cells. Once this was done the contents of the micro-centrifuge tube were scraped into a 50 ml centrifuge tube and 2 ml of dispase without calcium, magnesium and EDTA at a concentration of 0.6 units per ml were added. This mixture was then incubated for 30 minutes, before being neutralised with 8 ml of media. A cell count and viability measurement was then carried out with a hemocytometer slide and trypan blue, using a trypan blue exclusion assay. Some of the cells were then diluted with DMEM media and plated up on a 6 well plate before being imaged using a Zeiss Axio Observer Z1 microscope.

The image processing was all done in $MATLAB$, using the $CAMINO$ [23] package produced by UCL's Microstructure Imaging Group to fit the ball and the ball and sphere model [81], with in house $MATLAB$ software. The ball model is a subset of the ball and sphere model consisting of the ball compartment alone. The ball model can be used to estimate ADC. The ball and sphere model consist of a ball compartment which represents an isotropic diffusion tensor which gives a signal model for isotropic hindered diffusion and the sphere compartment which represents a signal model describing isotropic restricted diffusion. The intracellular volume fraction is determined by the proportion of signal coming from the sphere compartment. The predicted cell radius is the radius of the sphere compartment [80, 68, 81]. Hindered and restricted diffusion are covered in more detail in chapter 3.

4.2.2 Methods used to evaluate DEXSY

The biological phantoms used to evaluate DEXSY were produced from cells that came from the SW1222 colorectal carcinoma cell line. Two protocols were used to produce biological phantoms to evaluate DEXSY, ECM-gel biological phantoms were used for biological phantoms 1-5, and collagen gel biological phantoms made using the RAFT 3D Culture kit were used for biological phantoms 6 and 7.

In our final version of the protocol, 7 T-175 flasks of luciferase positive SW1222 cells were used to produce each ECM-gel biological phantom. The flasks were washed with 7 ml of PBS (Phosphate Buffer Solution), before being trypsinised using 3 ml of trypsin each, and incubated at 37 $^\circ$ C in 5% CO_2 for 5 minutes. Each flask was then neutralised using 5 ml of media. The media and cells were transferred to a 50 ml centrifuge tube. The cells were counted using a hemocytometre slide and trypan blue, whilst the 50 ml centrifuge tube was centrifuged for 5 minutes at 1290 rpm. The media and trypsin were aspirated out of the centrifuge tube leaving a cell pellet. Then 50 ml of PBS was added to the cell pellet, which was broken down and mixed with the PBS using a pipette gun before being centrifuged for another 5 minutes at 1290 rpm. The PBS was aspirated out of the centrifuge tube leaving a cell pellet.

Before the experiment ECM-gel, was left in the refrigerator to defrost overnight. The ECM-gel was placed on ice alongside the 0.5 ml filtered micro-centrifuge tube and the 1000 micro-litre Gilson pipette tips before being transferred to the biological safety cabinet. The centrifuge tube with the cell pellet was placed on ice, inside the biological safety cabinet. The ECM-Gel and media were then added to the cell pellet using the Gilson pipette. The mixture was mixed with the 1000 micro-litre Gilson pipette, before 0.75 ml of the mixture was transferred to the micro-centrifuge tube. We intended to produce a mixture that consisted of 3/5 cell pellet, 1/5 DMEM media and 1/5 ECM-Gel. The micro-centrifuge tube con-

taining the cells, ECM-gel and media was placed in a 15 ml centrifuge tube filled with DMEM media to keep the cells viable for the duration of the experiment. The biological phantoms used to evaluate DEXSY have been numbered 1-7 in table 4.1 and this protocol was used to create biological phantoms 1-5. According to our protocol biological phantoms 1-5 should be identical.

Two phantoms were produced using the RAFT 3D Culture kit [21], consisting of SW1222 cells placed into a collagen gel that is then compressed to give a high cell density. The micro-centrifuge tube containing the cells in collagen-gel was placed in a 15 ml centrifuge tube filled with DMEM media to keep the cells viable for the duration of the experiment. This protocol was used to create biological phantom 6 and 7. This protocol was trialled as it is faster and simpler to produce phantoms using the RAFT 3D Culture Kit than with ECM-Gel.

The biological phantoms held inside a 15 ml centrifuge tube were inserted into the MRI scanner. The data were acquired using a 9.4 T Varian MRI scanner (Agilent technologies) using a 26 mm RF coil (Rapid MR International). We used a slice-selective DEXSY sequence created by adding slice selective imaging gradients to the basic DEXSY pulse sequence shown in figure 3.2. The biological phantoms were scanned using the DEXSY scan parameters listed in table 4.1, with 4 averages and a duration of 102 minutes for each scan. A variety of parameters were used to determine which diffusion times and diffusion gradient strengths are sensitive to the intracellular diffusion in the cancer cells, and to determine which mixing times are sensitive to diffusion-exchange across the cell membrane.

2D inverse Laplace software was used to generate diffusion-diffusion exchange plots from the raw data and the applied b-values [17, 100]. The contribution due to imaging gradients was incorporated into the calculation of the b-values. The

Phantom	δ	Δ	t_m	TR	$G_1\&G_2$ in 16×16 steps
1	15 ms	17 ms	100 ms	3000 ms	0-720 mT/m
2	5 ms	23 ms	100 ms	3000 ms	0-800 mT/m
3	15 ms	17 ms	100 ms	3000 ms	0-800 mT/m
4	15 ms	17 ms	100 ms	3000 ms	0-800 mT/m
5 scan 1	15 ms	17 ms	200 ms	3000 ms	0-800 mT/m
5 scan 2	9 ms	14 ms	200 ms	3000 ms	0-800 mT/m
6	15 ms	17 ms	200 ms	3000 ms	0-640 mT/m
7	15 ms	17 ms	200 ms	3000 ms	0-640 mT/m

Table 4.1: Table of biological phantom DEXSY scan parameters

Diffusion Exchange Index (DEI) is defined as the ratio of the volume of exchange peaks to non-exchange peaks and could be used as a quantitative indicator of cell membrane permeability.

4.3 Results

4.3.1 Results from the final protocol used to evaluate the ball and sphere model

The earliest versions of the protocol used to produce a biological phantom to evaluate the ball and sphere model, used a 1.5 ml micro-centrifuge tube before we decided to use a 0.5 ml micro-centrifuge tube, the number of cells used for these was between 4×10^7 - 8×10^7 cells as counted using trypan blue and a hemocytometre slide. In each attempt there was a high cell viability of greater than 95 %, demonstrating that I could keep the cells mixed with ECM-gel viable in a micro-centrifuge tube. I have not included information about the phantoms produced using the earliest versions of the protocol as the main difference between the final protocol and the earliest versions of the protocol is the number of flasks of cells used to produce the phantom, as the earliest versions of the protocol failed to produce enough cells.

In the first experiment, carried out using the final protocol used to evaluate the ball and sphere model, the phantom consisted of a 0.5 ml micro-centrifuge

tube. In the first experiment the number of cells harvested was significantly less than expected. A total of 7.3×10^7 SW1222 cells at greater than 95 % viability were harvested for the experiment. The data acquired by the MRI scanner from the first experiment using the final protocol used to evaluate the ball and sphere model is shown in figures 4.1-4.4. Figures 4.1 shows a plot of the normalised signal from the biological phantom, plotted against the b-value at which it was acquired. The normalised signal (S/S_0) for the biological phantom is taken from a region of interest drawn around the micro-centrifuge tube in a single slice of our MRI acquisition. The parameters are then calculated from the area within the ROI for all three slices acquired. In order to fit the right model only the simplest model that fits the data should be used in accordance with Occam's razor. The normalised signal from the biological phantom, appears to follow a mono-exponential decay in signal with increasing b-value. This is what we would expect if the ball model of unrestricted diffusion is applicable, as it is characterised by a simple mono-exponential decay in signal intensity with increasing b-values. The simple mono-exponential relationship is what would be expected if the phantom consisted of a mixture of media and ECM-gel alone. The results of a preliminary biological phantom experiment suggest that this is the case in a mixture of ECM-gel and media, with the mixture having an ADC = 2.3 m^{-9}/s. Figure 4.2 confirms that the ball model is an appropriate model, as the measured signal marked by blue crosses matches with the ball model predicted signal marked by the red boxes. The ball model predicted signal for each b-value was calculated by in house $MATLAB$ software using the ADC estimated using the ball model for the MRI data acquired. When using compartment models of diffusion MRI. The simplest model that describes the data is always used, which means that the ball model is an appropriate model for this data set [80]. Figure 4.3 shows the b = 0 image which was acquired with no diffusion weighting. There are no obvious artifacts present in the b = 0 image and relatively little variation in signal intensity across the biological phantom, showing that the data is sound. Figure 4.4 shows the apparent diffusion coefficient (ADC) map generated from the data acquired

from the biological phantom using the ball model.

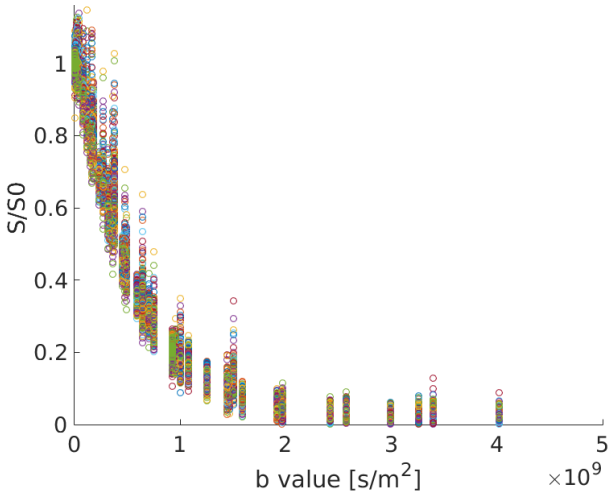

Figure 4.1: Plot of the normalised signal from the cells and ECM-gel, plotted against b value for our first experiment using the final protocol used to evaluate the ball and sphere model. The different colours represent the 12 directions for each of the shells as well as the 42 directions for the DT42 shell

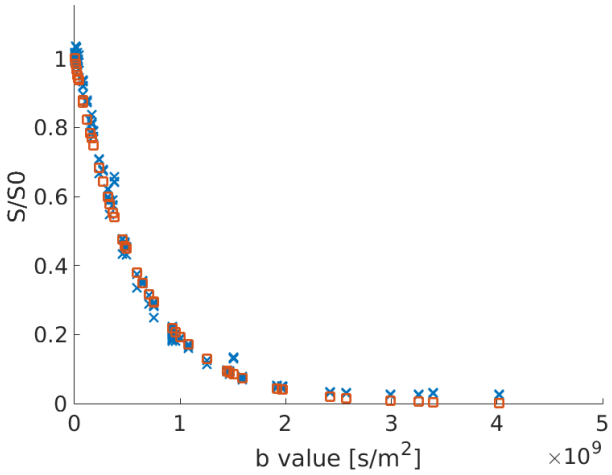

Figure 4.2: Plot showing mean normalised signal represented by the blue crosses and ball model predicted signal represented by the red boxes for the cells and ECM-gel, from our first experiment using the final protocol used to evaluate the ball and sphere model

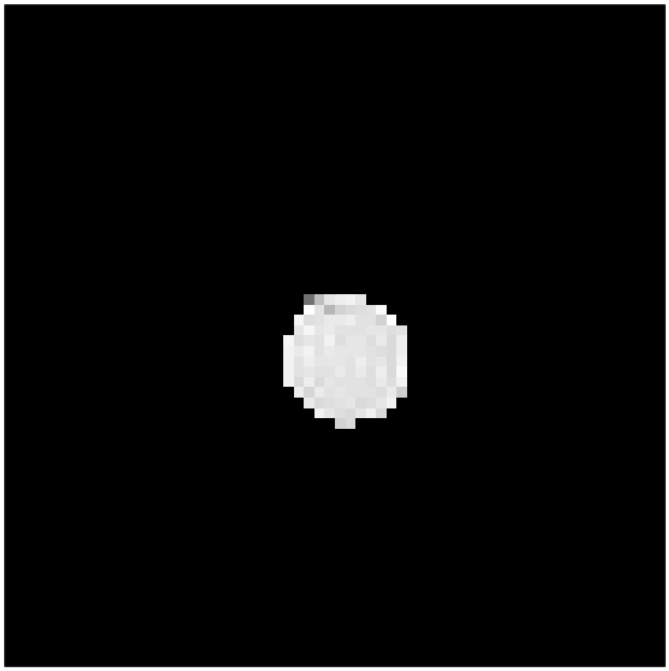

Figure 4.3: B=0 from our first experiment using the final protocol used to evaluate the ball and sphere model

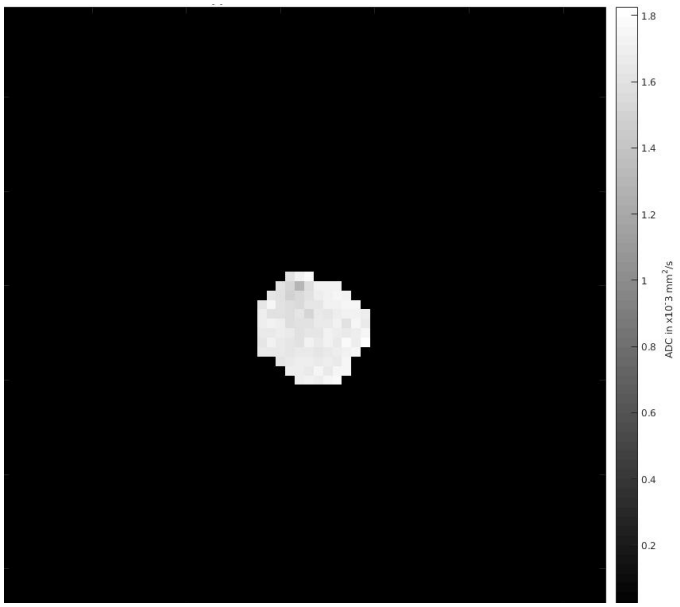

Figure 4.4: ADC map from our first experiment using the final protocol used to evaluate the ball and sphere model

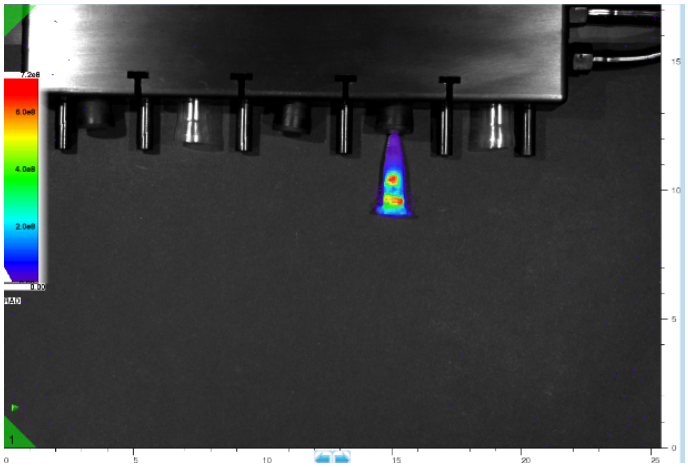

Figure 4.5: Bioluminescence image, for the first experiment using the final protocol used to evaluate the ball and sphere model. This Image shows the intensity of the light emitted from the luciferase positive cells in the phantom when luciferin is added.

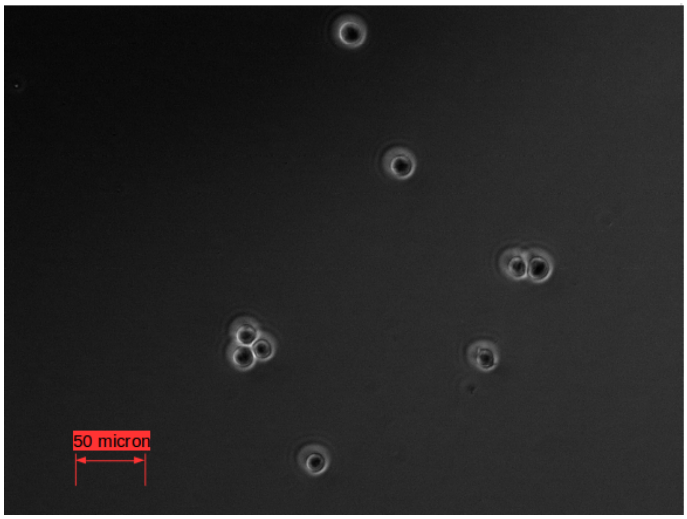

Figure 4.6: Cells extracted from the ECM-gel imaged with a Zeiss Axio Observer Z1 during the first experiment using the final protocol used to evaluate the ball and sphere model

Figure 4.5 shows the AMI-X bioluminescence image acquired after the cells in the micro-centrifuge tube were scanned using the MRI scanner. This shows what looks like a slightly uneven distribution of viable cells. The cells extracted from the ECM-gel using dispase were over 95 % viable. However we were unable to extract all of the cells using dispase and there were groups of cells still in ECM-gel. Because they were still in ECM-gel the number of cells in the groups could not be determined. An image of the cells taken with the Zeiss Axio Observer Z1 is shown in figure 4.6. The average cell radius measured using the Zeiss Axio Observer Z1 microscope was 5.9 $\pm$ 0.1 microns as measured manually. The average cell radius as measured manually is the mean cell size as calculated from the cell diameter measured by an untrained user for each of the cells in figure 4.6. The diameter of each cell can be measured manually using the Zeiss Axio Observer Z1 software in which the user can identify a cell by eye and draw a line across the cell. The software provides the user with the length of the line and this can be recorded as the cell diameter. The average cell radius measured using the Zeiss Axio Observer Z1 microscope was 8.8 $\pm$ 0.4 microns measured automatically using $FIJI$ [89]. The discrepancy in the measurement seems to be due to the automated method measuring the radius of the halo surrounding the cell in the phase contrast images, rather than measuring the radius of the cell. The Halo is the bright ring around the cells caused by the contrast between the cell and the background, and it is a common artifact in phase contrast microscopy images [78]. This would give an estimated intracellular volume fraction of 0.09 according to the manual cell size measurement and 0.3 according to the automatic cell size measurement. The cell size reported here is smaller than that published in the original VERDICT study [81]. This may be due to a difference in the size of cells grown in-vitro and in-vivo. Alternatively, the process used to extract cells from the ECM-gel may have extracted a larger proportion of smaller cells. Another possibility is that the protocol may have altered the cell's size as the cells are trypsinised at the start of the protocol and extracted from ECM-gel with dispase at the end of the protocol.

In the second experiment using the final protocol used to evaluate the ball and sphere model, the number of cells harvested was as expected. A total of 1.166×10^8 - 2.56×10^8 SW1222 cells were harvested for the experiment. Figures 4.7 -4.10 show the data acquired from the MRI scanner. We can see in figure 4.7 that there is a poor match between the ball predicted values marked by the red boxes, and the mean normalised signal marked by the blue crosses. In contrast, in figure 4.8 there is a good match between the ball and sphere model predicted values marked by the red boxes and the mean normalised signal marked with the blue crosses. The ball and ball and sphere model predicted signal for each b-value was calculated by in house MATLAB software for the model parameters (ADC, cell size and intracellular volume fraction) estimated using the ball and ball and sphere model for the MRI data acquired. This shows that the ball and sphere model is an appropriate model for this data.

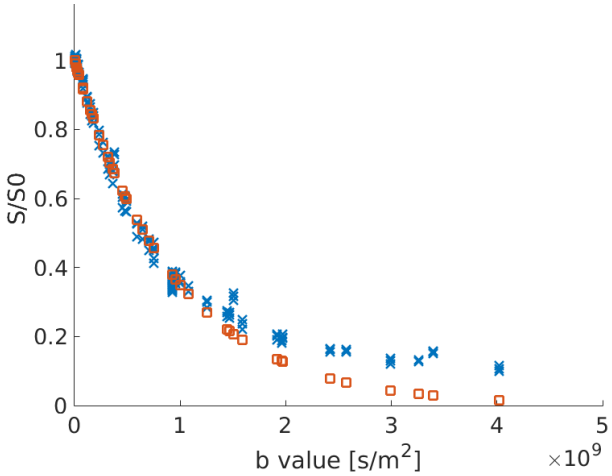

Figure 4.7: Plot showing mean normalised signal from the cells and ECM-gel represented by the blue crosses and ball model predicted signal represented by the red boxes, for the second experiment using the final protocol used to evaluate the ball and sphere model

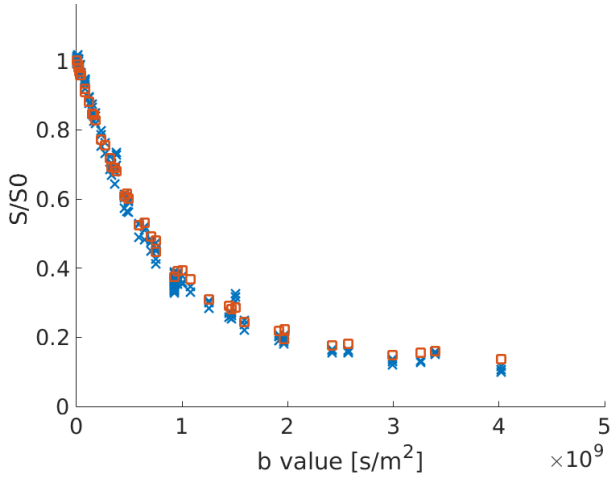

Figure 4.8: Plot showing mean normalised signal from the cells and ECM-gel represented by blue crosses and ball and sphere model predicted signal represented by red boxes, for the second experiment using the final protocol used to evaluate the ball and sphere model

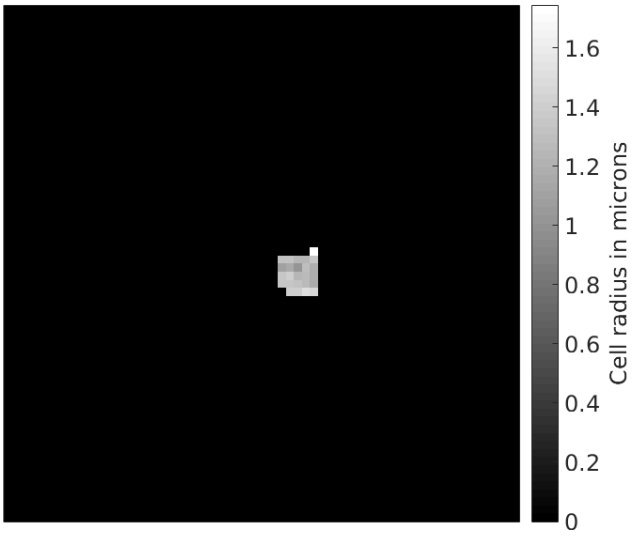

Figure 4.9: Image showing cell size as predicted by the ball and sphere model for the second experiment using the final protocol used to evaluate the ball and sphere model

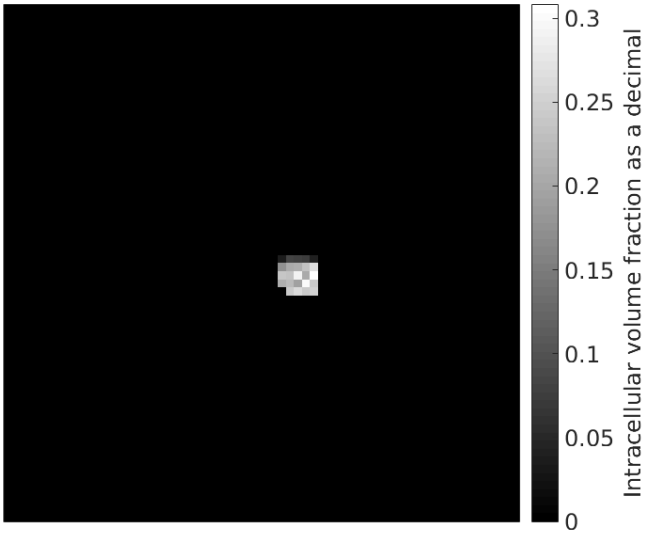

Figure 4.10: Image showing intracellular volume fraction as predicted by the ball and sphere model for the second experiment using the final protocol used to evaluate the ball and sphere model

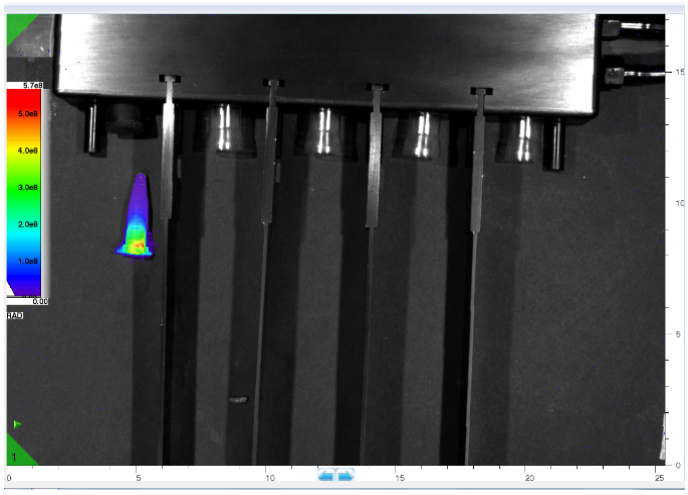

Figure 4.11: Biouminescence image, for the second experiment using the final protocol used to evaluate the ball and sphere model. This Image shows the intensity of the light emitted from the luciferase positive cells in the phantom when luciferin is added

Figure 4.9 shows a cell size map, and figure 4.10 shows an intracellular volume fraction map. Both were produced using the ball and sphere model from MRI data acquired from the cells in ECM-gel. Figure 4.11 shows the AMI-X bioluminescence image from the same experiment. The intensity of the signal from the bioluminescence is much less than would be expected if all of the cells were viable. The viability of the cells after they had been imaged with the AMI-X was around 50%. Unfortunately we were unable to measure cell size on this occasion as the Zeiss Axio Observer Z1 microscope was out of service. However, we assume that the cell size would have been similar to that measured previously. This means that the cell size predicted by the ball and sphere model, is less than a third of the actual size of that would be expected with viable SW1222 cells. The intracellular volume fraction predicted with the ball and sphere model is approximately half what we would have expected had all of the cells remained viable (0.15 as opposed to 0.3). This would suggest that the ball and sphere model is valid.

4.3.2 Results from the biological phantoms used to evaluate DEXSY

The ability of the revised biological phantom to maintain cell viability was evaluated with a 5 hour long bioluminescence experiment. In this experiment luciferin was added hourly to a phantom made from 559 million cells. The intensity of the bioluminesence signal was greater after 5 hours than it was at the start of the experiment. An increase in bioluminescence should correspond to an increase in cell viability and this suggests that the experiment's design had failed to account for the build up of luciferin that occured in the course of the experiment. However, the results also suggest that the cells in the biological phantom that were viable at the start of the experiment remained viable for the duration of the 5 hour long experiment (greater than 90% of the cells were viable at the start of the experiment).

Figures 4.12-4.17 show diffusion-diffusion exchange plots produced from the ECM-Gel biological phantoms used to evaluate DEXSY and composed of ECM-gel and SW1222 cells. The number of cells used are 635 $\pm$ 5, 108 $\pm$ 5, 526 $\pm$ 5, 133 $\pm$ 5 and 298 $\pm$ 5 million cells per phantom. According to our protocol, and assuming the measured cell size reported for the SW1222 cells in the histological results from the published in-vivo VERDICT study [81], we can expect an intracellular volume fraction of 0.6, for each of the biological phantoms shown in figures 4.12-4.17. However, this assumption may be incorrect as the cell size measured from the image in figure 4.7, is smaller than that measured in the VERDICT study.

In diffusion-diffusion exchange plots, diagonal peaks represent diffusion within different compartments (here, intracellular and extracellular) and off diagonal peaks represent diffusion exchange between compartments. No diffusion exchange peaks are present in figures 4.12-4.19. Nevertheless, based on the diffusivity of the diagonal peaks observed, likely intracellular and extracellular peaks are present in figure 4.12, 4.14 and 4.16. However, these peaks can not be separated completely, and there is a third peak which probably represents free diffusion in media due to the high diffusivity of that peak, in figure 4.12. In the diffusion-diffusion exchange plot in figure 4.13, 4.15 and 4.17 there is a single peak, even though figure 4.15 has the same DEXSY scan parameters as figure 4.14. The diffusion-diffusion exchange plot shown in figure 4.14 looks much more consistent with a biological phantom peak and a media peak, than an intracellular and extracellular compartment peak. This is inferred because the media surrounding the biological phantom would have a much higher diffusivity than the intracellular and extracellular space in the biological phantom.

Figures 4.18-4.19 shows diffusion-diffusion exchange plots produced from collagen gels with 1.92 million cells and 5.61 million cells. Only a single peak is present in these two plots. The number of cells in these phantoms was insufficient to achieve the intracellular volume fraction required for the intracellular diffusion to be discernible with diffusion MRI.

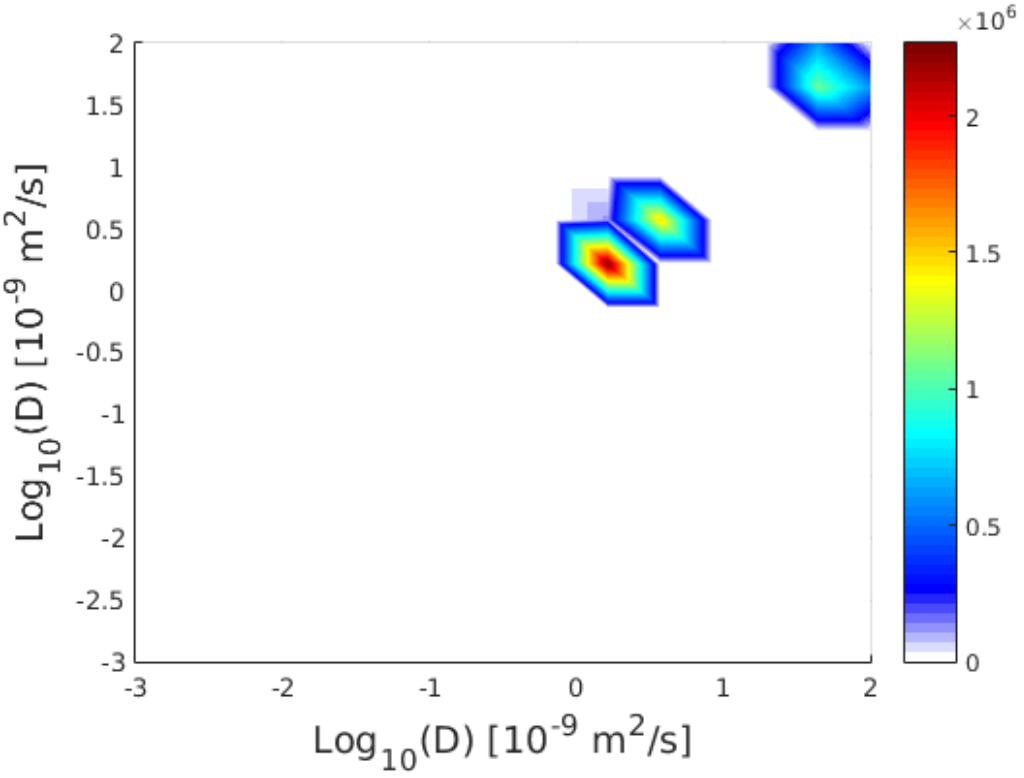

Figure 4.12: Diffusion-diffusion exchange plot from phantom 1, which is made from cancer cells in ECM-gel

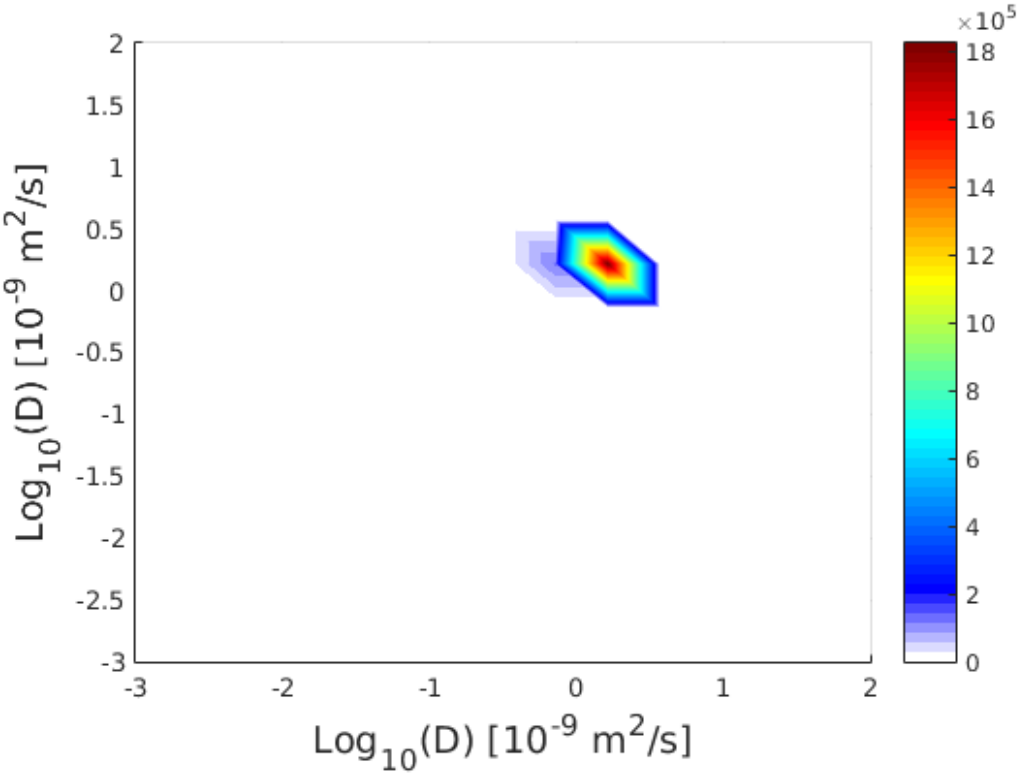

Figure 4.13: Diffusion-diffusion exchange plot from phantom 2, which is made from cancer cells in ECM-gel

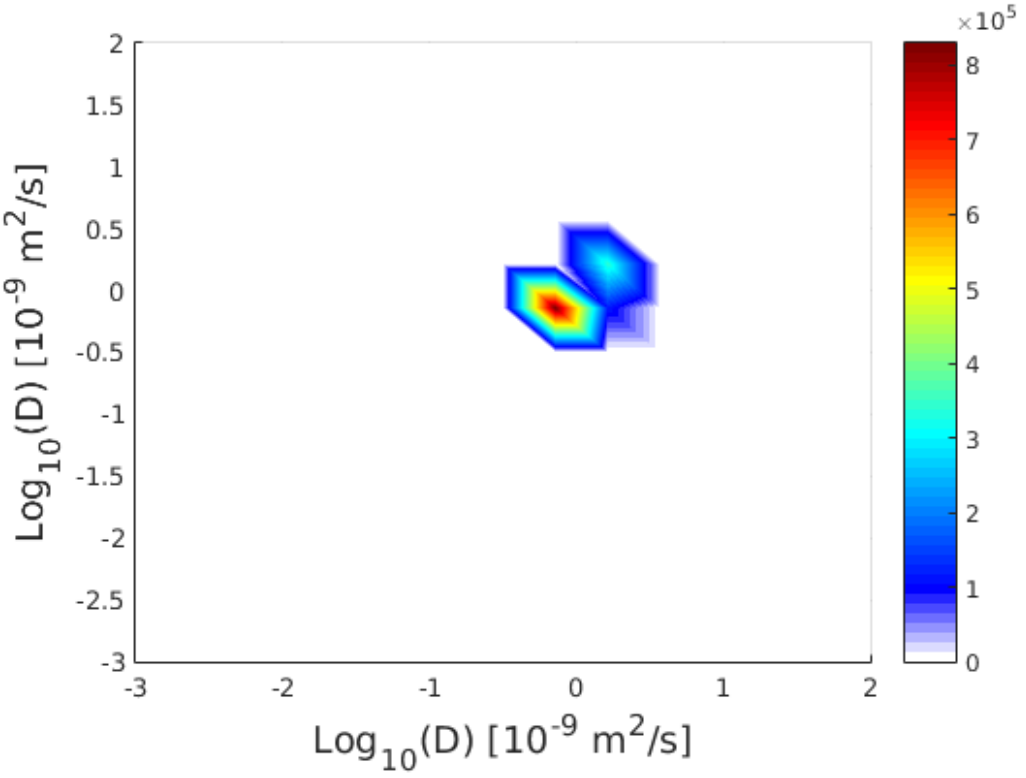

Figure 4.14: Diffusion-diffusion exchange plot from phantom 3, which is made from cancer cells in ECM-gel

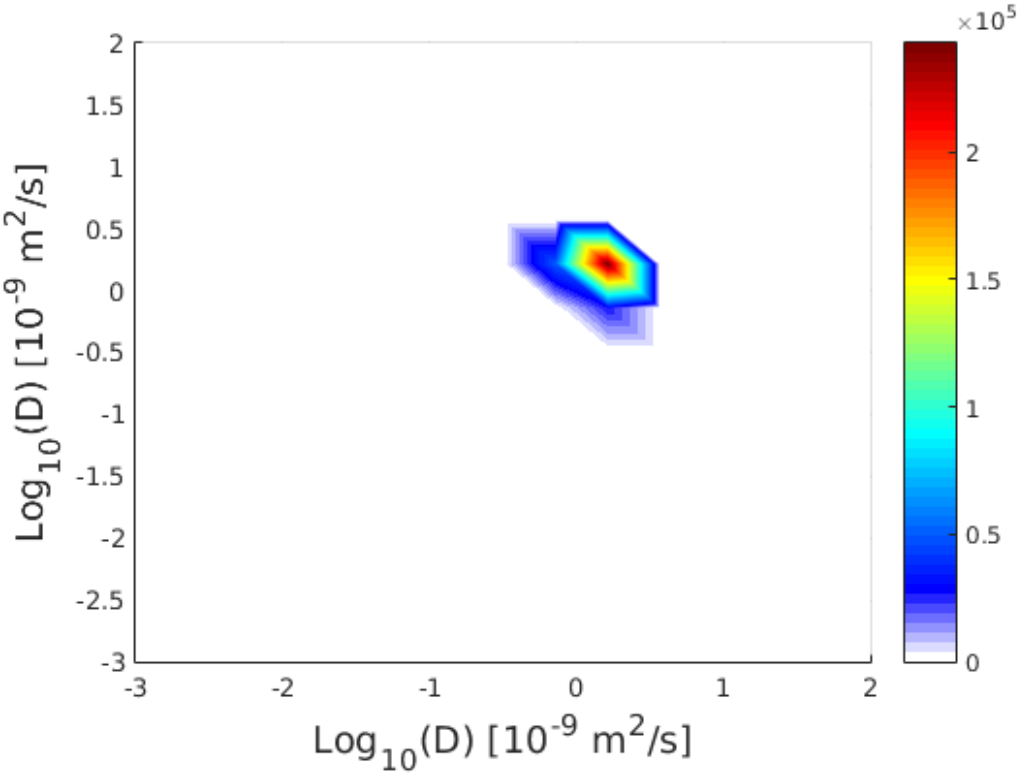

Figure 4.15: Diffusion-diffusion exchange plot from phantom 4, which is made from cancer cells in ECM-gel

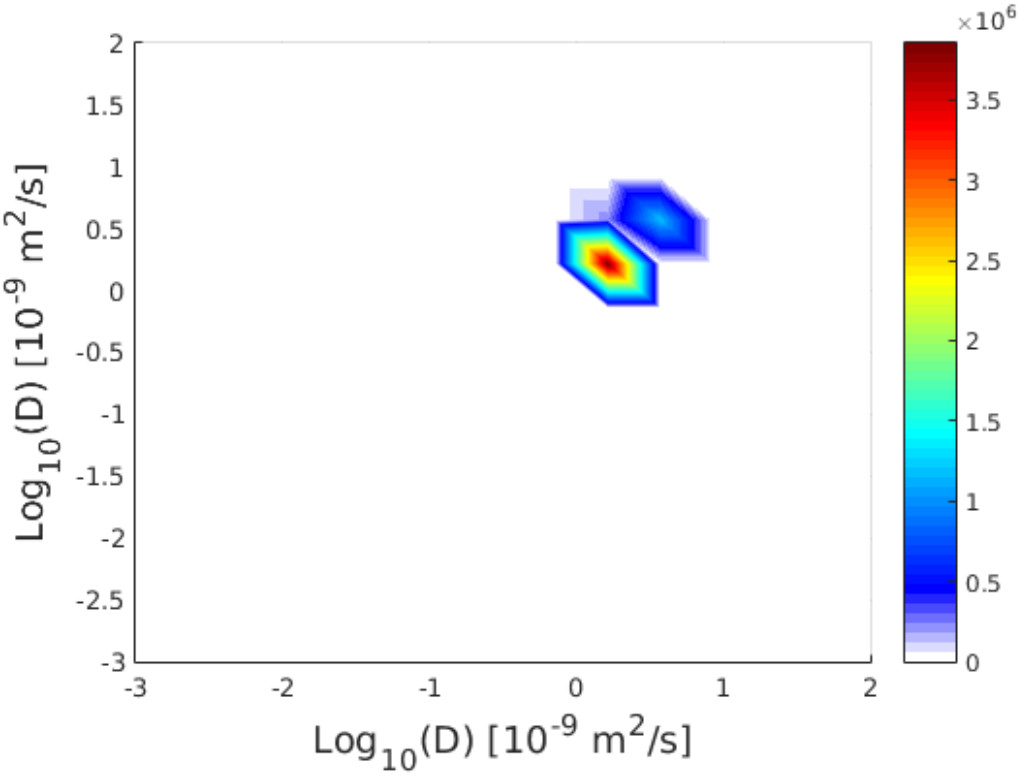

Figure 4.16: Diffusion-diffusion exchange plot from phantom 5 acquisition 1, which is made from cancer cells in ECM-gel

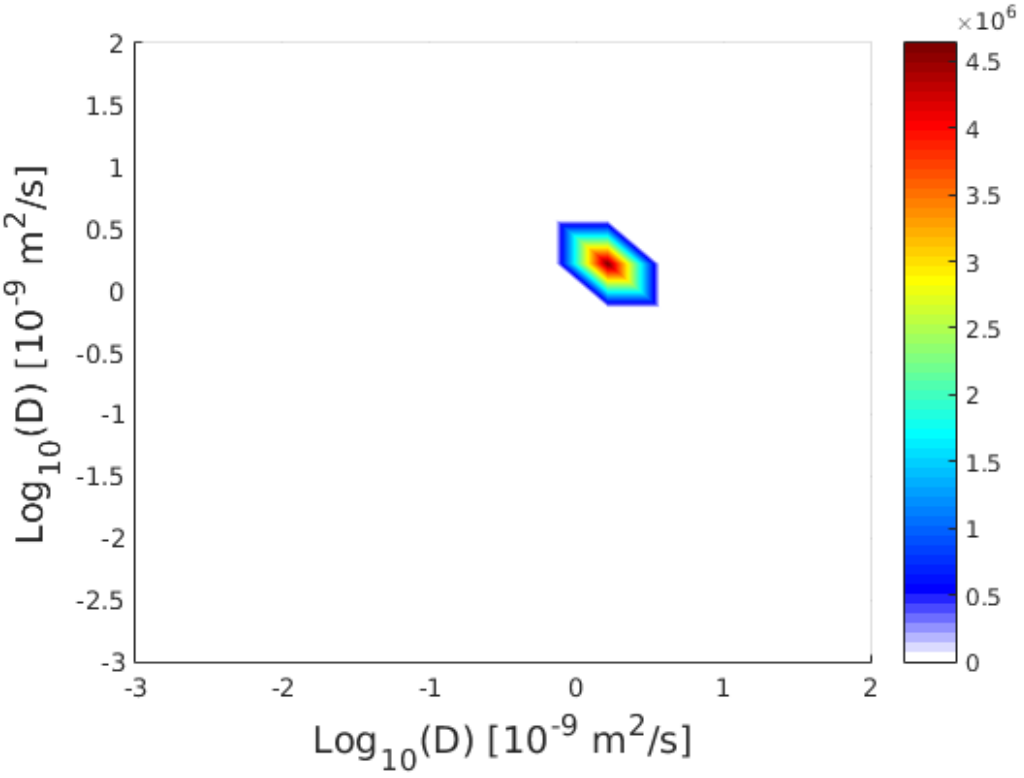

Figure 4.17: Diffusion-diffusion exchange plot from phantom 5 acquisition 2, which is made from cancer cells in ECM-gel

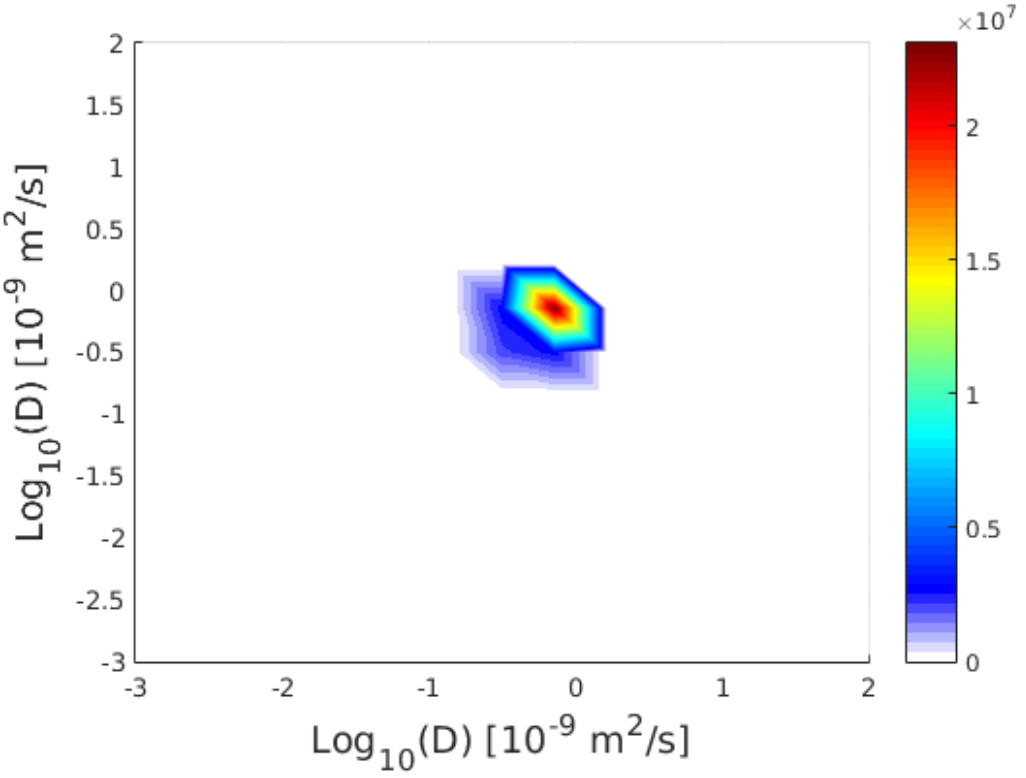

Figure 4.18: Diffusion-diffusion exchange plot from phantom 6, which is made from cancer cells in collagen gel

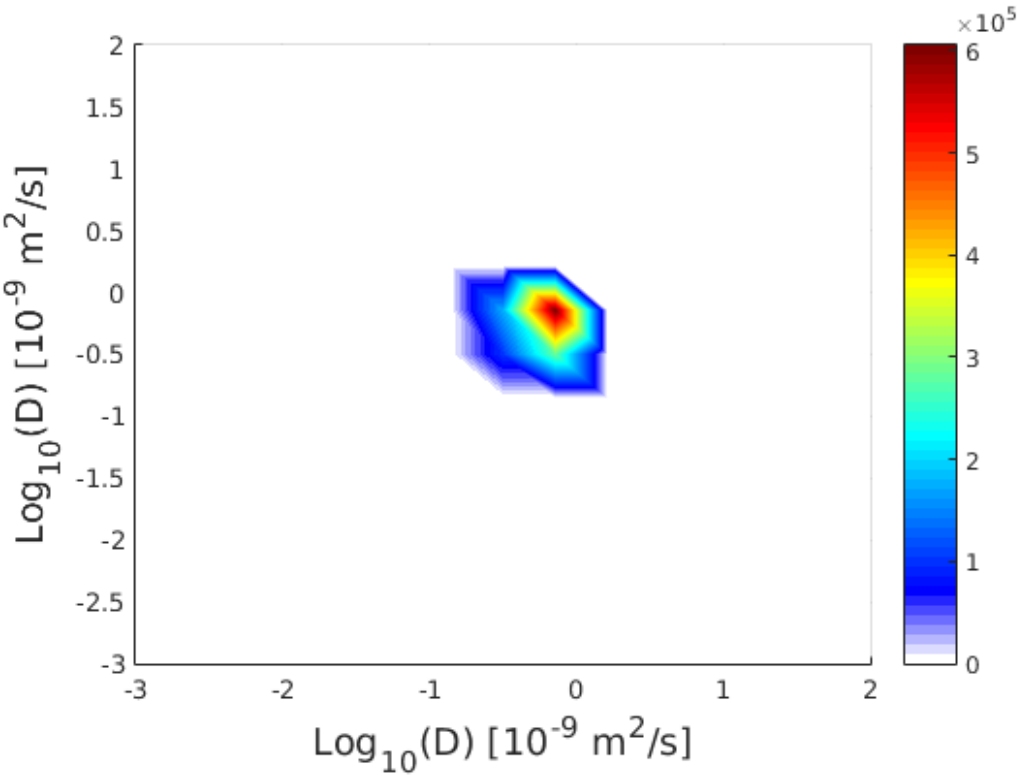

Figure 4.19: Diffusion-diffusion exchange plot from phantom 7, which is made from cancer cells in collagen gel

4.4 Discussion

4.4.1 Discussion of the results from the final protocol used to evaluate the ball and sphere model

The values of the intracellular volume fraction and cell size predicted by the ball and sphere model shown in figures 4.9 and 4.10 are not what would have been expected had the cells been 100 % viable at the end of the experiment. Approximately 50 % of the cells were not viable at the end of the experiment. Our initial hypothesis was that the ball and sphere model describes the diffusion MRI signal produced from the intracellular and extracellular space in our biological phantom. Thus we did not expect that it would describe the signal from cells undergoing cell death. During cell death the cell membrane becomes more permeable and there are changes in the size of the cell and, as a consequence the modelling assumptions underlying the ball and sphere model can break down. The intracellular volume fraction predicted by the ball and sphere model was half of that which we estimated had all of the cells remained viable, whilst the cell size was less than a third of what we would have expected. This suggests that the intracellular volume fraction predicted by the ball and sphere model may have been close to the intracellular volume fraction at the end of the experiment, whilst the predicted cell size is probably incorrect. As we stated before, our model was not expected to describe a situation with such a high degree of cell death, so we would not necessarily expect our results to be accurate in this situation. In the next section this problem is addressed in more detail. This means in order to attempt to evaluate the model we would have to repeat the experiment with a higher intracellular volume fraction of 60 % and a cell viability of 95 % or higher at the end of the experiment. The good fit between the values of the signal predicted by the ball and sphere model and the normalised signal in figure 2.8 is encouraging. However, the predicted cell size is probably incorrect, suggesting that the model may have been over-fitted.

In order to carry out biological phantom experiments with a larger intracellular volume fraction and a higher degree of cell viability, we have refined the protocol for carrying out the experiment. The cells remained viable for the duration of the experiment in our initial experiments, which were carried out with relatively few cells. There were no differences in the conditions of the first and second experiment using the final protocol used to evaluate the ball and sphere model, apart from the number of cells present. Thus the decrease in cell viability that occurred in the second experiment can probably be attributed to an inadequate supply of glucose and oxygen. A revised protocol for producing a biological phantom was developed to remedy this but it was only used for DEXSY.

4.4.2 Discussion of the results from the biological phantoms used to evaluate DEXSY

The revised protocol uses a micro-centrifuge tube, with a filter unit consisting of a semi-porous membrane. The semi-porous membrane keeps the mixture of cells, ECM-gel and DMEM media inside the micro-centrifuge tube, whilst allowing glucose and oxygen to diffuse across the semi-porous membrane. Our preliminary bioluminescence experiment suggests that the revised protocol produces a phantom that can keep cells viable.

The biological phantoms used in this chapter to evaluate and develop DEXSY, as a technique to measure diffusion exchange across the cell membrane in cancer require an intracellular volume fraction of approximately 0.6 in order to model tumours. If the assumptions made regarding cells size in the revised protocol are correct then the biological phantoms made using ECM-gel; phantoms 1-5 have the required intracellular volume fraction. However, in the collagen phantoms; phantoms 6 and 7 there were insufficient cells to achieve the required intracellular volume fraction. As such we would need to develop a means of maintaining a higher intracellular volume fraction in the collagen phantoms, before they could be used to evaluate DEXSY.

It is clear from figures 4.12-4.19 that no diffusion exchange peaks are present, and that the intracellular and extracellular peaks are not clearly differentiated. The results of biological phantom 1 shown in figure 4.12 suggest that the diffusion gradients chosen are incorrect, as the two peaks are very close together. This suggests that we need to use a smaller maximum diffusion gradient strength.

If our assumptions regarding cell size and cell viability, are correct and there are no significant partial volume effects. Then it would seem likely that all of the DEXSY scan parameters trialled lack sensitivity to the cancer cells intracellular diffusion and diffusion-exchange across the cell membrane. However, if our assumptions regarding cell size and viability are incorrect, there could have been a smaller than expected intracellular volume fraction. This could have resulted in too little signal coming from the intracellular compartment for that signal to make a significant contribution to the DEXSY diffusion-diffusion exchange plots. Nevertheless, the biological phantom was positioned in a centrifuge tube full of media and given that a slice selective sequence was used it is likely that the DEXSY data presented in this chapter has been effected by partial volume effects.

Figures 4.12-4.16 show diffusion-diffusion exchange plots which may suffer from a combination of sub-optimal DEXSY scan parameters and a sub-optimal experimental design with regards to the positioning of the phantom. It is likely that the study suffers from partial volume effects as the position of the slice is such that it would have cut across the centrifuge tube and the micro-centrifuge tube with the filter containing the cells mixed with ECM-gel and media. Therefore, there would be some media in between the micro-centrifuge tube and the centrifuge tube wall. This, combined with the small volume of the phantom would have resulted in a small proportion of the total signal originating from cells in the phantom. The contribution from the rest of the set up could also have had a substantial impact on the acquisition. Also, the mixing time used for biological phantom 1-4 was also 100 ms which may be too short to capture diffusion exchange across the cell membrane. The intracellular volume fraction of the cells may also

be less than expected. As explained in the results section, and this would also reduce the likelihood of seeing clear intracellular and extracellular compartments.

It is clear from the results presented in this chapter that partial volume effects need to be eliminated and the mass/volume of cells used for each experiment has to be controlled. If, we are to eliminate all variation in our in-vitro experiments other than those caused by altering the DEXSY scan parameters. Given we are using a slice selective DEXSY sequence this could only be achieved by filling a centrifuge tube with a known volume/mass of cells in a suspension/mixture. Yeast is the obvious choice for in-vitro work as it is easy to work with and it is a well established model for eukaryotic cells [57]. Yeast has also been used to evaluate FEXSY in the past [6].

4.5 Conclusion

Biological phantoms have been produced with the required intracellular volume fraction according to the protocol. However, the protocol requires a large amount of time to produce a single biological phantom. The Centre for Advanced Biomedical Imaging has also lost some of its bioluminescence imaging capabilities, as such it is no longer possible to asses the viability of biological phantoms in-vitro. It also takes two weeks of preparation to produce a single biological phantom, whilst it takes up to 6 hours to conduct an experiment with the phantom. It also seems clear that the slice selective DEXSY sequence may have difficulty capturing the biological phantom using a single slice, as the mixture of cells and ECM-gel takes up such a small volume. The intracellular volume fraction according to the protocol may also be incorrect as the cells used to produce the phantom may be smaller than the cell size assumed. The amount of time required to produce biological phantoms and the practical difficulties in conducting diffusion MRI experiments using biological phantoms, make it impractical for them to be used to develop DEXSY as an imaging technique in a timely fashion. As such, alternative techniques to evaluate DEXSY are needed before moving on to in-vivo valida-

tion of DEXSY as a means to measure cell membrane permeability in tumour xenograft models.

Prior to applying DEXSY to in-vivo xenograft models, it must be established, that the DEXSY sequence makes accurate measurements of diffusion, that DEXSY produces measurements that provide a quantitative indicator of cell membrane permeability, and that DEXSY can measure diffusion-diffusion exchange in living cells. If these criteria are fulfilled, then DEXSY should be able to measure diffusion exchange and provide a quantitative indicator of cell membrane permeability in-vivo. The following chapters show work with physical and chemical phantoms which demonstrate that DEXSY can measure diffusion accurately. Simulations demonstrating that DEXSY can provide a quantitative indicator of cell membrane permeability in-silico, and experimental data demonstrating the measurement of diffusion exchange in-vitro in yeast with DEXSY. Yeast is used for in-vitro work as it is easy to work with and it is a well established model for eukaryotic cells [57]. The work presented prior to the final experimental chapter demonstrates that there is sufficient evidence presented in this thesis to justify the application of DEXSY in-vivo. The final experiential chapter presents DEXSY data acquired in-vivo from tumour xenograft models.

Chapter 5

Chemical and Physical DEXSY Phantoms

5.1 Introduction

As is stated in the previous chapter, it must be established that DEXSY can make accurate measurements of diffusion. Chemical and physical phantoms can prove a useful means of validating the technique before moving onto biological samples. Once we demonstrate the accuracy of diffusion measurements using a physical or chemical phantom, we can move onto using simulations which evaluate DEXSY in-silico demonstrating that DEXSY can be used to measure cell membrane permeability in an idealised situation. We can then move onto biological samples and in-vitro DEXSY acquisitions in yeast suspensions.

DEXSY is an established technique for studying soft matter [17, 37, 85], however, the diffusion measurements have not been verified with another established technique. Thus we needed to demonstrate the accuracy of diffusion measurements made with DEXSY. We initially considered a range of physical phantoms, but none of the phantoms considered would have simulated a two compartment exchange model. Then we looked at chemical phantoms involving substances with different diffusivities and with chemical exchange of hydroxyl protons between them. In order to evaluate the DEXSY sequence as a technique for mea-

suring diffusion exchange we used a sucrose water phantom, which simulates a two compartment diffusion exchange model. The fast diffusing water and the slow diffusing sucrose act as two separate compartments, whilst the chemical exchange of a hydroxyl proton between the sucrose and water simulates diffusion exchange. The sucrose has a lower diffusivity than water because it is a larger molecule. This method has previously been used by Schilling et al. to validate FEXI [88].

In this chapter I present experimental work in which measurements of the diffusivity of sucrose and water made using a DEXSY scan acquired from a chemical phantom are validated independently using DOSY. When we conduct a DEXSY experiment on a sucrose water phantom we would expect to observe four peaks on a diffusion-diffusion exchange plot; a slow diffusion peak due to the slow diffusing sucrose molecules, a fast diffusion peak due to the fast diffusing water molecules, and two diffusion exchange peaks due to the exchange of the hydroxyl proton between the hydroxyl group on the sucrose molecules and the water molecules. However, there are a number of properties of the phantom which may influence the DEXSY acquisition. These include a difference in relaxation times between the sucrose and water, and an unknown hydroxyl proton chemical exchange rate (Schilling did not have a ground truth value). The DEXSY sequence I am validating was written by my tertiary supervisor Dr Siow, and based on Callaghan's work [17]. Whilst the DOSY sequence was also written by Dr Siow and based on work by Morris [66]. DOSY is a well established technique for measuring the diffusivity of different chemicals, by measuring the diffusivity of different spectral peaks. Both DOSY and DEXSY are covered in more detail in chapter 3.

5.2 Method

Here we present the method used to acquire diffusion-diffusion exchange plots and diffusion spectra using DEXSY and DOSY, in order to validate the measurement of diffusivity using DEXSY.

As a pilot study, a DEXSY sequence was trialled on 4 different concentrations of 0, 0.5, 1, and 1.5 molar sucrose in 1 ml syringes placed in a 25 ml syringe. However because DOSY is a purely spectroscopic technique the different concentrations of sucrose had to be scanned separately for our DOSY acquisitions. Our DEXSY and DOSY data were acquired from 0, 0.5, 1.0, 1.5 and 2.0 molar sucrose solutions in 15 ml centrifuge tubes scanned with the DEXSY and DOSY sequences using the 26 mm RF coil (Rapid MR International) in the 9.4 T Varian MRI scanner (Agilent Technologies) the phantom was scanned at room temperature (21 $^{\circ}$ C). A range of parameters were used and a number of different data sets were acquired before we got an informative data set (the results of the pilot study are in the appendix 10.1-10.5). As there were a number of problems with the existing sequence, the DEXSY pulse sequence was re-written. The problems included a 9 hour acquisition time, concerns regarding the sequences timing and uncertainty about how the diffusion encoding would be affected by the combination of imaging gradients and crushers. These concerns motivated Dr Siow to write a new DEXSY sequence which was slice selective, with no frequency or phase encoding. The re-written slice selective DEXSY sequence was also used to acquire the DEXSY data in chapter 4, the chapter covering diffusion MRI experiments in biological phantoms.

In order to determine an appropriate maximum diffusion encoding gradient strength. NMR spectra were acquired at a range of diffusion encoding strengths, in a sample consisting of a 2 molar sucrose water solution. The smallest diffusion encoding gradient strength in which the NMR spectrum acquired was indiscernible from noise, was used as the maximum diffusion encoding gradient

strength in the DEXSY acquisitions. The DEXSY data were acquired using the following parameters Δ = 23 ms, δ = 21 ms, t_m = 100 ms, TE = 150 ms, the TR = 3000 ms, G_1 and G_2 = 0-800 mT/m in 16 $\times$ 16 steps. The DOSY data were acquired using Δ = 23 ms, δ = 21 ms, TE = 200 ms, the TR = 3000 ms and the diffusion gradients were set to vary between 0 and 800 mT/m in 256 even increments. The data acquired using this combination of parameters produced a data matrix dominated by noise, so the data were reacquired. The data were reacquired using a log spacing of the diffusion encoding gradients for the DEXSY sequence, and the maximum gradient strength used for each concentration of sucrose were 800 mT/m, 465.6 mT/m, 309.36 mT/m, 231.28 mT/m and 231.28 mT/m for the 2.0, 1.5, 1.0, 0.5 and 0.0 molar sucrose. A range of maximum gradient strengths were used as it was clear that the variation in physical properties between the different concentrations was such that different parameters were required to capture the necessary information from each scan. The DOSY data were reacquired without any change in the acquisition parameters. The water peak in the NMR spectra was not present in the reacquired DEXSY data. The reacquisition was repeated, however, due to time constraints only the 1.5 molar sucrose water solution was scanned. The T2 of the water peak was measured and it was found to be very short (188ms). As a consequence the timings were adjusted in our optimised DEXSY sequence, in order to capture the water signal.

In our most recent reacquisition of the DEXSY data, a slice selective DEXSY sequence was used and the optimised parameters used were as follows Δ = 11 ms, δ = 9 ms, t_m = 300 ms, TE = 52.5 ms, the TR = 3000 ms, G_1 and G_2 = 0-600 mT/m in 16 $\times$ 16 steps. The parameters for the DOSY acquisition were as follows the TE = 50.0 ms, Δ = 10 ms, δ = 8 ms and the diffusion gradients were set to vary between 0 and 800 mT/m in 256 even increments.

2D inverse Laplace software was used to generate diffusion-diffusion exchange plots from the raw data and the applied b-values [17, 100]. The spectroscopic data was Fourier transformed before the inverse Laplace transform was applied.

The contribution due to imaging gradients was incorporated into the calculation of the b-values. The DOSY data was 1D inverse Laplace transformed and the DEXSY data was 2D inverse Laplace transformed. This gave a diffusion spectrum for the DOSY acquisition and a diffusion-diffusion exchange plot for the DEXSY acquisition.

5.3 Results

In a diffusion-diffusion exchange plot generated using DEXSY data acquired from a sucrose water phantom we expect to see two peaks on the identity line (diagonal peaks), a lower and a higher diffusivity peak corresponding to diffusing sucrose and water molecules. Any off-diagonal peaks are attributed to protons that exchange between the hydroxyl group on the sucrose molecule and the water. The identity line on a diffusion-diffusion exchange plot is where diffusion is measured to be equivalent by both diffusion encoding gradients.

Our initial DEXSY experiment had very little signal with higher concentrations of sucrose. We had even less signal with the lower concentrations of sucrose. Thus we decided to reacquire the data using a different set of parameters. The b=0 DEXSY chemical shift spectrum acquired without diffusion encoding gradients is equivalent to the NMR spectrum produced by a slice selective NMR experiment. The b=0 DEXSY chemical shift spectrum was first acquired for 2 molar sucrose during the first experiment which is shown in figure 5.1, and the spectrum acquired during the second experiment is shown in figure 5.3. The peaks with a chemical shift of 0 are due to water. The peak with a negative chemical shift is due to the hydroxyl group on a sucrose molecule and the peaks with positive chemical shifts are due to hydrogen bound to the carbon on a sucrose molecule. The DEXSY diffusion-diffusion exchange plot for the two experiments is shown in figures 5.2 and 5.4. It is obvious from the figures that one of the spectral peaks has disappeared; the water peak, which was also not present in the lower concentration samples. The most likely explanation for this is that the sucrose had

not fully dissolved the first time the sample was scanned even though the sample was prepared hours before the data were acquired. However, the sucrose would have fully dissolved by the time the data were reacquired. We made a multi echo T2 measurement of the water in the 1.5 molar sucrose sample and found out that it was very short, being only 188 ms. Whilst adding sucrose to water reduces the T2, we were not aware of any easily available substance, which we could add to the phantom in small quantities to increase the T2. (Data not presented in this chapter is present in the appendix 10.5-10.73)

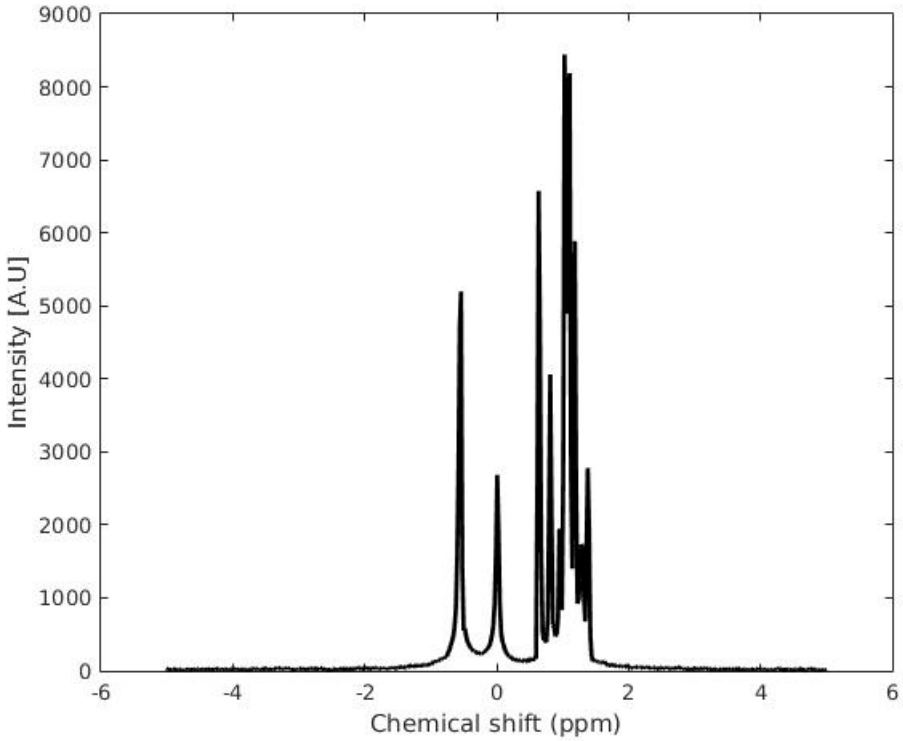

Figure 5.1: DEXSY MR Chemical Shift spectrum acquired from a 2.0 M sucrose phantom on the 27/11/2015 using non-optimal DEXSY scan parameters. The MR chemical shift spectrum shows that there is signal from the hydroxyl group on the sucrose molecules, water molecules, and the hydrogen bound to carbon in the sucrose molecules.

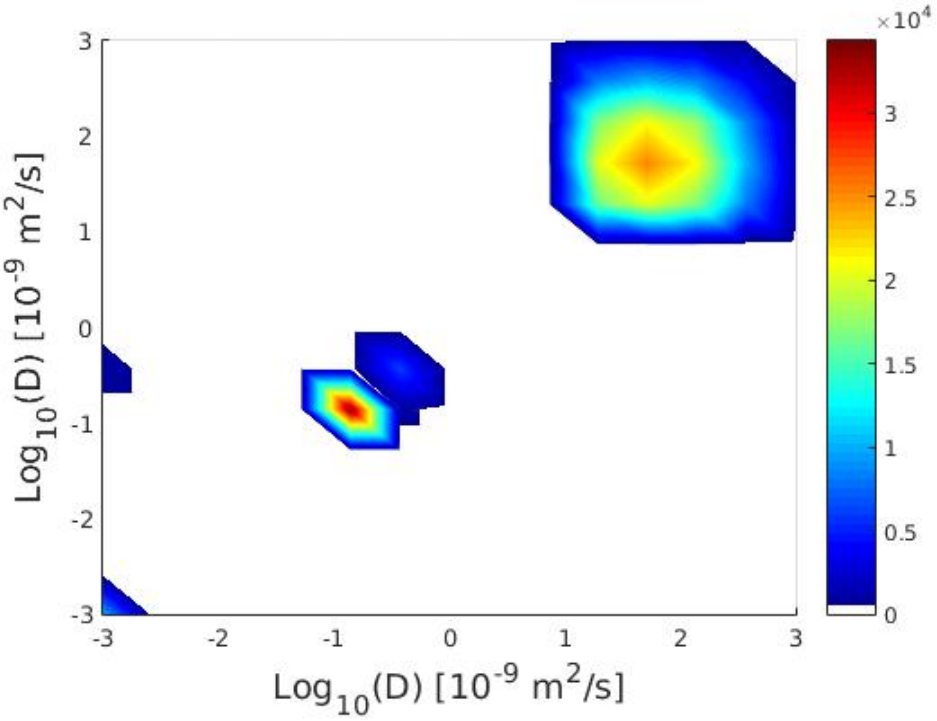

Figure 5.2: DEXSY Diffusion-Diffusion exchange plot acquired from a 2.0 M sucrose phantom on the 27/11/2015 using non-optimal DEXSY scan parameters. This shows diffusion-diffusion peaks consistent with the presence of sucrose and water molecules.

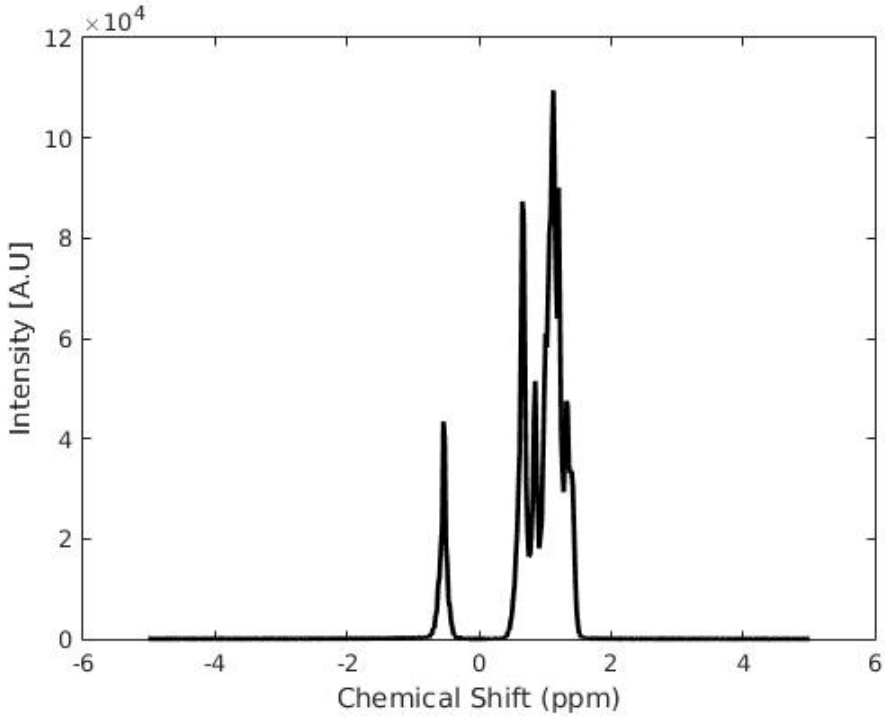

Figure 5.3: DEXSY MR Chemical Shift spectrum acquired from a 2.0 M sucrose phantom on the 20/01/2016 using non-optimal DEXSY scan parameters. The MR chemical shift spectrum shows that there is signal from the hydroxyl group on the sucrose molecules and the hydrogen bound to carbon in the sucrose molecules. However, the signal from the water molecules is missing.

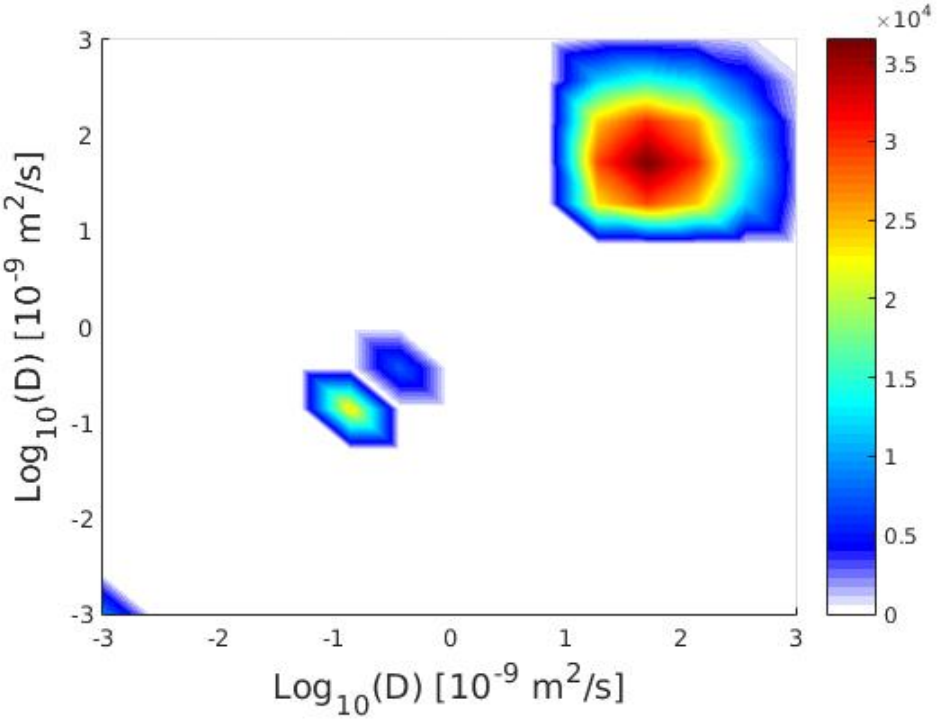

Figure 5.4: DEXSY Diffusion-Diffusion exchange plot acquired from a 2.0 M sucrose phantom on the 20/01/2016 using non-optimal DEXSY scan parameters. This shows diffusion-diffusion peaks consistent with the presence of sucrose and water molecules.

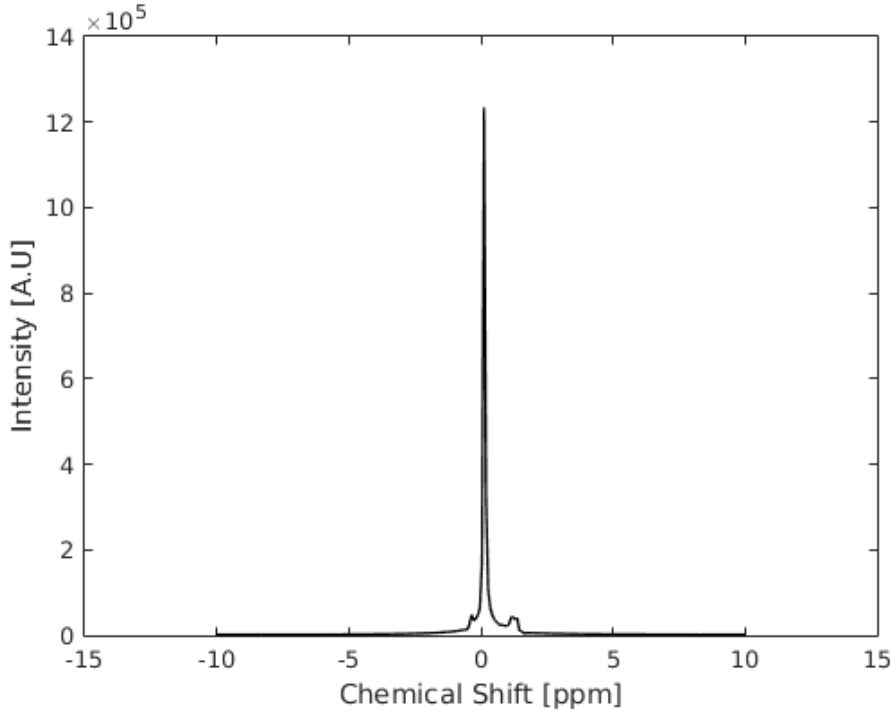

Figure 5.5: DEXSY MR Chemical Shift spectrum acquired from a 0.5 M sucrose phantom on the 24/10/2016 using optimised DEXSY scan parameters.The MR chemical shift spectrum shows that there is signal from the water molecules.

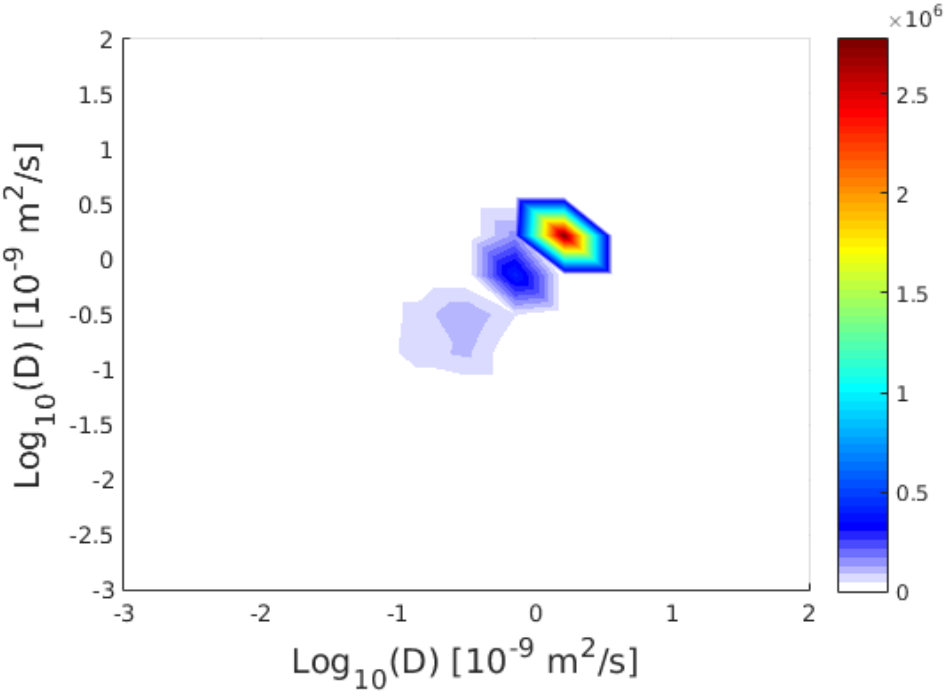

Figure 5.6: DEXSY Diffusion-Diffusion exchange plot acquired from a 0.5 M sucrose phantom on the 24/10/2016 using optimised DEXSY scan parameters. This shows diffusion-diffusion peaks consistent with the presence of sucrose and water molecules.

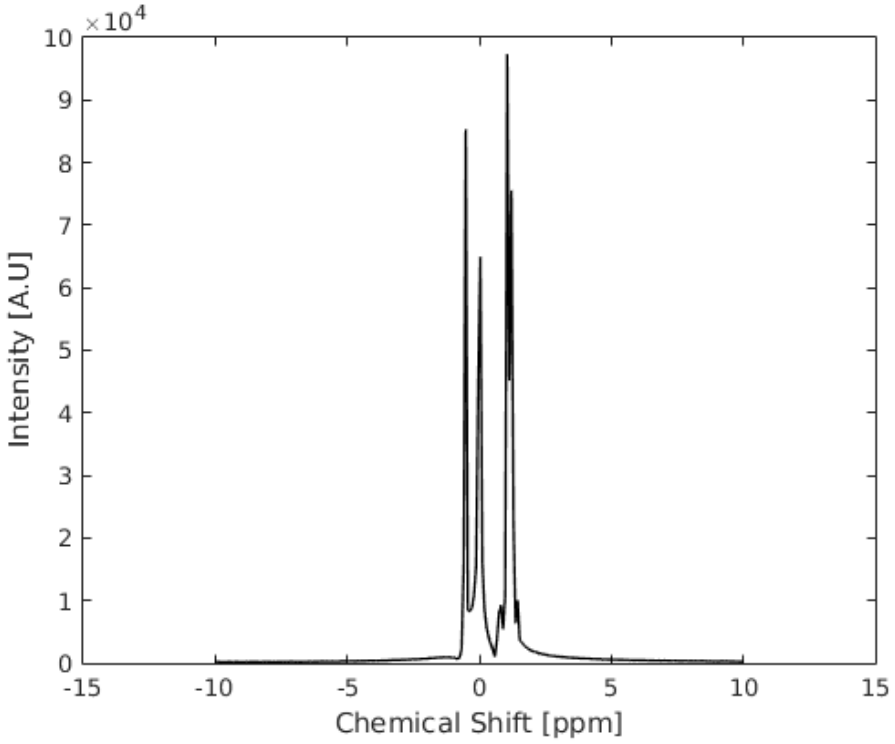

Figure 5.7: DEXSY MR Chemical Shift spectrum acquired from a 1.0 M sucrose phantom on the 24/10/2016 using optimised DEXSY scan parameters. The MR chemical shift spectrum shows that there is signal from the hydroxyl group on the sucrose molecules, water molecules, and the hydrogen bound to carbon in the sucrose molecules.

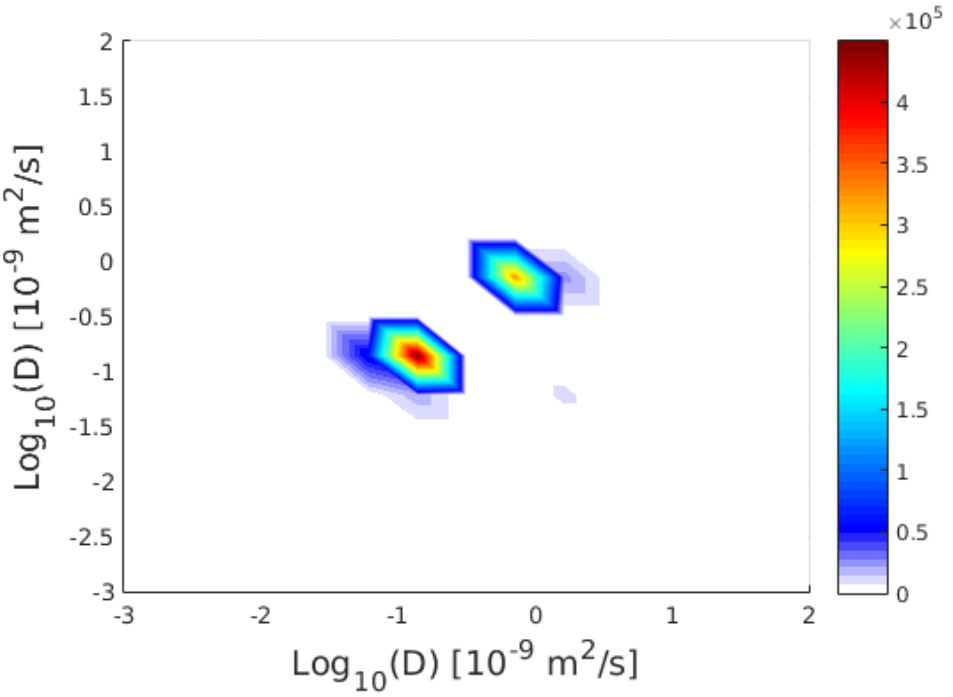

Figure 5.8: DEXSY Diffusion-Diffusion exchange plot acquired from a 1.0 M sucrose phantom on the 24/10/2016 using optimised DEXSY scan parameters. This shows diffusion-diffusion peaks consistent with the presence of sucrose and water molecules.

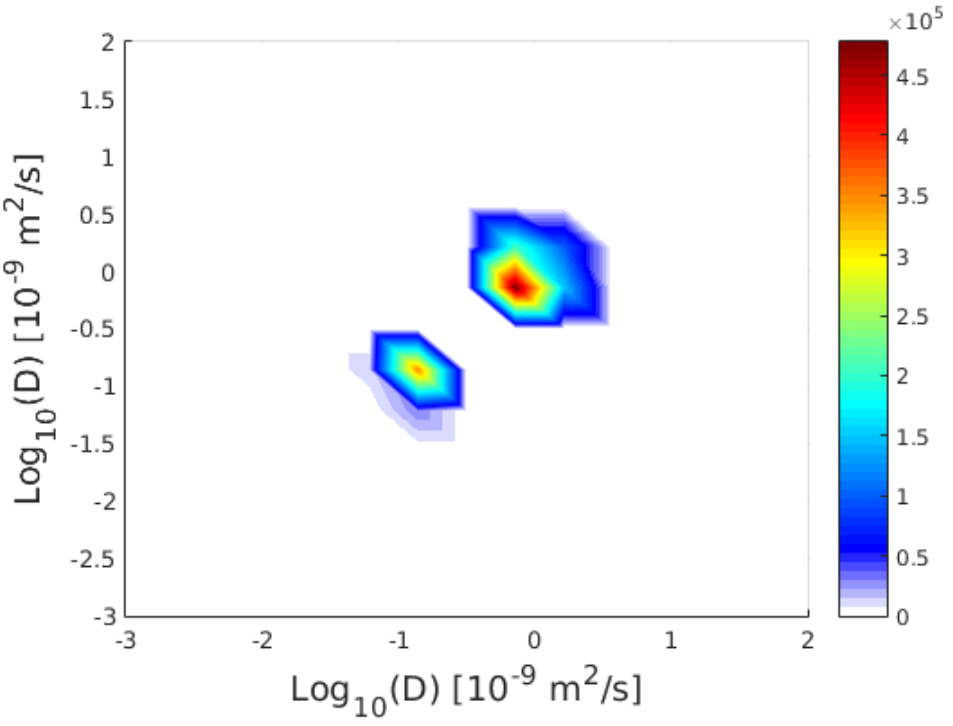

Figure 5.9: DEXSY Diffusion-Diffusion exchange plot acquired from a 1.0 M sucrose phantom on the 12/09/2016 using optimised DEXSY scan parameters. This shows diffusion-diffusion peaks consistent with the presence of sucrose and water molecules.

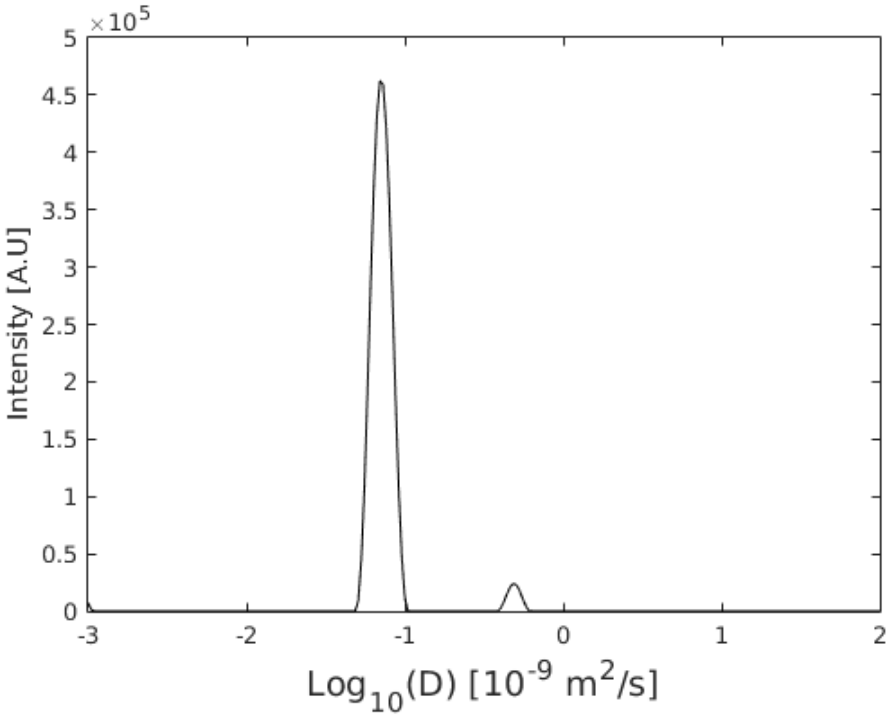

Figure 5.10: DOSY Diffusion spectra acquired from a 1.0 M sucrose phantom. This shows diffusion peaks consistent with the presence of sucrose and water molecules.

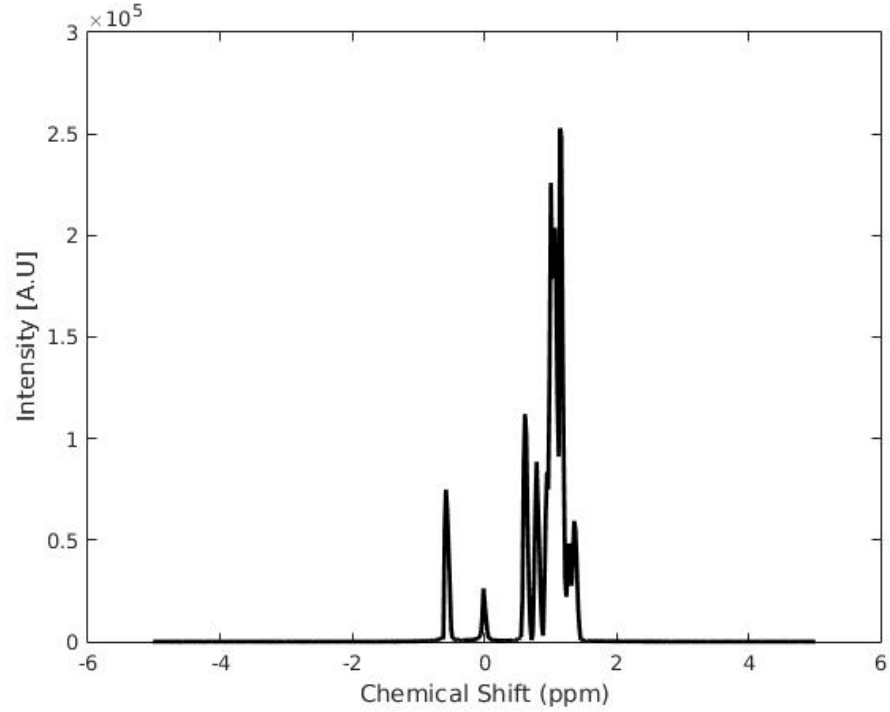

Figure 5.11: DOSY MR Chemical Shift spectrum acquired from a 1.0 M sucrose phantom. The MR chemical shift spectrum shows that there is signal from the hydroxyl group on the sucrose molecules, water molecules, and the hydrogen bound to carbon in the sucrose molecules.

The most recent DEXSY data acquired with optimised scan parameters from the 0.5 molar and 1 molar sucrose are displayed in figures 5.5-5.9, with a DOSY plot for the 1 molar sucrose displayed in figure 5.10.

Figure 5.5 shows the chemical shift spectrum from the 0.5 molar sucrose. There is a very prominent water peak and very subtle traces of what might be other peaks. However, these can be ignored as it is clear from their relative intensity that these would contribute little to the the MRI signal. Figure 5.6 shows a diffusion-diffusion exchange plot from this acquisition. There is a high diffusivity water peak and a low diffusivity water peak. The low diffusivity water peak is likely to represent water bound to sucrose by inter-molecular bonds. This is likely to be the case, as the peaks diffusivity is closer to the diffusivity of sucrose than the free diffusivity of water and inter-molecular bonds can form between sucrose and water molecules.

Figure 5.7 and 5.8 shows the chemical shift spectrum and diffusion-diffusion exchange plot from a DEXSY acquisition acquired from a 1.0 molar sucrose phantom. In the chemical shift spectrum there is a series of peaks and from their position we establish that they correspond to the hydroxyl group on the sucrose, the water, and the hydrogen bonded to a carbon on the sucrose. There is also some overlap for the hydroxyl group and water. The diffusion-diffusion exchange plot clearly shows a sucrose peak positioned at approximately [-1,-1] and water peak at approximately [0,0], and there is also a possible exchange peak positioned at approximately [0,-1]. Figure 5.9 show another DEXSY acquisition from this sample, with the same two diffusion peaks present, but no signs of an exchange peak. Figure 5.10 show an earlier DOSY diffusion spectra from the same sample. It shows a sucrose peak at approximately -1 and a water peak just below 0. However, the intensity of the water peak is less than 10 % of the intensity of the sucrose peak. If the DOSY diffusion spectra are superimposed on the the line of identity for the DEXSY diffusion-diffusion exchange plots, then the two main DOSY diffusion peaks will lie inside the two main DEXSY diffusion peaks

demonstrating that the DOSY and DEXSY diffusion measurements are equivalent. Figure 5.11 shows the chemical shift spectrum from the DOSY acquisition shown on figure 5.10. In the chemical shift spectrum there is a series of peaks corresponding to the hydroxyl group on the sucrose molecule, the water, and the hydrogen bound to carbon on the sucrose molecule.

5.4 Discussion

Our experiments initially demonstrated a relatively weak water signal resulting from a short T2 for water due to the high sucrose concentration. One can see that there is a relatively weak water signal in our initial DEXSY acquisition due to the short T2. The DEXSY spectrum is shown in figure 5.1. A weak water signal makes it unlikely that there would be enough signal to measure exchange from the protons being exchanged between the hydroxyl group on the sucrose molecule and the water molecule. This is because only a small proportion of the water molecules will be involved in diffusion exchange. As such, when there is a weak water signal there will be an even weaker exchange signal. The chemical exchange rate in the sucrose and water phantoms is unknown, and although previous work suggests otherwise [88], it may be too fast to detect with the mixing times used for these experiments.

There is correspondence between DOSY and DEXSY measurements, shown in figure 5.8, 5.9 and 5.10. It seems clear that if the DOSY diffusion spectra are superimposed on the the line of identity for the diffusion-diffusion exchange plots, then the two main DOSY diffusion peaks will lie inside the two main DEXSY diffusion peaks. The correspondence is not however, exact as the position of the centre of the water peaks is slightly different. However, this may be due to T2 effects. It seems likely that DOSY measurements have been subject to T2 effects, as the water peak has a very small magnitude. However, the DOSY data

were acquired with a much higher resolution diffusion spectra and this is why the DOSY peaks are narrower, which may also have resulted in a more precise and accurate measurement of diffusivity.

A range of other chemical and physical phantoms were initially considered but none of the phantoms would have simulated a two compartment exchange model. Preliminary work was performed involving visking tubing, ethanol and acetone. However the preliminary results revealed that their physical or chemical properties were such that I could not design a suitable experiment to validate DEXSY with these materials.

5.5 Conclusion

The results presented in this chapter suggest that we can rely on the diffusion measurements made using DEXSY, as there was a reasonable correspondence with the DOSY diffusion measurements, and the minor inconstancies can be explained by the higher resolution of the DOSY diffusion spectra and T2 effects influencing the DOSY diffusion measurement. However we were unable to observe any clear diffusion exchange peaks, this may be due to T2 effects or it may be due to the chemical exchange rate. Nevertheless, the results provide sufficient validation of the accuracy of the diffusion measurements made with DEXSY. Thus we can move onto in-silico and in-vitro validation even though there were no conclusive observations of exchange in our chemical phantoms.

Chapter 6

Simulations of diffusion exchange

6.1 Introduction

In the previous chapter we demonstrated the validity of diffusion measurements made using DEXSY in chemical phantoms. In this chapter we use simulations to evaluate DEXSY as a technique for measuring diffusion exchange across the cell membrane in-silico. The work presented in this chapter demonstrates that DEXSY can be used to measure diffusion exchange across the cell membrane in an idealised situation. In the next chapter we present in-vitro validation of our simulation results using yeast, which will provide sufficient evidence to justify an in-vivo DEXSY experiment.

Measurements of diffusion exchange across the cell membrane can be used to generate a quantitative indicator of cell membrane permeability. Measuring the diffusion exchange between populations of water diffusing inside and outside the cell is feasible, as previous work has shown that intracellular and extracellular diffusion can be differentiated. This is because extracellular water forms a fast moving compartment due to its hindered diffusion environment and intracellular water forms a slower moving compartment because of its semi-restricted diffusion environment created by the cell membrane [81]. In this chapter we simulate diffusion exchange across the cell membrane in-silico. In addition to this we trialled some fluid exchange model simulations to model the sucrose water phantom.

DEXSY could be used to measure the diffusion exchange of water across the cell membrane, and this can be used to generate a quantitative indicator of cell membrane permeability. Diffusion exchange across the cell membrane refers to the exchange of water between diffusing populations of water inside and outside the cell. It covers diffusion across the lipid bilayer and water transport in and out of the cell through aquaporins. In this chapter we use numerical simulations to assess the feasibility of using DEXSY to measure diffusion exchange across the cell membrane in nerve bundles and yeast suspensions. We compare the results with corresponding simulations for FEXSY (Filter Exchange Spectroscopy) [17, 6]. We use yeast as it is a well-established model for cellular biology studies in eukaryotes [57] . We expect that we should be able to extend this work to measure cell membrane permeability in tumour xenograft models in-vivo, subject to the yeast simulations being validated in-vitro in yeast.

6.2 Method

In this chapter we simulate the measurement of diffusion exchange across the cell membrane using DEXSY and FEXSY in two substrates; a nervous tissue substrate modelling nerve bundles, and a yeast substrate modelling a yeast suspension. A yeast substrate is used as yeast is a well established model for eukaryotic cells such as cancer cells [49] and we could validate our simulations through in-vitro measurement of diffusion exchange in yeast. In addition to this we simulated the measurement of diffusion-diffusion exchange in a fluid exchange model and this served as a model of the sucrose water phantom. In the next chapter we present in-vitro measurements of diffusion exchange in yeast using DEXSY in order to validate our simulations.

In order to simulate diffusion exchange across the cell membrane in a nervous tissue substrate mimicking a nerve bundle a substrate used by Alexander et al. [4, 40] to simulate diffusion MRI measurements of the corpus callosum was modified to allow walkers (simulated water spins) to cross the cell membrane. The

probability of a walker crossing the cell membrane was adjusted to correspond to a wide range of cell membrane permeabilities, including the range of permeabilities measured in the squid axon [86]. A gamma distribution of cylinder radii was used in order to mimic bundles of nerve fibers with a shape parameter of 5.3316, a scale parameter of 1.0242 $\times$ 10^{-7} with 100 cylinders and a lattice size of 1.65 $\times$ 10^{-5} m. Simulations were also carried out using a yeast substrate mimicking a yeast suspension. The yeast substrate was created by Dr Damien McHugh using the Lubachevsky-Stillinger packing algorithm which packs spheres in order to achieve a high packing fraction by seeding spheres randomly and then expanding them [62]. The substrate used in our simulations consisted of a total of 500 spheres packed together with a volume fraction of 0.62 and a diameter of $5\mu m$.

The Monte Carlo simulations were performed using CAMINO with 100,000 walkers, a duration of 0.400 s, a diffusivity of 2.0 $\times$ 10^{-9} m^2/s and 16,000 time steps. The duration used is longer than the duration of the DEXSY sequence. The value of diffusivity used for CAMINO simulations in nervous tissue has been established in previous studies [4]. Simulations were performed using the yeast substrate and the nervous tissue substrate. Simulations were carried out with DEXSY and FEXSY in order to determine the relationship between diffusion exchange measurements and permeability using these techniques. 25 different probabilities of a walker crossing the cell membrane were used ranging between p = 0.0 and 0.1. There is a linear relationship between cell membrane permeability and the probability of a walker crossing the cell membrane [69]. The probabilities were not spaced evenly as we focused around p = 0.0003 which corresponds to a physiological cell membrane permeability of $1.0\mu m/s$, which is similar to that measured in the squid axon [86].

We also carried out simulations in a fluid exchange model which simulates two fluids of differing diffusivity with spins exchanging between the two fluids. The Monte Carlo simulations were performed using CAMINO with 1,000 walkers, a duration of 0.400 s, a diffusivity of 1.0 $\times$ 10^{-9} m^2/s in the fast fluid, and 1.0 $\times$

10^{-12} m^2/s in the slow fluid. There were 610 walkers in the slow and 390 in the fast fluid with 16,000 time steps. The exchange probabilities were the same for both fluids and we used a range of probabilities between p = 0 and 0.00055. Only DEXSY acquisitions were simulated for the fluid exchange substrate.

The parameters of the DEXSY acquisition simulated were δ = 15 ms, Δ = 17 ms, t_m = 100 ms, G_1 and G_2 = 0-900 mT/m in 16 $\times$ 16 steps. The parameters used for our simulations were chosen before any in-vitro DEXSY data were acquired. The range of diffusion encoding gradients were chosen to sample the widest range of b-values possible. Whilst, the mixing time was chosen because FEXSY data already published [50], suggested that 100 ms would be long enough to capture diffusion exchange. A DOSY (Diffusion Ordered Spectroscopy) acquisition was also simulated with the following parameters δ = 15 ms, Δ = 17 ms and encoding gradients set to vary between 0 - 900 mT/m in 256 even increments. A FEXSY acquisition is simulated using the following parameters: δ = 15 ms, Δ = 17 ms and a filter gradient strength of 68 mT/m and an encoding strength varying between 0-68 mT/m in 9 increments with t_m = 0, 10, 100, 200, 300 ms.

The results of the DEXSY and DOSY simulations were inverse Laplace transformed to give diffusion-diffusion exchange plots and diffusion spectra using 2D inverse Laplace software [17, 100]. The Diffusion Exchange Index (DEI) is defined as the ratio of the sum of the volume of the exchange peaks to the sum of the volume of the intracellular and extracellular diffusion peaks and can be used as a quantitative indicator of cell membrane permeability. The FEXSY simulations were processed following a method similar to that used by Nilsson et al [71]. This consisted of calculating the ADC for the data acquired for each mixing time and then fitting a mono-exponential recovery curve to the series of ADC values acquired at each mixing time in order to calculate the apparent exchange rate (AXR).

6.3 Results

In the diffusion-diffusion exchange plots from the simulations carried out in a nervous tissue substrate and the yeast substrate, peaks on the identity line (diagonal peaks), A and B, correspond to diffusing water molecules that remained within the same diffusion environment during both sets of diffusion encoding gradients. Off-diagonal peaks, C and D, correspond to diffusion exchange between environments. As intracellular and extracellular compartments have different diffusivities [80], off-diagonal peaks were interpreted as evidence of exchange between intracellular and extracellular compartments.

The results of our simulations of diffusion exchange in the nervous tissue substrate are shown in figure 6.1. Figure 6.1:a) shows a diffusion-diffusion exchange plot from a simulation carried out in the nervous tissue substrate with p = 0.0 where there is no exchange. There are two peaks lying on the line of identity. Peak B is identified as an intracellular diffusion peak, due to its lower diffusivity attributed to the semi-restricted intracellular diffusion environment. Peak A is identified as an extracellular peak due to its higher diffusivity attributed to the hindered extracellular diffusion environment. Figure 6.1:b) shows a diffusion-diffusion exchange plot from a simulation carried out in the same substrate at p = 0.0003 and an additional two peaks, C and D, are observed and these are identified as diffusion exchange peaks. Figure 6.1:c) shows a diffusion-diffusion exchange plot from a simulation carried out in the same substrate at p = 0.001. Due to the high permeability the peaks all merge into a single diffusion peak D. Figure 6.1:d) shows a DOSY plot from the same simulation shown in figure 6.1:a). It demonstrates that the measurement of diffusivity made with DOSY and DEXSY is equivalent. Figure 6.1:e) shows DEI plotted against permeability in the range in which diffusion exchange can be observed. This corresponds to a range of p =0.0001 to 0.00055, corresponding to a permeability of $0.365 - 2.008 \mu m/s$. The relationship is clearly monotonic, with a Spearman's rank correlation coefficient of 1 (P $<$ 0.05). (The full set of results for the simulations using the nervous tissue

substrate are shown in the appendix)

The results of our simulations of diffusion exchange in a yeast substrate are shown in figure 6.2. Figure 6.2:a) shows a diffusion-diffusion exchange plot from a simulation carried out in the yeast substrate with p =0.0 where there is no exchange. There are two peaks lying on the line of identity. Peak B is identified as an intracellular diffusion peak, due to its lower diffusivity attributed to the semi-restricted intracellular diffusion environment. Peak A is identified as an extracellular peak due to its higher diffusivity attributed to the hindered extracellular diffusion environment. Figure 6.2:b) shows a diffusion-diffusion exchange plot from a simulation carried out in the same substrate at p = 0.0003 and an additional two peaks, C and D, can be observed. These are identified as diffusion exchange peaks. Figure 6.2:c) shows a diffusion-diffusion exchange plot from a simulation carried out in the same substrate at p = 0.1. Due to the high permeability the peaks all merge into a single diffusion peak D. Figure 6.2:d) show a DOSY plot from the same simulation shown in figure 6.2:a). It demonstrates that the measurement of diffusivity made with DOSY and DEXSY is equivalent. Figure 6.2:e) shows DEI plotted against permeability in the range in which diffusion exchange can be observed which corresponds to a range of p = 0.0001 to 0.00055. The relationship is clearly monotonic, with a Spearman's rank correlation coefficient of 1 (P $<$ 0.05). (The full set of results for the simulations using the yeast substrate are shown in the appendix)

Figure 6.3: a) shows AXR plotted against permeability in the range p = 0.0001 to 0.00055 for the nervous tissue substrate. The relationship is also monotonic. However, it seems to break down at between p=0.0004 and 0.0005. Figure 6.3: b) Shows AXR plotted against permeability within the range of p = 0.0001 to 0.00055 for the yeast substrate. The relationship is clearly monotonic.

Figure 6.4:a) shows a diffusion-diffusion exchange plot for the fluid exchange model with no exchange p = 0.0. Figure 6.4:b) shows a diffusion-diffusion exchange plot for the fluid model for an exchange probability of p = 0.0003. Figure 6.4:c) shows a diffusion-diffusion exchange plot for the fluid model for an exchange probability of p = 0.00055. Figure 6.4:d) shows DEI plotted against exchange probability in the range p = 0.0001 to 0.00055. (The full set of results for the simulations using the fluid exchange model are shown in the appendix)

In diffusion-diffusion exchange plots the angle of off diagonal peaks relative to the diagonal peaks can be affected by diffusion exchange. This is due to the nature of the experiment and the inverse Laplace transform. As a result, diffusion exchange peaks often appear to be offset slightly [17]. This is can be seen in the data presented in figure 6.1, 6.2 and 6.4.

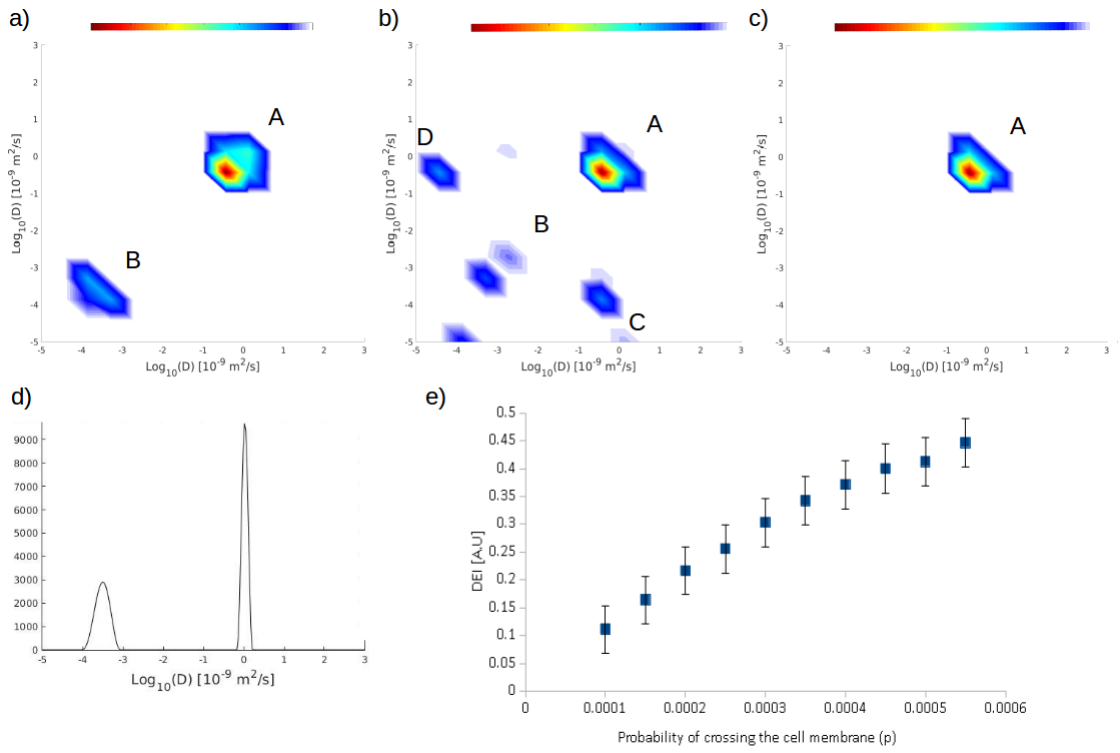

Figure 6.1: Results of diffusion exchange simulations carried out in the nervous tissue substrate at different permeabilities a) A diffusion-diffusion exchange plot for p = 0.0 b) A diffusion-diffusion exchange plot for p = 0.0003 c) A diffusion-diffusion exchange plot for p = 0.001. Peaks A and B are extracellular and intracellular diffusion peaks whilst peaks C and D are diffusion exchange peaks. d) Displays the DOSY diffusion spectra for p = 0.0 e) Shows DEI plotted against permeability in the range of p = 0.0001 to 0.00055.

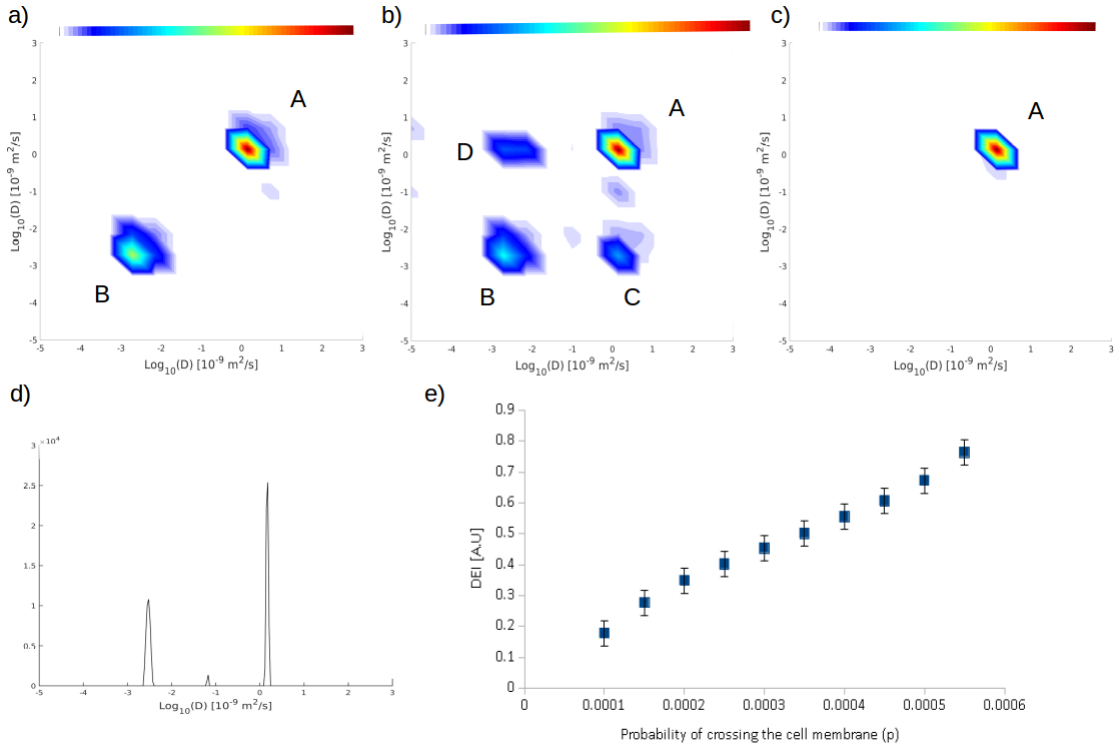

Figure 6.2: Results of diffusion exchange simulations carried out in the yeast substrate at different permeabilities a) A diffusion-diffusion exchange plot for p = 0.0 b) A diffusion-diffusion exchange plot for p = 0.0003 c) A diffusion-diffusion exchange plot for p = 0.1. Peaks A and B are extracellular and intracellular diffusion peaks whilst peaks C and D are diffusion exchange peaks d) Displays the DOSY diffusion spectra for p = 0.0 e) Shows DEI plotted against permeability in the range of p = 0.0001 to 0.00055.

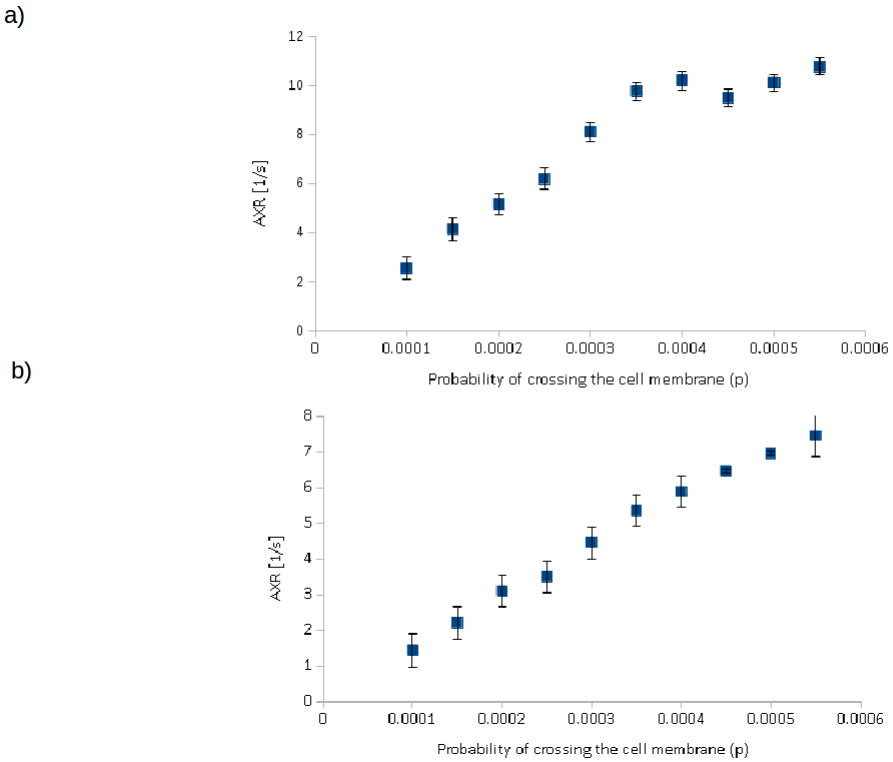

Figure 6.3: a) AXR plotted against permeability in the range of p = 0.0001 to 0.00055 for the nervous substrate. b) Shows AXR plotted against permeability in the range of p = 0.0001 to 0.00055 for the yeast substrate.

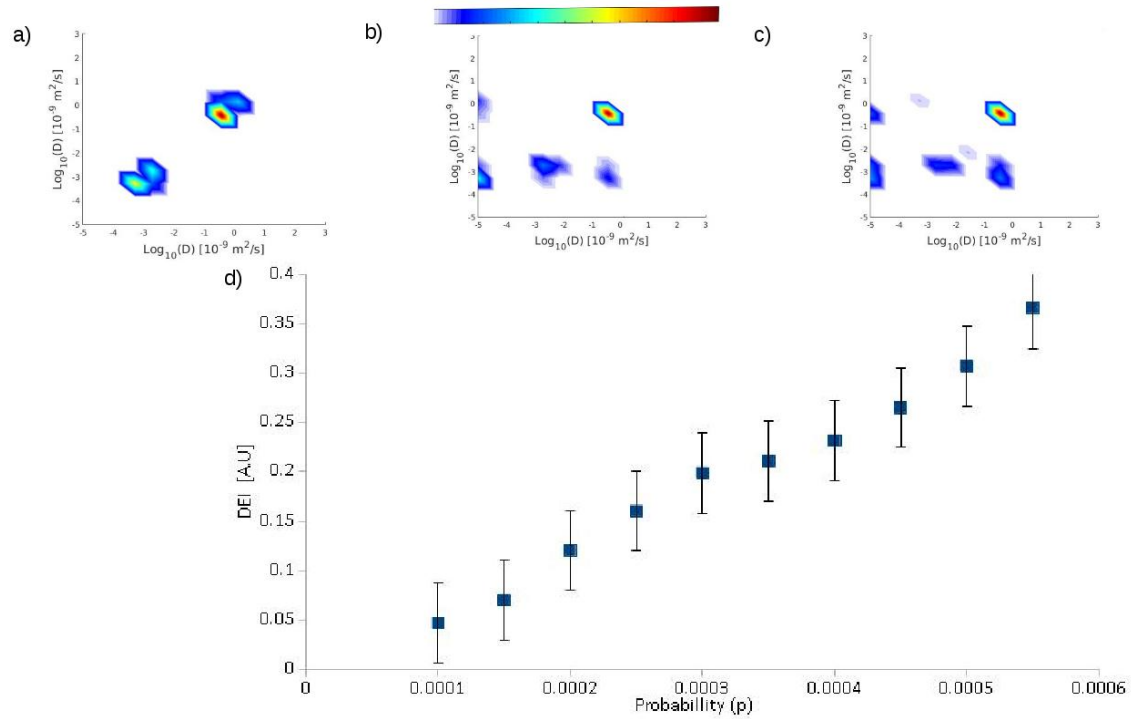

Figure 6.4: Results of diffusion exchange simulations carried out in a two compartment fluid exchange model at different exchange probabilities a) A diffusion-diffusion exchange plot for p = 0.0 b) A diffusion-diffusion exchange plot for p = 0.0003 c) A diffusion-diffusion exchange plot for p = 0.00055 d) Shows DEI plotted against probability for the fluid exchange model.

6.4 Discussion

In this chapter we present numerical simulations that demonstrate the feasibility of measuring diffusion exchange across the cell membrane using DEXSY (Diffusion Exchange spectroscopy). The simulations demonstrate that diffusion exchange can be observed with DEXSY, for a wide range of permeabilities in both a nervous tissue substrate and a yeast substrate. These simulations suggest that we can observe diffusion exchange over a range cell membrane permeabilities that can be found in biological tissue ($1.0\mu m/s - 1.4\mu m/s$), using DEXSY. The simulations demonstrate a monotonic relationship between cell membrane permeability (the probability of a walker crossing the cell membrane) and DEI, in both the nervous tissue substrate and the yeast substrate, with a Spearman's rank coefficient of 1. Whereas the FEXSY simulations demonstrated a clear monotonic correlation between AXR and permeability in the yeast substrate. However, the correlation between AXR and permeability demonstrated in the FEXSY simulations in the nervous tissue substrate was less clear as the relationship seemed to break down between p=0.0004 and 0.00055. This suggests that DEI can be used as a quantitative indicator of cell membrane permeability and that it may be more robust than AXR.

6.5 Conclusion

Our findings suggest that DEXSY may be used to make in-vivo measurements of diffusion exchange and that DEI shows potential as a quantitative indicator of cell membrane permeability in a range of pathologies including neurological disorders and cancer. However, in-vitro yeast measurements of diffusion exchange using DEXSY are required to validate our simulation results before we can move onto in-vivo work. The next chapter will present work demonstrating in-vitro measurement of diffusion exchange in yeast, validating the simulation results presented here.

Chapter 7

Diffusion exchange measurements in yeast

7.1 Background

In the previous chapters we demonstrated the accuracy of diffusion measurements made in chemical phantoms using DEXSY and we used simulations to evaluate DEXSY in-silico, demonstrating that DEXSY can measure diffusion exchange across the cell membrane in an idealised situation. The simulations also demonstrate that DEI can be used as a quantitative indicator of cell membrane permeability in-silico. As mentioned in previous chapters, cell membrane permeability varies in both healthy and diseased tissue, and has particular significance in oncology and neurology [50]. In this chapter we investigate the ability of DEXSY to measure diffusion exchange across the cell membrane in-vitro in a yeast suspension. We have used yeast as it is a well-defined and stable model for studying eukaryotic cells in-vitro [57]. In this chapter we also carry out in-vitro validation of the yeast substrate simulations. We expect that we should be able to extend this work to apply DEI as quantitative indicator of cell membrane permeability in tumour xenograft models in-vivo, following the yeast simulations being validated in-vitro in yeast.

7.2 Method

Experimental data were acquired to validate the in-silico DEXSY diffusion exchange measurements made in the yeast substrate simulations. Our experimental data were acquired using a 20 cm horizontal bore 9.4 T Varian MRI scanner (Agilent Technologies) with a 26 mm RF coil (Rapid MR International).

The DEXSY data acquired from biological phantoms presented in chapter 4, demonstrated that the signal acquired at gradient strengths greater than 720 mT/m is dominated by noise. The data presented in chapter 4, also suggests that a mixing time of 100 ms is too short to capture diffusion-exchange in-vitro. As a consequence the acquisition parameters used for the simulations have been adapted for in-vitro yeast experiments using the knowledge gained from our earlier experiments.

The first sample consisted of a 15 ml centrifuge tube containing a mixture of 22 g l'hirondelle cake yeast in 10 ml of PBS (kept at approximately 22° C). The sample was agitated to ensure an even suspension at the start of the experiment. We used the same slice-selective DEXSY sequence as used in previous chapters. The following parameters were used: number of averages = 4, δ = 15 ms, Δ = 17 ms, t_m = 200 ms, TR = 3000 ms, G_1 and G_2 = 0-720 mT/m in 16 $\times$ 16 steps. The measurement was repeated three times, with a duration of 102 minutes for each acquisition.

The second and third samples consisting of 15 ml centrifuge tubes full of a suspension of l'hirondelle cake yeast in PBS, were scanned using different DEXSY scan parameters sensitive to different diffusion lengths. Data were acquired from sample 2 which was made from a suspension of 18g of yeast suspended in 10 ml of PBS, with DEXSY scan parameters of δ = 15 ms, Δ = 17 ms, t_m = 200 ms, G_1 and G_2 = 0-640 mT/m in 16 $\times$ 16 steps. Data were also acquired separately from sample 3, a suspension consisting of 22 g of yeast suspended in 10 ml PBS,

with DEXSY scan parameters of δ = 9 ms, Δ = 14 ms, t_m = 200 ms, G_1 and G_2 = 0-640 mT/m in 16 $\times$ 16 steps.

2D inverse Laplace software was used to generate diffusion-diffusion exchange plots from the raw data and the applied b-values [17, 100]. The contribution due to imaging gradients was incorporated into the calculation of the b-values. The Diffusion Exchange Index (DEI) is defined as the ratio of the sum of the volume of the exchange peaks to the sum of the volume of the intracellular and extracellular diffusion peaks and can be used as a quantitative indicator of cell membrane permeability.

7.3 Results

Diffusion-diffusion exchange plots are shown in figure 7.1a). Peaks on the identity line (diagonal peaks), A and B, correspond to diffusing water molecules that remained within the same diffusion environment during both sets of diffusion encoding gradients. Off-diagonal peaks, C and D, correspond to diffusion exchange between environments. As intracellular and extracellular compartments have different diffusivities [80], off-diagonal peaks were interpreted as evidence of exchange between intracellular and extracellular compartments.

Diagonal peaks corresponding to water molecules remaining in the intracellular or extracellular compartments were assigned based on their measured diffusivity (intracellular, (0.032 $\pm$ 0.006) $\times$ 10^{-9} m^2/s labelled as B; extracellular, (1.0 $\pm$ 3.0) $\times$ 10^{-9} m^2/s labelled as A). Both diagonal peaks were evident at all three time points (t = 0, 102 and 204 minutes). Interestingly, intracellular diffusion peaks appeared to be split, which could correspond to vacuole and cytoplasm compartments [49]. A peak is also evident in the lower left corner of the diffusion-diffusion exchange plot, which could correspond to a dot compartment representing the nucleus [80] or it could be an artifact of the inverse Laplace transform.

Two exchange (off-diagonal) peaks, labelled as C and D in figure 7.1a) were observed at the first two time points, but only one (D) was evident at t = 204 minutes. Peak C corresponds to exchange from extracellular to intracellular compartments; peak D corresponds to exchange from intracellular to extracellular compartments. Figure 7.1b) shows measurements of peak areas, which reveal changes with time. Peak C rapidly decreases with time, whilst D remains relatively stable; peak B, remains relatively constant whereas A decreases gradually with time. The apparent position of peak C moves with time, this is probably due to a change in the rate of diffusion exchange between the two compartments over time, affecting the inverse Laplace transform [17].

The changes in the diffusion-diffusion exchange plots observed over time in figure 7.1a) were reflected in DEI measurements, which were DEI = 0.0461 $\pm$ 0.0006, 0.0371 $\pm$ 0.0007 and 0.0303 $\pm$ 0.00006 at t = 0, 102 and 204 minutes, respectively, indicating a decrease in the diffusion exchange rate with time (see figure 7.1c). The cause of these changes is unclear but it could be due to the degradation of the sample.

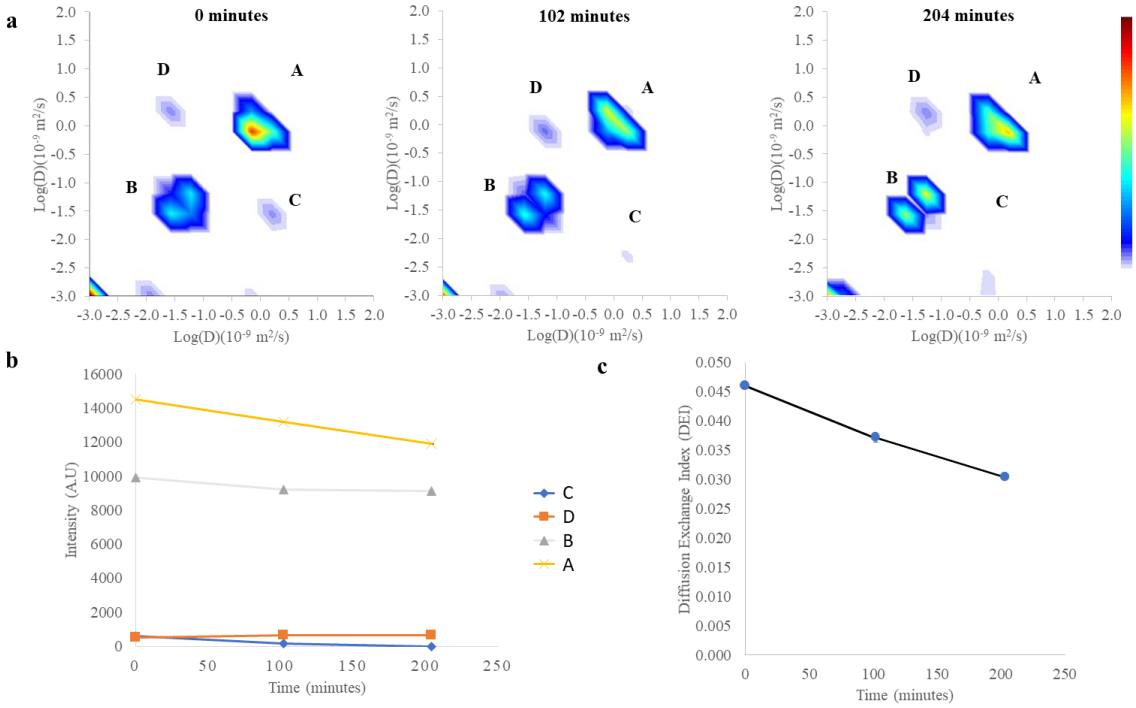

Figure 7.1: a) diffusion-diffusion exchange plots for the yeast suspension, at 0, 102 and 204 minutes into the experiment. Colour corresponds to the magnitude of the data (arb. units), which is scaled uniformly across the spectra. b) A graph showing the intensity of each peak assigned in (a) with time. c) A graph showing DEI (a measure of diffusion exchange) in the yeast suspension with time.

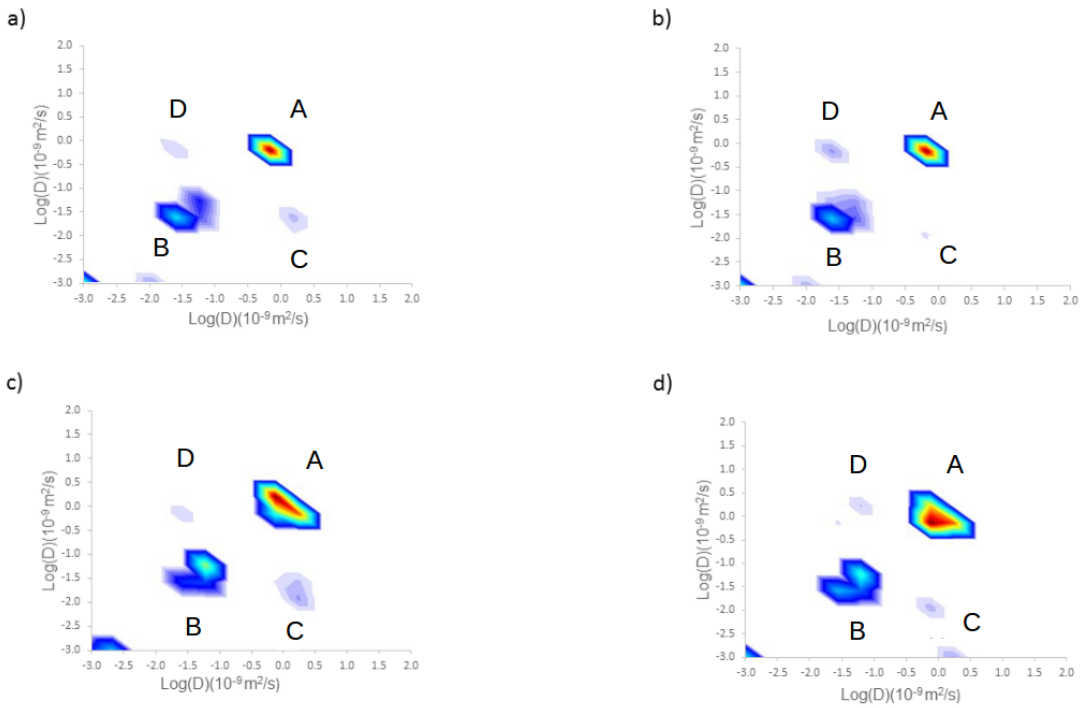

Figure 7.2: data acquired from two samples consisting of a yeast suspension a) diffusion-diffusion exchange plot from sample 2 at time 0 b) diffusion-diffusion exchange plot from sample 2 at time 102 minutes, c) diffusion-diffusion exchange plot from sample 3 at time, 0 d) diffusion-diffusion exchange plot from sample 3 at time 102 minutes.

Figure 7.2: presents data acquired from sample 2 and 3 which both contain a yeast suspension. Figure 7.2:a) and b) show DEXSY scans from the first and second acquisition from sample 2. Diffusion exchange peaks, intracellular and extracellular diffusion peaks labelled C, D, B and A are present in both scans. However, the relative size of the peaks changed between the first and second scan. We measured the DEI = 0.0449 for the first acquisition and the DEI = 0.0445 for the second acquisition. (No standard error is recorded for these measurements from sample 2 and 3, as there was no variation in the DEI measurement when repeated for each diffusion-diffusion exchange plot and there was no obvious other way of estimating the standard error). Figures 7.2:c) and d) show DEXSY scans from the first and second acquisition from sample 3. Diffusion exchange peaks, intracellular and extracellular diffusion peaks are present, labelled C, D, B and A in both acquisitions. However, the size of the peaks changed between the first and second scan. For the first scan the DEI = 0.0385 and for the second scan the DEI = 0.0385. (No standard error is recorded for these measurements from sample 2 and 3, as there was no variation in the DEI measurement when repeated for each diffusion-diffusion exchange plot and there was no obvious other way of estimating the standard error). We can see that the values of DEI for the first and second scans for both samples are relatively consistent, suggesting good repeatability. (The data produced from all of my in-vitro DEXSY scans of yeast suspensions are in the appendix, the three samples presented in this chapter are not the only samples we scanned).

7.4 Discussion

The work presented in this chapter demonstrates that the diffusion exchange of water between intracellular and extracellular compartments in yeast can be observed in-vitro using DEXSY. Interestingly, our measurements of DEI in the first sample indicated that the diffusion exchange rate decreased with time during the experiment, presumably due to degradation of the sample resulting from either

physiological changes in the yeast, sedimentation, or an as-yet undefined source of variation.

The results demonstrate that we can observe diffusion exchange in-vitro in a yeast suspension using DEXSY with two different sets of DEXSY scan parameters which are sensitive to two different diffusion lengths. The DEI measured in the yeast suspensions in sample 2 and 3 varies between 0.0385-0.045 which is within the range of DEI measured in-silico in a yeast substrate with cell membrane permeabilities corresponding to those found in biological tissue. This can be taken as validation of the results of our simulations. However, further work could be done to demonstrate if the relationship between DEI and permeability found in-silico is also found in-vitro. This could be achieved by conducting an experiment in which the yeast's permeability is altered with detergent before DEXSY data is acquired.

I attempted to carry out just such an investigation to determine the relationship between diffusion-diffusion exchange measurements made using DEXSY and permeability in-vitro. I scanned a series of yeast suspensions treated with varying strengths of detergent in order to alter the yeasts permeability. The results of this experiment were, however, inconclusive and as such I excluded these results from the main text. (The results of the yeast permeability experiment are however found in the appendix 10.3.3)

In-vivo validation is needed to test the feasibility of the technique in animal tissue. Future studies using DEXSY to measure cell membrane permeability in tumour xenograft models and the brain may demonstrate that DEI can be used as a quantitative indicator of cell membrane permeability in-vivo. If the technique can be implemented in-vivo it should be superior to FEXSY as it is better able to cope with the complexity of animal tissue as it does not use a physiological model, whereas FEXSY is limited by the assumptions underlying its two compartment exchange model. This is supported by the simulations presented here.

7.5 Conclusion

Our findings suggest that DEXSY may be used to make in-vivo measurements of diffusion exchange. When the in-vitro data presented in this chapter is combined with our in-silico results they suggest that DEI could be used as a quantitative indicator of cell membrane permeability in a range of pathologies including neurological disorders and cancer.

Chapter 8

Diffusion exchange measurements in-vivo

8.1 Background

In the previous chapters we have developed DEXSY as a technique for measuring diffusion exchange across the cell membrane. However, in order for DEXSY to become established as a technique for measuring diffusion exchange across the cell membrane in-vivo, it needs to be evaluated in-vivo. In this chapter we present tumour xenograft model experiments in which we attempt to evaluate DEXSY as a technique for measuring diffusion exchange across the cell membrane in-vivo.

8.2 Method

All in-vivo experiments were performed in accordance with the UK Home Office Animals Scientific Procedures Act, 1986 and United Kingdom Coordinating Committee on Cancer Research (UKCCCR) guidelines.

In an initial study 5 nude mice with compromised immune systems (CD-1 mice provided by Charles River) were inoculated with 1 million SW1222 cancer cells in-order to create a subcutaneous xenograft tumour model. However the tumours failed to grow.

One of the mice was scanned using an axial slice through the mouse skull using a slice-selective DEXSY sequence. The following parameters were used: number of averages n = 4, δ = 15 ms, Δ = 17 ms, t_m = 200 ms, TR = 3000 ms, G_1 and G_2 = 0-720 mT/m in 16 $\times$ 16 steps. The 9.4 T Varian MRI scanner (Agilent Technologies) with the 39 mm RF coil (Rapid MR International) was used and the mouse was scanned under anaesthetic with a mixture consisting of 1-2.5 $\%$ Isoflurane in 1 L/min of oxygen. Unfortunately, we could only scan one mouse as the pre-amplifier for the scanner malfunctioned and the mice had to be culled before the scanner became available again.

In the second study 5 nude mice with compromised immune systems (CD-1 mice provided by Charles River) were inoculated with 3 million SW1222 cancer cells suspended in PBS and injected into the left flank of the mice in-order to create a subcutaneous tumour xenograft model. In the second study the inoculations were successful and table 8.1, gives the dimensions of the tumours when the mice were scanned. The mice were scanned using a slice-selective DEXSY sequence. The following parameters were used: number of averages n= 4, δ = 15 ms, Δ = 17 ms, t_m = 200 ms, TR = 3000 ms, G_1 and G_2 = 0-640 mT/m in 16 $\times$ 16 steps. The 9.4 T Varian MRI scanner (Agilent Technologies) with the 39 mm RF coil (Rapid MR International) was used and the mice were scanned under anaesthetic with a mixture consisting of 1-2.5 $\%$ Isoflurane in 1 L/min of oxygen. Each DEXSY scan was acquired as a coronal slice through the tumour, the slice was slightly thicker than the height of the tumour. The scans were planned using a series of T2 weighted axial images. It was clear from these that the slices used for the DEXSY acquisitions intersected with other parts of the animals anatomy in all of the mice, apart from mouse 5 in which the slice captured the whole tumour and little in the way of other tissue. Mouse 5, 3 and 1 were rescanned with a slice profile capturing the entire tumour and little in the way of other tissue. We managed to position the slices with greater ease in the rescans as the tumours had grown significantly and we were more comfortable with the set up.

Mouse	Weight	Tumour W	Tumour L	Tumour H	Tumour volume
1	24.8 g	3.5 mm	5.7 mm	1.3 mm	108.6 mm^3
2	26.6 g	4.7 mm	3.2 mm	1.1 mm	69.3 mm^3
3	23.3 g	3.6 mm	3.7 mm	1.0 mm	55.8 mm^3
4	24.0 g	3.8 mm	5.0 mm	3.6 mm	386.5 mm^3
5	26.4 g	5.3 mm	5.3 mm	2.7 mm	317.7 mm^3
5 rescan	26.5 g	7.1 mm	6.0 mm	3.0 mm	530.9 mm^3
3 rescan	23.7 g	6.0 mm	9.0 mm	4.9 mm	1129.9 mm^3
1 rescan	26.1 g	5.7 mm	8.4 mm	4.3 mm	849.9 mm^3

Table 8.1: List of mice used for our in-vivo DEXSY scan of subcutaneous tumours, they are listed in the order they were scanned alongside their weight and the tumour size and volume at the time they were scanned as measured using callipers.

2D inverse Laplace transform software was used to generate diffusion-diffusion exchange plots from the raw data and the applied b-values [17, 100]. The contribution due to imaging gradients was incorporated into the calculation of the b-values.

8.3 Results

Figure 8.1 shows a diffusion-diffusion exchange plot from the axial slice acquired in the mouse brain in the initial study. There is a peak at approximately [-1.5,-1.5] which may correspond to an intracellular peak whilst at approximately [0,0] we have what may correspond to an extracellular peak, and off diagonal to these, is a possible diffusion exchange peak. The peaks between [0.5,1] and the top corner are possibly due to the perfusion of blood. However this is taken over a slice including the whole mouse head and not just the brain. As such no firm conclusions can be drawn from this plot.(A structural image of this slice through the mouse brain can be seen in the appendix)

Figures 8.2-8.6 show diffusion-diffusion exchange plots for DEXSY scans acquired from a coronal slice through a subcutaneous tumour, for the 5 mice used in the second study. The slices include the entire tumour in all 5 mice, however, there is also a significant amount of healthy tissue in the slices taken through the

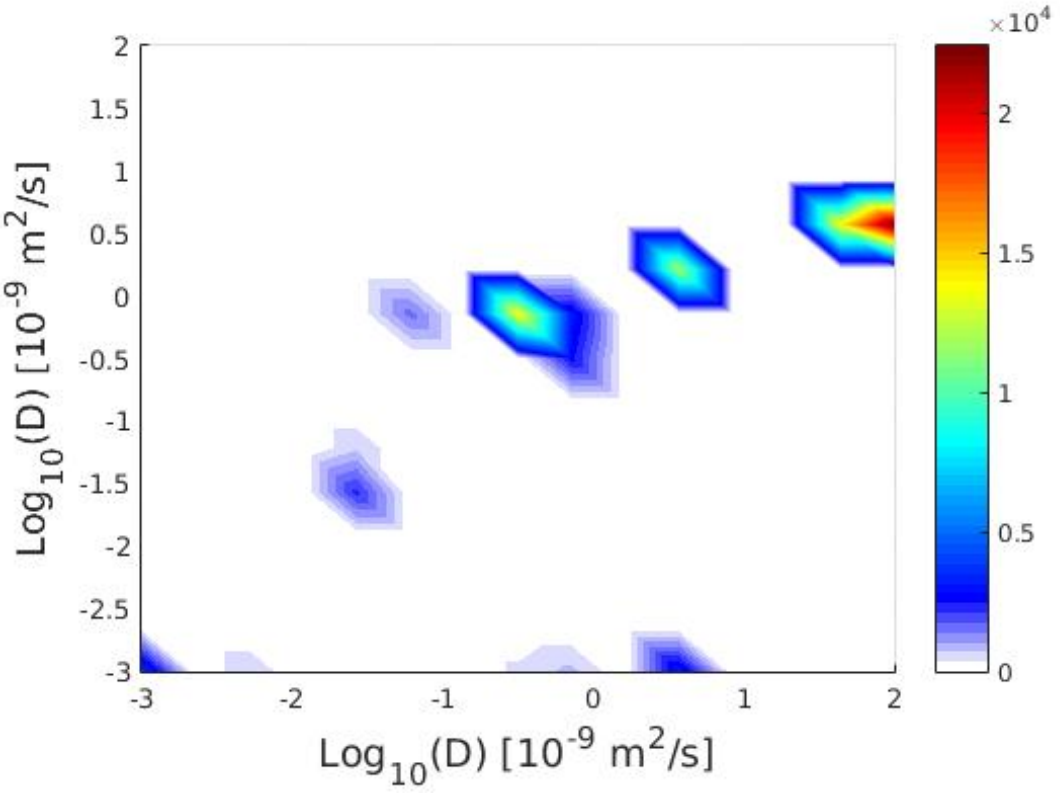

Figure 8.1: In-vivo diffusion exchange plot from a mouse brain

tumours in the first scan acquired from mouse 1-4. The first scan acquired from mouse 5 is the first case in which the slice captures the whole tumour and little in the way of other tissue. Figures 8.7-8.9 show diffusion-diffusion exchange plots for DEXSY rescans of mouse 5, 3 and 1 acquired using a slice which included the whole tumour and little in the way of other tissue. Previous studies including our own in-vitro work with DEXSY and published work with VERDICT [81], provide information on what diffusivity to expect for different compartments, the data presented in published work with VERDICT suggests that intracellular, extracellular and perfusion peaks are positioned at approximately [-1,-1], [-0.4,-0.4] and [1,1] for tumours, whilst the in-vitro work suggest that intracellular and extracellular peaks are positioned at approximately [-1.5,-1.5] and [0,0] for yeast suspensions. In the diffusion-diffusion exchange plots generated in this study a peak positioned near to [-1.5,-1.5] - [-1.0,-1.0] is considered a likely intracellular peak, a peak positioned near to [-0.4,-0.4] - [0.0,0.0] is considered a likely extracellular peak, and a peak positioned near to [1,1] is considered to be a likely perfusion peak. Peaks off-diagonal from the intracellular and extracellular peaks are likely diffusion ex-

change peaks. Figures 8.2-8.9 show diffusion-diffusion exchange plots from the five mice. Figure 8.10 shows the four diffusion-diffusion exchange plots produced from slices consisting of tumour and little in the way of other tissue with all of the peaks labelled. Each of the figures are considered individually.

Figure 8.2 shows the diffusion exchange plot from mouse 1. A likely extracellular peak is positioned at approximately [0,0], whilst the nature of the other peaks is unclear.

Figure 8.3 shows the diffusion-diffusion exchange plot from mouse 2. Likely and possible intracellular peaks are positioned at approximately [-1.5,-1] and [-2,-2]. Possible extracellular peaks are positioned at approximately [-1,0] and [0,-1]. These are possible extracellular peaks because an extracellular peak would be expected to lie between these two peaks.

Figure 8.4 shows the diffusion-diffusion exchange plot from mouse 3. Likely intracellular and perfusion peaks are positioned at approximately [-1.5,-1.5] and [1,0.5].

Figure 8.5 shows the diffusion-diffusion exchange plot from mouse 4. Likely intracellular, extracellular and perfusion peaks are positioned at approximately [-1.0,-1.0], [0.0,0.0] and [0.5,1.0].

Figure 8.6 shows the diffusion-diffusion exchange plot from mouse 5. Likely intracellular, extracellular and possible perfusion peaks are positioned at approximately [-1.5,-1.5], [-0.5,-0.25] and [0.5,0]. Likely diffusion exchange peaks are positioned at approximately [-0.5,-1.5] and [-1.5,0.25]. This is the first slice in which we managed to capture a whole tumour and little in the way of healthy tissue, and it is also the first plot which captures likely diffusion exchange, intracellular, extracellular and a possible perfusion peaks.

Figure 8.7 shows the diffusion-diffusion exchange plot from the rescan of mouse 5. Likely intracellular, extracellular and possible perfusion peaks are positioned at approximately [-2.0,-1.5] , [0.5, -0.5] and [1.0,0.5]. Likely diffusion exchange peaks are positioned at approximately [1,-2] and [-1.5,0.5].

Figure 8.8 shows the diffusion-diffusion exchange plot from the rescan of mouse 3. Likely intracellular, extracellular and possible perfusion peaks are positioned at approximately [-2.0,-1.5], [-0.5, -0.5] and [0.5,1.5]. A likely diffusion exchange peak is positioned at approximately [-0.5,-1.5].

Figure 8.9 shows the diffusion-diffusion exchange plot from the rescan of mouse 1. Likely intracellular, extracellular and possible perfusion peaks are positioned at approximately [-1.5,-1.5], [0.5, 0.5] and [1.0,1.5]. Likely and possible diffusion exchange peaks are positioned at approximately [-1.0,0.5] and [0.5,-3.0]. (The structural images used to plan the slices are in the appendix)

The diffusion-diffusion exchange plots shown in figures 8.6-8.9 are displayed in figure 8.10, with likely diffusion exchange peaks labelled as A and B, whereas likely intracellular and extracellular peaks labelled C and D. Likely or possible perfusion peaks are labelled E. This is to enable easier identification of the peaks by the reader.

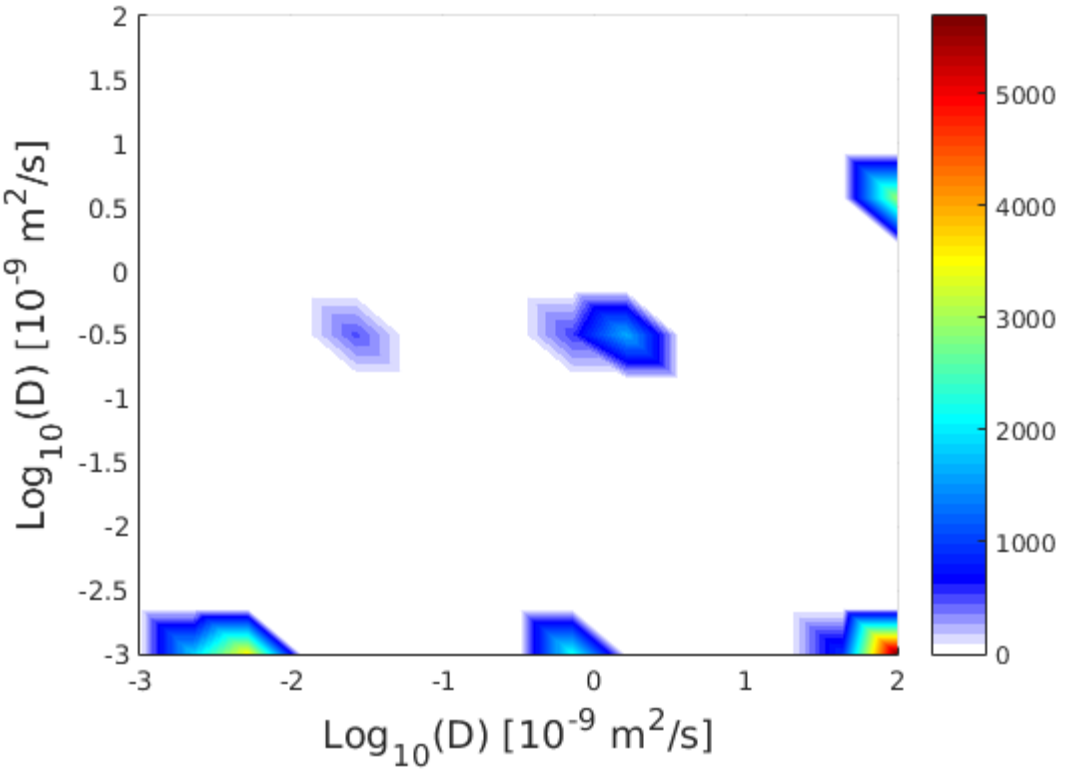

Figure 8.2: Diffusion-Diffusion exchange plot for a DEXSY scan acquired from a coronal slice through a subcutaneous tumour in mouse 1, scanned 15/10/2018

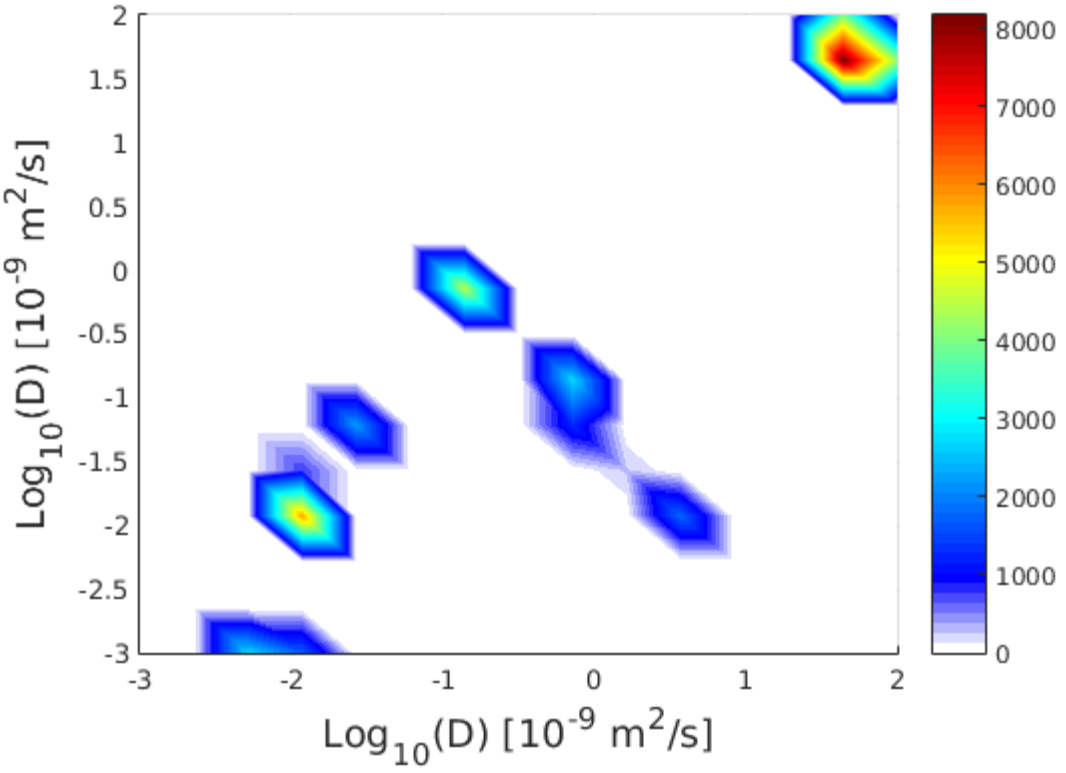

Figure 8.3: Diffusion-Diffusion exchange plot for a DEXSY scan acquired from a coronal slice through a subcutaneous tumour in mouse 2, scanned 15/10/2018

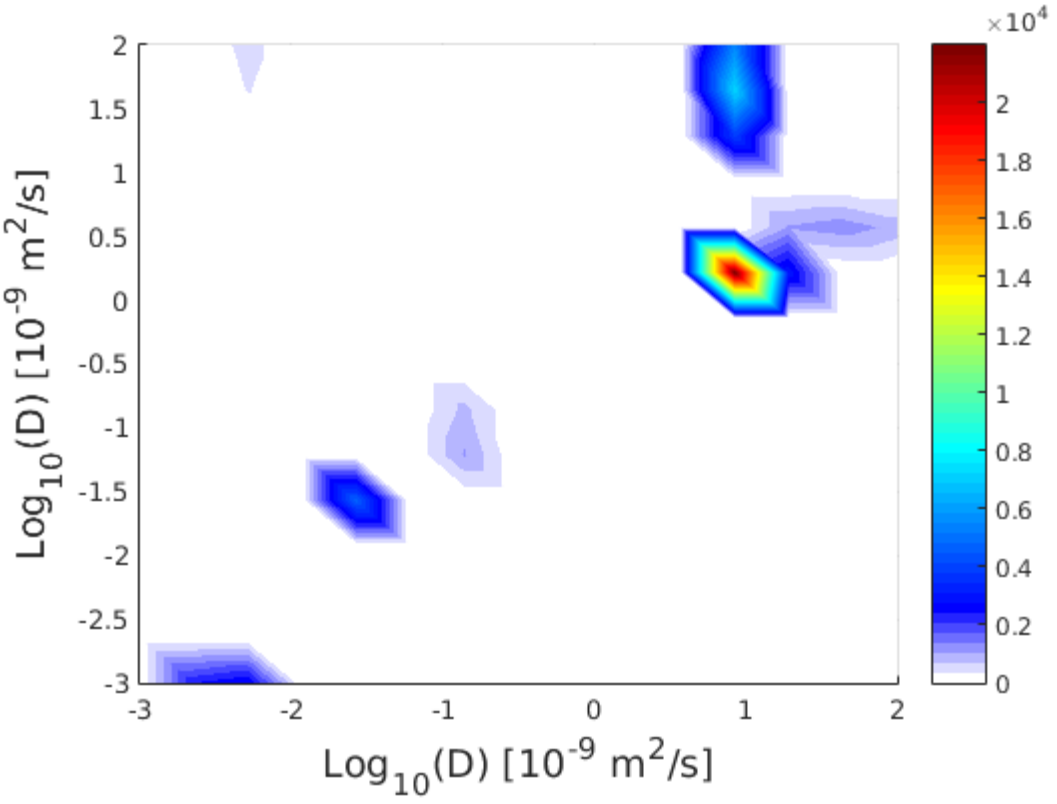

Figure 8.4: Diffusion-Diffusion exchange plot for a DEXSY scan acquired from a coronal slice through a subcutaneous tumour in mouse 3, scanned 16/10/2018

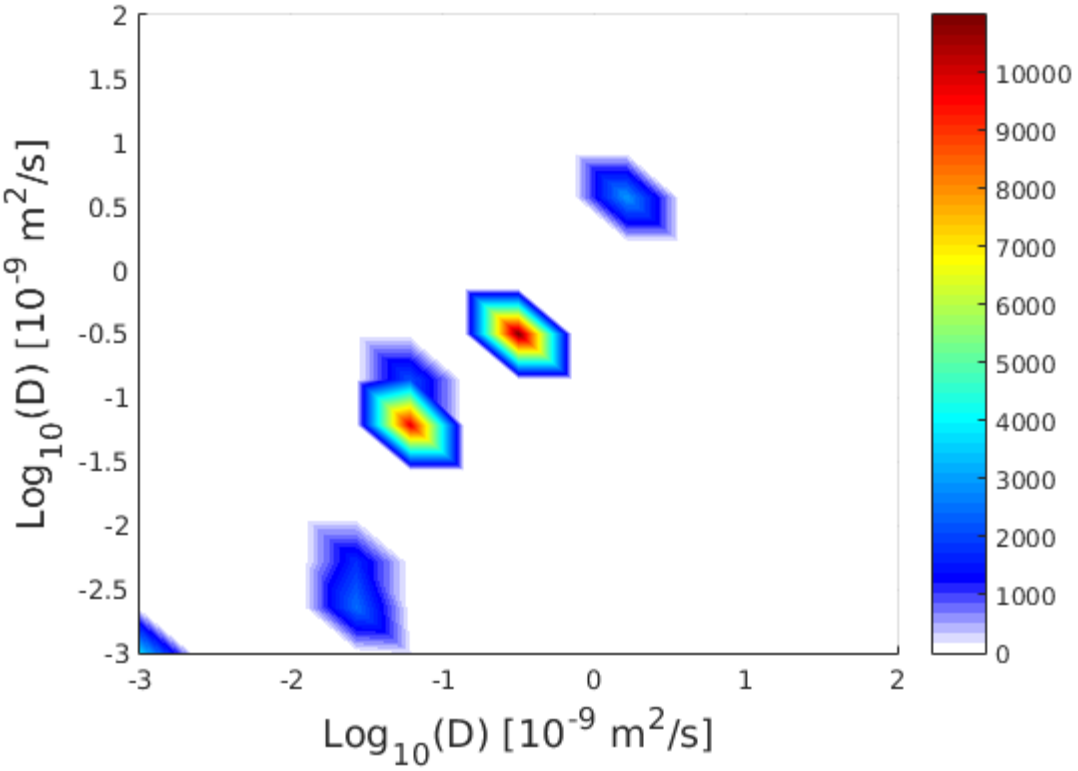

Figure 8.5: Diffusion-Diffusion exchange plot for a DEXSY scan acquired from a coronal slice through a subcutaneous tumour in mouse 4, scanned 19/10/2018

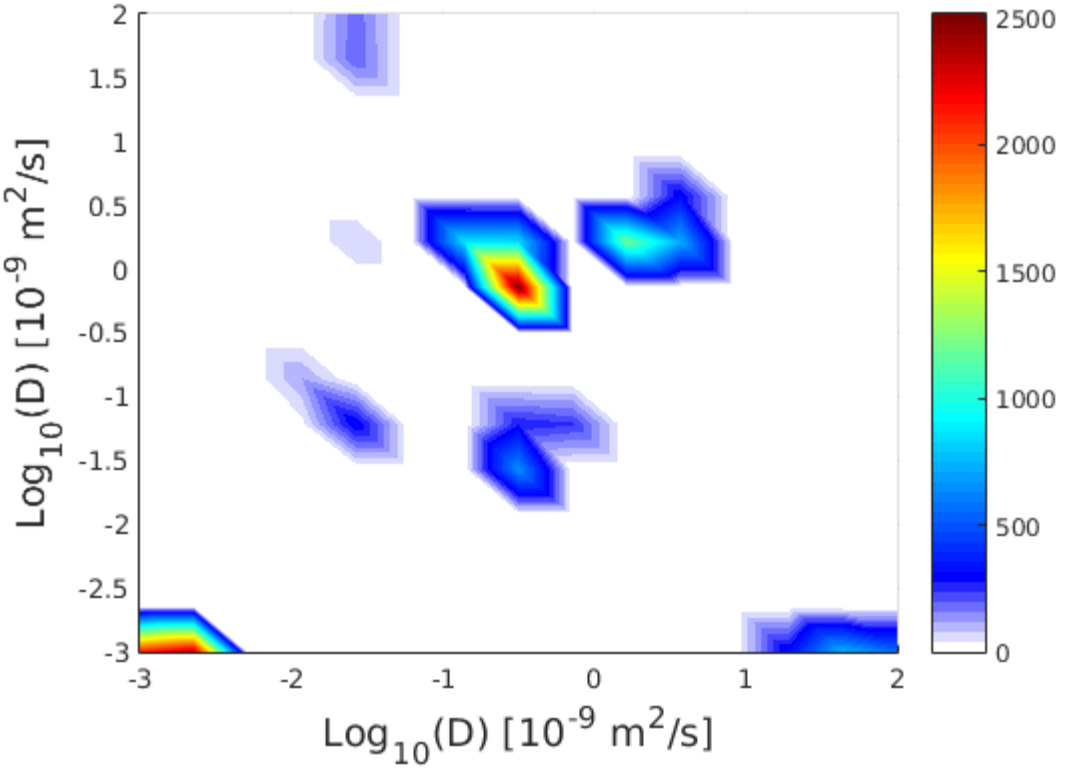

Figure 8.6: Diffusion-Diffusion exchange plot for a DEXSY scan acquired from a coronal slice through a subcutaneous tumour in mouse 5, scanned 19/10/2018

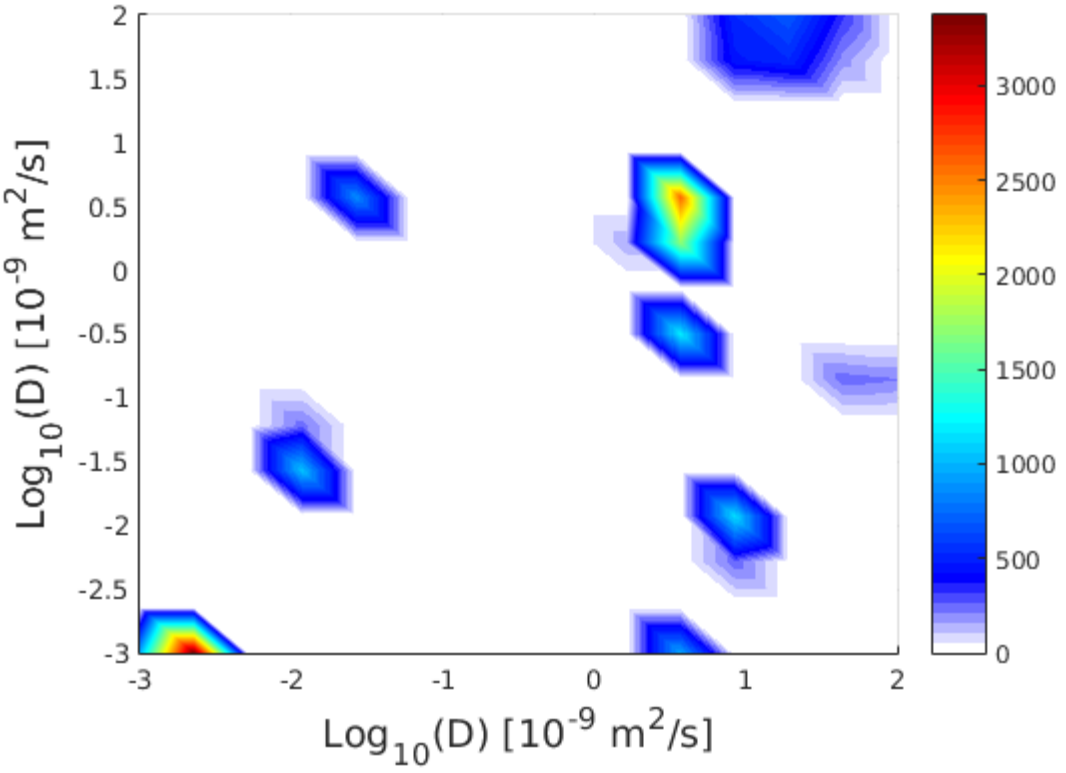

Figure 8.7: Diffusion-Diffusion exchange plot for a DEXSY scan acquired from a coronal slice through a subcutaneous tumour in mouse 5, scanned 29/10/2018

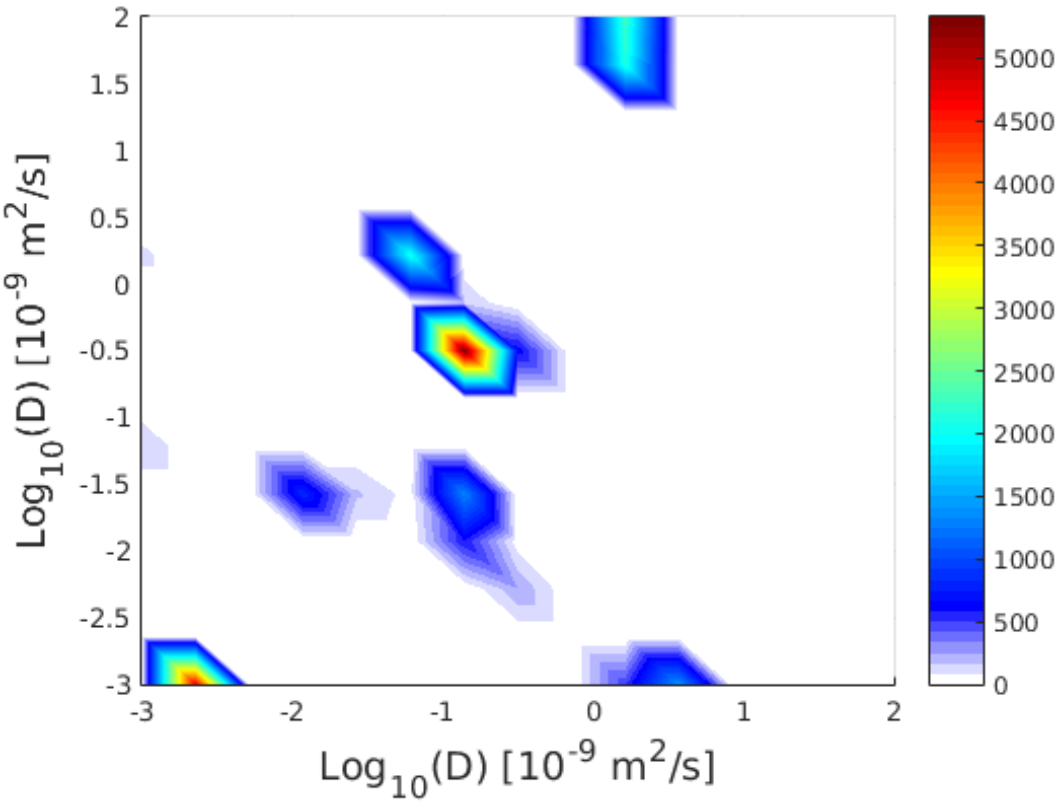

Figure 8.8: Diffusion-Diffusion exchange plot for a DEXSY scan acquired from a coronal slice through a subcutaneous tumour in mouse 3, scanned 29/10/2018

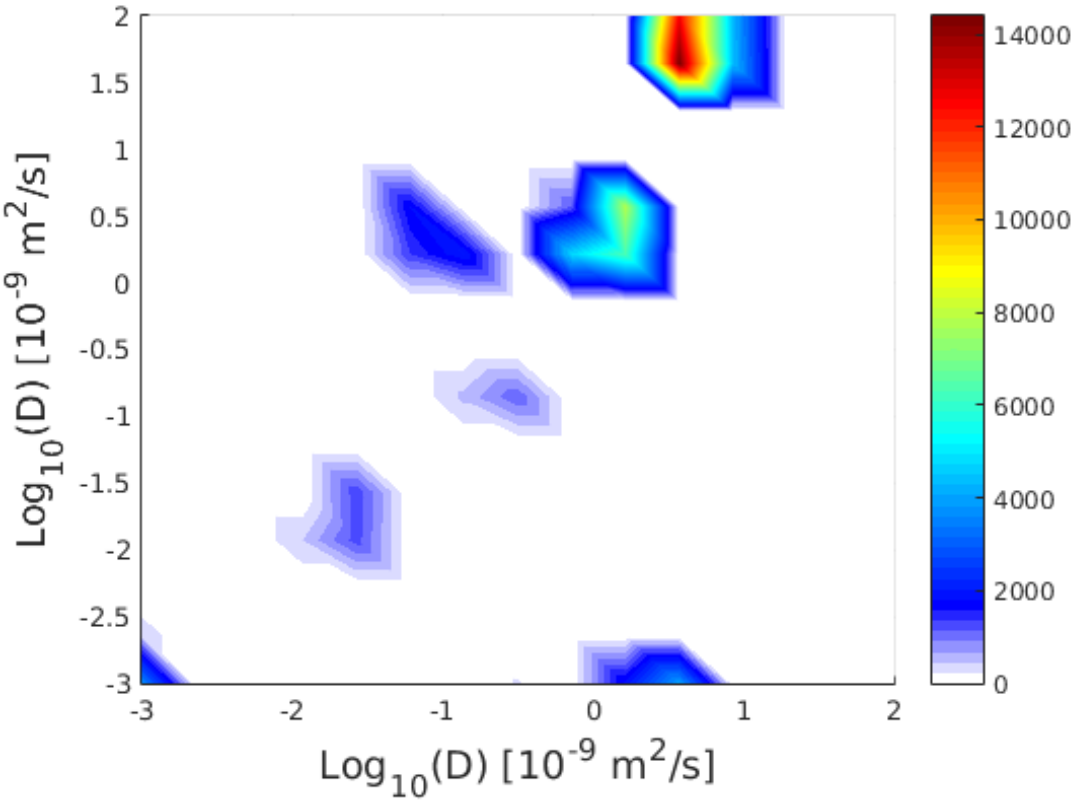

Figure 8.9: Diffusion-Diffusion exchange plot for a DEXSY scan acquired from a coronal slice through a subcutaneous tumour in mouse 1, scanned 29/10/2018

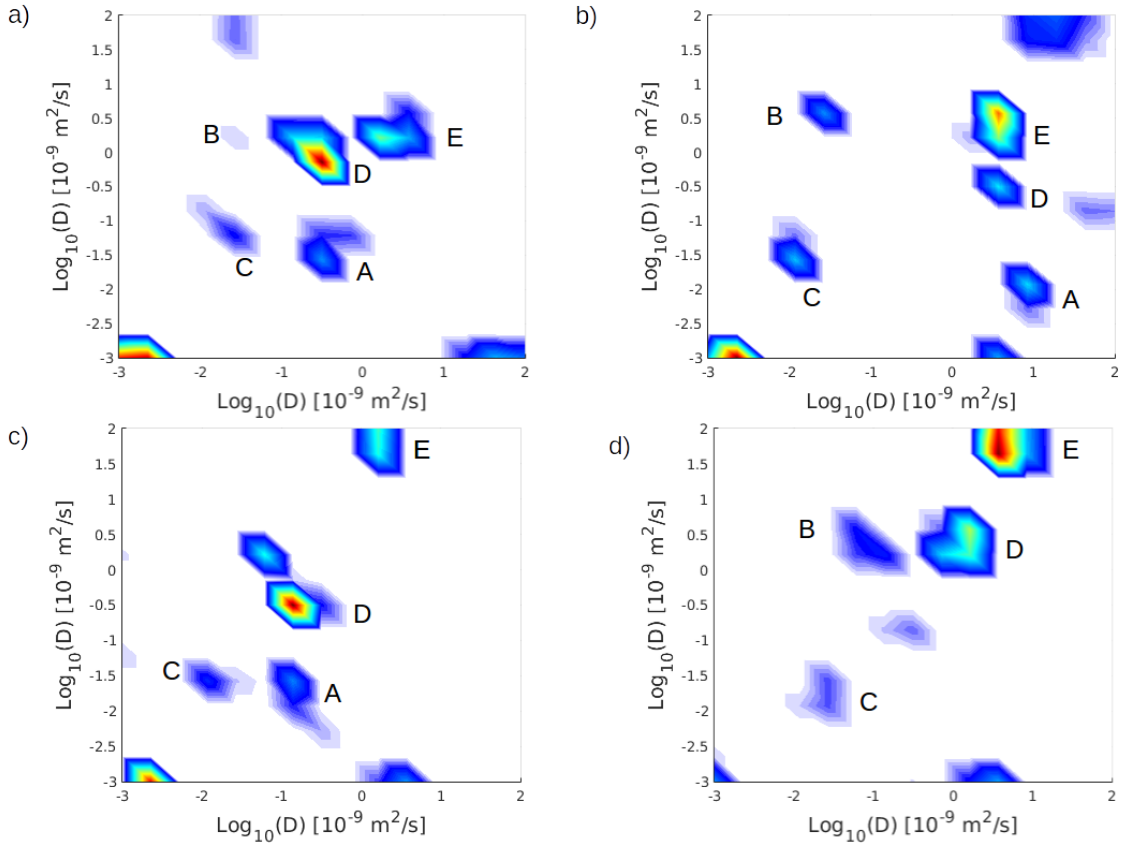

Figure 8.10: a) shows the diffusion-diffusion exchange plot shown in figure 8.6, b) shows the diffusion-diffusion exchange plot shown in figure 8.7, c) shows the diffusion-diffusion exchange plot shown in figure 8.8, d) shows the diffusion-diffusion exchange plot shown in figure 8.9. Likely diffusion exchange peaks are labelled A and B, whereas likely intracellular and extracellular peaks labelled C and D. Likely or possible perfusion peaks are labelled E.

8.4 Discussion

The results of our second study demonstrate clearly that our DEXSY scans can capture information about the micro-structure of our tumours, with what look like intracellular, extracellular and perfusion peaks present. However, only four of the eight scans shown in figure 8.6-8.9 show likely intracellular, extracellular diffusion-exchange and perfusion peaks. However, these are the only cases in which the DEXSY scan was acquired using a slice capturing the whole tumour and little in the way of other tissue. However these limited results suggest the technique is highly sensitive to tissue microstructure and capable of detecting diffusion exchange in-vivo.

The DEXSY scans acquired using slices containing other tissue suffer from partial volume effects. Whilst, the DEXSY data acquired from slices capturing the whole tumour and little in the way of other tissue produce results which can not be replicated reliably when the tumour is rescanned. This can be attributed to variations in the experimental set up and the tissue micro-structure. When the tumour is rescanned the mouse is not in exactly the same position as it was in the first scan, and as a consequence the slice is not orientated or positioned consistently. The tumours have also grown in-between scan and rescan, which would also be accompanied by changes in the tissue micro-structure.

The second study suffered from a major limitation which was that we were only able to acquire data from a whole tumour with little in the way of other tissue in half of the scans. This is in part due to the size and location of four of the tumours, and in part due to the use of a DEXSY sequence which was only slice selective. In order to demonstrate conclusively that DEXSY can be used to consistently capture intracellular, extracellular, diffusion-exchange and perfusion peaks, we would need to repeat the xenograft experiment with a series of acquisitions in which the data is only acquired from a tumour. This can be done by modifying the set up so that the positioning of the tumour is such that it stands above all other

tissue. However, this may be difficult to implement consistently, due to the nature of the tumours and the variation in their position, size and shape when they grow. Alternatively it could be done by adding spatial encoding and acquiring a single voxel including the tumour with as little neighbouring tissue as possible. This should be feasible, as the initial DEXSY sequence presented in 5.2 had spatial encoding. The slice selective sequence has been used throughout the rest of our work as there were some problems with the initial sequence which incorporated imaging gradients. This led to the use of a slice selective sequence which was easier to implement, the slice selective sequence used to acquire the data in this chapter also incorporates eight step phase cycling (although we only use four step phase cycling in this chapter) which was not in the original sequence.

8.5 Conclusion

This first application of DEXSY in-vivo suggests, that DEXSY is highly sensitive to tissue microstructure and capable of detecting diffusion exchange, in subcutaneous tumour xenograft models.

Chapter 9

Conclusion

The purpose of the work presented in this thesis was to develop DEXSY as a technique for making comprehensive measurements of diffusion exchange across the cell membrane and to develop a quantitative indicator of cell membrane permeability derived from DEXSY measurements. A quantitative indicator of cell membrane permeability could enable earlier diagnosis, assist in monitoring treatment response, and enable the characterisation of cells in malignant disease. In this thesis biological phantoms, physical phantoms, simulations, in-vitro yeast suspensions and in-vivo subcutaneous tumour xenograft models have been used to establish if DEXSY can be used to make comprehensive measurements of diffusion exchange across the cell membrane, and if this can be used to produce a quantitative indicator of cell membrane permeability. The work presented here suggests that DEI, which is derived from DEXSY measurements, is a quantitative indicator of cell membrane permeability. As such DEI is a potential imaging biomarker in cancer.

Although I have managed to successfully produce biological phantoms with the required intracellular volume fraction, the protocol requires a large amount of time to produce a biological phantom and we have been unable to assess the viability of the biological phantoms due to the centre for advanced biomedical imaging losing some of its bioluminescence imaging capabilities. In addition to this there appeared to be some inconsistency in the experimental set-up which

may have caused variability in the results. This combined with a number of other factors led to an alternative approach to validating DEXSY, which consisted of chemical phantoms, simulations, and in-vitro work with yeast suspensions before we moved onto in-vivo DEXSY scans.

The chemical phantom results presented in this thesis suggest that we can rely on the diffusion measurements made using DEXSY, as there was a reasonable correspondence with the DOSY diffusion measurements, and the minor inconstancies can be explained by T2 effects influencing the DOSY diffusion measurement. However, the chemical phantom results failed to demonstrate the measurement of exchange. There is no obvious alternative to the phantoms used in our experiments.

The numerical simulations and experimental data presented in this thesis demonstrate the feasibility of measuring diffusion exchange across the cell membrane using DEXSY. The simulations demonstrate that diffusion exchange can be observed with DEXSY, for a wide range of permeabilities, in both a nervous tissue substrate and a yeast substrate. These simulations suggest we can observe diffusion exchange over a range of physiologically meaningful cell membrane permeabilities ($1.0\mu m/s - 1.4\mu m/s$) using DEXSY. The simulations demonstrate a monotonic relationship between cell membrane permeability (the probability of a walker crossing the cell membrane) and DEI, in both the nervous tissue substrate and the yeast substrate, with a Spearman's rank coefficient of 1. Whereas the FEXSY simulations do not show the same clear relationship between AXR and permeability in both the yeast substrate and the nervous tissue substrate. This suggests that DEI can be used as a quantitative indicator of cell membrane permeability and that it may be more robust than AXR.

The simulations fail to take account of the relaxation times of the tissue being modelled. Repeating our simulations using a model that incorporates the differences in relaxation time between different tissues and compartments could

improve the accuracy of the simulations.

The data presented in this thesis demonstrate that we can observe diffusion exchange in-vitro in a yeast suspension using DEXSY with different sets of DEXSY scan parameters, which are sensitive to different diffusion lengths. The DEI measured in the yeast suspensions using DEXSY falls within the range of DEI measured in-silico in a yeast substrate with cell membrane permeabilities corresponding to those found in biological tissue. This can be taken as validation of the results of our simulations. There was some variability in our in-vitro yeast data due to degradation of the samples resulting from either physiological changes in the yeast, sedimentation, or an as-yet undefined source of variation.

Further work could be done to determine if the relationship between DEI and permeability found in-silico is also found in-vitro. This could be achieved by conducting an experiment in which the yeast's permeability is altered with detergent before DEXSY data is acquired. The DEI calculated from DEXSY data acquired from yeast samples treated with different concentrations of detergent, is expected to have a monotonic correlation with the strength of detergent used to treat the yeast. Such a result would validate the in-silico findings and support the use of DEI as a quantitative indicator of cell membrane permeability.

In-vivo validation is needed to test the feasibility of the technique in animal tissue. Future studies using DEXSY to measure cell membrane permeability in tumor xenograft models and the brain may demonstrate that DEI can be used as a quantitative indicator of cell membrane permeability in-vivo. If the technique can be implemented in-vivo effectively, it should be superior to FEXSY as it is better able to cope with the complexity of animal tissue because it uses a model free approach whereas FEXSY is limited by the assumptions underlying its two compartment exchange model. This is supported by the simulations presented here.

We attempted to use DEXSY to measure cell membrane permeability in tumour xenograft models. However, only a limited data set was acquired. The in-vivo results presented here suggest that DEXSY is highly sensitive to tissue microstructure and capable of detecting diffusion exchange in-vivo in subcutaneous tumour xenograft models. However, further work needs to be conducted to confirm this. Ideally using a spatially localised DEXSY acquisition covering the whole tumour in a single voxel.

The DEXSY scans acquired using slices containing other tissue suffer from partial volume effects. Whilst, the DEXSY data acquired from slices capturing the whole tumour and little in the way of other tissue produce results which can not be replicated reliably when the tumour is rescanned. This can be attributed to variations in the experimental set up and the tissue micro-structure. It is possible this can be resolved by carrying out spatially localised DEXSY experiments, provided the acquisition time is feasible.

One of the disadvantages of DEXSY compared to FEXSY that we have not discussed is its lengthy acquisition time. Our DEXSY acquisitions currently take 102 minutes using a comprehensive acquisition consisting of a 16x16 acquisition matrix. However, work has been published which advocates a new method for reducing the acquisition time. The MADCO framework constrains the acquisition parameters based on a 1D diffusion spectra in order to reduce the number of data points acquired [11, 10]. In the MADCO experiments conducted to date an initial acquisition is acquired in which the first pair of diffusion encoding gradients are not applied, and as few as 10 gradient strengths are used for the second pair of diffusion encoding gradients to acquire a 1D diffusion spectra. A second 2D acquisition in which as few as 4 random gradient strengths are used for each pair of diffusion encoding gradients, at each mixing time, are used to acquire data at 3 mixing times. The 1D diffusion spectra from the first acquisition is then used to constrain the MADCO fitting which provides a 2D diffusion-diffusion exchange plot from the data provided in the two acquisitions. This technique could reduce the

acquisition time required to image the whole human brain with spatially localised DEXSY to 22 minutes [11], which would make DEXSY a viable technique for in-vivo and in-man imaging.

In summary there are a number of key findings contained within this thesis. The phantom work presented in this thesis demonstrate that DEXSY can make accurate measurements of diffusivity. The simulations demonstrate that DEI can be used as a quantitative indicator of cell membrane permeability in-silico, in yeast suspensions, and nerve bundles. In-vitro DEXSY acquisitions demonstrate that we can observe diffusion exchange in yeast suspensions using DEXSY. Whilst in-vivo data suggests that DEXSY can measure diffusion exchange in tumour xenograft models.

Nevertheless, the results contained within this thesis have a number of key limitations. The work presented here does not demonstrate that the relationship between DEI and cell membrane permeability found in-silico is also found in living tissue. In addition to this, the in-vivo results presented here are variable. As such it is not clear how reliable the conclusions drawn from the in-vivo data are. Another limitation to the work presented here is that the data were acquired using a slice selective sequence over a lengthy acquisition period.

The results of this experiment suggest that DEXSY experiments could be used to help estimate signal loss due to diffusion exchange in PGSE acquisitions. DEI could be used estimate the proportion of signal loss in a PGSE acquisition that can be attributed to diffusion exchange. A DEXSY experiment used for this purpose would use the same diffusion parameters as the PGSE sequence being investigated, and a mixing time equivalent to the PGSE sequence's echo time. This could enable the design of compartment models such as VERDICT, that compensate for signal loss due to diffusion exchange.

There are a number of avenues to pursue in order to extend the work presented in this thesis. Further work is needed to reduce the acquisition time so that these experiments can be carried out as imaging experiments. Further in-vitro work is required to determine if the relationship found between DEI and permeability in-silico is also found in-vitro. Further in-vivo work is needed to confirm that DEXSY is sensitive to diffusion exchange in tumour xenograft models. However the main avenue for further work is to build on our in-vivo experiments to develop an imaging experiment to quantify changes in cell membrane permeability in-vivo in tumour xenograft models treated with cytoxic drugs.

In conclusion the findings presented in this thesis suggest that DEXSY may be used to make in-vivo measurements of diffusion exchange, and that DEI may be used as a quantative indicator of cell membrane permeability, in a range of pathologies including neurological disorders and cancer. If DEXSY can be sucesfully adapted for preclinical and clinical imaging, then DEI can be used as an imaging biomarker in cancer.

Chapter 10

Appendix

10.1 Sucrose Water figures

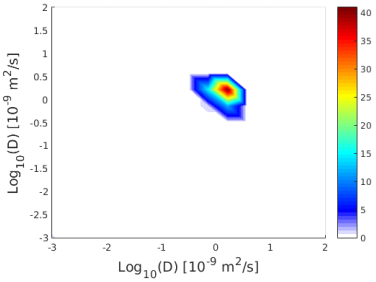

Figure 10.1: DEXSY Diffusion exchange plot from the first DESXY experiment with imaging gradients, $\delta = 0.008s$, $\Delta = 0.015s$, $t_m = 0.072s$ spectrum 0.0 M sucrose

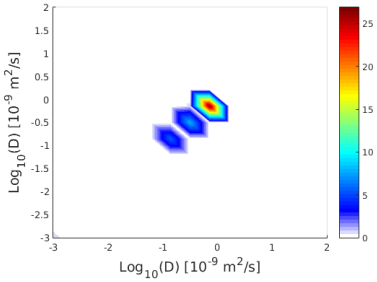

Figure 10.2: DEXSY Diffusion exchange plot from the first DESXY experiment with imaging gradients,$\delta = 0.008s$, $\Delta = 0.015s$, $t_m = 0.072s$ spectrum 0.5 M sucrose

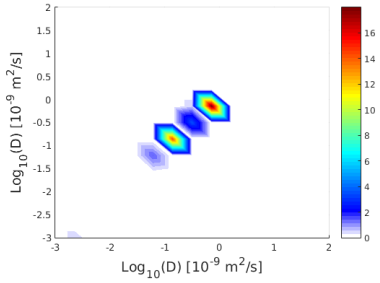

Figure 10.3: DEXSY Diffusion exchange plot from the first DESXY experiment with imaging gradients,$\delta = 0.008s$, $\Delta = 0.015s$, $t_m = 0.072s$ spectrum 1.0 M sucrose

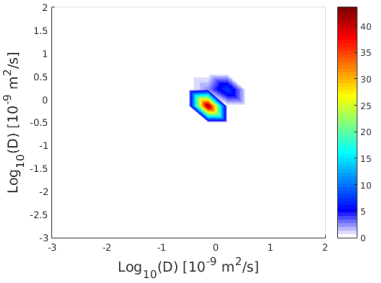

Figure 10.4: DEXSY Diffusion exchange plot from the first DESXY experiment with imaging gradients,$\delta = 0.008s$, $\Delta = 0.015s$, $t_m = 0.072s$ spectrum 1.5 M sucrose

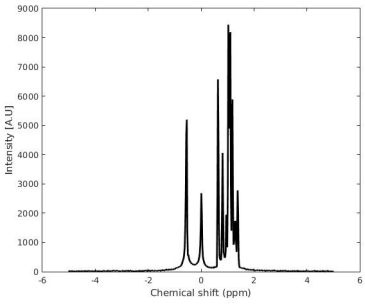

Figure 10.5: DEXSY MR spectrum 2 M sucrose

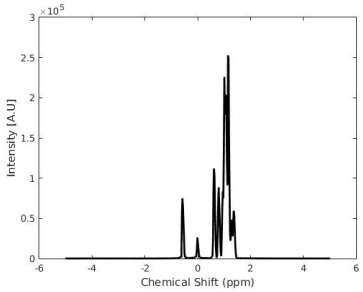

Figure 10.6: DEXSY MR spectrum 1.5 M sucrose

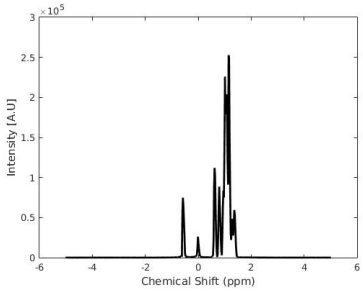

Figure 10.7: DEXSY MR spectrum 1 M sucrose

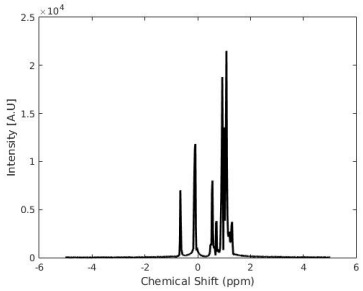

Figure 10.8: DEXSY MR spectrum 0.5 M sucrose

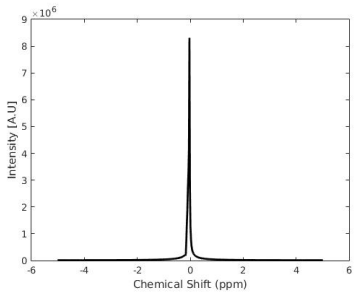

Figure 10.9: DEXSY MR spectrum water

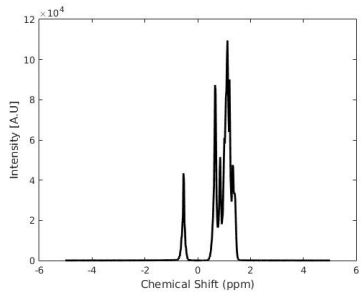

Figure 10.10: DEXSY MR spectrum 2 M sucrose

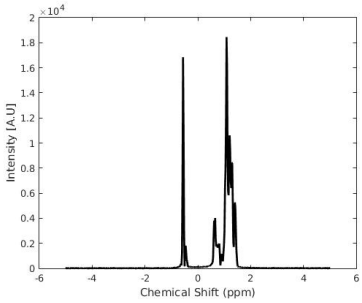

Figure 10.11: DEXSY MR spectrum 1.5 M sucrose

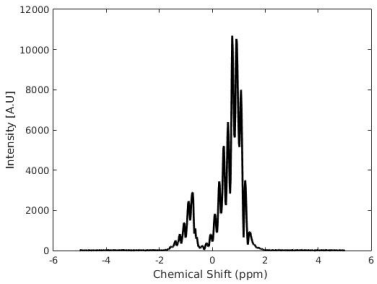

Figure 10.12: DEXSY MR spectrum 1 M sucrose

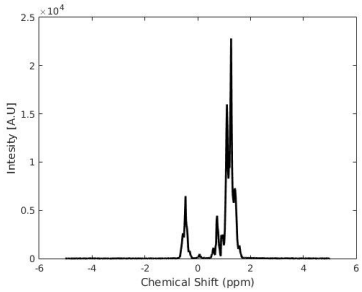

Figure 10.13: DEXSY MR spectrum 0.5 M sucrose

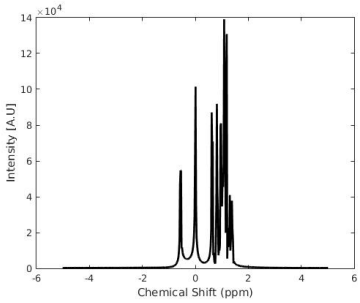

Figure 10.14: DOSY MR spectrum 2 M sucrose

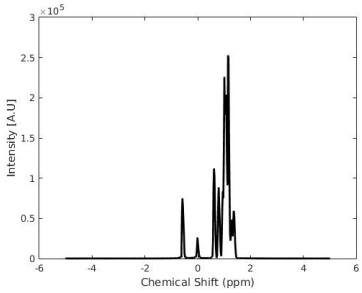

Figure 10.15: DOSY MR spectrum 1 M sucrose

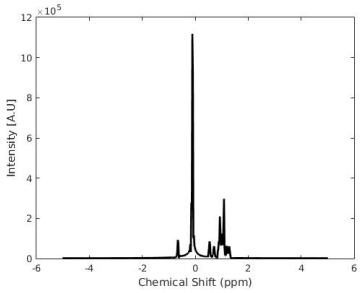

Figure 10.16: DOSY MR spectrum 0.5 M sucrose

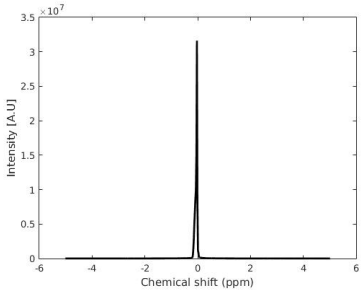

Figure 10.17: DOSY MR spectrum water

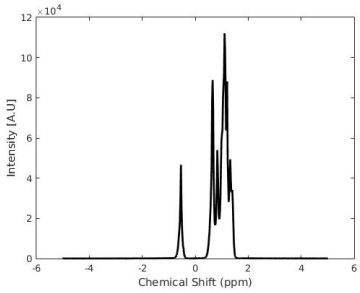

Figure 10.18: DOSY MR spectrum 2 M sucrose

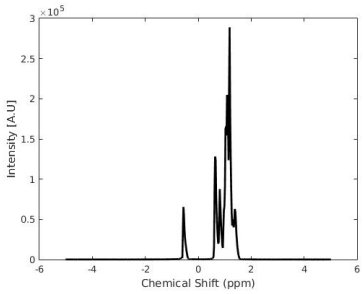

Figure 10.19: DOSY MR spectrum 1.5 M sucrose

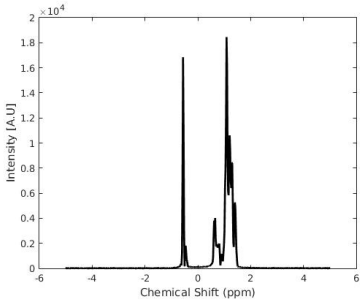

Figure 10.20: DOSY MR spectrum 1 M sucrose

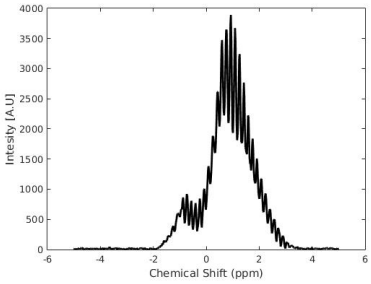

Figure 10.21: DOSY MR spectrum water

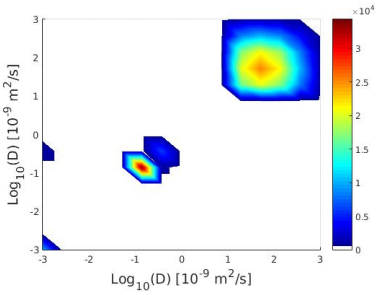

Figure 10.22: Diffusion-Diffusion exchange plot 2 M sucrose

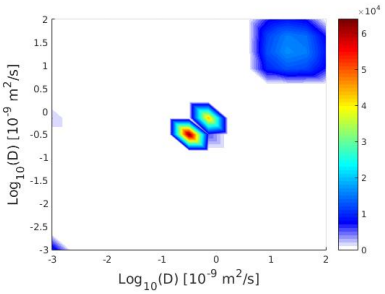

Figure 10.23: Diffusion-Diffusion exchange plot 1.5 M sucrose

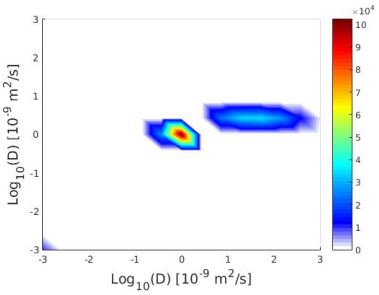

Figure 10.24: Diffusion-Diffusion exchange plot 1 M sucrose

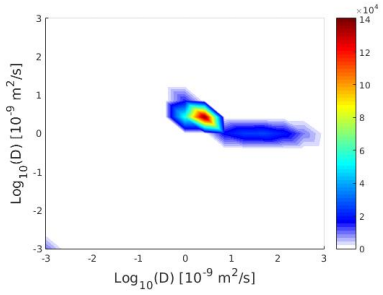

Figure 10.25: Diffusion-Diffusion exchange plot 0.5 M sucrose

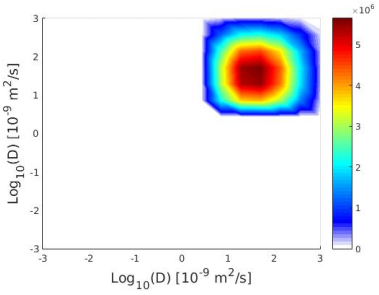

Figure 10.26: Diffusion-Diffusion exchange plot water

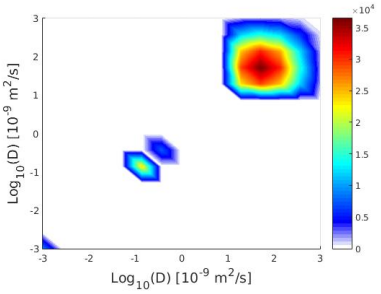

Figure 10.27: Diffusion-Diffusion exchange plot 2 M sucrose

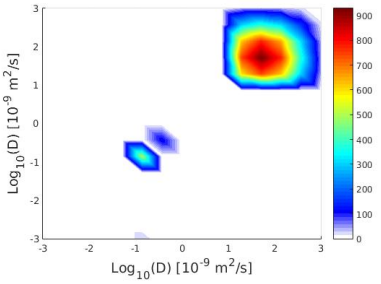

Figure 10.28: Diffusion-Diffusion exchange plot 2 M sucrose hydroxyl peak

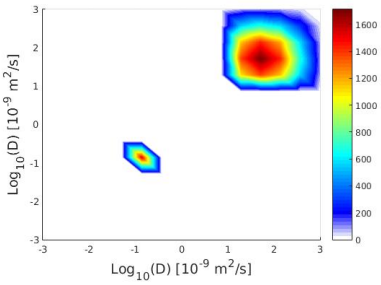

Figure 10.29: Diffusion-Diffusion exchange plot 2 M sucrose CH peak

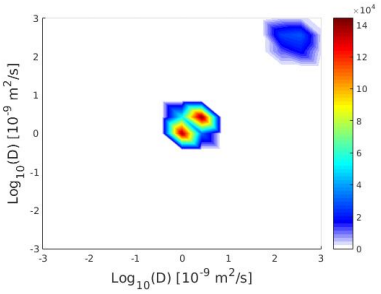

Figure 10.30: Diffusion-Diffusion exchange plot 1 M sucrose

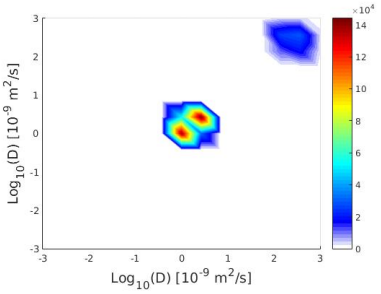

Figure 10.31: Diffusion-Diffusion exchange plot 1.5 M sucrose

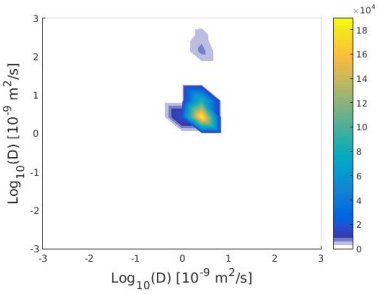

Figure 10.32: Diffusion-Diffusion exchange plot 0.5 M sucrose

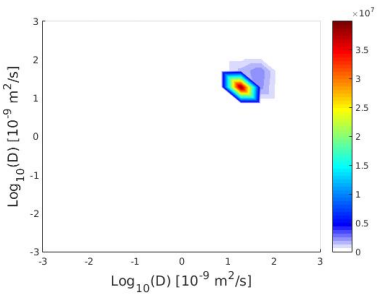

Figure 10.33: Diffusion-Diffusion exchange plot water

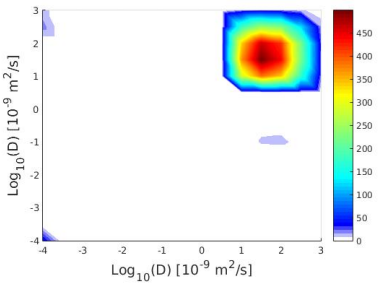

Figure 10.34: Diffusion-Diffusion exchange plot 2 M sucrose for water peak

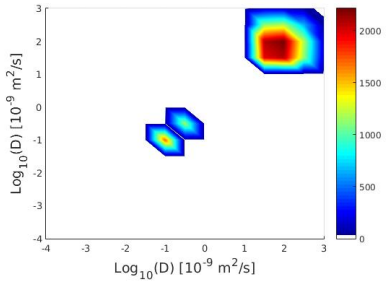

Figure 10.35: Diffusion-Diffusion exchange plot 2 M sucrose for CH peak

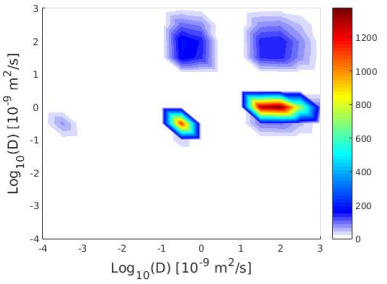

Figure 10.36: Diffusion-Diffusion exchange plot 1.5 M sucrose for hydroxyl peak

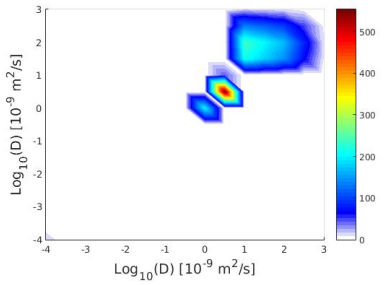

Figure 10.37: Diffusion-Diffusion exchange plot 1.5 M sucrose for water peak

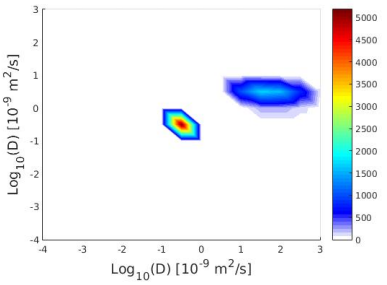

Figure 10.38: Diffusion-Diffusion exchange plot 1.5 M sucrose for CH peak

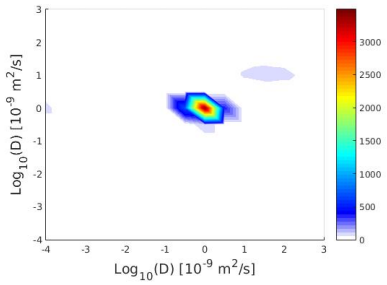

Figure 10.39: Diffusion-Diffusion exchange plot 1 M sucrose hydroxyl peak

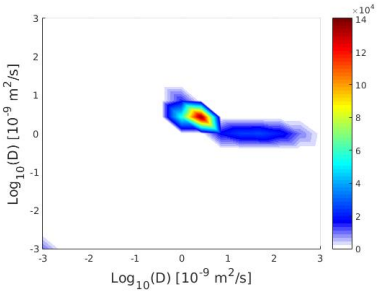

Figure 10.40: Diffusion-Diffusion exchange plot 0.5 M sucrose for hydroxyl peak

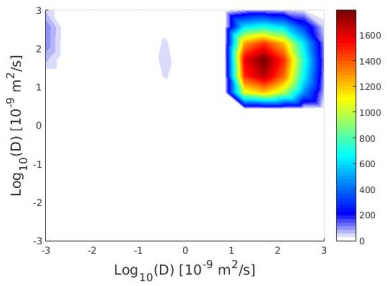

Figure 10.41: Diffusion-Diffusion exchange plot 1.5 M sucrose for water peak

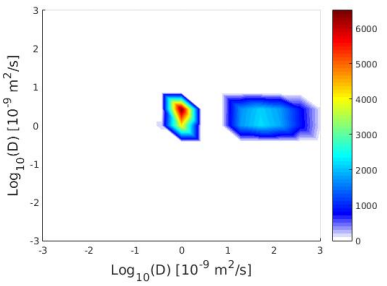

Figure 10.42: Diffusion-Diffusion exchange plot 1.5 M sucrose for CH peak

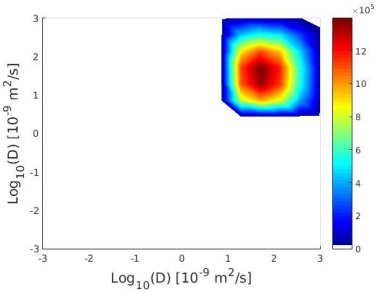

Figure 10.43: Diffusion-Diffusion exchange plot water, main peak

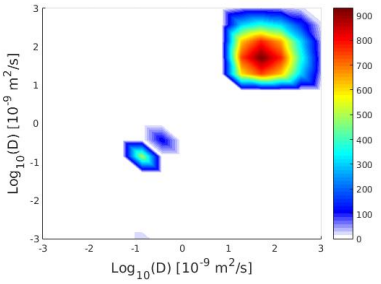

Figure 10.44: Diffusion-Diffusion exchange plot 2 M sucrose hydroxyl peak

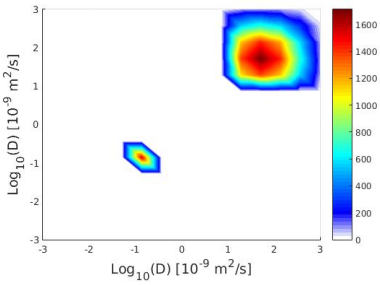

Figure 10.45: Diffusion-Diffusion exchange plot 2 M sucrose CH peak

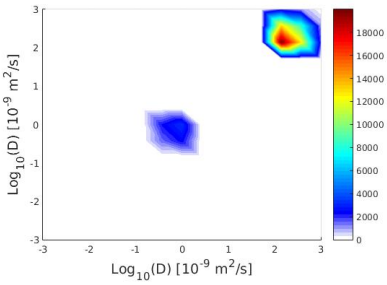

Figure 10.46: Diffusion-Diffusion exchange plot 1.5 M sucrose water peak

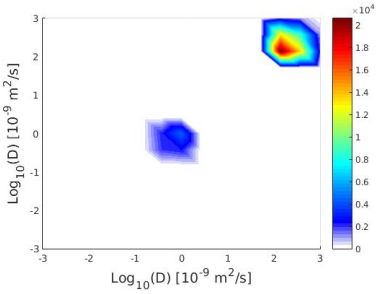

Figure 10.47: Diffusion-Diffusion exchange plot 1.5 M sucrose CH peak

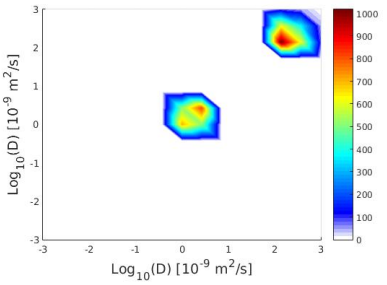

Figure 10.48: Diffusion-Diffusion exchange plot 1.5 M sucrose hydroxyl peak

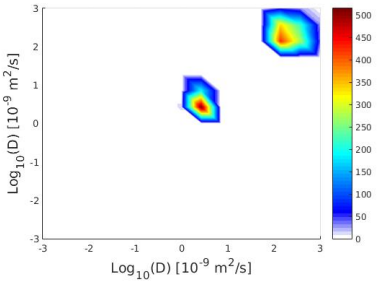

Figure 10.49: Diffusion-Diffusion exchange plot 0.5 M sucrose hydroxyl peak

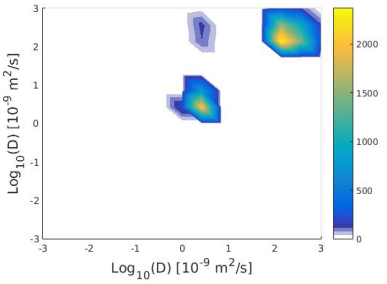

Figure 10.50: Diffusion-Diffusion exchange plot 0.5 M sucrose CH peak

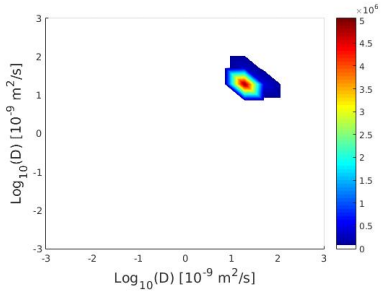

Figure 10.51: Diffusion-Diffusion exchange plot water main peak

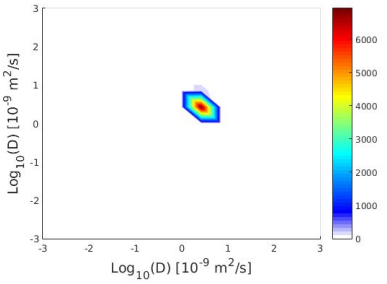

Figure 10.52: Diffusion-Diffusion exchange plot 0.5 M sucrose hydroxyl peak

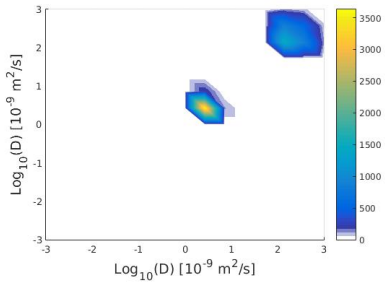

Figure 10.53: Diffusion-Diffusion exchange plot 0.5 M CH peak

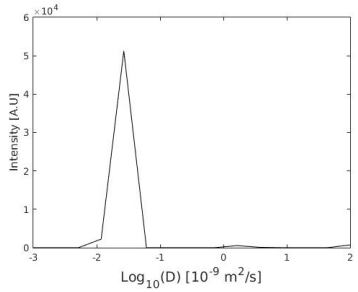

Figure 10.54: Diffusion spectra 2 M sucrose hydroxyl peak

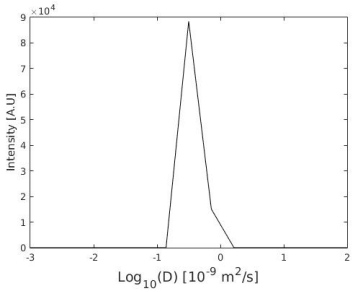

Figure 10.55: Diffusion spectra 2 M sucrose water peak

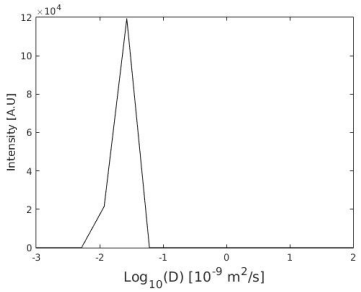

Figure 10.56: Diffusion-Diffusion exchange plot 2 M sucrose CH peak

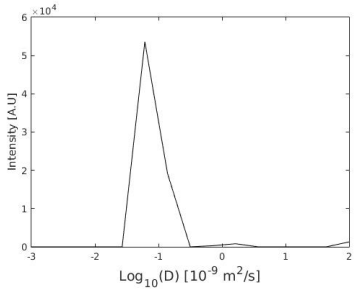

Figure 10.57: Diffusion spectra 1.5 M sucrose hydroxyl peak

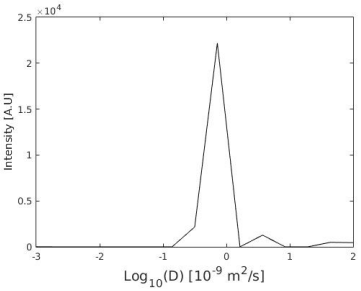

Figure 10.58: Diffusion spectra 1.5 M sucrose water peak

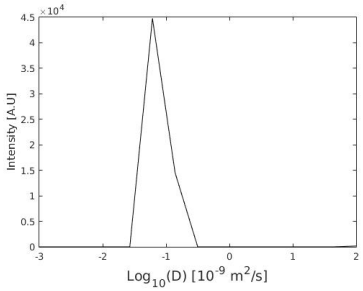

Figure 10.59: Diffusion spectra plot 2 M sucrose CH peak

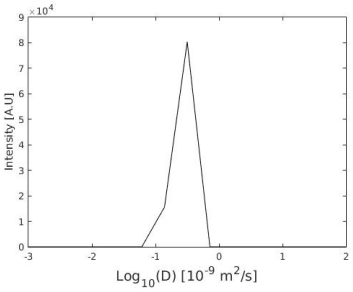

Figure 10.60: Diffusion spectra 0.5 M sucrose hydroxyl peak

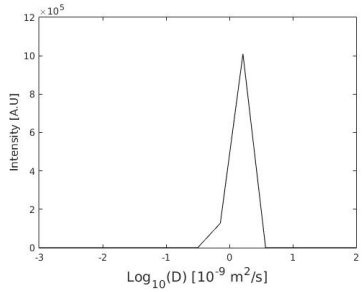

Figure 10.61: Diffusion spectra 0.5 M sucrose water peak

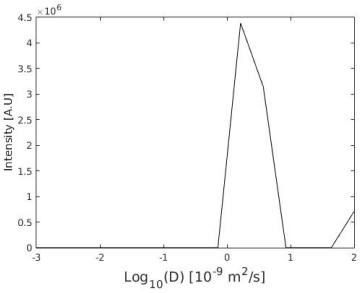

Figure 10.62: Diffusion spectra water

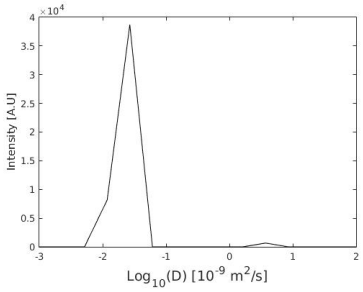

Figure 10.63: Diffusion spectra 2 M sucrose hydroxyl peak

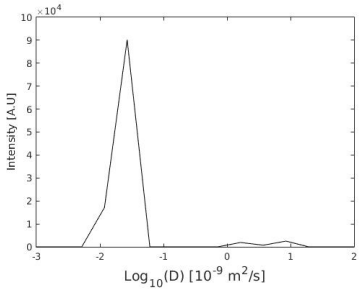

Figure 10.64: Diffusion spectra 2 M sucrose CH peak

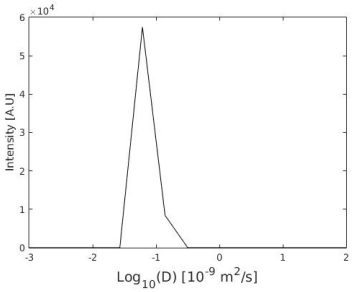

Figure 10.65: Diffusion spectra 2 M sucrose hydroxyl peak

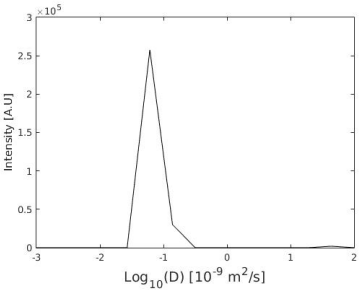

Figure 10.66: Diffusion spectra 2 M sucrose CH peak

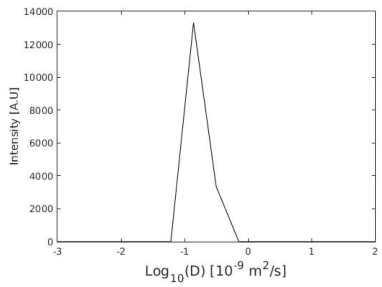

Figure 10.67: Diffusion spectra 1.0 M sucrose hydroxyl peak

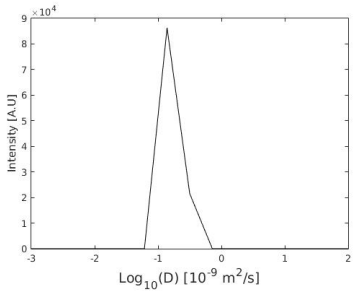

Figure 10.68: Diffusion spectra 1.0 M sucrose CH peak

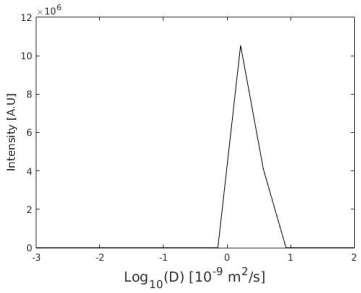

Figure 10.69: Diffusion spectra water

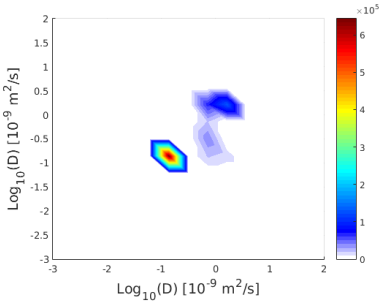

Figure 10.70: Diffusion spectra 0.5 M sucrose hydroxyl peak

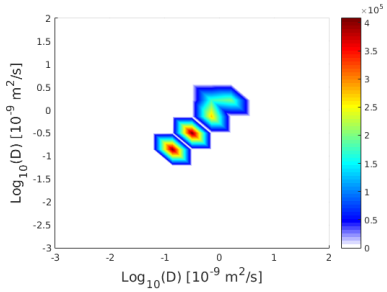

Figure 10.71: 1 M sucrose diffusion-diffusion exchange plot, with log diffusion encoding

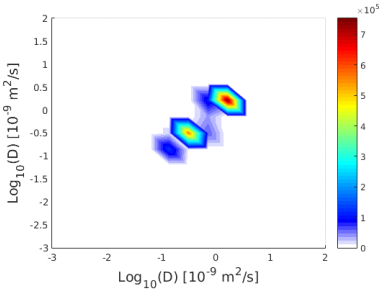

Figure 10.72: 0.75 M sucrose diffusion-diffusion exchange plot, with log diffusion encoding

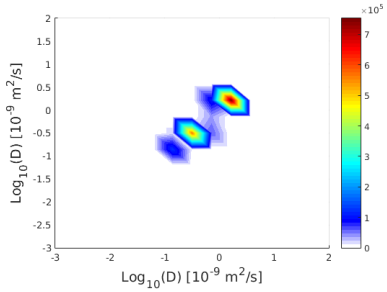

Figure 10.73: 0.5 M sucrose diffusion-diffusion exchange plot, with log diffusion encoding

10.2 Diffusion Simulation figures

10.2.1 Diffusion Simulation figures not used for figures in the main text

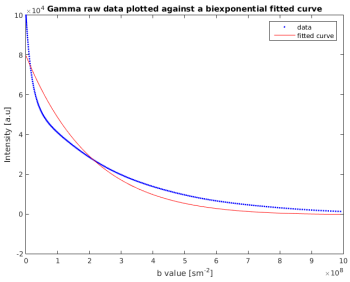

Figure 10.74: Fit of a bi-exponential to the diffusion signal from a simulation in a gamma cylinder substrate

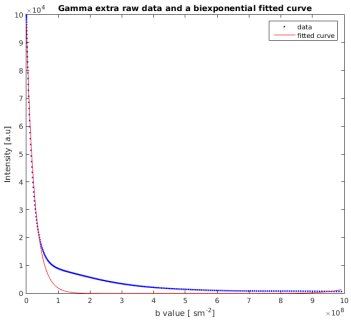

Figure 10.75: Fit of a bi-exponential to the diffusion signal from outside the cylinders from a simulation in a gamma cylinder substrate

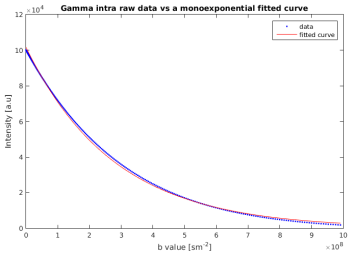

Figure 10.76: Fit of a mono-exponential to the diffusion signal from inside the cylinders from a simulation in a gamma cylinder substrate

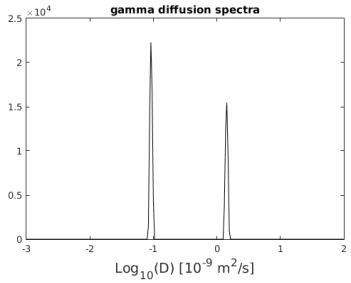

Figure 10.77: Diffusion spectra acquired using DOSY from the gamma distribution

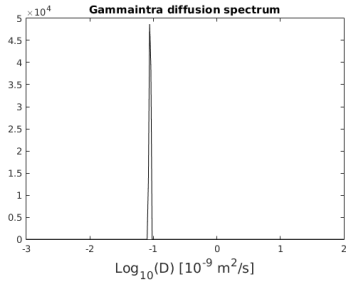

Figure 10.78: Diffusion spectra acquired using DOSY from the spins inside the cylinders in the gamma distribution

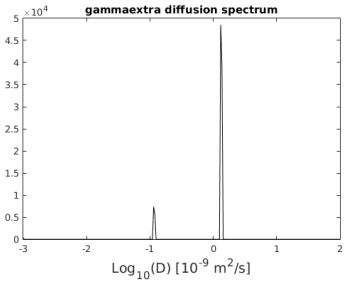

Figure 10.79: Diffusion spectra acquired using DOSY from the spins outside the cylinders in the gamma distribution

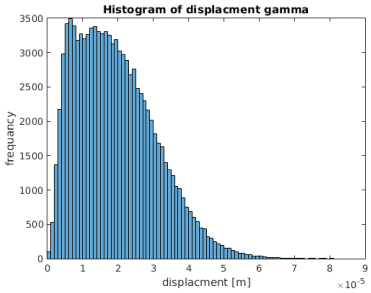

Figure 10.80: Histogram of displacement for spins in the gamma distribution

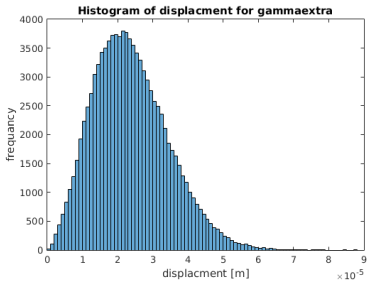

Figure 10.81: Histogram of displacement for spins outside the cylinders in the gamma distribution

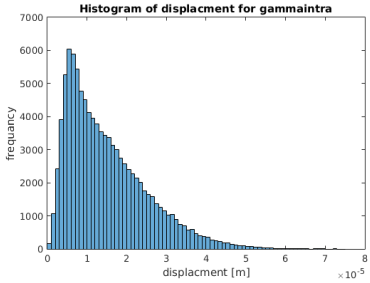

Figure 10.82: Histogram of displacement for spins inside the cylinders in the gamma distribution

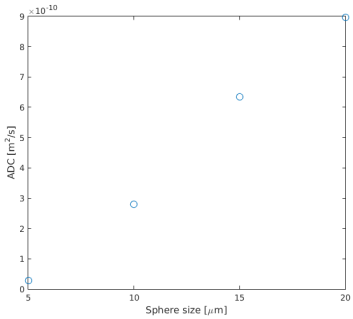

Figure 10.83: Plot showing how ADC changes with sphere size from a CAMINO simulation.

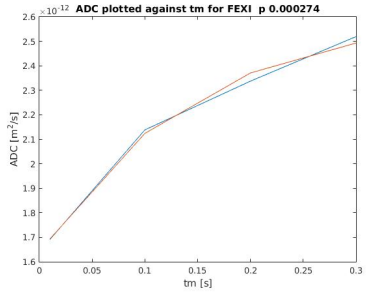

Figure 10.84: ADC plotted against tm for a FEXSY acquisition for p=0.000274, $p = 1.0\mu m/s$ in the nervous tissue simulation, $AXR = 7.0 \pm 0.4s^{-1}$

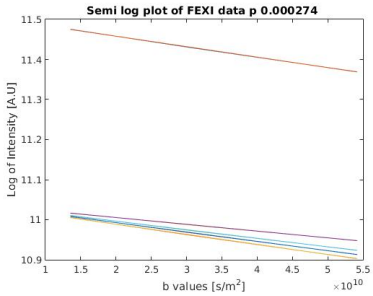

Figure 10.85: Semi log plot of FEXSY data for p=0.000274, $p = 1.0\mu m/s$ in the nervous tissue simulation

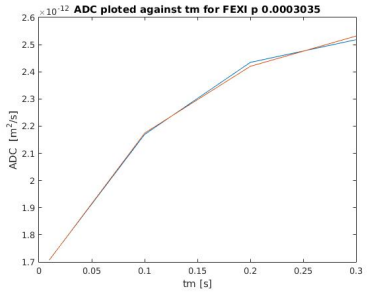

Figure 10.86: ADC plotted against tm for a FEXSY acquisition for p=0.0003035, $p = 1.2\mu m/s$ in the nervous tissue simulation, , $AXR = 7.9 \pm 0.4s^{-1}$

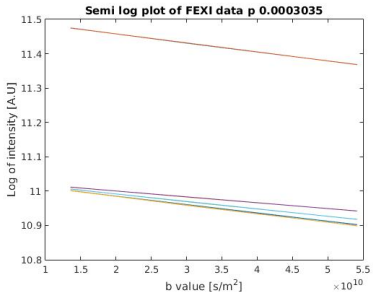

Figure 10.87: Semi log plot of FEXSY data for p=0.0003035, $p = 1.2\mu m/s$ in the nervous tissue simulation

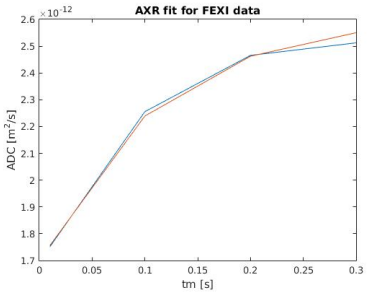

Figure 10.88: ADC plotted against tm for a FEXSY acquisition for p=0.000383, $p = 1.4\mu m/s$ in the nervous tissue simulation, , $AXR = 9.3 \pm 0.4s^{-1}$

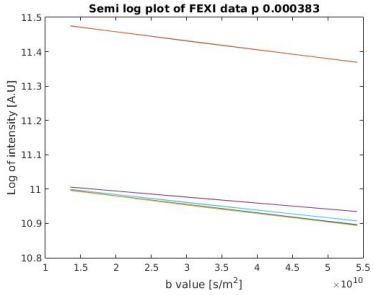

Figure 10.89: Semi log plot of FEXSY data for p=0.000383, $p = 1.4\mu m/s$ in the nervous tissue simulation

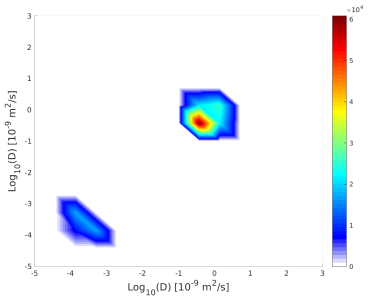

Figure 10.90: Diffusion exchange plot nervous tissue simulation p=0.0, $p = 0.0\mu m/s$

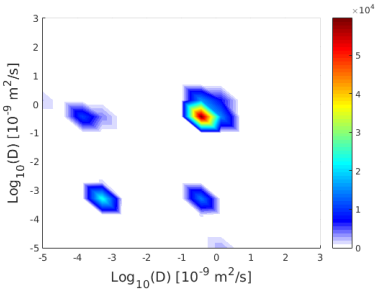

Figure 10.91: Diffusion exchange plot nervous tissue simulation p=0.000274, $p = 1.0\mu m/s$

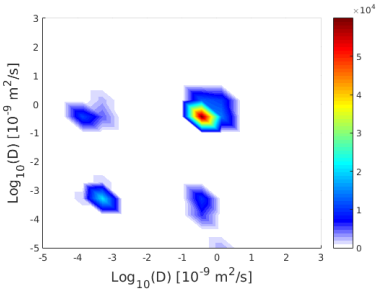

Figure 10.92: Diffusion exchange plot nervous tissue simulation, p=0.0003035, $p = 1.2\mu m/s$

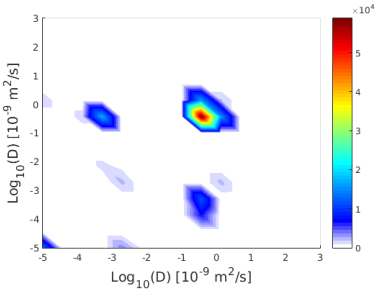

Figure 10.93: Diffusion exchange plot nervous tissue simulation, p=0.000383, $p = 1.4\mu m/s$

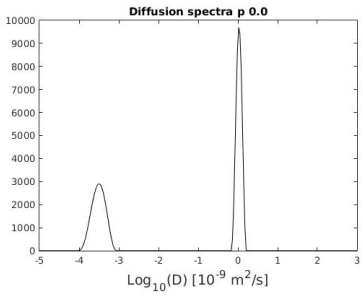

Figure 10.94: DOSY diffusion spectra nervous tissue simulation $p = 0.0$, $p = 0.0\mu m/s$

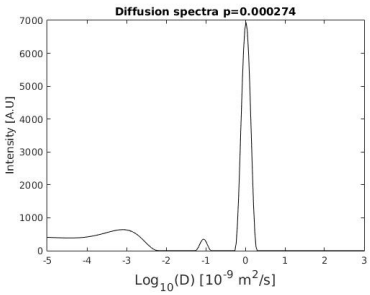

Figure 10.95: DOSY diffusion spectra nervous tissue simulation $p = 0.000274$, $p = 1.0\mu m/s$

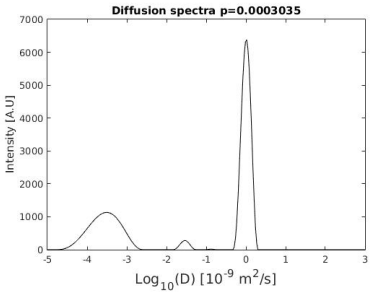

Figure 10.96: DOSY diffusion spectra nervous tissue simulation $p = 0.0003035$, $p = 1.2\mu m/s$

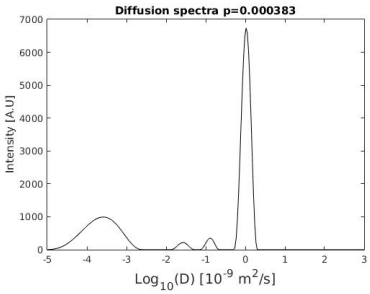

Figure 10.97: DOSY diffusion spectra nervous tissue simulation $p = 0.000383$, $p = 1.4\mu m/s$

10.2.2 Diffusion-diffusion exchange plots for the nervous tissue substrate simulation

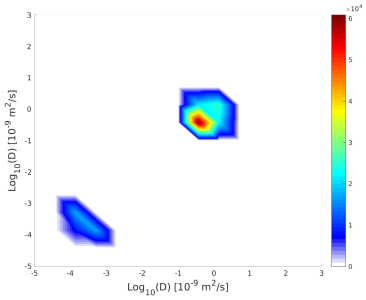

Figure 10.98: Diffusion exchange plot nervous tissue simulation p=0.0

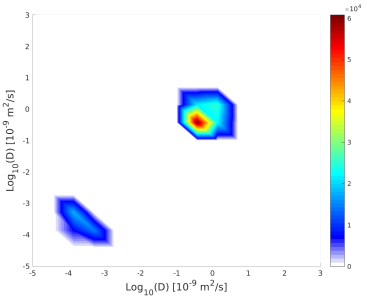

Figure 10.99: Diffusion exchange plot nervous tissue simulation p=0.0000015

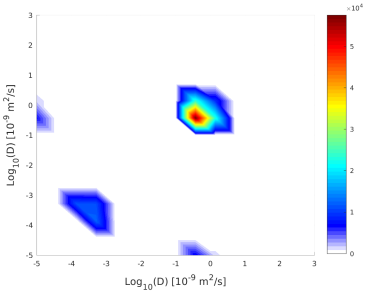

Figure 10.100: Diffusion exchange plot nervous tissue simulation p=0.0001

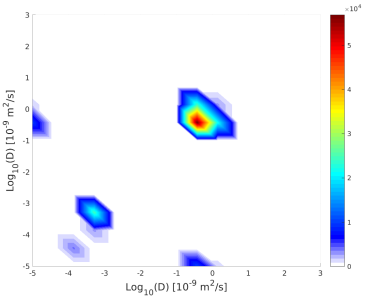

Figure 10.101: Diffusion exchange plot nervous tissue simulation p=0.00015

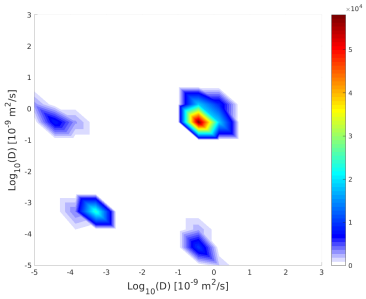

Figure 10.102: Diffusion exchange plot nervous tissue simulation p=0.0002

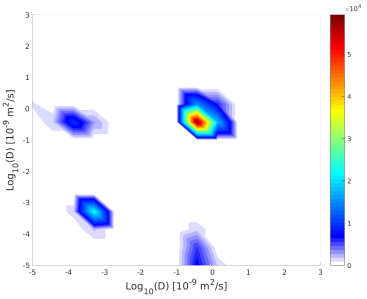

Figure 10.103: Diffusion exchange plot nervous tissue simulation p=0.00025

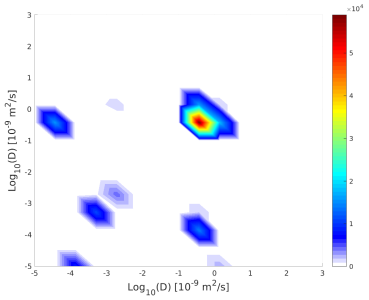

Figure 10.104: Diffusion exchange plot nervous tissue simulation p=0.0003

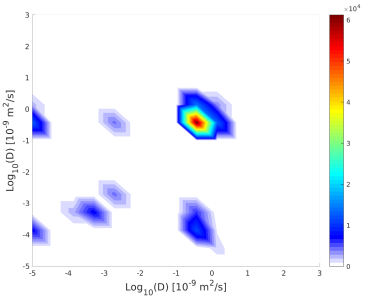

Figure 10.105: Diffusion exchange plot nervous tissue simulation p=0.00035

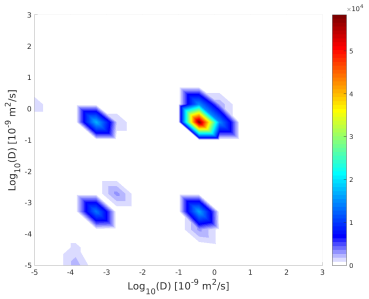

Figure 10.106: Diffusion exchange plot nervous tissue simulation p=0.0004

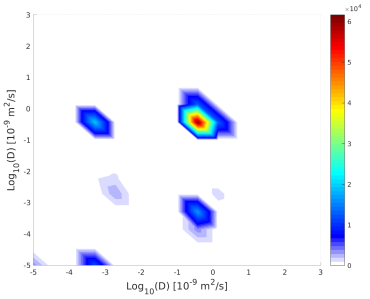

Figure 10.107: Diffusion exchange plot nervous tissue simulation p=0.00045

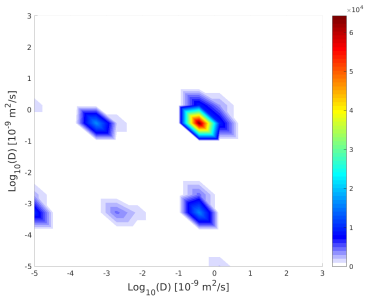

Figure 10.108: Diffusion exchange plot nervous tissue simulation p=0.0005

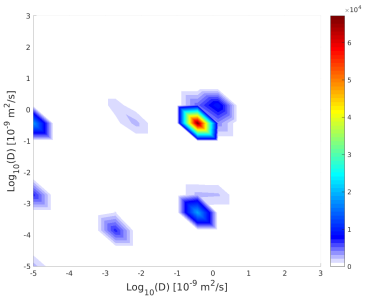

Figure 10.109: Diffusion exchange plot nervous tissue simulation p=0.00055

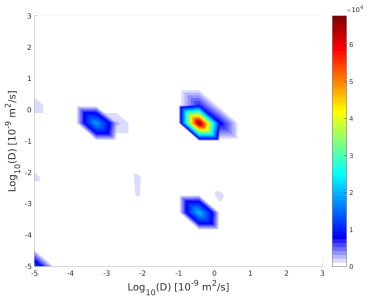

Figure 10.110: Diffusion exchange plot nervous tissue simulation p=0.0006

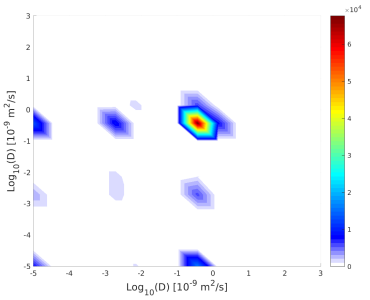

Figure 10.111: Diffusion exchange plot nervous tissue simulation p=0.00065

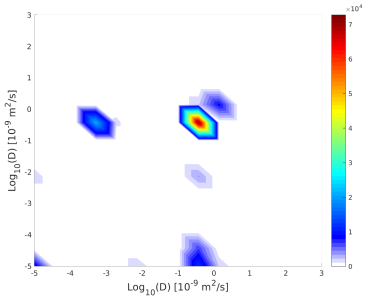

Figure 10.112: Diffusion exchange plot nervous tissue simulation p=0.0007

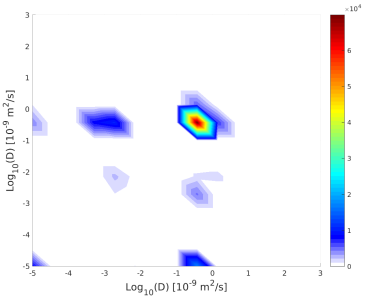

Figure 10.113: Diffusion exchange plot nervous tissue simulation p=0.00075

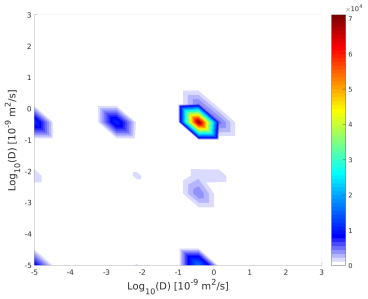

Figure 10.114: Diffusion exchange plot nervous tissue simulation p=0.0008

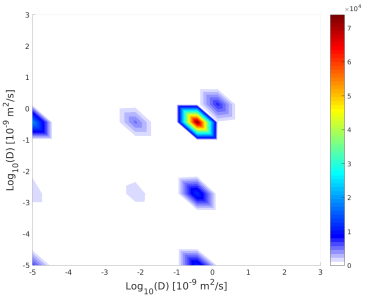

Figure 10.115: Diffusion exchange plot nervous tissue simulation p=0.00085

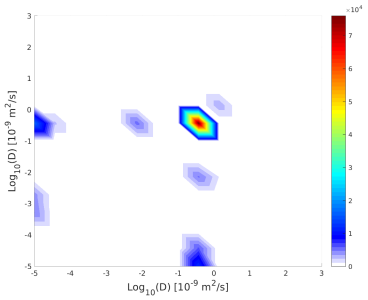

Figure 10.116: Diffusion exchange plot nervous tissue simulation p=0.0009

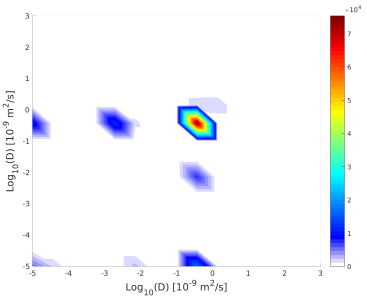

Figure 10.117: Diffusion exchange plot nervous tissue simulation p=0.00095

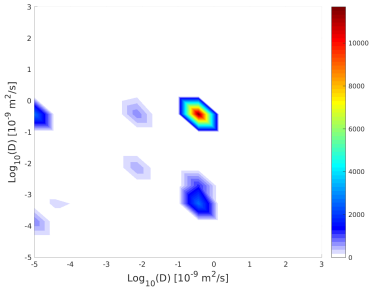

Figure 10.118: Diffusion exchange plot nervous tissue simulation p=0.001

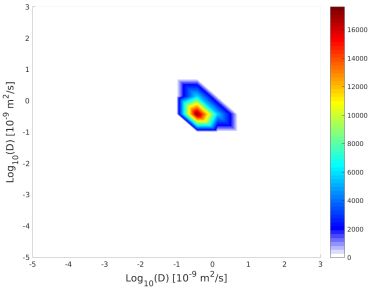

Figure 10.119: Diffusion exchange plot nervous tissue simulation p=0.01

10.2.3 Diffusion spectra plots for the nervous tissue substrate simulation

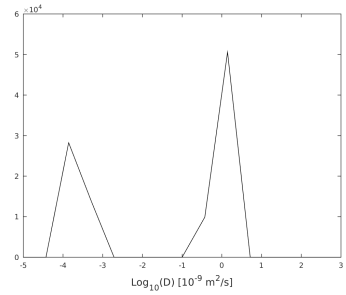

Figure 10.120: DOSY diffusion spectra nervous tissue simulation p=0.0

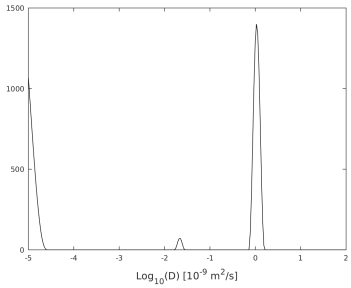

Figure 10.121: DOSY diffusion spectra nervous tissue simulation p=0.00001

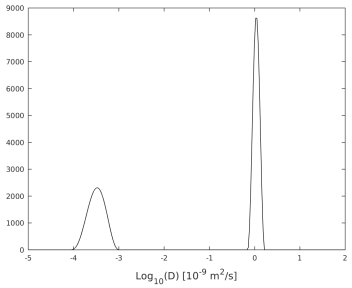

Figure 10.122: DOSY diffusion spectra nervous tissue simulation p=0.000015

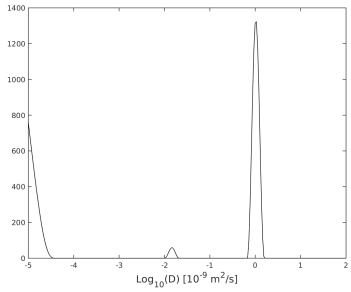

Figure 10.123: DOSY diffusion spectra nervous tissue simulation p=0.0001

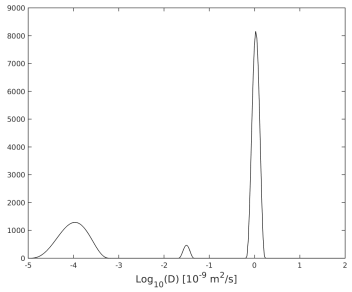

Figure 10.124: DOSY diffusion spectra nervous tissue simulation p=0.00015

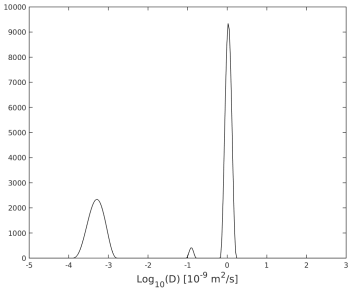

Figure 10.125: DOSY diffusion spectra nervous tissue simulation p=0.0002

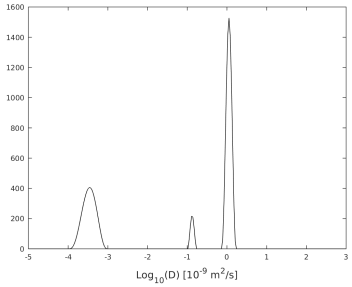

Figure 10.126: DOSY diffusion spectra nervous tissue simulation p=0.00025

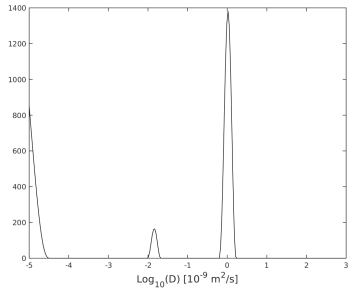

Figure 10.127: DOSY diffusion spectra nervous tissue simulation p=0.0003

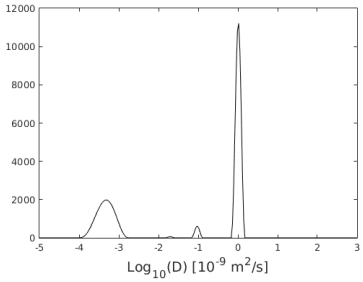

Figure 10.128: DOSY diffusion spectra nervous tissue simulation p=0.00035

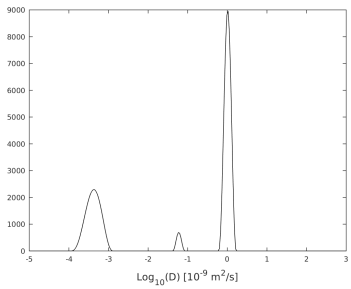

Figure 10.129: DOSY diffusion spectra nervous tissue simulation p=0.0004

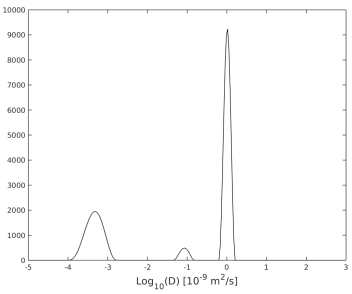

Figure 10.130: DOSY diffusion spectra nervous tissue simulation p=0.00045

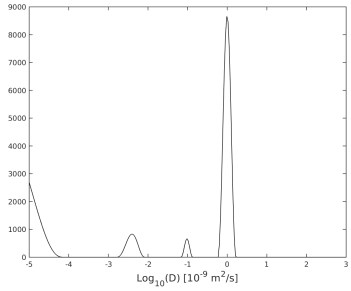

Figure 10.131: DOSY diffusion spectra nervous tissue simulation p=0.0005

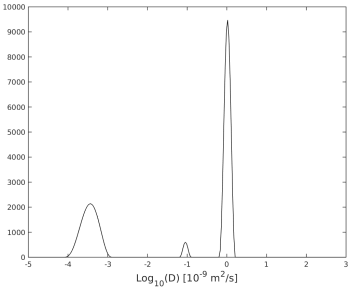

Figure 10.132: DOSY diffusion spectra nervous tissue simulation p=0.00055

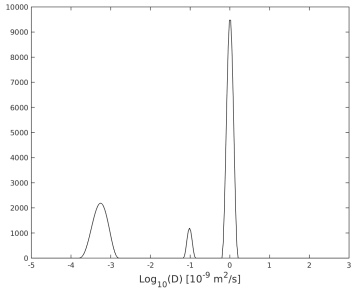

Figure 10.133: DOSY diffusion spectra nervous tissue simulation p=0.0006

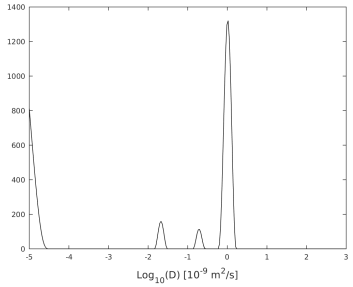

Figure 10.134: DOSY diffusion spectra nervous tissue simulation p=0.00065

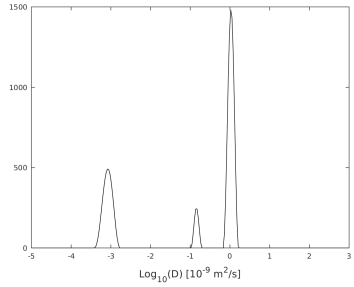

Figure 10.135: DOSY diffusion spectra nervous tissue simulation p=0.0007

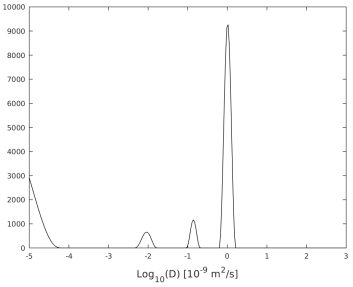

Figure 10.136: DOSY diffusion spectra nervous tissue simulation p=0.00075

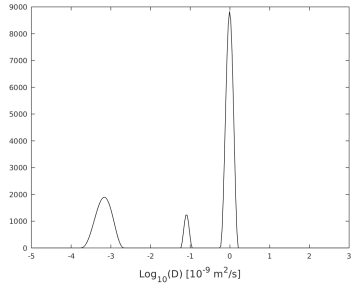

Figure 10.137: DOSY diffusion spectra nervous tissue simulation p=0.0008

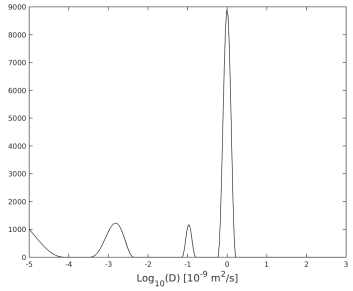

Figure 10.138: DOSY diffusion spectra nervous tissue simulation p=0.00085

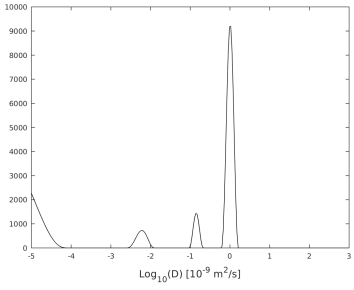

Figure 10.139: DOSY diffusion spectra nervous tissue simulation p=0.0009

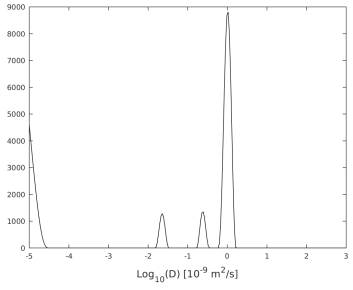

Figure 10.140: DOSY diffusion spectra nervous tissue simulation p=0p00095

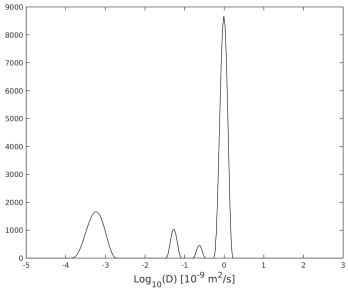

Figure 10.141: DOSY diffusion spectra nervous tissue simulation p=0p001

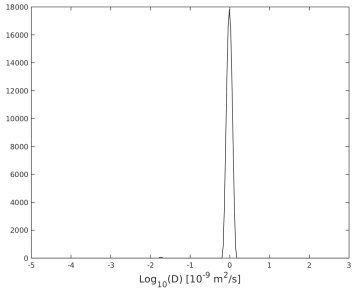

Figure 10.142: DOSY diffusion spectra nervous tissue simulation p=0p01

10.2.4 Diffusion simulation figures for the yeast substrate

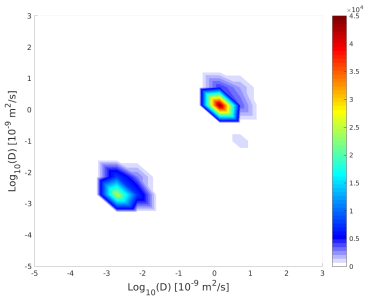

Figure 10.143: Diffusion exchange plot yeast simulation p=0.0

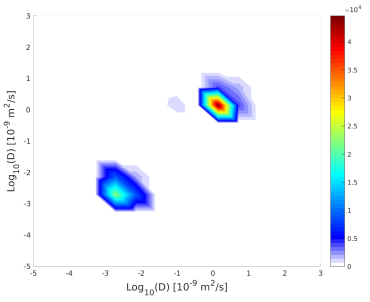

Figure 10.144: Diffusion exchange plot yeast simulation p=0.00001

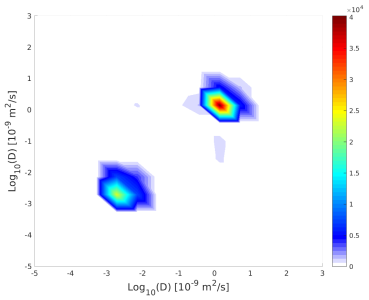

Figure 10.145: Diffusion exchange plot yeast simulation p=0.000015

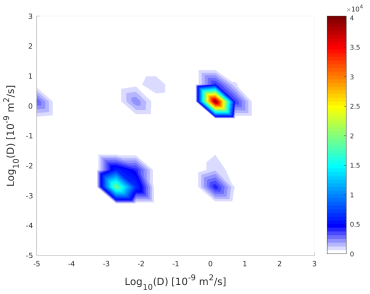

Figure 10.146: Diffusion exchange plot yeast simulation p=0.0001

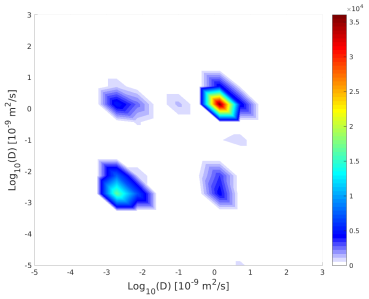

Figure 10.147: Diffusion exchange plot yeast simulation p=0.00015

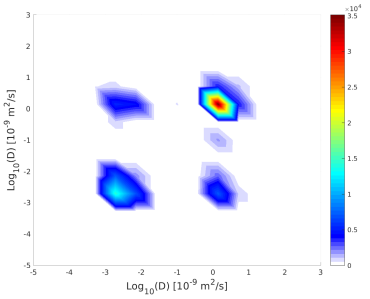

Figure 10.148: Diffusion exchange plot yeast simulation p=0.0002

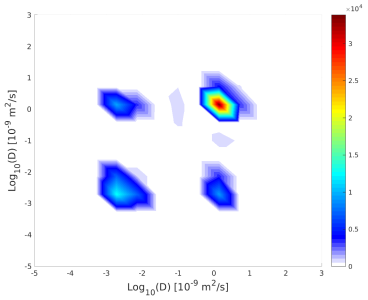

Figure 10.149: Diffusion exchange plot yeast simulation p=0.00025

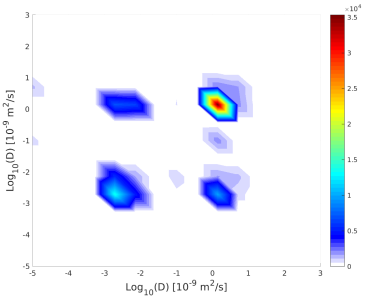

Figure 10.150: Diffusion exchange plot yeast simulation p=0.0003

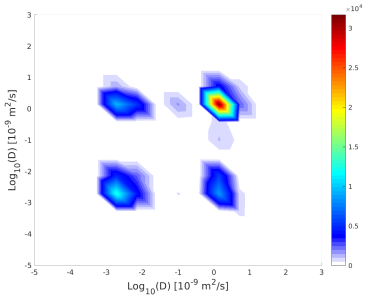

Figure 10.151: Diffusion exchange plot yeast simulation p=0.00035

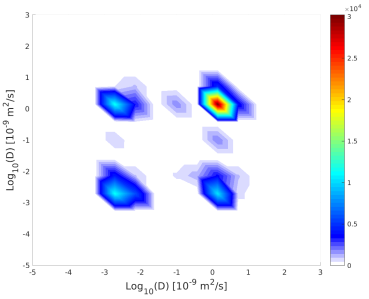

Figure 10.152: Diffusion exchange plot yeast simulation p=0.0004

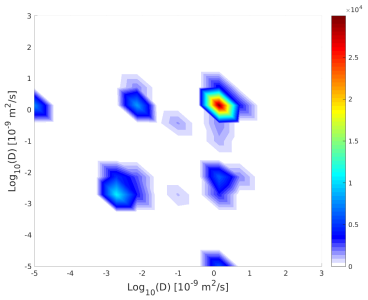

Figure 10.153: Diffusion exchange plot yeast simulation p=0.00045

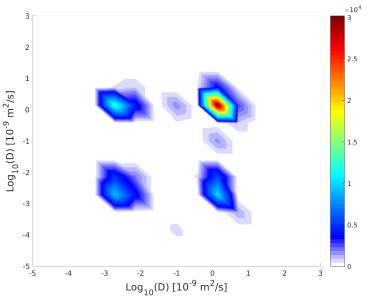

Figure 10.154: Diffusion exchange plot yeast simulation p=0.0005

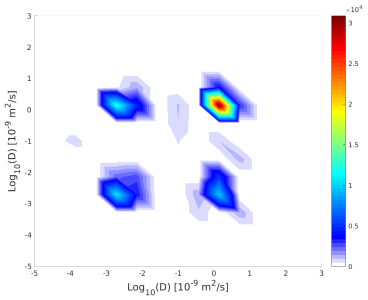

Figure 10.155: Diffusion exchange plot yeast simulation p=0.00055

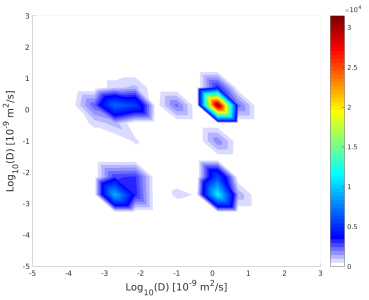

Figure 10.156: Diffusion exchange plot yeast simulation p=0.0006

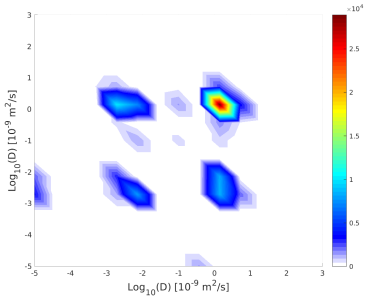

Figure 10.157: Diffusion exchange plot yeast simulation p=0.00065

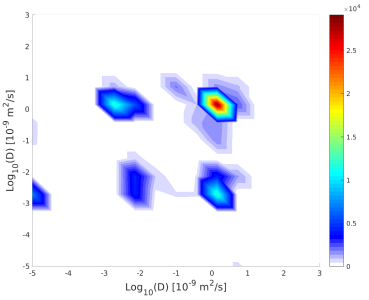

Figure 10.158: Diffusion exchange plot yeast simulation p=0.0007

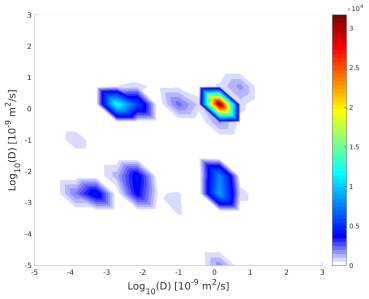

Figure 10.159: Diffusion exchange plot yeast simulation p=0.00075

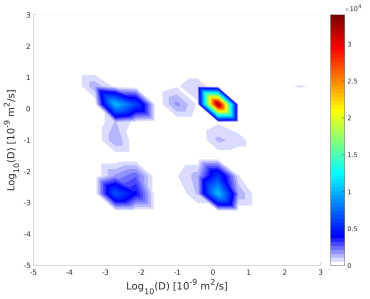

Figure 10.160: Diffusion exchange plot yeast simulation p=0.0008

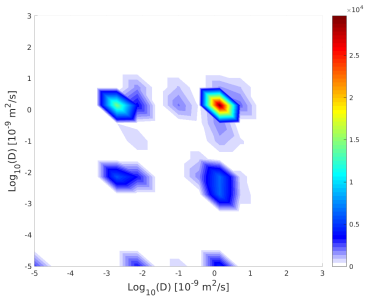

Figure 10.161: Diffusion exchange plot yeast simulation p=0.00085

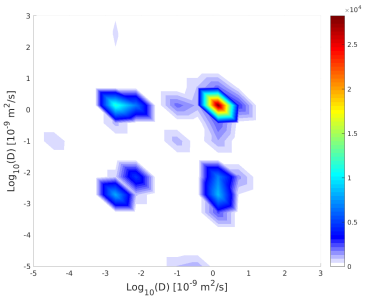

Figure 10.162: Diffusion exchange plot yeast simulation p=0.0009

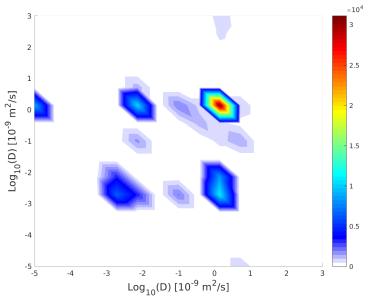

Figure 10.163: Diffusion exchange plot yeast simulation p=0.00095

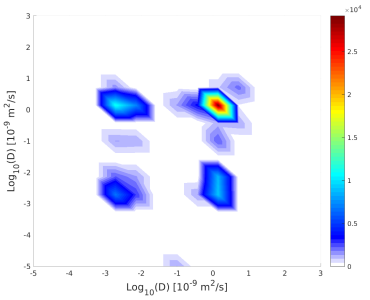

Figure 10.164: Diffusion exchange plot yeast simulation p=0.001

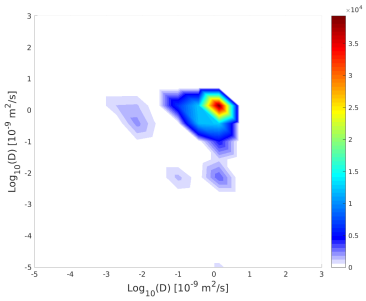

Figure 10.165: Diffusion exchange plot yeast simulation p=0.01

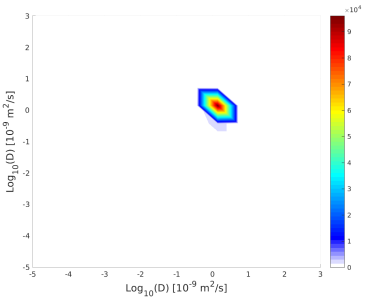

Figure 10.166: Diffusion exchange plot yeast simulation p=0.1

10.2.5 DOSY diffusion spectra for the yeast substrat simulations

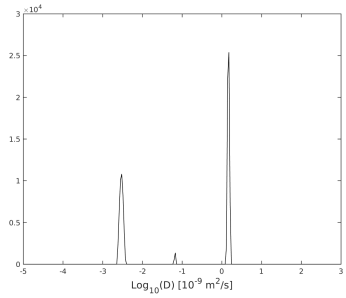

Figure 10.167: DOSY diffusion spectra yeast simulation p=0.0

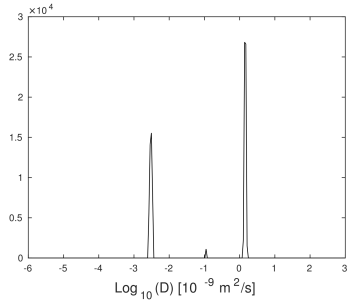

Figure 10.168: DOSY diffusion spectra yeast simulation p=0.00001

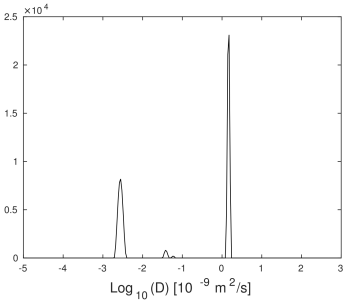

Figure 10.169: DOSY diffusion spectra yeast simulation p=0.000015

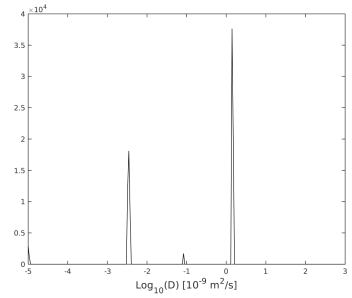

Figure 10.170: DOSY diffusion spectra yeast simulation p=0.0001

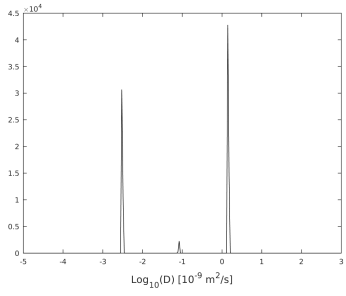

Figure 10.171: DOSY diffusion spectra yeast simulation p=0.00015

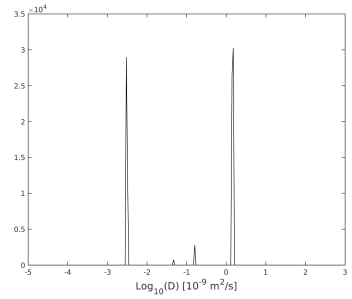

Figure 10.172: DOSY diffusion spectra yeast simulation p=0.0002

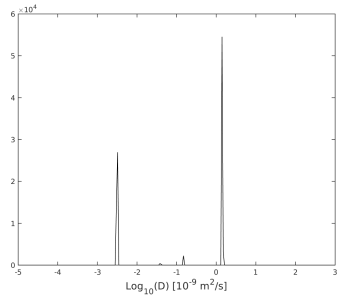

Figure 10.173: DOSY diffusion spectra yeast simulation p=0.00025

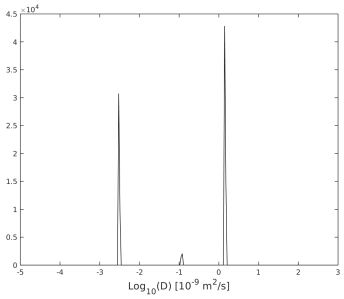

Figure 10.174: DOSY diffusion spectra yeast simulation p=0.0003

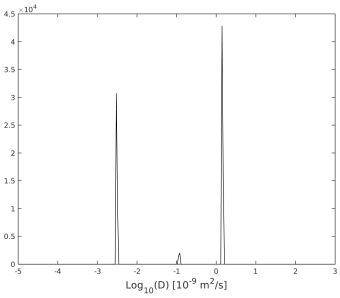

Figure 10.175: DOSY diffusion spectra yeast simulation p=0.00035

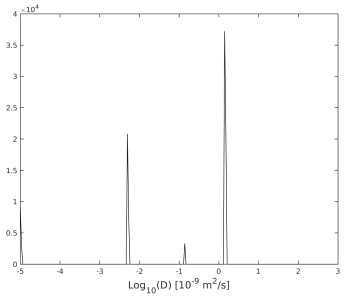

Figure 10.176: Diffusion exchange plot yeast simulation p=0.0004

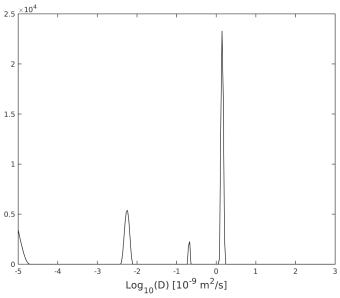

Figure 10.177: Diffusion exchange plot yeast simulation p=0.00045

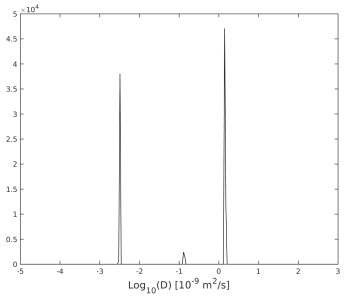

Figure 10.178: DOSY diffusion spectra yeast simulation p=0.0005

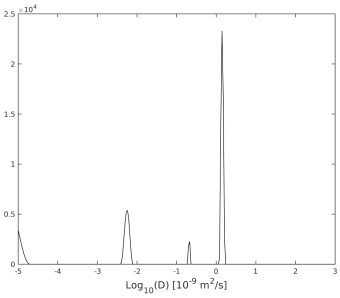

Figure 10.179: DOSY diffusion spectra yeast simulation p=0.00045

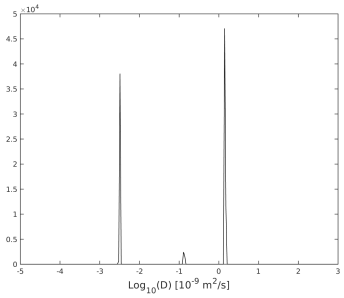

Figure 10.180: DOSY diffusion spectra yeast simulation p=0.0005

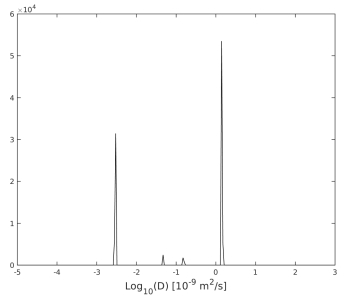

Figure 10.181: DOSY diffusion spectra yeast simulation p=0.00055

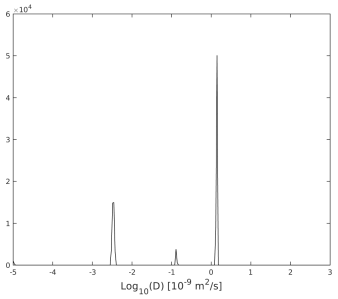

Figure 10.182: DOSY diffusion spectra yeast simulation p=0.0006

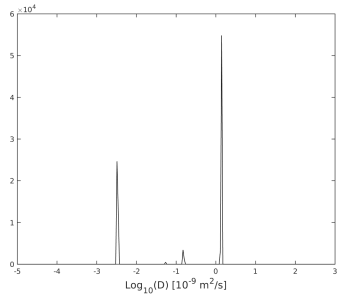

Figure 10.183: DOSY diffusion spectra yeast simulation p=0.00065

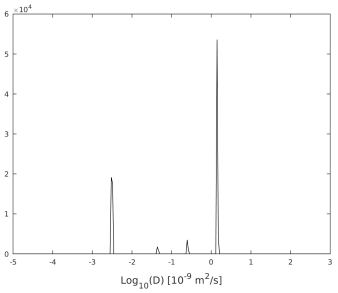

Figure 10.184: DOSY diffusion spectra yeast simulation p=0.0007

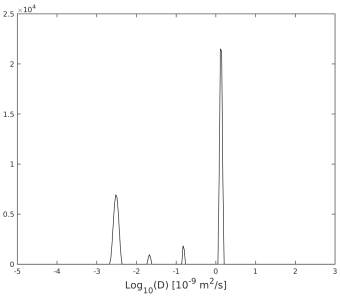

Figure 10.185: DOSY diffusion spectra yeast simulation p=0.00075

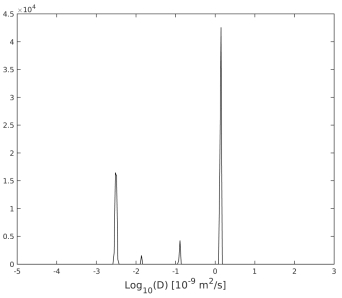

Figure 10.186: DOSY diffusion spectra yeast simulation p=0.0008

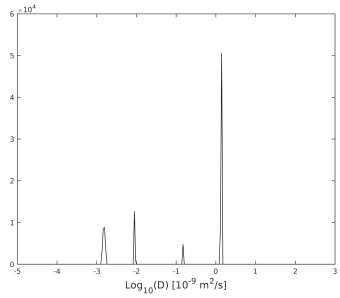

Figure 10.187: DOSY diffusion spectra yeast simulation p=0.00085

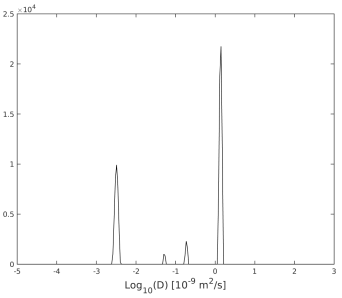

Figure 10.188: DOSY diffusion spectra yeast simulation p=0.0009

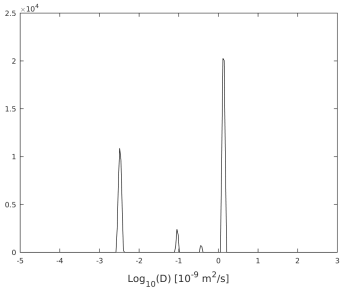

Figure 10.189: DOSY diffusion spectra yeast simulation p=0.00095

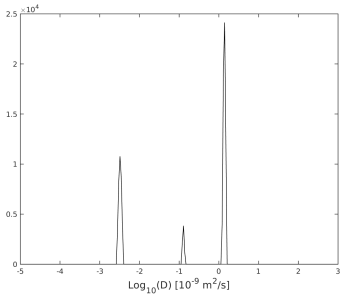

Figure 10.190: DOSY diffusion spectra yeast simulation p=0.001

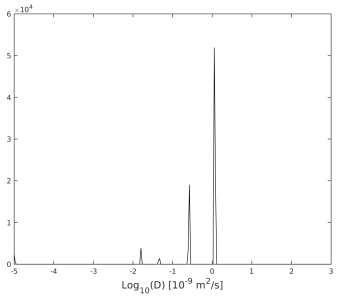

Figure 10.191: Diffusion exchange plot yeast simulation p=0.01

10.2.6 Plots showing the combined results of the diffusion exchange simulations

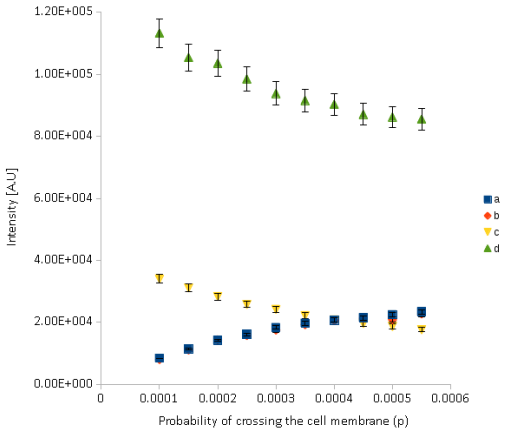

Figure 10.192: Shows the intensity of the peaks where all four peaks can be found for the nervous tissue simulation

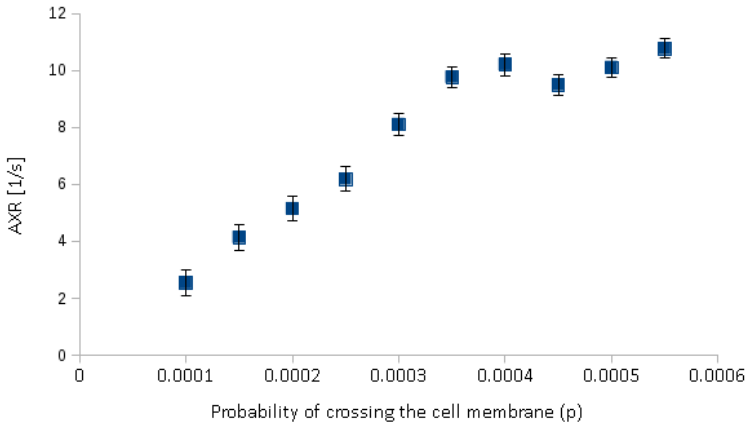

Figure 10.193: Shows the AXR for the simulations where all four peaks can be found in the nervous tissue simulation

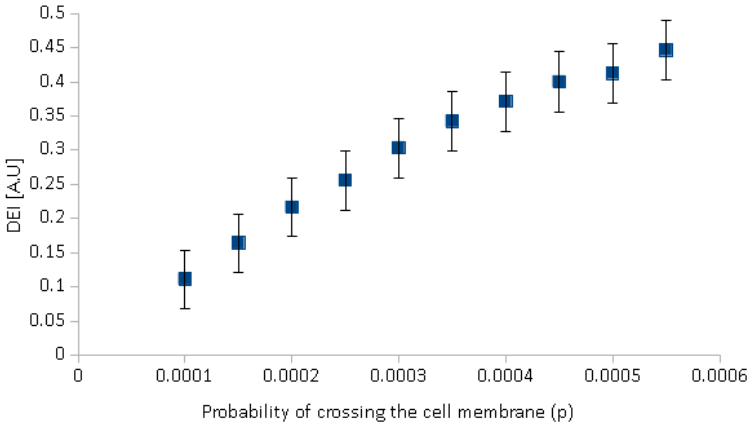

Figure 10.194: Shows the DEI for the simulations where all four peaks can be found for in nervous tissue simulation

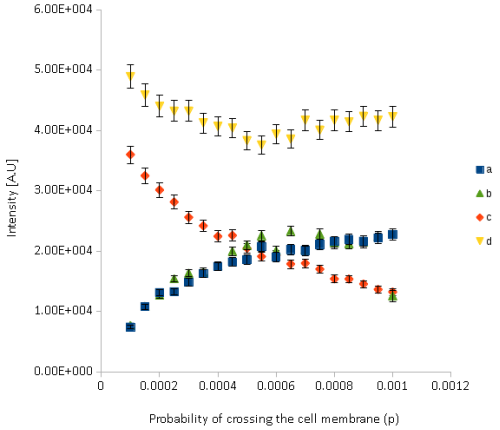

Figure 10.195: Shows the intensity of the peaks where all four peaks can be found in the yeast simulation

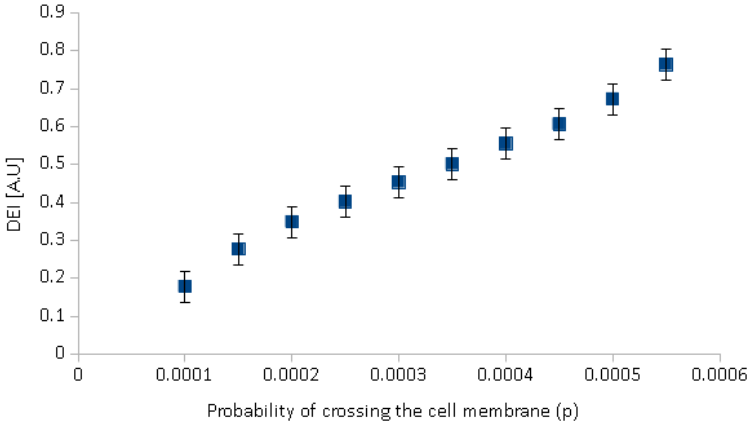

Figure 10.196: Shows the DEI for the simulations where all four peaks can be found in the yeast simulation

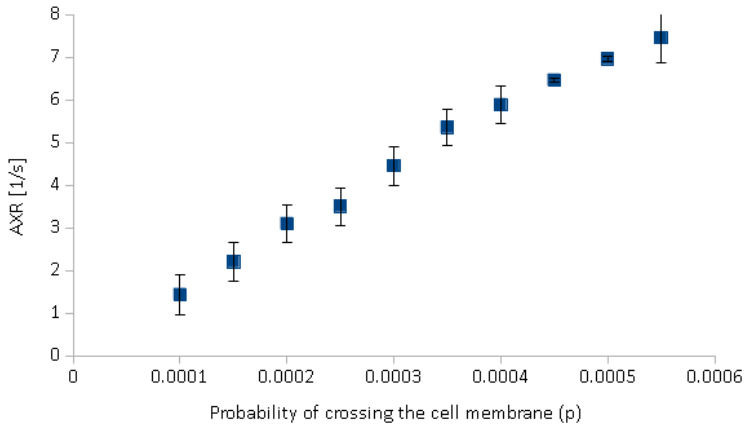

Figure 10.197: Shows the AXR for the simulations where all four peaks can be found in the yeast simulation

10.2.7 Diffusion Simulation figures not used from the fluid exchange model

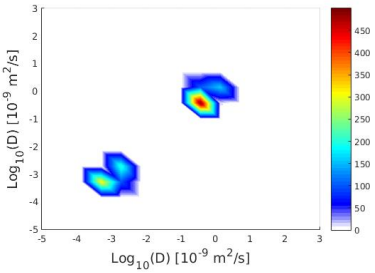

Figure 10.198: Diffusion exchange plot fluid exchange simulation p=0.00015

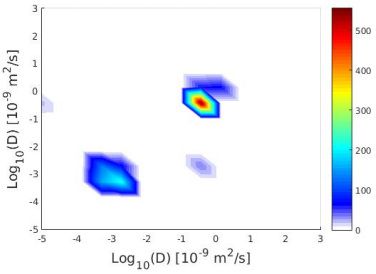

Figure 10.199: Diffusion exchange plot fluid exchange simulation p=0.0001

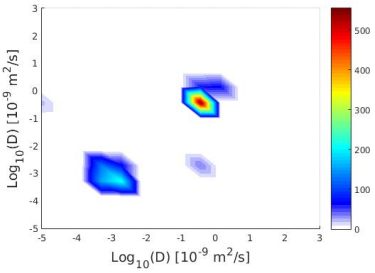

Figure 10.200: Diffusion exchange plot fluid exchange simulation p=0.00015

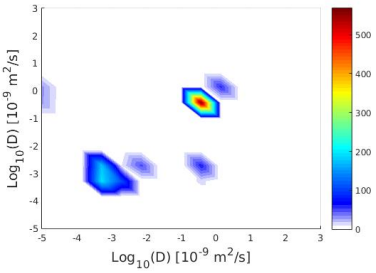

Figure 10.201: Diffusion exchange plot fluid exchange simulation p=0.0002

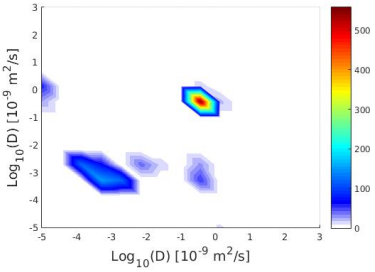

Figure 10.202: Diffusion exchange plot fluid exchange simulation p=0.00025

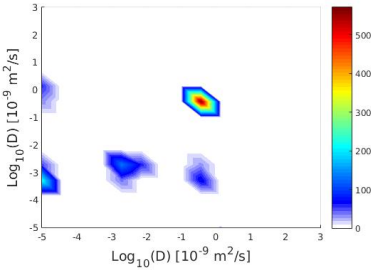

Figure 10.203: Diffusion exchange plot fluid exchange simulation p=0.0003

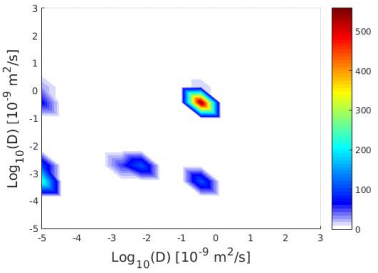

Figure 10.204: Diffusion exchange plot fluid exchange simulation p=0.00035

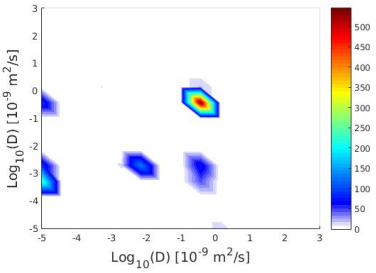

Figure 10.205: Diffusion exchange plot fluid exchange simulation p=0.0004

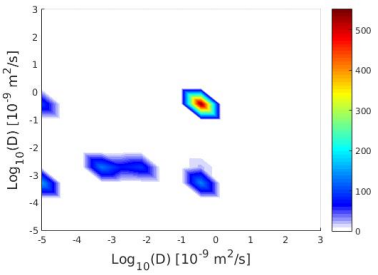

Figure 10.206: Diffusion exchange plot fluid exchange simulation p=0.00045

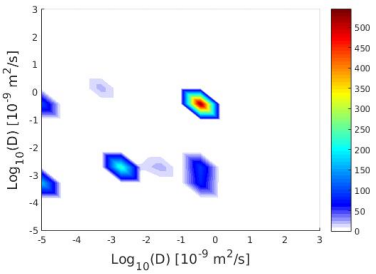

Figure 10.207: Diffusion exchange plot fluid exchange simulation p=0.0005

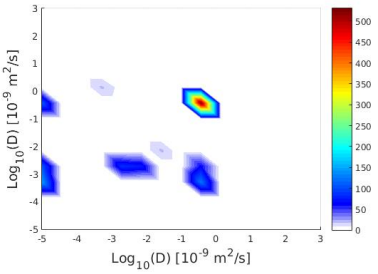

Figure 10.208: Diffusion exchange plot fluid exchange simulation p=0.00055

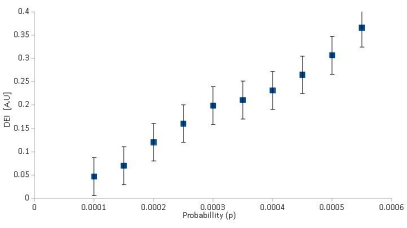

Figure 10.209: Diffusion exchange index plotted against probability for the fluid exchange model

10.3 In-vitro DEXSY data acquired from yeast suspensions

10.3.1 Preliminary data

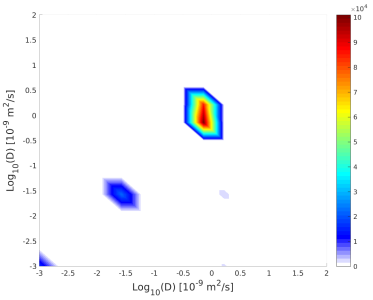

Figure 10.210: Diffusion exchange plot Yeast 2:1 PBS $\delta = 9ms$, $\Delta = 14ms$, $t_m = 200ms$, $G = 0.72T/m$

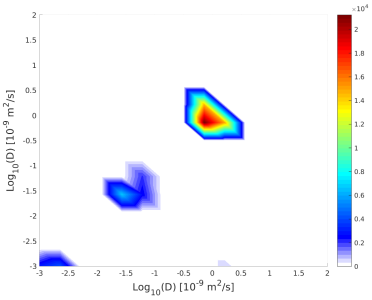

Figure 10.211: Diffusion exchange plot Yeast 2:1 (10 microgram digitonin / ml DPBS) $\delta = 9ms$, $\Delta = 14ms$, $t_m = 200ms$, $G = 0.72T/m$

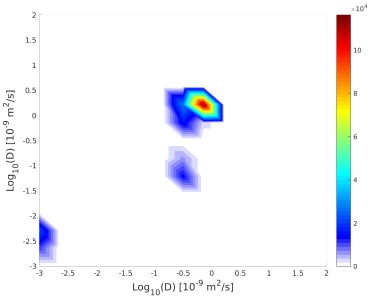

Figure 10.212: Diffusion exchange plot Yeast 2:1 PBS $\delta = 9ms$, $\Delta = 14ms$, $t_m = 200ms$, $G = 0.42T/m$ scan 1

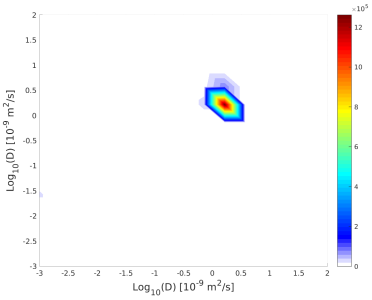

Figure 10.213: Diffusion exchange plot Yeast 2:1 PBS $\delta = 9ms$, $\Delta = 14ms$, $t_m = 200ms$, $G = 0.42T/m$ scan 2

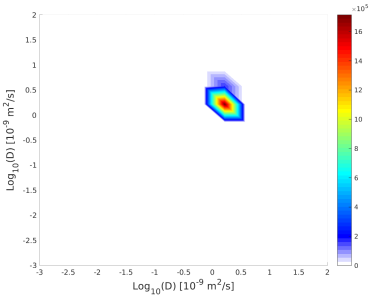

Figure 10.214: Diffusion exchange plot Yeast 2:1 PBS $\delta = 9ms$, $\Delta = 14ms$, $t_m = 200ms$, $G = 0.42T/m$ scan 3

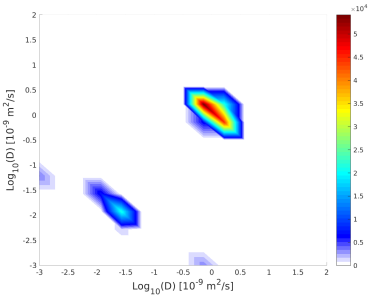

Figure 10.215: Diffusion exchange plot Yeast 2:1 (10 microgram digitonin / ml DPBS) $\delta = 9ms$, $\Delta = 14ms$, $t_m = 200ms$, $G = 0.42T/m$

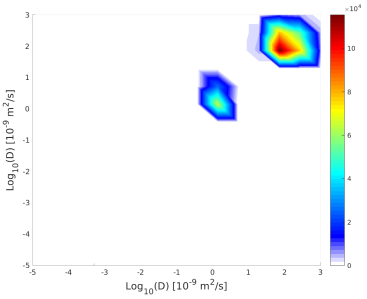

Figure 10.216: Diffusion exchange plot Yeast 2:1 PBS $\delta = 9ms$, $\Delta = 14ms$, $t_m = 200ms$, $G = 0.72T/m$

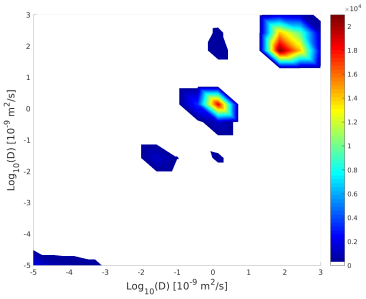

Figure 10.217: Diffusion exchange plot Yeast 2:1 PBS $\delta = 9ms$, $\Delta = 14ms$, $t_m = 200ms$, $G = 0.72T/m$ scan 1

10.3.2 In-vitro DEXSY data acquired from yeast suspensions

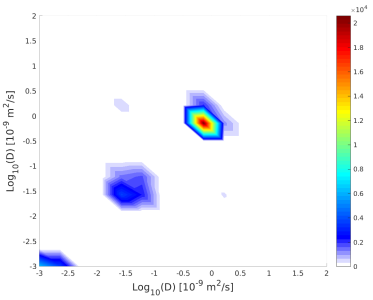

Figure 10.218: Diffusion exchange plot 22g Yeast : 10 ml PBS $\delta = 15ms$, $\Delta = 17ms$, $t_m = 200ms$, $G = 0.64T/m$ scan 1

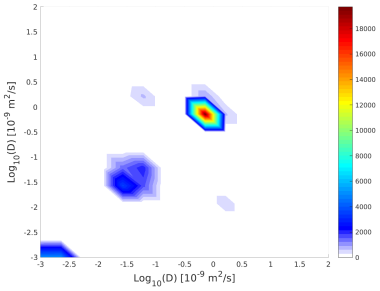

Figure 10.219: Diffusion exchange plot 22g Yeast : 10 ml PBS $\delta = 15ms$, $\Delta = 17ms$, $t_m = 200ms$, $G = 0.64T/m$ scan 2

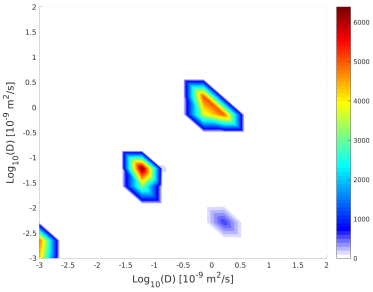

Figure 10.220: Diffusion exchange plot 22g Yeast : 10 ml PBS $\delta = 9ms$, $\Delta = 14ms$, $t_m = 200ms$, $G = 0.64T/m$ scan 1

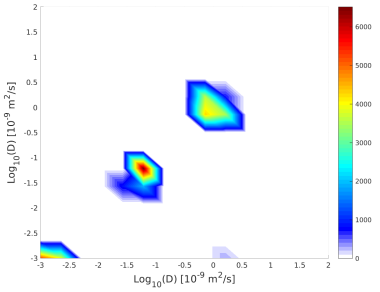

Figure 10.221: Diffusion exchange plot 22g Yeast : 10 ml PBS $\delta = 9ms$, $\Delta = 14ms$, $t_m = 200ms$, $G = 0.64T/m$ scan 2

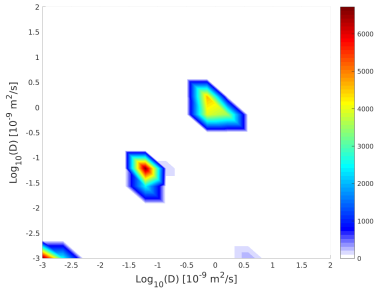

Figure 10.222: Diffusion exchange plot 22g Yeast : 10 ml PBS $\delta = 9ms$, $\Delta = 14ms$, $t_m = 200ms$, $G = 0.64T/m$ scan 3

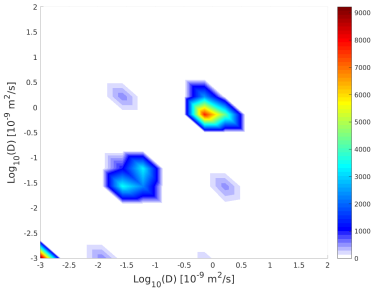

Figure 10.223: Diffusion exchange plot 22g Yeast : 10 ml PBS $\delta = 15ms$, $\Delta = 17ms$, $t_m = 200ms$, $G = 0.72T/m$ scan 1

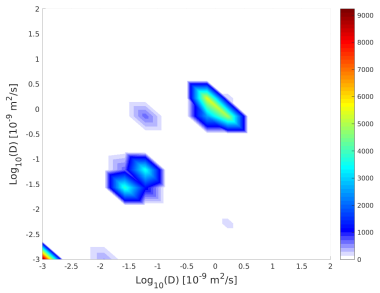

Figure 10.224: Diffusion exchange plot 22g Yeast : 10 ml PBS $\delta = 15ms$, $\Delta = 17ms$, $t_m = 200ms$, $G = 0.72T/m$ scan 2

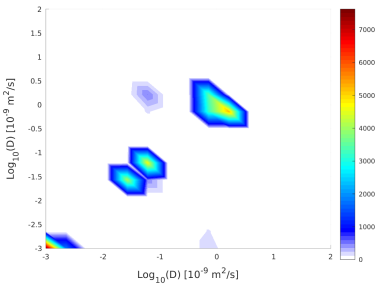

Figure 10.225: Diffusion exchange plot 22g Yeast : 10 ml PBS $\delta = 15ms$, $\Delta = 17ms$, $t_m = 200ms$, $G = 0.72T/m$ scan 3

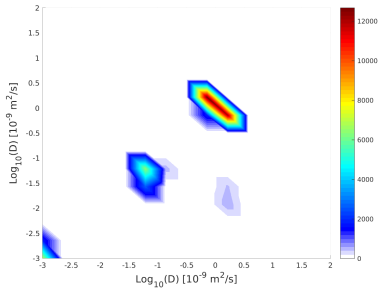

Figure 10.226: Diffusion exchange plot 22g Yeast : 10 ml PBS $\delta = 15ms$, $\Delta = 17ms$, $t_m = 200ms$, $G = 0.64T/m$ scan 1

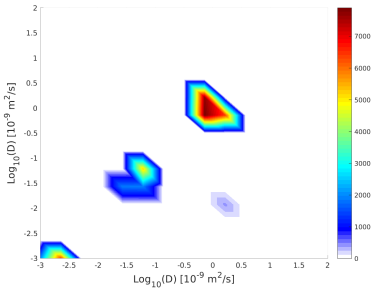

Figure 10.227: Diffusion exchange plot 22g Yeast : 10 ml PBS $\delta = 15ms$, $\Delta = 17ms$, $t_m = 200ms$, $G = 0.64T/m$ scan 2

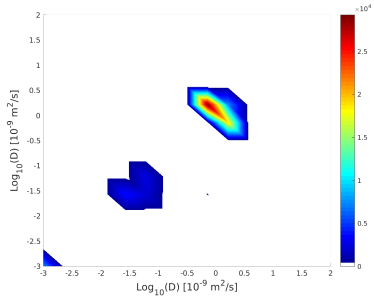

Figure 10.228: Diffusion exchange plot 22g Yeast : 10 ml PBS $\delta = 15ms$, $\Delta = 17ms$, $t_m = 200ms$, $G = 0.64T/m$ scan 3

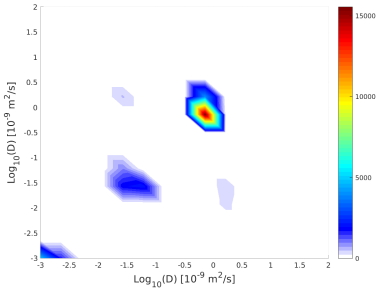

Figure 10.229: Diffusion exchange plot 22g Yeast : 10 ml PBS $\delta = 15ms$, $\Delta = 17ms$, $t_m = 200ms$, $G = 0.64T/m$ scan 1

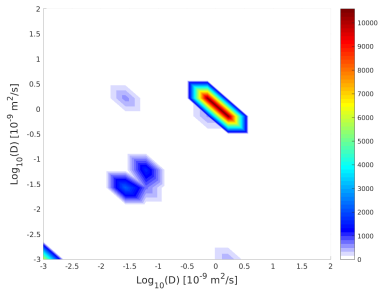

Figure 10.230: Diffusion exchange plot 22g Yeast : 10 ml PBS $\delta = 15ms$, $\Delta = 17ms$, $t_m = 200ms$, $G = 0.64T/m$ scan 2

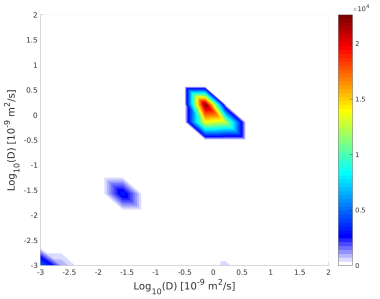

Figure 10.231: Diffusion exchange plot 22g Yeast : 10 ml PBS $\delta = 15ms$, $\Delta = 17ms$, $t_m = 200ms$, $G = 0.64T/m$ scan 3

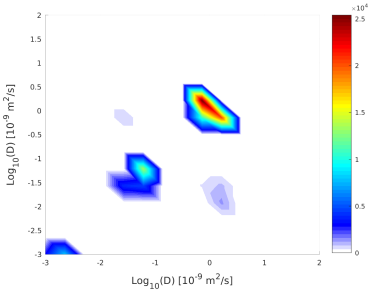

Figure 10.232: Diffusion exchange plot 22g Yeast : 10 ml PBS $\delta = 15ms$, $\Delta = 17ms$, $t_m = 200ms$, $G = 0.64T/m$ scan 1

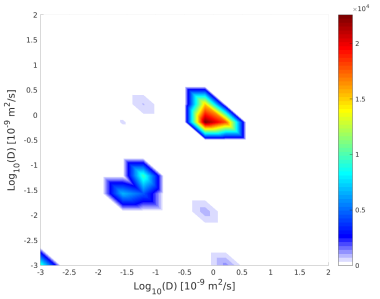

Figure 10.233: Diffusion exchange plot 22g Yeast : 10 ml PBS $\delta = 15ms$, $\Delta = 17ms$, $t_m = 200ms$, $G = 0.64T/m$ scan 2

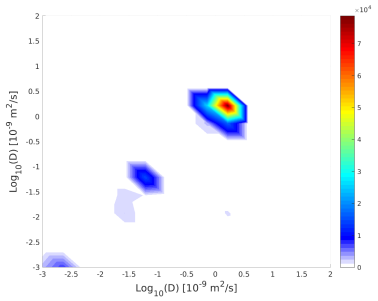

Figure 10.234: Diffusion exchange plot 22g Yeast : 10 ml PBS $\delta = 15ms$, $\Delta = 17ms$, $t_m = 200ms$, $G = 0.64T/m$ scan 3

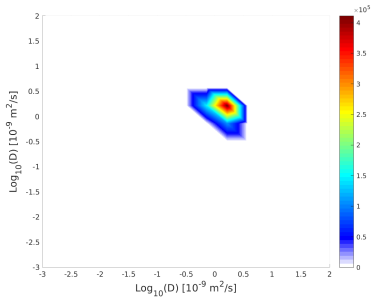

Figure 10.235: Diffusion exchange plot 6g Yeast : 10 ml PBS $\delta = 15ms$, $\Delta = 17ms$, $t_m = 200ms$, $G = 0.64T/m$

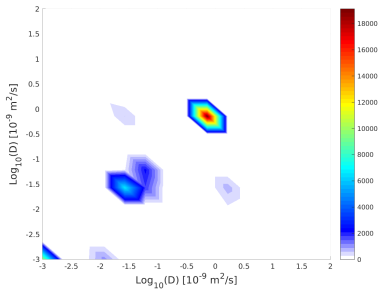

Figure 10.236: Diffusion exchange plot 18g Yeast : 10 ml PBS $\delta = 15ms$, $\Delta = 17ms$, $t_m = 200ms$, $G = 0.64T/m$ scan 1

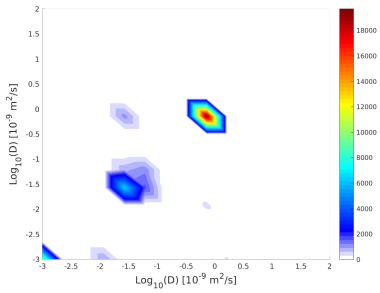

Figure 10.237: Diffusion exchange plot 18g Yeast : 10 ml PBS $\delta = 15ms$, $\Delta = 17ms$, $t_m = 200ms$, $G = 0.64T/m$ scan 2

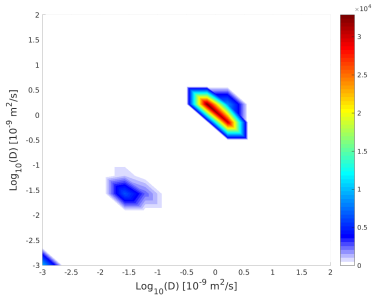

Figure 10.238: Diffusion exchange plot 18g Yeast : 10 ml PBS $\delta = 15ms$, $\Delta = 17ms$, $t_m = 200ms$, $G = 0.64T/m$ scan 3

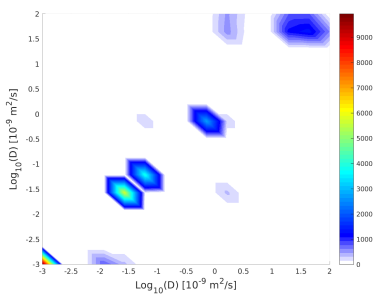

Figure 10.239: Diffusion exchange plot 24g Yeast : 10 ml PBS $\delta = 15ms$, $\Delta = 17ms$, $t_m = 200ms$, $G = 0.64T/m$ scan 1

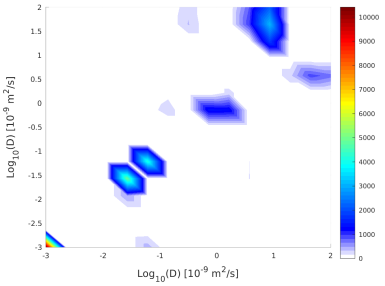

Figure 10.240: Diffusion exchange plot 24g Yeast : 10 ml PBS $\delta = 15ms$, $\Delta = 17ms$, $t_m = 200ms$, $G = 0.64T/m$ scan 2

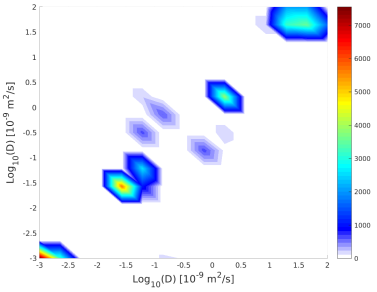

Figure 10.241: Diffusion exchange plot 24g Yeast : 10 ml PBS $\delta = 15ms$, $\Delta = 17ms$, $t_m = 200ms$, $G = 0.64T/m$ scan 3

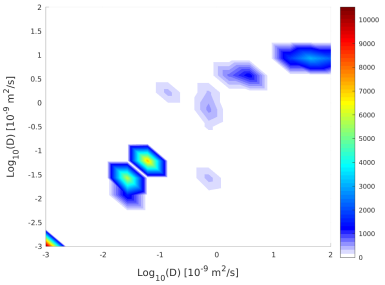

Figure 10.242: Diffusion exchange plot 36g Yeast : 10 ml PBS $\delta = 15ms$, $\Delta = 17ms$, $t_m = 200ms$, $G = 0.64T/m$ scan 1

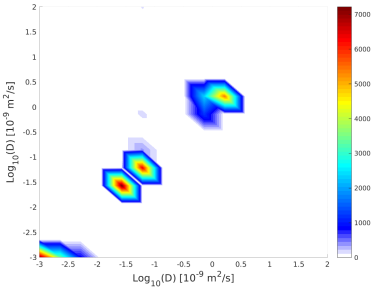

Figure 10.243: Diffusion exchange plot 36g Yeast : 10 ml PBS $\delta = 15ms$, $\Delta = 17ms$, $t_m = 200ms$, $G = 0.64T/m$ scan 2

10.3.3 In-vitro yeast permeability experiment DEXSY data

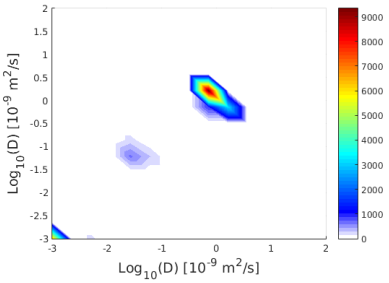

Figure 10.244: Diffusion exchange plot yeast 30g : 15 ml PBS 2ml 10 % tween : 13 ml yeast suspension $\delta = 15ms$, $\Delta = 17ms$, $t_m = 200ms$, $G = 0.8T/m$

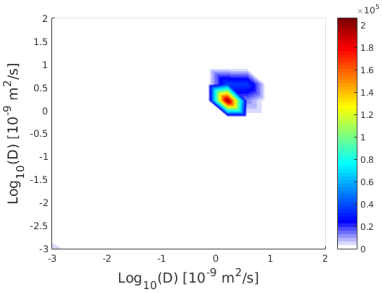

Figure 10.245: Diffusion exchange plot yeast 30g : 15 ml PBS 2ml 1 % tween : 13 ml yeast suspension $\delta = 15ms$, $\Delta = 17ms$, $t_m = 200ms$, $G = 0.8T/m$

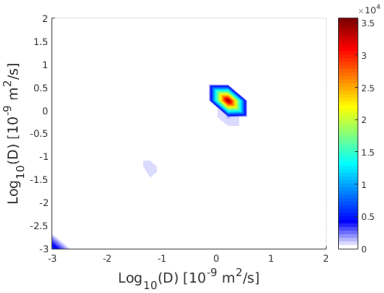

Figure 10.246: Diffusion exchange plot yeast 30g : 15 ml PBS 2ml 0.1 % tween : 13 ml yeast suspension $\delta = 15ms$, $\Delta = 17ms$, $t_m = 200ms$, $G = 0.8T/m$

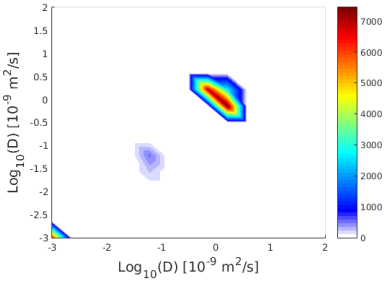

Figure 10.247: Diffusion exchange plot yeast 30g : 15 ml PBS 2ml 0.01 % tween : 13 ml yeast suspension $\delta = 15ms$, $\Delta = 17ms$, $t_m = 200ms$, $G = 0.8T/m$

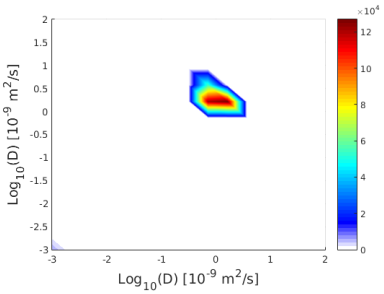

Figure 10.248: Diffusion exchange plot yeast 30g : 15 ml PBS 2ml 2ml water : 13 ml yeast suspension $\delta = 15ms$, $\Delta = 17ms$, $t_m = 200ms$, $G = 0.8T/m$ scan 1

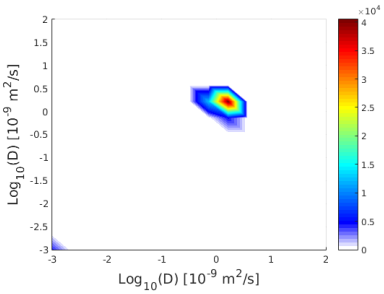

Figure 10.249: Diffusion exchange plot yeast 30g : 15 ml PBS 2ml 2ml water : 13 ml yeast suspension $\delta = 15ms$, $\Delta = 17ms$, $t_m = 200ms$, $G = 0.8T/m$ scan 2

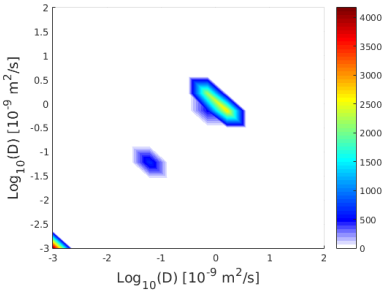

Figure 10.250: Diffusion exchange plot Yeast 30g : 15 ml PBS 2ml 0.01 % tween : 13 ml yeast suspension $\delta = 15ms$, $\Delta = 17ms$, $t_m = 200ms$, $G = 0.8T/m$

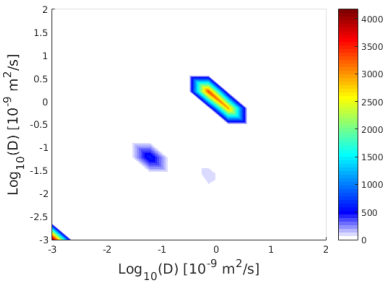

Figure 10.251: Diffusion exchange plot Yeast 30g : 15 ml PBS 15 ml yeast suspension $\delta = 15ms$, $\Delta = 17ms$, $t_m = 200ms$, $G = 0.8T/m$

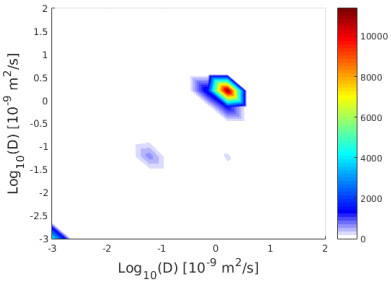

Figure 10.252: Diffusion exchange plot Yeast 30g : 15 ml PBS 15 ml yeast suspension $\delta = 15ms$, $\Delta = 17ms$, $t_m = 200ms$, $G = 0.8T/m$

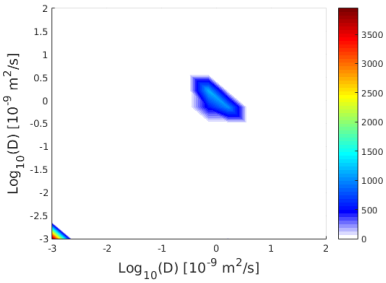

Figure 10.253: Diffusion exchange plot Yeast 30g : 15 ml PBS 15 ml yeast suspension $\delta = 9ms$, $\Delta = 14ms$, $t_m = 200ms$, $G = 0.8T/m$ scan 1

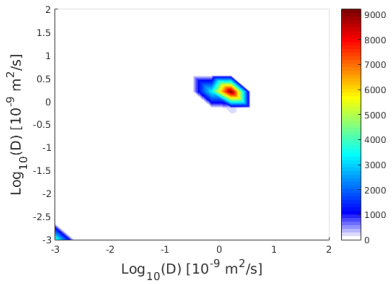

Figure 10.254: Diffusion exchange plot Yeast 30g : 15 ml PBS 15 ml yeast suspension $\delta = 9ms$, $\Delta = 14ms$, $t_m = 200ms$, $G = 0.8T/m$ scan 2

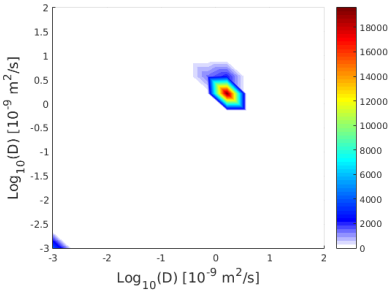

Figure 10.255: Diffusion exchange plot Yeast 30g : 15 ml PBS 15 ml yeast suspension $\delta = 9ms$, $\Delta = 14ms$, $t_m = 200ms$, $G = 0.8T/m$ scan 3

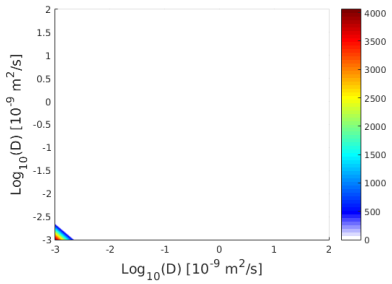

Figure 10.256: Diffusion exchange plot Yeast 22g : 7 ml PBS 15 ml yeast suspension $\delta = 15ms$, $\Delta = 17ms$, $t_m = 200ms$, $G = 0.8T/m$ scan 1

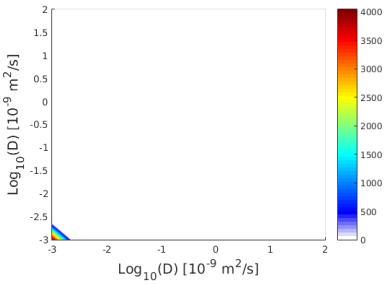

Figure 10.257: Diffusion exchange plot Yeast 22g : 7 ml PBS 15 ml yeast suspension $\delta = 15ms$, $\Delta = 17ms$, $t_m = 200ms$, $G = 0.8T/m$ scan 2

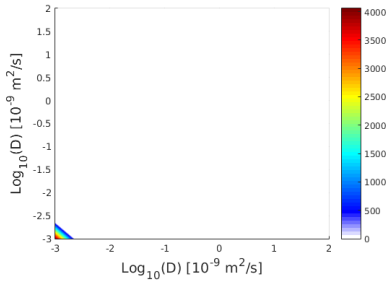

Figure 10.258: Diffusion exchange plot Yeast 22g : 7 ml PBS 15 ml yeast suspension $\delta = 15ms$, $\Delta = 17ms$, $t_m = 200ms$, $G = 0.8T/m$ scan 3

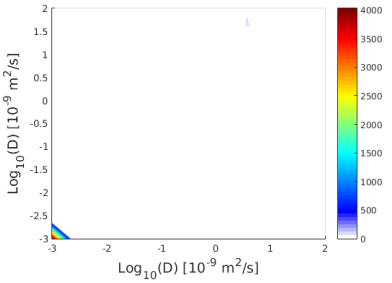

Figure 10.259: Diffusion exchange plot Yeast 22g : 7.5 ml PBS 15 ml yeast suspension $\delta = 15ms$, $\Delta = 17ms$, $t_m = 200ms$, $G = 0.8T/m$ scan 1

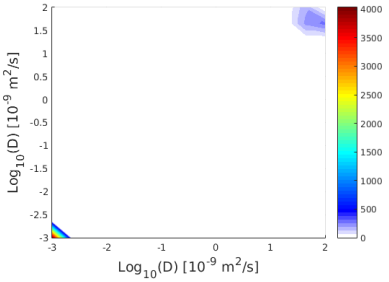

Figure 10.260: Diffusion exchange plot Yeast 22g : 7.5 ml PBS 15 ml yeast suspension $\delta = 15ms$, $\Delta = 17ms$, $t_m = 200ms$, $G = 0.8T/m$ scan 2

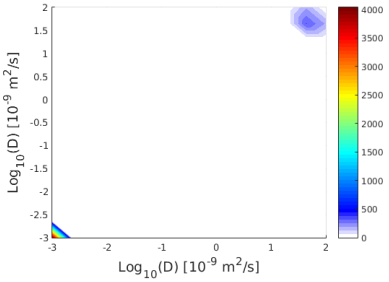

Figure 10.261: Diffusion exchange plot Yeast 22g : 7.5 ml PBS 15 ml yeast suspension $\delta = 15ms$, $\Delta = 17ms$, $t_m = 200ms$, $G = 0.8T/m$ scan 3

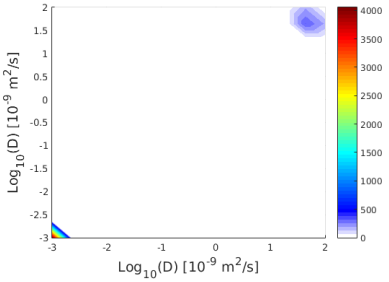

Figure 10.262: Diffusion exchange plot Yeast 30 g : 15 ml PBS 15 ml yeast suspension $\delta = 15ms$, $\Delta = 17ms$, $t_m = 200ms$, $G = 0.8T/m$ scan 1

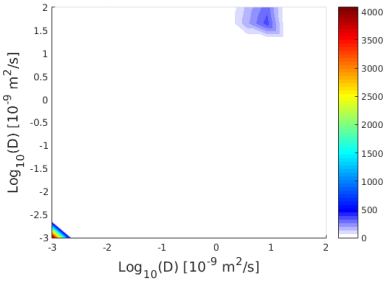

Figure 10.263: Diffusion exchange plot Yeast 30 g : 15 ml PBS 15 ml yeast suspension $\delta = 15ms$, $\Delta = 17ms$, $t_m = 200ms$, $G = 0.8T/m$ scan 2

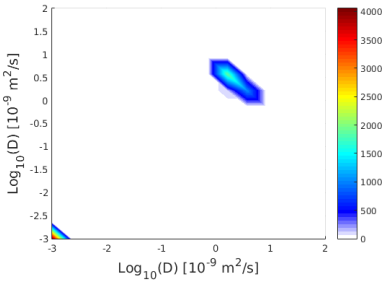

Figure 10.264: Diffusion exchange plot Yeast 30 g : 15 ml PBS 15 ml yeast suspension $\delta = 15ms$, $\Delta = 17ms$, $t_m = 200ms$, $G = 0.8T/m$ scan 3

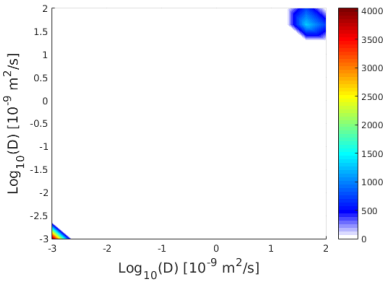

Figure 10.265: Diffusion exchange plot Yeast 22 g : 10 ml PBS 15 ml yeast suspension $\delta = 15ms$, $\Delta = 17ms$, $t_m = 200ms$, $G = 0.72T/m$ scan 1

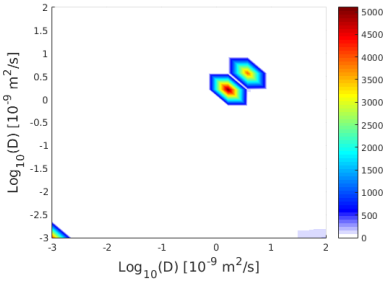

Figure 10.266: Diffusion exchange plot Yeast 22 g : 10 ml PBS 15 ml yeast suspension $\delta = 15ms$, $\Delta = 17ms$, $t_m = 200ms$, $G = 0.72T/m$ scan 2

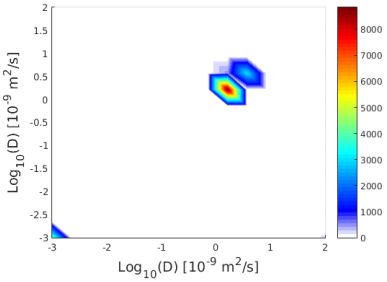

Figure 10.267: Diffusion exchange plot Yeast 22 g : 10 ml PBS 15 ml yeast suspension $\delta = 15ms$, $\Delta = 17ms$, $t_m = 200ms$, $G = 0.72T/m$ scan 3

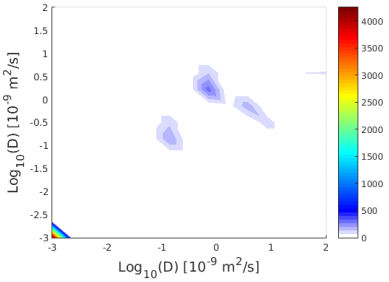

Figure 10.268: Diffusion exchange plot Yeast 22 g : 10 ml PBS 15 ml yeast suspension $\delta = 15ms$, $\Delta = 17ms$, $t_m = 200ms$, $G = 0.72T/m$ scan 1

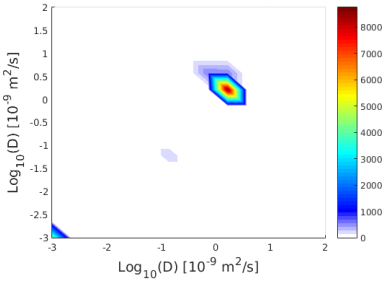

Figure 10.269: Diffusion exchange plot Yeast 22 g : 10 ml PBS 15 ml yeast suspension $\delta = 15ms$, $\Delta = 17ms$, $t_m = 200ms$, $G = 0.72T/m$ scan 2

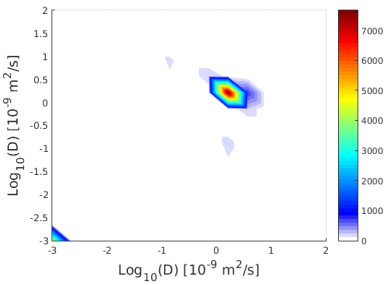

Figure 10.270: Diffusion exchange plot Yeast 22 g : 10 ml PBS 15 ml yeast suspension $\delta = 15ms$, $\Delta = 17ms$, $t_m = 200ms$, $G = 0.72T/m$ scan 3

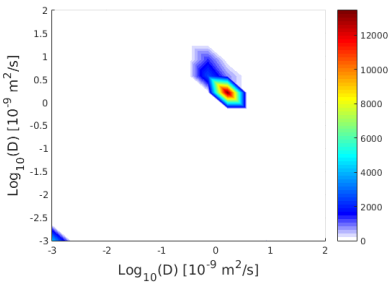

Figure 10.271: Diffusion exchange plot Yeast 22 g : 10 ml PBS 15 ml yeast suspension $\delta = 15ms$, $\Delta = 17ms$, $t_m = 200ms$, $G = 0.72T/m$

10.4 In-vivo positioning scans

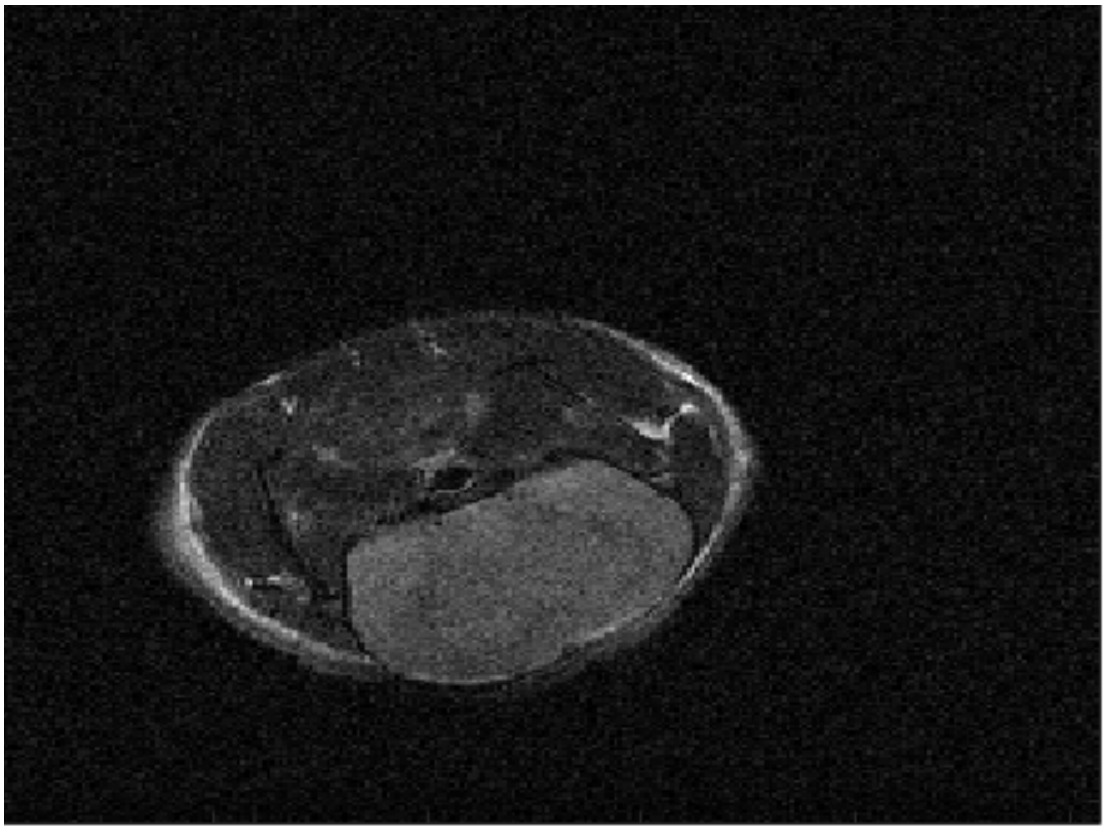

Figure 10.272: Slice of a mouse brain scanned in 8.1

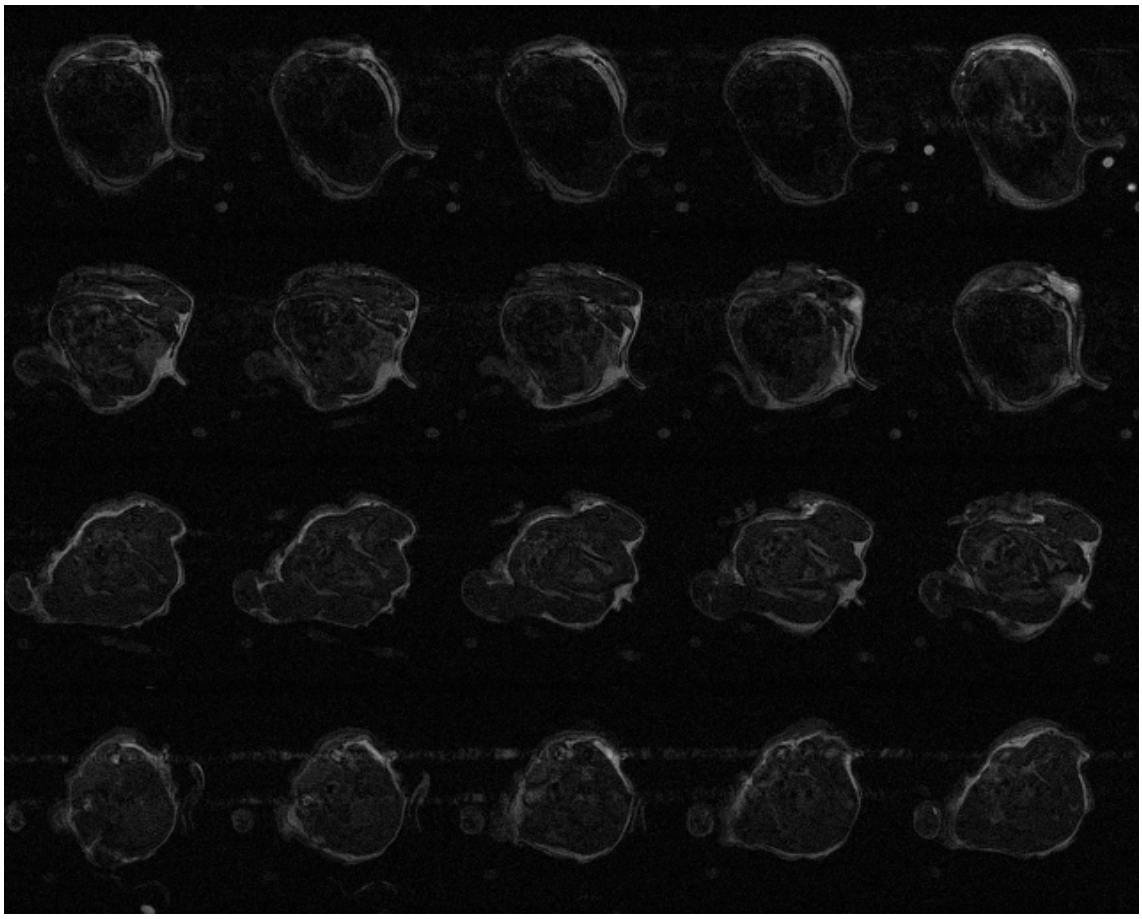

Figure 10.273: Scan taken to position the slice used to acquire a DEXSY scan acquired from a subcutaneous tumour in mouse 1, scanned 15/10/2018

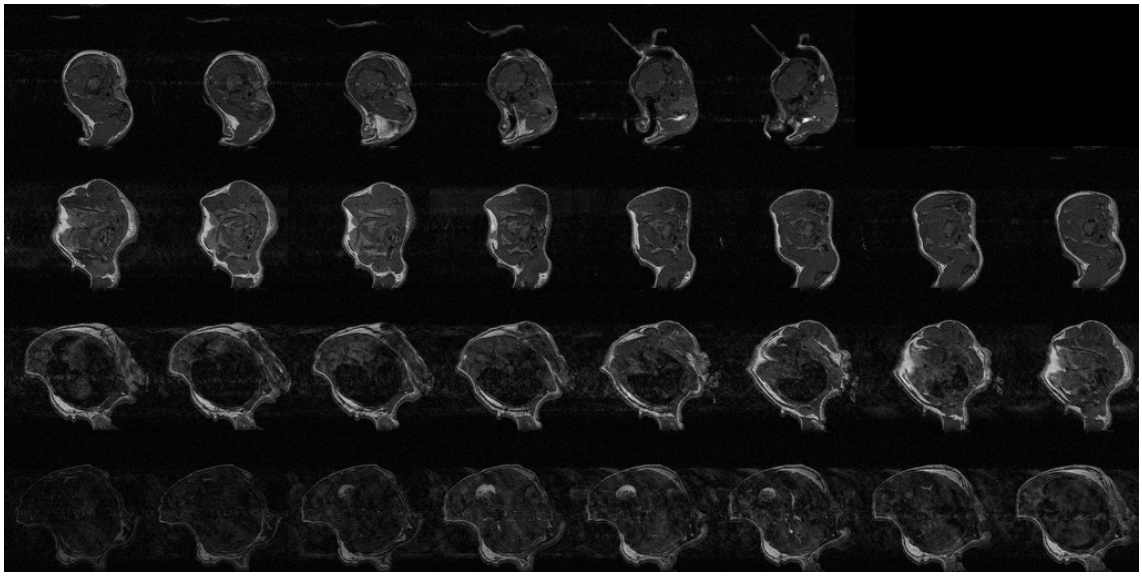

Figure 10.274: Scan taken to position the slice used to acquire a DEXSY scan acquired from a subcutaneous tumour in mouse 2, scanned 15/10/2018

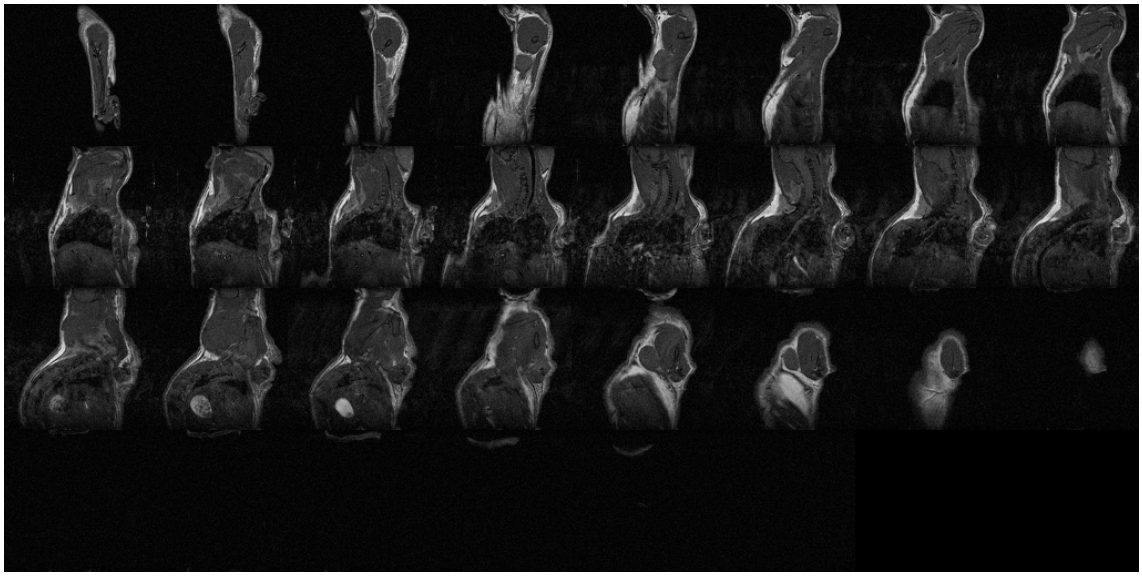

Figure 10.275: Scan taken to position the slice used to acquire a DEXSY scan acquired from a subcutaneous tumour in mouse 2, scanned 15/10/2018

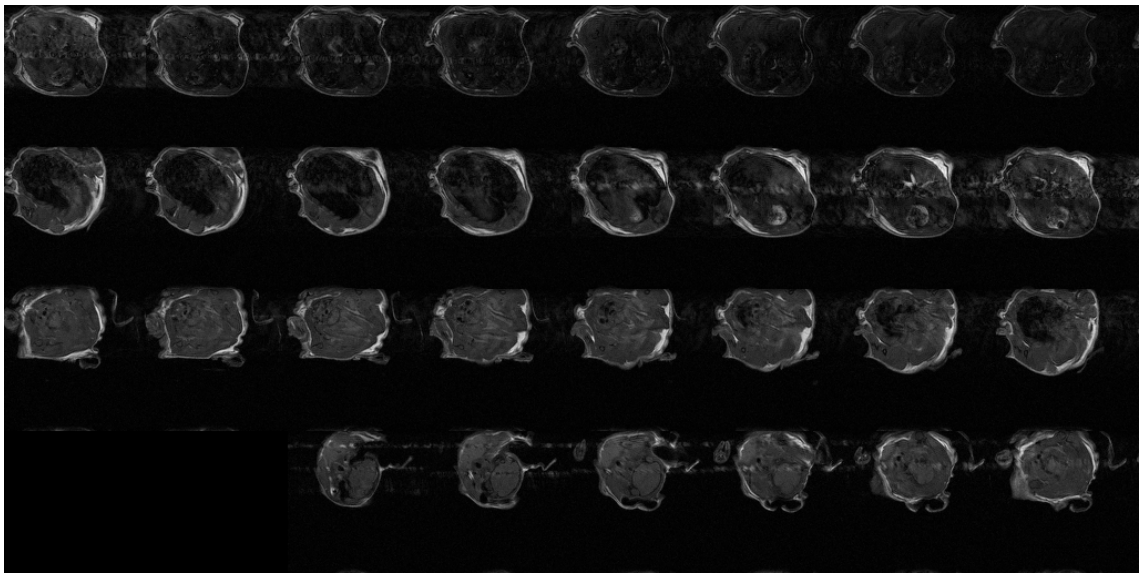

Figure 10.276: Scan taken to position the slice used to acquire a DEXSY scan acquired from a subcutaneous tumour in mouse 3, scanned 16/10/2018

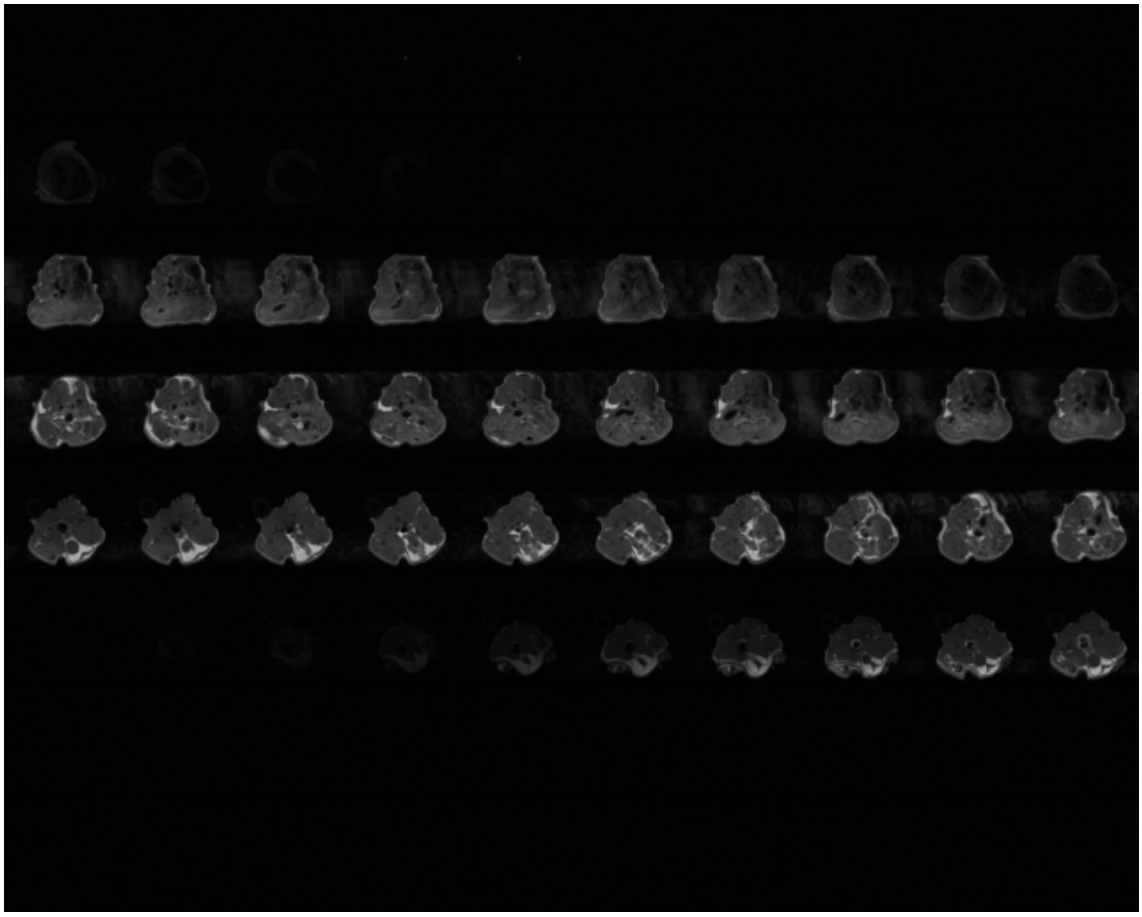

Figure 10.277: Scan taken to position the slice used to acquire a DEXSY scan acquired from a subcutaneous tumour in mouse 4, scanned 19/10/2018

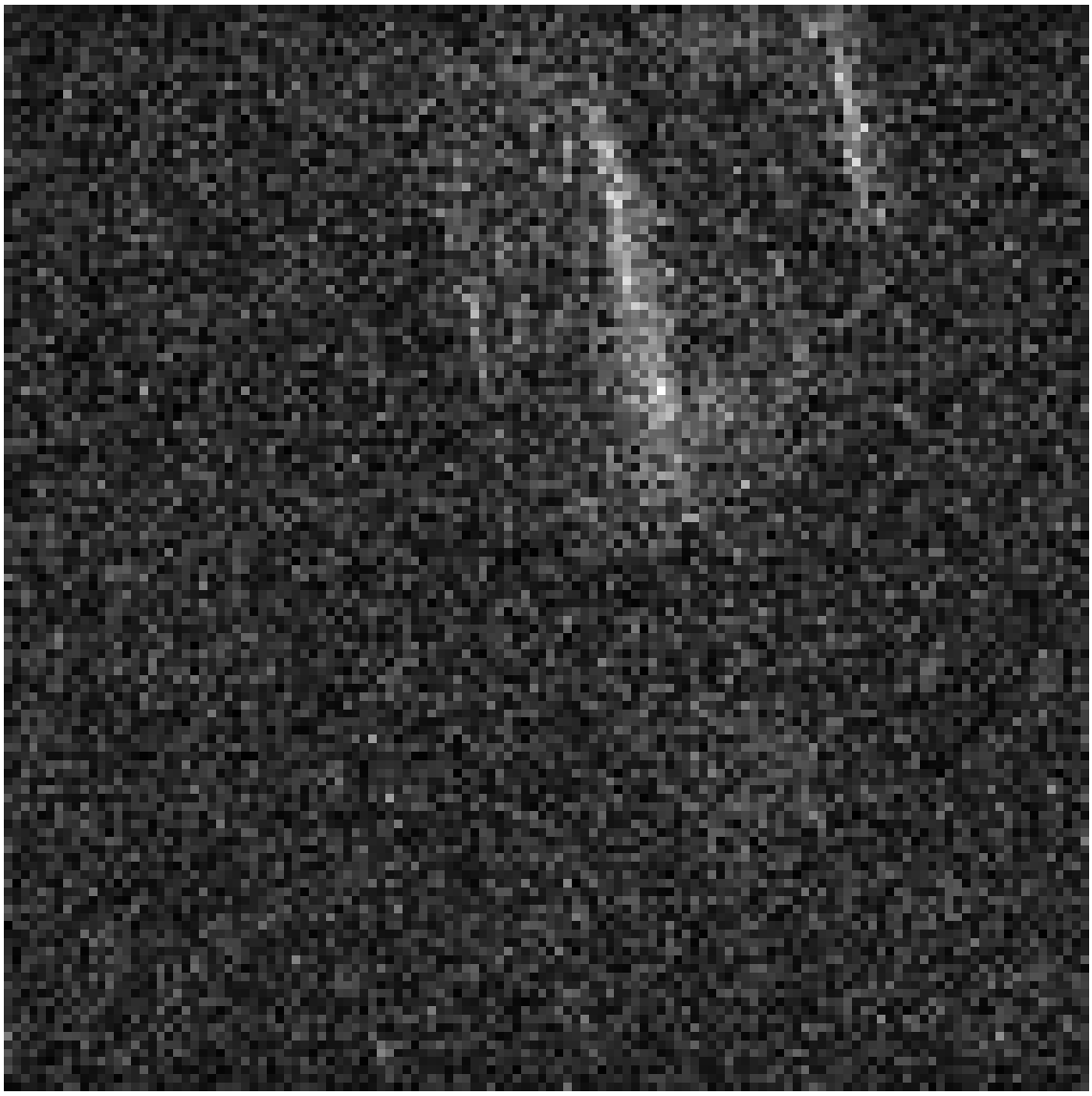

Figure 10.278: Scan taken to position the slice used to acquire a DEXSY scan acquired from a subcutaneous tumour in mouse 4, scanned 19/10/2018

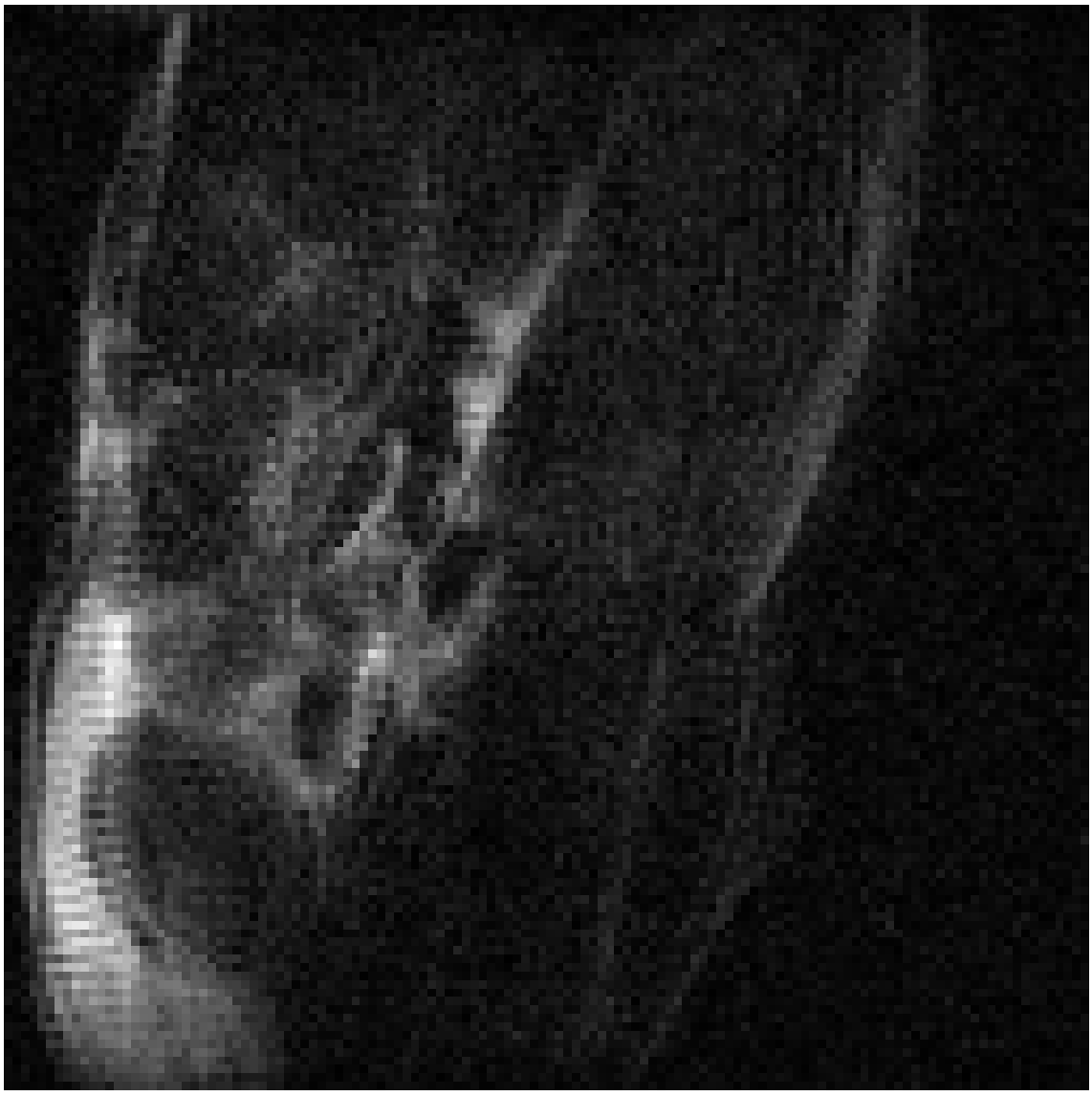

Figure 10.279: Scan taken to position the slice used to acquire a DEXSY scan acquired from a subcutaneous tumour in mouse 4, scanned 19/10/2018

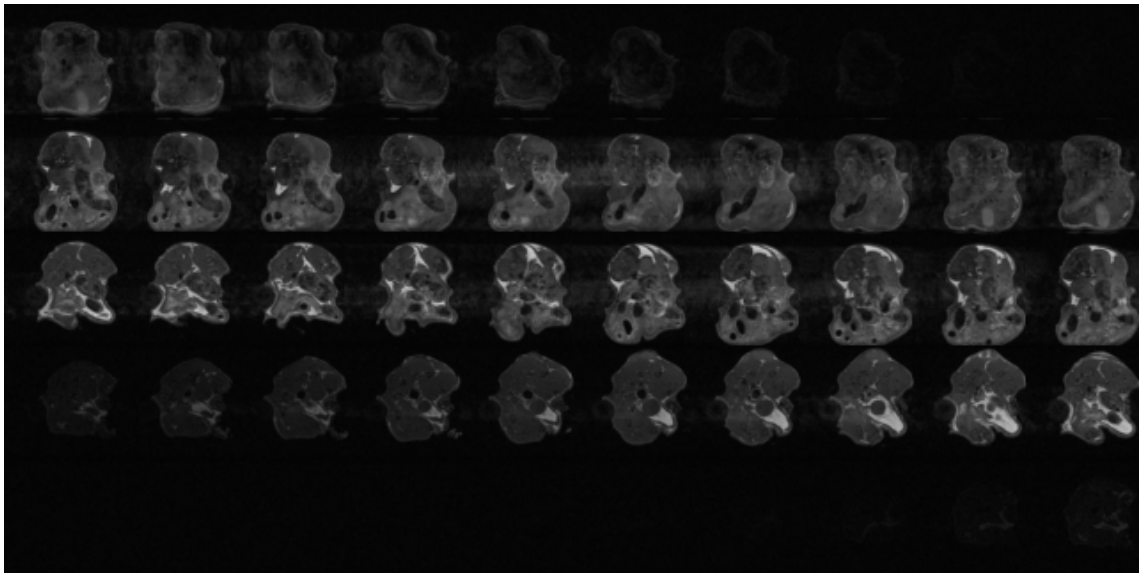

Figure 10.280: Scan taken to position the slice used to acquire a DEXSY scan acquired from a subcutaneous tumour in mouse 5, scanned 19/10/2018

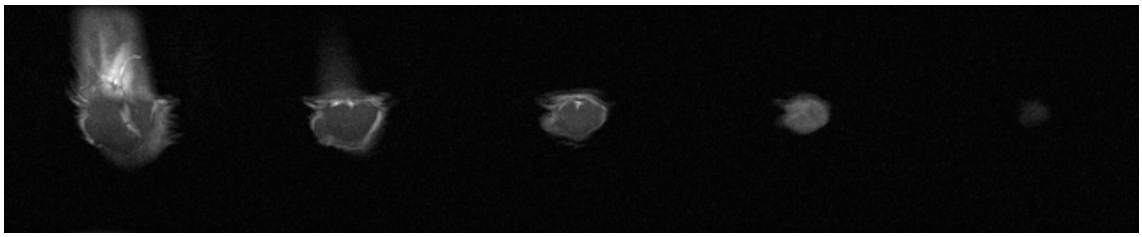

Figure 10.281: Scan taken to position the slice used to acquire a DEXSY scan acquired from a subcutaneous tumour in mouse 5, scanned 19/10/2018

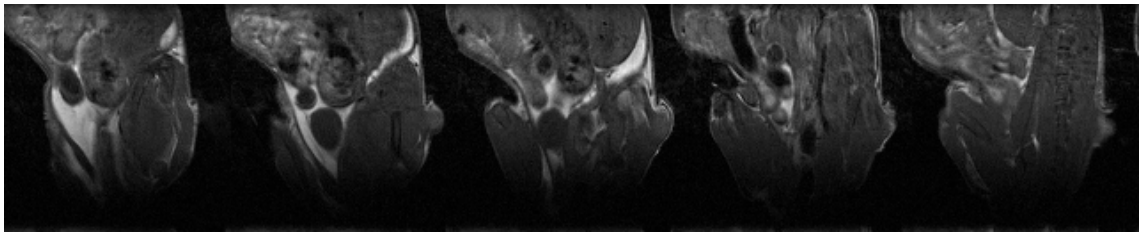

Figure 10.282: Scan taken to position the slice used to acquire a DEXSY scan acquired from a subcutaneous tumour in mouse 5, scanned 19/10/2018

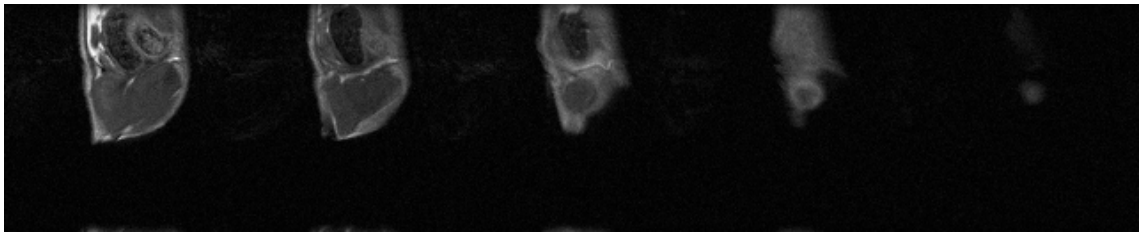

Figure 10.283: Scan taken to position the slice used to acquire a DEXSY scan acquired from a subcutaneous tumour in mouse 5, scanned 29/10/2018

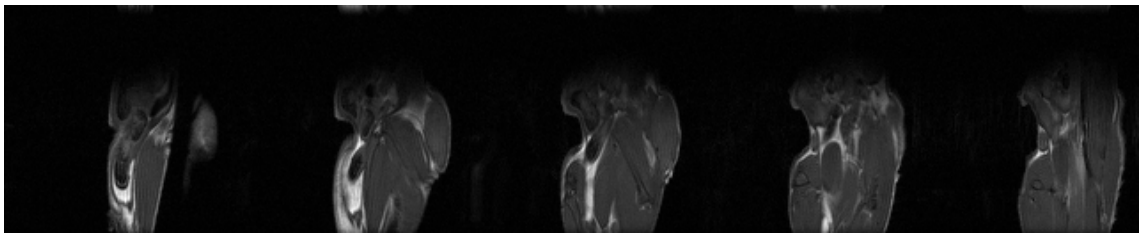

Figure 10.284: Scan taken to position the slice used to acquire a DEXSY scan acquired from a subcutaneous tumour in mouse 5, scanned 29/10/2018

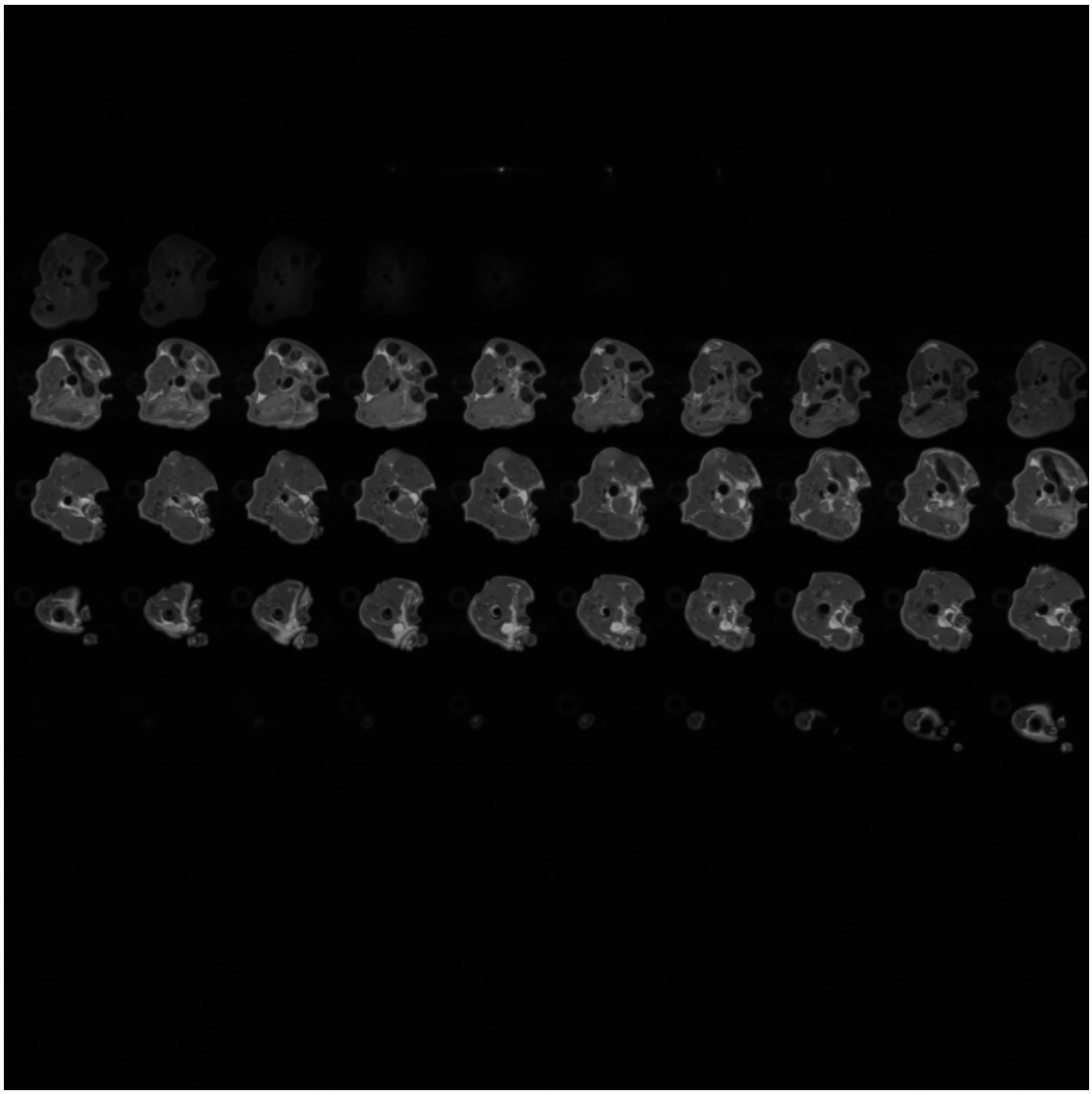

Figure 10.285: Scan taken to position the slice used to acquire a DEXSY scan acquired from a subcutaneous tumour in mouse 5, scanned 29/10/2018

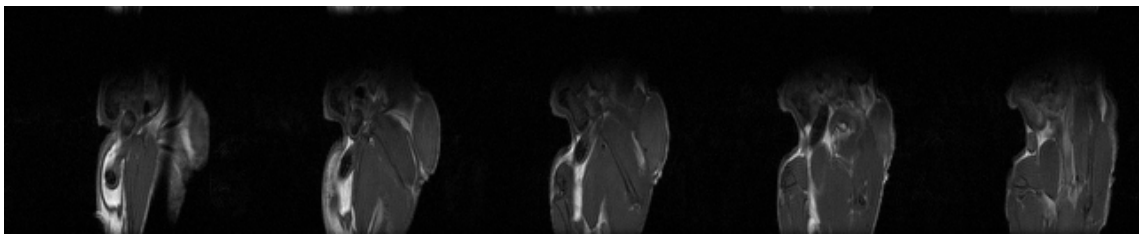

Figure 10.286: Scan taken to position the slice used to acquire a DEXSY scan acquired from a subcutaneous tumour in mouse 3, scanned 29/10/2018

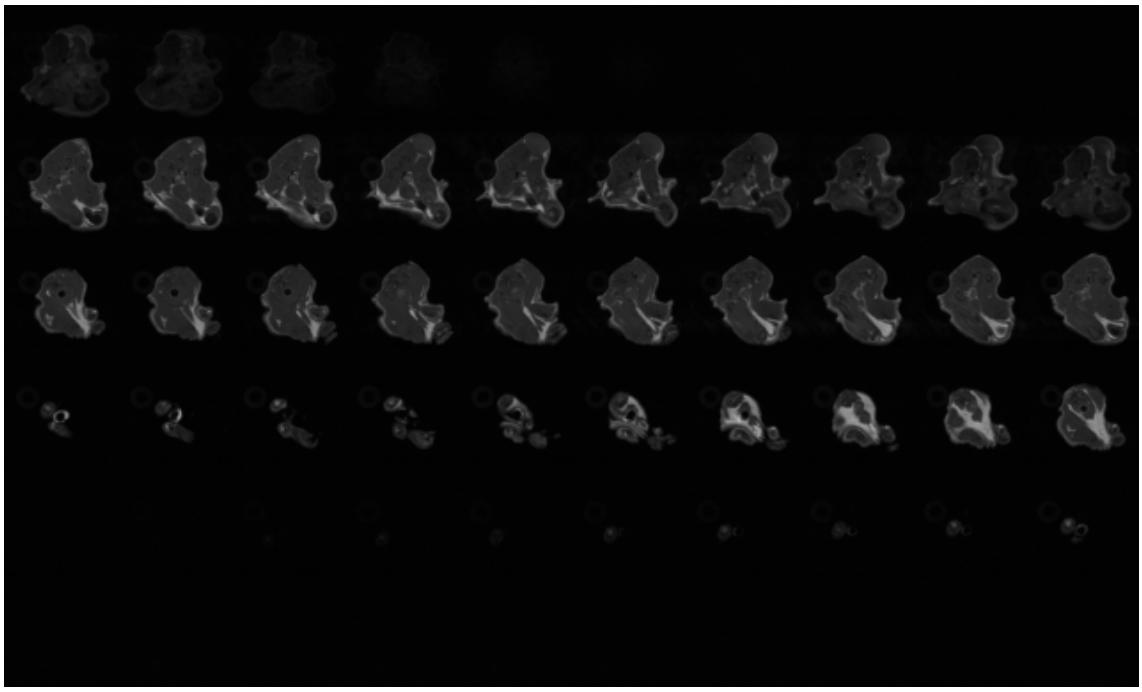

Figure 10.287: Scan taken to position the slice used to acquire a DEXSY scan acquired from a subcutaneous tumour in mouse 3, scanned 29/10/2018

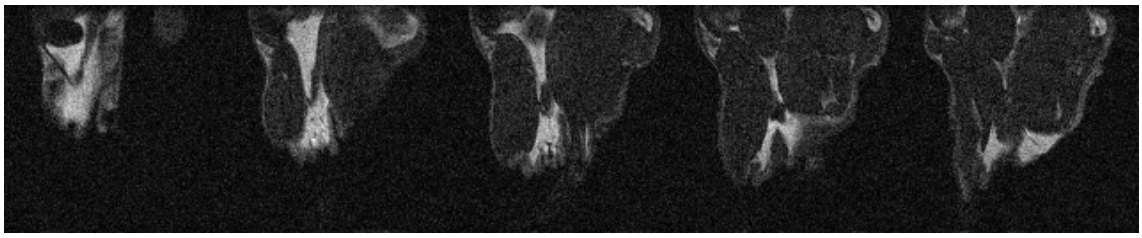

Figure 10.288: Scan taken to position the slice used to acquire a DEXSY scan acquired from a subcutaneous tumour in in mouse 1, scanned 29/10/2018

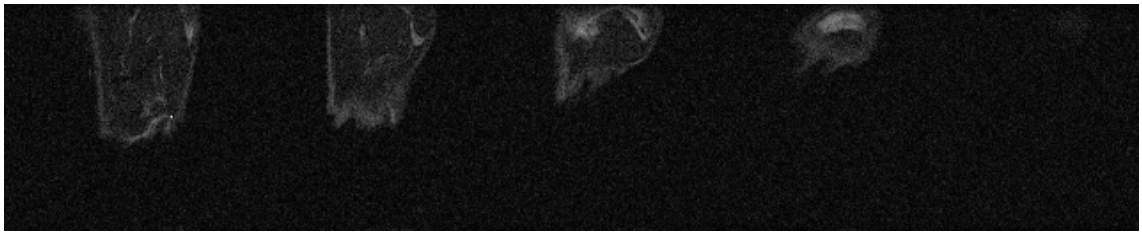

Figure 10.289: Scan taken to position the slice used to acquire a DEXSY scan acquired from a subcutaneous tumour in in mouse 1, scanned 29/10/2018

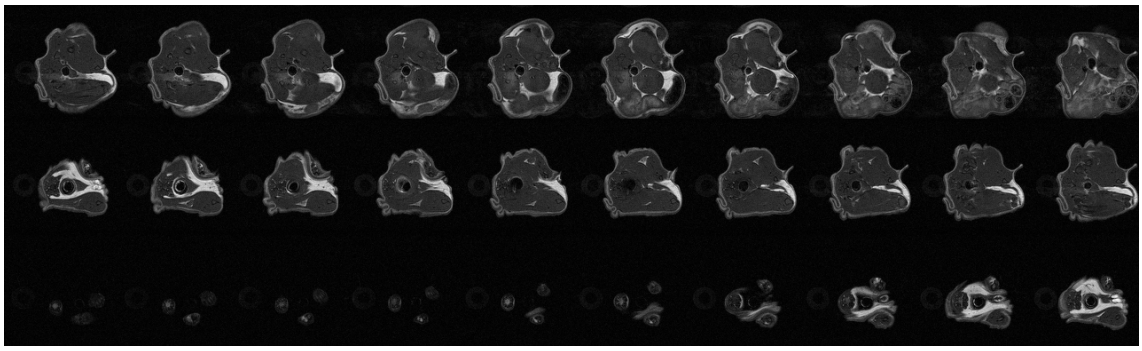

Figure 10.290: Scan taken to position the slice used to acquire a DEXSY scan acquired from a subcutaneous tumour in in mouse 1, scanned 29/10/2018

Bibliography

[1] A. Afaq, D.-M. Koh, A. Padhani, N. van As, and S. A. Sohaib. Clinical utility of diffusion-weighted magnetic resonance imaging in prostate cancer. *BJU International*, 108(11):1716–1722, 2011.

[2] M. Aggarwal, M. V. Jones, P. A. Calabresi, S. Mori, and J. Zhang. Probing mouse brain microstructure using oscillating gradient diffusion MRI. *Magnetic Resonance in Medicine*, 67(1):98–109, 2012.

[3] B. Alberts. *Molecular Biology of the Cell*. 2008.

[4] D. C. Alexander, P. L. Hubbard, M. G. Hall, E. A. Moore, M. Ptito, G. J. Parker, and T. B. Dyrby. Orientationally invariant indices of axon diameter and density from diffusion MRI. *NeuroImage*, 52(4):1374–1389, 2010.

[5] A. W. Anderson, J. Xie, J. Pizzonia, R. A. Bronen, D. D. Spencer, and J. C. Gore. Effects of cell volume fraction changes on apparent diffusion in human cells. *Magnetic Resonance Imaging*, 18(6):689–695, 2000.

[6] I. Åslund, S. Lasič, A. Nowacka, M. Nilsson, and D. Topgaard. Measuring Molecular Exchange for Water in a Yeast Cell Suspension through NMR Diffusometry. *diffusion-fundementals.org*, 11(69):1–2, 2009.

[7] A. I. Baba. Apoptosis and Necrosis. *LUCRRI TIINłIFICE MEDICIN VETERINAR VOL.*, XLII(2):3–5, 2009.

[8] A. Bardelli, S. Saha, J. A. Sager, K. E. Romans, B. Xin, S. D. Markowitz, C. Lengauer, V. E. Velculescu, K. W. Kinzler, and B. Vogelstein. PRL-3

Expression in Metastatic Cancers. *Clinical Cancer Research*, 9(15):5607–5615, 2003.

[9] P. J. Basser. Inferring Microstructural Features and the Physiological State of Tissues from Diffusion-Weighted Images. *NMR in Biomedicine*, Vol. 8:333–344, 1995.

[10] D. Benjamini and P. J. Basser. Use of marginal distributions constrained optimization (MADCO) for accelerated 2D MRI relaxometry and diffusometry. *Journal of Magnetic Resonance*, 271:40–45, 2016.

[11] D. Benjamini, M. E. Komlosh, and P. J. Basser. Imaging Local Diffusive Dynamics Using Diffusion Exchange Spectroscopy MRI. *Physical Review Letters*, 118(15):27–31, 2017.

[12] S. J. Blackband, D. L. Buckley, J. D. Bui, and M. I. Phillips. NMR microscopy–beginnings and new directions. *Magnetic Resonance Materials in Physics, Biology and Medicine*, 9(3):112–116, 1999.

[13] F. Bloch, W. W. Hansen, and M. Packard. Nuclear Induction. *Physical Review*, 70(1938):474–485, 1946.

[14] K. Brindle. New approaches for imaging tumour responses to treatment. *Nature Reviews Cancer*, 8(2):94–107, 2008.

[15] B. H. Brown. *Biological and Medical Physics , Biomedical Engineering Biological and Medical Physics , Biomedical Engineering*. 1999.

[16] R. W. Brown, Y. C. N. Cheng, E. M. Haacke, M. R. Thompson, and R. Venkatesan. *Magnetic Resonance Imaging: Physical Principles and Sequence Design: Second Edition*. 2014.

[17] P. T. Callaghan and I. Furó. Diffusion-diffusion correlation and exchange as a signature for local order and dynamics. *Journal of Chemical Physics*, 120(8):4032–4038, 2004.

[18] P. T. Callaghan, S. Godefroy, and B. N. Ryland. Use of the second dimension in PGSE NMR studies of porous media. *Magnetic Resonance Imaging*, 21(3-4):243–248, 2003.

[19] P. T. Callaghan and A. A. Khrapitchev. Time-dependent velocities in porous media dispersive flow. *Magnetic Resonance Imaging*, 19(3-4):301–305, 2001.

[20] H. Y. Carr and E. M. Purcell. Effects of Diffusion on Free Precession in Nuclear Magnetic Resonance Experiments. *Physical Review*, 94(3), 1954.

[21] R. Cell and C. Kit. RAFT 3D Cell Culture Kit Protocol.

[22] T. L. Chenevert, P. E. McKeever, and B. D. Ross. Monitoring early response of experimental brain tumors to therapy using diffusion magnetic resonance imaging. *Clinical cancer research*, 3:1457–1466, 1997.

[23] P. A. Cook, Y. Bai, G. L. Nedjati-gilani, K. Seunarine, K, M. G. Hall, G. J. Parker, and D. C. Alexander. Camino: Open-Source Diffusion-MRI Reconstruction and Processing. *Procedings of ISMRM 2006*, page 2759, 2006.

[24] A. Doskaliyev, F. Yamasaki, M. Ohtaki, Y. Kajiwara, Y. Takeshima, Y. Watanabe, T. Takayasu, V. J. Amatya, Y. Akiyama, K. Sugiyama, and K. Kurisu. Lymphomas and glioblastomas: Differences in the apparent diffusion coefficient evaluated with high b-value diffusion-weighted magnetic resonance imaging at 3 T. *European Journal of Radiology*, 81(2):339–344, 2012.

[25] W. A. Edelstein, J. M. S. Hutchison, G. Johnson, and T. Redpath. Spin warp NMR imaging and applications to human whole-body imaging. *Physics in Medicine and Biology*, 25(4):751–756, 1980.

[26] A. Einstein. On the Motion of Small Particles Suspended in Liquids at Rest Required by the Molecular-Kinetic Theory of Heat. *Annalen der Physik*, 17:549–560, 1905.

[27] B. M. Ellingson, M. G. Malkin, S. D. Rand, J. M. Connelly, C. Quinsey, P. S. LaViolette, D. P. Bedekar, and K. M. Schmainda. Validation of functional diffusion maps (fDMs) as a biomarker for human glioma cellularity. *Journal of Magnetic Resonance Imaging*, 31(3):538–548, 2010.

[28] S. Elmore. Apoptosis: a review of programmed cell death. *Toxicologic pathology*, 35(4):495–516, 2007.

[29] L. Fass. Imaging and cancer: A review. *Molecular Oncology*, 2(2):115–152, 2008.

[30] A. Fernández-Medarde and E. Santos. Ras in cancer and developmental diseases. *Genes and Cancer*, 2(3):344–358, 2011.

[31] I. J. Fidler. The pathogenesis of cancer metastasis: The 'seed and soil' hypothesis revisited. *Nature Reviews Cancer*, 3(6):453–458, 2003.

[32] H. Fischer, R. Stenling, C. Rubio, and A. Lindblom. Differential expression of aquaporin 8 in human colonic epithelial cells and colorectal tumors. *BMC Phsiology*, 1:1, 2001.

[33] P. Galvosas, Y. Qiao, M. Schönhoff, and P. T. Callaghan. On the use of 2D correlation and exchange NMR spectroscopy in organic porous materials. *Magnetic Resonance Imaging*, 2007.

[34] K. M. Gauvain, R. C. McKinstry, P. Mukherjee, a. Perry, J. J. Neil, B. a. Kaufman, and R. J. Hayashi. Evaluating pediatric brain tumor cellularity with diffusion-tensor imaging. *American Journal of Roentgenology*, 177(2):449–454, 2001.

[35] D. M. Gilkes, G. L. Semenza, and D. Wirtz. Hypoxia and the extracellular matrix: drivers of tumour metastasis. *Nature reviews. Cancer*, 14(6):430–9, 2014.

[36] S. Godefroy, B. Ryland, and P. T. Callaghan. *2d laplace inversion instruction manual*. Wellington, New Zealand, 2003.

[37] M. Gratz and P. Galvosas. Investigation of molecular exchange using DEXSY with ultra-high pulsed field gradients. *AIP Conference Proceedings*, 1081:91–94, 2008.

[38] E. M. Haacke, Y. Xu, Y. C. N. Cheng, and J. R. Reichenbach. Susceptibility weighted imaging (SWI). *Magnetic Resonance in Medicine*, 52(3):612–618, 2004.

[39] E. L. Hahn. Spin Echoes. *Physical Review*, 80, 1950.

[40] M. G. Hall. Convergence and parameter choice for monte carlo simulations of diffusion MRI data. 28(9):1354–1364, 2009.

[41] D. Hanahan and R. A. Weinberg. Hallmarks of cancer: the next generation. *Cell*, 144(5):646–74, 2011.

[42] K. D. Harkins and M. D. Does. Simulations on the influence of myelin water in diffusion-weighted imaging. *Physics in Medicine and Biology*, 61(13):4729–4745, 2016.

[43] W. K. Hasting. Monte Carlo sampling methods using Markov chains and their applications. *Biometrica*, 57(1):97, 1970.

[44] J. Hillengass, T. Bäuerle, R. Bartl, M. Andrulis, F. Mcclanahan, F. B. Laun, C. M. Zechmann, R. Shah, B. Wagner-Gund, D. Simon, C. Heiss, K. Neben, A. D. Ho, H. P. Schlemmer, H. Goldschmidt, S. Delorme, and B. Stieltjes. Diffusion-weighted imaging for non-invasive and quantitative monitoring of bone marrow infiltration in patients with monoclonal plasma cell disease: A comparative study with histology. *British Journal of Haematology*, 153(6):721–728, 2011.

[45] T. Hirai, S. Morishita, M. Kitajima, R. Murakami, Y. Korogi, K. Makino, H. Nakamura, I. Ikushima, M. Yamura, M. Kochi, and J. Kuratsu. Diffusion-weighted Imaging of Metastatic Brain Tumors : Comparison with Histologic Type and. *American Journal of Neuroradiology*, 27:1419–25, 2006.

[46] B. Jordan, T. Roberts, A. D. Esposito, J. Connell, A. Ianus, and E. Panagiotaki. Non-Invasively Assessing the Microstructural Changes in Tissue Post-Fixation using VERDICT MRI . In *Procedings of ISMRM 2016*, 2016.

[47] S. K. Kang, Y. K. Chae, J. Woo, M. S. Kim, J. C. Park, J. Lee, J. C. Soria, S. J. Jang, D. Sidransky, and C. Moon. Role of Human Aquaporin 5 In Colorectal Carcinogenesis. *The American Journal of Pathology*, 173(2):518–525, 2008.

[48] J. Kärger. NMR self-diffusion studies in heterogeneous systems. *Advances in Colloid and Interface Science*, 23:129–148, 1985.

[49] D. J. Klionsky, P. K. Herman, and S. D. Emr. The Fungal Vacuole: Composition, Function, and Biogenesis. 54(3):266–292, 1990.

[50] S. Lasič, M. Nilsson, J. Lätt, F. Ståhlberg, and D. Topgaard. Apparent exchange rate mapping with diffusion MRI. *Magnetic Resonance in Medicine*, 66(2):356–365, 2011.

[51] S. Lasič, S. Oredsson, S. C. Partridge, L. H. Saal, D. Topgaard, M. Nilsson, and K. Bryskhe. Apparent exchange rate for breast cancer characterization. *NMR in Biomedicine*, 2016.

[52] P. C. Lauterbur. Image Formation by Induced Local Interactions: Examples Employing Nuclear Magnetic Resonance. *Nature*, 242:117–118, 1973.

[53] D. Le Bihan. Seperation of Diffusion and Perfusion in Intravoxel Incoherant Motion MRI Imaging. *Radiology*, 168(2):566–567, 1988.

[54] D. Le Bihan. Molecular diffusion, tissue microdynamics and microstructure. *NMR in biomedicine*, 8:375–386, 1996.

[55] A. C. Lloyd. The Regulation of Cell Size. *Cell*, 154(6):1194–1205, 2013.

[56] H. Lyng, O. Haraldseth, and E. K. Rofstad. Measurement of cell density and necrotic fraction in human melanoma xenografts by diffusion weighted

magnetic resonance imaging. *Magnetic Resonance in Medicine*, 43:828–836, 2000.

[57] W. H. Mager and J. Winderickx. Yeast as a model for medical and medicinal research. *Trends in Pharmacological Sciences*, 26(5):265–273, 2005.

[58] G. Majno and I. Joris. Apoptosis, oncosis, and necrosis. An overview of cell death. *The American journal of pathology*, 146(1):3–15, 1995.

[59] Malcom H. Levitt. *Spin Dynamics Basics of Nuclear Magnetic Resonance*. John Wiley & Sons, Ltd, 2nd edition, 2008.

[60] P. Mansfield and Maudsley A. A. Planar Spin Imaging by NMR. *Journal of Magnetic Resonance*, 27:101–119, 1977.

[61] Y. Matsumoto, M. Kuroda, R. Matsuya, H. Kato, K. Shibuya, M. Oita, A. Kawabe, H. Matsuzaki, J. Asaumi, J. Murakami, K. Katashima, M. Ashida, T. Sasaki, T. Sei, S. Kanazawa, S. Mimura, S. Oono, T. Kitayama, S. Tahara, and K. Inamura. In vitro experimental study of the relationship between the apparent diffusion coefficient and changes in cellularity and cell morphology. *ONCOLOGY REPORTS*, 22(3):641–648, 2009.

[62] D. J. Mchugh. The effect of tumour microstructure on diffusion-weighted MRI measurements. *Thesis submitted to the university of Manchester in fulfilment of the degree of doctor of philosophy.*, 2014.

[63] D. W. McRobbie, E. A. Moore, M. J. Graves, and M. R. Prince. *MRI from picture to proton*. 2006.

[64] C. Meier, W. Dreher, and D. Leibfritz. Diffusion in compartmental systems. I. A comparison of an analytical model with simulations. *Magnetic Resonance in Medicine*, 50(3):500–509, 2003.

[65] C. Moon, J.-C. Soria, S. J. Jang, J. Lee, M. Obaidul Hoque, M. Sibony, B. Trink, Y. S. Chang, D. Sidransky, and L. Mao. Involvement of aquaporins in colorectal carcinogenesis. *Oncogene*, 22(43):6699–6703, 2003.

[66] K. F. Morris and C. S. Johnson. Diffusion-ordered 2-dimensional nuclear-magnetic-resonance spectroscopy. *Journal of the American Chemical Society*, 114:3139–3141, 1992.

[67] A. Mukherjee, D. Wu, H. C. Davis, and M. G. Shapiro. Non-invasive imaging using reporter genes altering cellular water permeability. *Nature Communications*, 7:13891, 2016.

[68] J. S. Murday. Self-Diffusion Coefficient of Liquid Lithium. *The Journal of Chemical Physics*, 48(11):4938, 1968.

[69] G. L. Nedjati-Gilani, T. Schneider, M. G. Hall, N. Cawley, I. Hill, O. Ciccarelli, I. Drobnjak, C. A. Wheeler-Kingshott, and D. C. Alexander. Machine learning based compartment models with permeability for white matter microstructure imaging. *NeuroImage*, 150:119–135, 2017.

[70] M. Nilsson. The DOSY Toolbox: A new tool for processing PFG NMR diffusion data. *Journal of Magnetic Resonance*, 200(2):296–302, 2009.

[71] M. Nilsson, J. Lätt, D. Van Westen, S. Brockstedt, S. Lasič, F. Ståhlberg, and D. Topgaard. Noninvasive mapping of water diffusional exchange in the human brain using filter-exchange imaging. *Magnetic Resonance in Medicine*, 69(6):1573–1581, 2013.

[72] M. Nilsson, D. Van Westen, F. Ståhlberg, P. C. Sundgren, and J. Lätt. The role of tissue microstructure and water exchange in biophysical modelling of diffusion in white matter. *Magnetic Resonance Materials in Physics, Biology and Medicine*, 26(4):345–370, 2013.

[73] NobelPrize.org. Nobel Media. The Nobel Prize in Physiology or Medicine 2003.

[74] D. S. Novikov, E. Fieremans, J. H. Jensen, and J. A. Helpern. Random walks with barriers. *Nature Physics*, 7(6):508–514, 2011.

[75] P. Nowell and P. C. The clonal evolution of tumor cell populations. *Science*, 194(4260):23–28, 1976.

[76] J. P. O'Connor, E. O. Aboagye, J. E. Adams, H. J. Aerts, S. F. Barrington, A. J. Beer, R. Boellaard, S. E. Bohndiek, M. Brady, G. Brown, D. L. Buckley, T. L. Chenevert, L. P. Clarke, S. Collette, G. J. Cook, N. M. Desouza, J. C. Dickson, C. Dive, J. L. Evelhoch, C. Faivre-Finn, F. A. Gallagher, F. J. Gilbert, R. J. Gillies, V. Goh, J. R. Griffiths, A. M. Groves, S. Halligan, A. L. Harris, D. J. Hawkes, O. S. Hoekstra, E. P. Huang, B. F. Hutton, E. F. Jackson, G. C. Jayson, A. Jones, D. M. Koh, D. Lacombe, P. Lambin, N. Lassau, M. O. Leach, T. Y. Lee, E. L. Leen, J. S. Lewis, Y. Liu, M. F. Lythgoe, P. Manoharan, R. J. Maxwell, K. A. Miles, B. Morgan, S. Morris, T. Ng, A. R. Padhani, G. J. Parker, M. Partridge, A. P. Pathak, A. C. Peet, S. Punwani, A. R. Reynolds, S. P. Robinson, L. K. Shankar, R. A. Sharma, D. Soloviev, S. Stroobants, D. C. Sullivan, S. A. Taylor, P. S. Tofts, G. M. Tozer, M. Van Herk, S. Walker-Samuel, J. Wason, K. J. Williams, P. Workman, T. E. Yankeelov, K. M. Brindle, L. M. McShane, A. Jackson, and J. C. Waterton. Imaging biomarker roadmap for cancer studies. *Nature Reviews Clinical Oncology*, 14(3):169–186, 2017.

[77] B. P. Olveczky and a. S. Verkman. Monte Carlo analysis of obstructed diffusion in three dimensions: application to molecular diffusion in organelles. *Biophysical journal*, 74(5):2722–2730, 1998.

[78] T. Otaki. Artifact halo reduction in phase contrast microscopy using apodization. *Optical Review*, 7(2):119–122, 2000.

[79] E. Panagiotaki, R. W. Chan, N. Dikaios, H. U. Ahmed, F. Urol, J. O. Callaghan, A. Freeman, D. Atkinson, S. Punwani, D. J. Hawkes, and D. C. Alexander. Microstructural Characterization of Normal and Malignant Human Prostate Tissue With Vascular , Extracellular , and Restricted Diffusion for Cytometry in Tumours Magnetic Resonance Imaging. *Investigative Radiology*, 00(00):1–10, 2015.

[80] E. Panagiotaki, T. Schneider, B. Siow, M. G. Hall, M. F. Lythgoe, and D. C. Alexander. Compartment models of the diffusion MR signal in brain white matter: A taxonomy and comparison. *NeuroImage*, 59(3):2241–2254, feb 2012.

[81] E. Panagiotaki, S. Walker-Samuel, B. Siow, S. P. Johnson, V. Rajkumar, R. B. Pedley, M. F. Lythgoe, and D. C. Alexander. Noninvasive quantification of solid tumor microstructure using VERDICT MRI. *Cancer Research*, 74(7):1902–1912, 2014.

[82] J. Pfeuffer, U. Flo, W. Dreher, and D. Leibfritz. Restricted diffusion and exchange of intracellular water : theoretical modelling and diffusion time dependence of 1 H NMR measurements on perfused glial cells. *NMR in Biomedicine*, 11:19–31, 1998.

[83] P.Mansfield. Multi-planar image formation using NMR spin echoes. *Journal of Physics C: Solid State Physics Multi-planar*, 10:580–594, 1977.

[84] E. M. Purcell, H. M. Torrey, and R. V. Pound. Resonance Absorption by Nuclear Magnetic Moments in a Solid. *Physical Review*, 69(1-2):37–38, 1946.

[85] Y. Qiao, P. Galvosas, T. Adalsteinsson, M. Schönhoff, and P. T. Callaghan. Diffusion exchange NMR spectroscopic study of dextran exchange through polyelectrolyte multilayer capsules. *Journal of Chemical Physics*, 122(21), 2005.

[86] J. D. Quirk, G. L. Bretthorst, T. Q. Duong, A. Z. Snyder, C. S. Springer, J. J. H. Ackerman, and J. J. Neil. Equilibrium water exchange between the intra- and extracellular spaces of mammalian brain. *Magnetic Resonance in Medicine*, 50(3):493–499, 2003.

[87] RABI I. I., J. R. ZACHARIAS, S. MILLMAN, and P. KUSCH. A New Method of Measuring Nuclear Magnetic Moment. *Physical Review Letters*, 51:652, 1938.

[88] F. Schilling, S. Ros, D. E. Hu, P. D'Santos, S. McGuire, R. Mair, A. J. Wright, E. Mannion, R. J. Franklin, A. A. Neves, and K. M. Brindle. MRI measurements of reporter-mediated increases in transmembrane water exchange enable detection of a gene reporter. *Nature Biotechnology*, 35(1):75–80, 2017.

[89] J. Schindelin, I. Arganda-Carreras, E. Frise, V. Kaynig, M. Longair, T. Pietzsch, S. Preibisch, C. Rueden, S. Saalfeld, B. Schmid, J. Y. Tinevez, D. J. White, V. Hartenstein, K. Eliceiri, P. Tomancak, and A. Cardona. Fiji: An open-source platform for biological-image analysis. *Nature Methods*, 9(7):676–682, 2012.

[90] D. Schnapauff, M. Zeile, M. B. Niederhagen, B. Fleige, P. U. Tunn, B. Hamm, and O. Dudeck. Diffusion-weighted echo-planar magnetic resonance imaging for the assessment of tumor cellularity in patients with soft-tissue sarcomas. *Journal of Magnetic Resonance Imaging*, 29(6):1355–1359, jun 2009.

[91] A. Schwab, A. Fabian, P. J. Hanley, and C. Stock. Role of ion channels and transporters in cell migration. *Physiological reviews*, 92(4):1865–913, 2012.

[92] M. J. Shafiee, S. A. Haider, A. Wong, D. Lui, A. Cameron, A. Modhafar, P. Fieguth, and M. A. M. Haider. Apparent Ultra-High b-value Diffusion-Weighted Image Reconstruction via Hidden Conditional Random Fields. *IEEE transactions on medical imaging*, 62:1–14, 2013.

[93] B. Siow, P. L. Hubbard, A. Esposito, M. F. Lythgoe, and D. C. Alexander. Towards model-free estimation of membrane permeability in biological samples. 59(3):214912.

[94] E. O. Stejskal and J. E. Tanner. Spin Diffusion Measurements: Spin Echoes in the Presence of a Time-Dependent Field Gradient. *The Journal of Chemical Physics*, 42(1965):288, 1965.

[95] T. Sugahara, Y. Korogi, M. Kochi, I. Ikushima, Y. Shigematu, T. Hirai, T. Okuda, L. Liang, Y. Ge, Y. Komohara, Y. Ushio, and M. Takahashi. Usefulness of diffusion-weighted MRI with echo-planar technique in the evaluation of cellularity in gliomas. *Journal of Magnetic Resonance Imaging*, 9(1):53–60, 1999.

[96] K. Takata, T. Matsuzaki, and Y. Tajika. Aquaporins: Water channel proteins of the cell membrane. *Progress in Histochemistry and Cytochemistry*, 39(1):1–83, 2004.

[97] T. Tamada, T. Sone, Y. Jo, A. Yamamoto, and K. Ito. Diffusion-weighted MRI and its role in prostate cancer. *NMR in Biomedicine*, 27(1):25–38, 2014.

[98] J. E. Tanner. Intracellular diffusion of water. *Archives of biochemistry and biophysics*, 224(2):416–428, 1983.

[99] H. C. Torrey. Bloch equations with diffusion terms. *Physical Review*, 104(3):563–565, 1956.

[100] Venkataramanan, L., Y. Q. Song and M. D. Hurlimann. Solving Fredholm integrals of the first kind with tensor product structure in 2 and 2.5 dimensions. *IEEE Trans. Signal Process.*, 50:1017–1026, 2002.

[101] A. Waldeck, P. W. Kuchel, A. J. Lennon, and B. E. Chapman. NMR diffusion measurements to characterise membrane transport and solute binding. *Progress in Nuclear Magnetic Resonance Spectroscopy*, 30(1-2):39–68, 1997.

[102] S. Walker-Samuel, R. Ramasawmy, F. Torrealdea, M. Rega, V. Rajkumar, S. P. Johnson, S. Richardson, M. Gonçalves, H. G. Parkes, E. Årstad, D. L. Thomas, R. B. Pedley, M. F. Lythgoe, and X. Golay. In vivo imaging of glucose uptake and metabolism in tumors. *Nature Medicine*, 19(8):1067–1072, 2013.

[103] W. Wang, Q. Li, T. Yang, G. Bai, D. Li, Q. Li, and H. Sun. Expression of AQP5 and AQP8 in human colorectal carcinoma and their clinical significance. *World Journal of Surgical Oncology*, 10(1):242, 2012.

[104] S. Webb. *The Physics of Medical Imaging*. 1988.

[105] R. A. Weinberg. *The Biology of Cancer*. 2014.

[106] World Health Organization. *The global burden of disease 2004*. 2004.

[107] J. Xu, M. D. Does, and J. C. Gore. Quantitative characterization of tissue microstructure with temporal diffusion spectroscopy. *Journal of Magnetic Resonance*, 200(2):189–197, 2009.

[108] B. Zelhof, M. Pickles, G. Liney, P. Gibbs, G. Rodrigues, S. Kraus, and L. Turnbull. Correlation of diffusion-weighted magnetic resonance data with cellularity in prostate cancer. *BJU International*, 103(7):883–888, 2009.